Graduate School in Civil Engineering and Architecture

University of Pavia, Italy

DICAr - Department of Civil Engineering and Architecture

INTEGRATED NONLINEAR MODELLING STRATEGIES FOR THE SEISMIC ANALYSIS OF MASONRY STRUCTURES

A Thesis Submitted in Partial Fulfilment of the Requirements

for the Degree of Doctor of Philosophy in

DESIGN, MODELING AND SIMULATION IN ENGINEERING

Candidate:

Chiara Morandini

Supervisors:

Prof. Andrea Penna – University of Pavia, Italy

Prof. Rui Pinho – University of Pavia, Italy

Prof. Daniele Malomo - McGill University, Canada

February, 2022

Abstract

In the last decades, significant interest has raised in modelling and analysing the structural response of unreinforced masonry (URM) buildings. This aims at conceiving and designing effective interventions to reduce the vulnerability towards seismic actions. Studies based on costly structural testing are often limited to a few benchmark cases, making numerical modelling an excellent option to extend experimental results and a valid solution for understanding URM structural behaviour. Advanced discrete models are widely employed among the available numerical strategies to predict the URM dynamic response, thanks to their ability to account for the heterogeneous nature of masonry and to simulate its behaviour up to the complete collapse. If, on the one hand, the low degree of idealisation of discrete models allows their employment for the extension of experimental tests, on the other hand, they require expert users, the definition of a large number of mechanical parameters and a high computational effort. This last drawback often prevents the use of advanced discontinuum models in the engineering practice or for seismic risk studies, which require the execution of multiple analyses.

In this work, a modelling approach, based on the Applied Element Method (AEM), was combined with more simplified models to exploit the discrete model potential and overcome its limits. To this aim, the AEM was employed as a benchmark to calibrate/validate simplified modelling strategies, improving their reliability when compared to advanced model outcomes. In this context, AEM models were used as a reference to enhance the Equivalent Frame Model (e.g. in the presence of irregular distribution of openings) and to validate a new strength criterion associated with the failure mechanism encountered in a new masonry typology. In the absence of a large suite of experimental tests exploring all the possible setup or configurations, the AEM can provide precious information. On the other hand, the AEM can help to investigate situations requiring a higher level of detail, such as the design of the timber retrofitting system analysed in this work. The ability of the AEM to simulate the structural behaviour up to the complete collapse was also used to investigate the effect of different percentages of ground floor opening on the dynamic response of Dutch terraced houses, performing benchmark analyses to calibrate SDOF models employed for the derivation of fragility functions associated with the different layouts. Finally, AEM models were employed for substructuring façade models of masonry buildings whose global response was effectively studied by EFM. The aim of the study was to predict the debris extent

involved in the collapse of URM façades in case of earthquake loadings. Such an integrated numerical procedure allowed considering a large suite of seismic inputs, overcoming the time-consuming issue.

Acknowledgments

(in Italian)

A Massimiliano

per l'amorevole sostegno e l'eroica pazienza.

Table of contents

List of figures

List of tables

List of symbols

ρ density

f_m compressive strength of masonry

E Young's modulus

G shear modulus

f_t tensile strength

c cohesion

μ friction coefficient

X_{mo} mechanical characteristic of mortar

X_u mechanical characteristic of units

G_{fI} mode I fracture energy

G_{fII} mode II fracture energy

Ψ dilatancy angle

X_i equivalent mechanical characteristic of mortar-units interface

X_w mechanical characteristic of timber elements

f_y yielding stress

X_{OSB} mechanical characteristic of OSB panels

G_{ct} nonlinear shear deformability parameter

β shear softening parameter

α_s shear damage parameter

f_{tu} equivalent tensile strength

f_{bt} tensile strength of brick

k_n spring normal stiffness

k_s spring shear stiffness

V_t volume of debris

A_t area occupied by debris

V_f volume of debris on the front side of the building

A_f area occupied by debris on the front side of the building

V_t volume of debris

D_{max} maximum distance

1.Introduction

1.1 Background

Masonry is one of the oldest and most commonly employed construction materials worldwide, therefore also in seismic prone regions (e.g. D'Ayala 2013). Recent and past seismic events have pointed out the vulnerability of unreinforced masonry (URM) buildings, often responsible for significant earthquake-induced human life and socio-economic losses (Coburn and Spence 2003). Most existing URM buildings are usually non-engineered structures conceived to stand vertical loads, often lacking the seismic details now modern building codes suggest. The lack of efficient connections between structural components, the presence of flexible floors without diaphragm behaviour and thrusting structures equilibrated only by out-of-plane resistance of structural walls significantly influence the seismic vulnerability of older URM buildings, preventing the development of the box-like behaviour required for the design of new masonry buildings. The lack of effective seismic design is even more common in regions not historically prone to earthquakes, as the region of Groningen, recently affected by seismicity induced by the local gas extraction. Recent earthquakes in Italy (L'Aquila 2009, Emilia 2012, Central Italy 2016-17) have raised public awareness regarding the vulnerability of the existing building stock, encouraging governments to promulgate new design codes paying more attention to enforcing minimum seismic requirements (e.g. D.M. 17/01/2018), and to incentivise strengthening interventions via dedicated funding policies.

The seismic response assessment represents the first step for designing seismic mitigation interventions. However, the uncertainties that characterise the mechanical behaviour of masonry and the irregular geometry of buildings, especially the historical ones, make identifying the sources of weakness and the evaluation of the building response a complex task. Researchers have always dedicated their efforts to investigate the sources of vulnerability of masonry buildings performing experimental tests on structural components (Magenes and Calvi 1997; Costa et al. 2011; Graziotti et al. 2019) and entire buildings (Tomaževič et al.1996; Calvi et al. 1996; Yi et al. 2006; Graziotti et al. 2017; Senaldi et al. 2020). Despite the importance of experimental tests for understanding the masonry buildings' response, they are usually expensive, and thus their employment is often limited to research problems. Numerical modelling represents a more economical and practical alternative, and this makes the development of numerical tools one of the main objects of the scientific community's effort in the last decades (D'Altri et al. 2020). Several approaches of varying levels of accuracy are proposed in the literature, ranging from simplified geometrical approaches to advanced micro-modelling methods (Lourenço 2002). The choice of the modelling approach and the level of approximation is related to the structural characteristics and the available time for the analyses, as the computational effort increases with to the model's accuracy.

Simplified approaches, such as story mechanism models (Tomaževič 1978; Braga and Dolce 1982), methods based on limit analysis (Block et al. 2006; Milani et al. 2006), equivalent single-degree-of-freedom systems (Graziotti et al. 2016; Snoj and Dolšek 2020) or continuum-based models (Lourenço et al. 1998; Milani et al. 2007) have been widely used over the years to study masonry structural behaviour. Amongst others, Equivalent Frame Model (EFM)-based approaches (e.g. Magenes and Della Fontana 1998; Lagomarsino et al. 2013) demonstrated to represent an acceptable solution for simulating the nonlinear response of large-scale URM buildings in a reasonable time (Raka et al. 2015; Penna et al. 2016; Kallioras et al. 2019; Vanin et al. 2020). Thanks to its limited computational cost and the easy interpretation of results, the EFM is widely employed by practitioners and researchers, and its use is also endorsed by several codes (Eurocode 8 (CEN 2005); NTC2018 (D.M. 17/01/2018)). The level of idealisation required by simplified approaches limits their ability to describe the heterogeneous nature of masonry, the interaction between its components and the possibility of representing the actual degree of connection between elements. Such a level of accuracy can be attained by applying micro-modelling approaches that can represent masonry characteristics at the micro-scale (Moreau 1988; Gambarotta and Lagomarsino 1997; Lourenço and Rots 1997; Casolo and Peña 2007; Lemos 2007). Among other discrete modelling approaches, the Applied Element Method (AEM, Meguro and Tagel-Din 2000) is one of the most employed for analysing extreme loading conditions such as seismic actions, demolition, and explosion. This level of detail requires expert users, complex constitutive models and the definition of several mechanical parameters, which are not frequently available from characterisation tests. Moreover, advanced micro-modelling strategies require a significant computation effort, generally making their use prohibitively expensive for practitioners' aims and for numerically-based seismic risk studies, where a large suite of numerical simulations is needed.

Despite those limitations, advanced micro-models offer valuable help in research problems and a reliable benchmark to improve and validate more simplified modelling approaches. The possibility to extend experimental results using numerical tools allows to consider a wide range of different setup or material/structural configurations, also enabling the optimisation of the most effective solution in the design phase. Among others, discrete models have the ability to reproduce the actual units arrangement, local weaknesses, and the masonry behaviour at micro-scale, including crack propagation, element separation, and recontact. These features allow the employment of discrete approaches to simulate the structural response up to the complete collapse, which is rarely reached in the experimental tests due to the risk of causing damage to the laboratory equipment and instruments.

1.2 Research motivation and objectives

In this work, the use of discrete models was combined with more simplified modelling approaches to maximise the benefits and limit the drawbacks of these tools. The AEM was chosen for its ability to reliably represent masonry behaviour up to the complete collapse, including separation and recontact between elements in a reasonable timeframe. In particular, the open issues outlined in the following paragraphs were investigated.

1.2.1 EF frame discretisation of URM walls with irregular opening layouts

The ability of discrete models to reproduce crack propagation in masonry walls was employed to discuss different discretisation criteria and to solve typical EFM issues. Indeed, despite the wide use of EFM for the assessment of masonry structures, the problem of choosing a proper discretisation criterion still represents an open challenge. The EFM idealisation of masonry structures into a frame with deformable regions and rigid nodes, is derived from experimental and post-earthquake observations indicating that damage is mainly located in spandrels and piers, while their intersections work as rigid parts. The geometry of these elements is defined according to a discretisation criterion selected a priori, a complex endeavour in the presence of irregular opening distributions and other factors affecting crack propagation. The problem of the EFM discretisation with irregular opening layouts was then investigated with AEM analyses to provide indications to define the frame geometry.

1.2.2 Influence of the openings percentage on seismic response of Dutch buildings

In the last decades, gas extraction activities that are exposing the region of Groningen (the Netherlands) to induced seismicity have required a complete regional seismic risk assessment. Extensive numerical and experimental campaigns have been performed to evaluate the seismic response of Dutch structures that are particularly vulnerable due to the lack of effective seismic detailing and the presence of large ground floor openings. This aspect was investigated in a full-scale shake-table test performed by Miglietta et al. (2021), which, however, was limited to a single configuration. The validation of an AEM model and the analyses of similar buildings with different opening percentages have been carried out in this study to evaluate the seismic vulnerability of the local building typologies. The creation of models of different configurations has also provided a reliable benchmark to validate simplified SDOF models for the development of fragility functions.

1.2.3 Numerical strategy for the seismic assessment of a timber retrofitting solution

The recently increased environmental awarness has pushed structural engineers to design new buildings and retrofit interventions with particular attention to sustainability, thus employing new strategies and materials. The need to design environmentally sustainable and seismically effective solutions has been faced with the lack of numerical models capable of simulating the response of structures, materials and retrofits not traditionally found in seismic prone regions. In this context, the light timber frame retrofit proposed by Miglietta et al. (2021) represents a sustainable, reversible and cost-effective solution combining thermal insulation with seismic enhancement. The availability of the experimental shake-table test results of a full-scale building retrofitted with this solution has encouraged the validation of a detailed AEM model to investigate the effect of different frame configurations on the dynamic response of URM buildings.

1.2.4 Numerical strategies for URM walls with unfilled head joints

As mentioned above, the increasing attention to the sustainability of the built environment led to the proposal of structural masonry adopting hollow clay units with very thin webs

and shells and unfilled head joints, to improve the thermal and acoustic performance of walls. A recent experimental campaign performed by Morandi et al. (2021) investigated the performance of this masonry typology to evaluate its possible use in moderate seismicity areas. The limited number of tests has been overvcome through the development of numerical AEM models, to extend the experimental results to different configurations and loading cases and to validate simplified EFM strategies to be used in the professional field. These models are capable of representing the in-plane response of these masonry walls, including the cyclic behaviour of the unfilled vertical joints, with the possible separation and recontact between units.

1.2.5 Integrated modelling strategy for the numerical prediction of debris distribution

Recent Italian earthquakes (e.g. the 2016 Central Italy sequence) highlighted once more the vulnerability of historical city centres and the need to prevent road obstructions that may slow down rescue operations. Predicting the amount and extent of debris after a seismic event is crucial for assessing the indirect vulnerability of the urban road system, hence allowing the draft of emergency plans that also prioritise retrofit interventions along selected rescue routes. Discrete numerical models can be employed for predicting debris distribution, but the time required for the analyses hinders their application to large suites of simulations. On the contrary, simplified modelling strategies cannot reproduce the building collapse. An integrated modelling strategy has thus been proposed, combining global EFM and local AEM models, to offer a valid alternative to empirical formulae for the evaluation of debris distribution which could also be employed in future risk studies.

1.3 Contents organisation

The thesis is organised into eight chapters. Each chapter is structured as a paper and refers to a journal or a conference paper to be submitted, under review or already published. The references related to the published papers are reported at the beginning of each section before the abstract.

After this brief introduction, i.e. Chapter 1, a review of the currently available discrete modelling approaches is provided in Chapter 2. First, masonry mechanical behaviour and its representation through the most commonly employed constitutive models are discussed. Then, the main features, differences and limits of discrete models are addressed in a practically oriented discussion.

In Chapter 3, the problem of the definition of the discretisation criterion for EFM in the presence of irregular distribution of openings is scrutinised. The ability of the AEM model to describe both stress and crack propagation was exploited to investigate the monotonic lateral response of irregular façades, extending the results of the experimental test performed only on a regular configuration. The AEM and the EFM models were first calibrated against the results of shear-compression tests on individual walls. Then, the models were validated against a monotonic quasi-static experimental test on a full-scale regular façade. Finally, the results of pushover analyses performed with the validated

discrete models on several façades with irregular opening layouts were employed as a benchmark to evaluate the reliability of EFM discretised with different criteria. Potential solutions to overcome typical EF discretisation issues are also proposed to better approximate micro-modelling outcomes.

In Chapter 4, a discrete model was employed to investigate the impact of ground floor openings percentage on the dynamic response of typical Dutch terraced houses. The model was first validated against experimental results of a full-scale shake-table test. A parametric study with various ground floor openings percentages was performed with various acceleration time-histories to investigate how the extent of openings may affect the seismic vulnerability of typical URM Dutch terraced houses. The AEM's capability to reproduce the building response up to the collapse was employed to perform incremental dynamic analyses at different intensity levels. These results were used to calibrate simplified models employed with a large number of acceleration time-histories needed for deriving fragility functions.

In Chapter 5, a discrete approach was employed to investigate the influence of different retrofit configurations on the seismic response of URM cavity-wall buildings. The modelling strategy for reproducing an innovative timber retrofitting solution was tested by simulating experimental shear-compression tests on retrofitted and non-retrofitted walls. Then, the model was validated through the simulation of a shake-table test on a full-scale retrofitted specimen. A parametric study was then conducted to investigate the influence of different retrofit layouts on the building's global seismic response, proving once again the capability of an advanced modelling approach to extend experimental findings to unexplored configurations improving the designed solution effectiveness.

In Chapter 6, the AEM was applied to simulate in-plane shear compression tests on walls made of a new masonry typology consisting of hollow units, unfilled head joints and thin glue mortar head joints. First, a discrete modelling strategy was developed and validated against experimental tests; to be used as a benchmark to validate and improve the reliability of simplified modelling strategies. The EFM was also employed to simulate this masonry behaviour, and a new strength criterion was implemented and tested against experimental shear-compression tests. The results were compared with those obtained with the AEM models with the aim to extend that comparison to different configurations and setups.

In Chapter 7, the combined application of EFM and an AEM-based discrete model to predict the extent of debris after the collapse is presented. The EFM were employed to evaluate the global response of a real full-scale building case study under ground motions of varying intensities. Among these, the ground motion causing the exceedance of established thresholds in the EFM were selected and considered for the next investigations. A discrete model was made to represent the portion of the building most probably involved in a local mechanism. The local analyses performed with the AEM models allowed of estimating the amount of debris and the maximum distance reached by rubbles. This information is crucial for drafting emergency plans to avoid infrastructures interruption and prioritise strengthening interventions.

In Chapter 8, the main outcomes of the present thesis are summarised, including a discussion on future developments.

Finally, two appendices, A and B, have been included to briefly present the main aspects of the two modelling approaches employed in this thesis: the Applied Element Method and the Equivalent Frame Model.

References

Block P, Ciblac T, Ochsendorf J (2006) Real-time limit analysis of vaulted masonry buildings. Comput Struct 84:1841–1852.

Braga F, Dolce M (1982) A method for the analysis of antiseismic multi-storey masonry buildings (In Italian). In: Proceedings of the 6th International Brick Masonry Conference. Rome, pp 1089–1099.

Calvi GM, Kingsley GR, Magenes G (1996) Testing of masonry structures for seismic assessment. Earthq Spectra 12:145–162.

Casolo S, Peña F (2007) Rigid element model for in-plane dynamics of masonry walls considering hysteretic behaviour and damage. Earthq Eng Struct Dyn 36:1029–1048. https://doi.org/10.1002/eqe.670

Coburn A, Spence R (2003) Earthquake protection. Second edition. Ed. John Wiley & Sons, Ltd. ISBN: 0-471-49614-6.

Costa AA, Penna A, Magenes G (2011) Seismic performance of autoclaved aerated concrete (AAC) masonry: from experimental testing of the in-plane capacity of walls to building response simulation. J Earthq Eng 15:1–31.

D.M. 17/01/2018 (2018) Norme Tecniche per le Costruzioni (NTC2018), Gazzetta Ufficiale, n. 42 del 20/ 02/2018- Supplemento ordinario n.8 (in Italian).

D'Altri AM, Sarhosis V, Milani G, et al (2020) Modeling Strategies for the Computational Analysis of Unreinforced Masonry Structures: Review and Classification. Arch Comput Methods Eng 27:1153–1185. https://doi.org/10.1007/s11831-019-09351-x.

D'Ayala D (2013) Assessing the seismic vulnerability of masonry buildings. In: Handbook of Seismic Risk Analysis and Management of Civil Infrastructure Systems. https://doi.org/10.1533/9780857098986.3.334.

European Committee for Standardization (CEN); (2005) Eurocode 8: Design of structures for earthquake resistance – Part 3: General rules, seismic actions and rules for buildings, Design Code EN 1998-3. Eur Comm Stand Brussels.

Gambarotta L, Lagomarsino S (1997) Damage Models for the Seismic Response of Brick Masonry Shear Walls. Part II: the Continuum Model and Its Applications. Earthq Eng Struct Dyn 26:441–462. https://doi.org/10.1002/(SICI)1096-9845(199704)26:4<441::AID-EQE651>3.0.CO;2-0.

Graziotti F, Penna A, Magenes G (2016) A nonlinear SDOF model for the simplified evaluation of the displacement demand of low-rise URM buildings. Bull Earthq Eng 14:1589–1612. https://doi.org/10.1007/s10518-016-9896-5.

Graziotti F, Tomassetti U, Kallioras S, et al (2017) Shaking table test on a full scale URM cavity wall building. Bull Earthq Eng 15:5329–5364. https://doi.org/10.1007/s10518-017-0185-8.

Graziotti F, Tomassetti U, Sharma S, et al (2019) Experimental response of URM single leaf and cavity walls in out-of-plane two-way bending generated by seismic excitation. Constr Build Mater 195:650–670. https://doi.org/10.1016/j.conbuildmat.2018.10.076.

Kallioras S, Graziotti F, Penna A (2019) Numerical assessment of the dynamic response of a URM terraced house exposed to induced seismicity. Bull Earthq Eng 17:1521–1552. https://doi.org/10.1007/s10518-018-0495-5.

Lagomarsino S, Penna A, Galasco A, Cattari S (2013) TREMURI program: An equivalent frame model for the nonlinear seismic analysis of masonry buildings. Eng Struct 56:1787–1799. https://doi.org/10.1016/j.engstruct.2013.08.002.

Lemos J V (2007) Discrete element modeling of masonry structures. Int J Archit Herit 1:190–213.

Lourenço PB (2002) Computations on historic masonry structures. Prog Struct Eng Mater 4:301–319. https://doi.org/10.1002/pse.120.

Lourenço PB, Rots J, Blaauwendraad J (1998) Continuum Model for Masonry: Parameter Estimation and Validation. J Struct Eng 124:642–652. https://doi.org/10.1061/(ASCE)0733-9445(1998)124:6(642).

Lourenço PB, Rots JG (1997) Multisurface Interface Model for Analysis of Masonry Structures. J Eng Mech 123:660–668. https://doi.org/10.1061/(ASCE)0733-9399(1997)123:7(660).

Magenes G, Calvi GM (1997) In-plane seismic response of brick masonry walls. Earthq Eng Struct Dyn 26:1091–1112.

Magenes G, Della Fontana A (1998) Siplified on-Linear Seismic Analysis of Masonry Buildings. In: Proceedings of the Fifth International Masonry Conference. London, United Kingdom, pp 1–313.

Meguro K, Tagel-Din H (2000) Applied element method for structural analysis: Theory and application for linear materials. Struct Eng Eng 17:21–35.

Miglietta M, Damiani N, Guerrini G, Graziotti F (2021) Full-scale shake-table tests on two unreinforced masonry cavity-wall buildings: effect of an innovative timber retrofit. Bull Earthq Eng 2561–2596. https://doi.org/10.1007/s10518-021-01057-5.

Milani G, Lourenço PB, Tralli A (2006) Homogenised limit analysis of masonry walls, Part I: Failure surfaces. Comput Struct 84:166–180. https://doi.org/10.1016/j.compstruc.2005.09.005.

Milani G, Zuccarello FA, Olivito RS, Tralli A (2007) Heterogeneous upper-bound finite element limit analysis of masonry walls out-of-plane loaded. Comput Mech 40:911–931. https://doi.org/10.1007/s00466-006-0151-9.

Morandi P, Albanesi L, Magenes G (2021) In-Plane Cyclic Response of New Urm Systems

with Thin Web and Shell Clay Units. J Earthq Eng 25:1533–1564. https://doi.org/10.1080/13632469.2019.1586801.

Moreau JJ (1988) Unilateral contact and dry friction in finite freedom dynamics. In: Nonsmooth mechanics and Applications. Springer, pp 1–82.

Penna A, Senaldi IE, Galasco A, Magenes G (2016) Numerical Simulation of Shaking Table Tests on Full-Scale Stone Masonry Buildings. Int J Archit Herit 10:146–163. https://doi.org/10.1080/15583058.2015.1113338.

Raka E, Spacone E, Sepe V, Camata G (2015) Advanced frame element for seismic analysis of masonry structures: model formulation and validation. Earthq Eng Struct Dyn 44:2489–2506.

Senaldi IE, Guerrini G, Comini P, et al (2020) Experimental seismic performance of a half-scale stone masonry building aggregate. Bull Earthq Eng 18:609–643. https://doi.org/10.1007/s10518-019-00631-2.

Snoj J, Dolšek M (2020) Pushover-based seismic risk assessment and loss estimation of masonry buildings. Earthq Eng Struct Dyn 49:567–588. https://doi.org/10.1002/eqe.3254.

Tomazevic M (1978) The computer program POR. Report ZRMK. Inst Test Res Mater Struct Ljubljana.

Tomaževič M, Lutman M, Petković L (1996) Seismic Behavior of Masonry Walls: Experimental Simulation. J Struct Eng 122:1040–1047. https://doi.org/10.1061/(ASCE)0733-9445(1996)122:9(1040).

Vanin F, Penna A, Beyer K (2020) Equivalent-Frame Modeling of Two Shaking Table Tests of Masonry Buildings Accounting for Their Out-Of-Plane Response. Front Built Environ 6:. https://doi.org/10.3389/fbuil.2020.00042.

Yi T, Moon FL, Leon RT, Kahn LF (2006) Lateral Load Tests on a Two-Story Unreinforced Masonry Building. J Struct Eng Eng 132:643–652. https://doi.org/10.1061/(ASCE)0733-9445(2006)132:5(643).

2. Discrete modelling approaches for unreinforced masonry structures: literature review

Morandini C, Davis L, Malomo D and Penna A. Discrete modelling approaches for existing unreinforced masonry structures *(to be submitted)*.

Abstract

Discrete modelling approaches are naturally suitable to represent the heterogeneity of masonry, although the associated high computational cost often restricts their application. However, recent computational developments have allowed the more widespread application of these advanced approaches for research purposes and engineering practice. The increasing use of these techniques and the proliferation of new tools require a careful selection of the more suitable discrete model based on the problem analysed. Currently available discrete models are presented in this work, and their main features and differences are discussed. The application of these modelling approaches is examined in a practically-oriented discussion.

2.1 Introduction

Unreinforced masonry structures (URM) are non-engineered systems representing a large portion of the existing building stock and one of the major causes of earthquake-induced socio-economic losses worldwide (Coburn and Spence 2003). The rehabilitation and retrofit of seismically vulnerable URM constructions are thus of utmost importance for ensuring public safety and protecting local economies. Assessing the seismic response of existing URM structures (i.e. the first step for designing seismic mitigation measures) is, however, a complex task. The development of numerical tools for the seismic assessment of URM structures became the object of the scientific community's effort in the last decades (D'Altri et al. 2020). Numerical modelling is nowadays the most employed seismic evaluation approach for URM structures and it is also endorsed by building codes (e.g D.M. 17/01/2018). Several approaches of varying complexity were made available in the literature throughout the years, ranging from simplified geometrical approaches (Heyman 1966) to advanced micro-modelling numerical methods (Meguro and Tagel-Din 2000; Lemos 2007). The adequacy of the selected modelling scale and level of detail is unavoidably related to the expected seismic response (e.g. in-plane, (IP), vs out-of-plane, (OOP), governed) and determines the required technical competency and analysis time. It

is therefore essential for both engineering professionals and researchers to identify the most appropriate modelling strategy.

Several classifications of modelling approaches for unreinforced masonry structures are available in literature. These include classifications based on modelling scale and strategy (Lourenço 2002; D'Altri et al. 2020) or on the analyses approach (Roca et al. 2010; Lagomarsino and Cattari 2015). Among these, the classification based on model scale proposed by Lourenço (2002) is nowadays widely accepted by researchers and it intuitively classifies modelling strategy based on modelling at different scales: macro (component scale), meso (masonry cell scale) and micro-models (joint scale), see Figure 2.1.
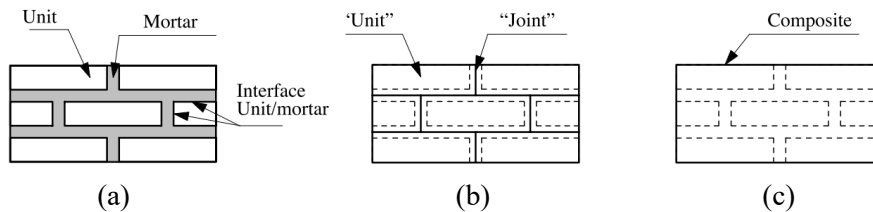
Figure 2.1 Modelling strategies for URM: a) detailed micro-modelling, b) simplified micro-modelling, c) macro-modelling (adapted from Lourenço et al. (1998))

Macro-models, typically implemented in Equivalent Frame-based models (Chen et al. 2008; Magenes et al. 2014; Raka et al. 2015; Vanin et al. 2020; Bracchi and Penna 2021; Bracchi et al. 2021), are usually preferred by practitioners because of their low computational cost, intuitive mesh generation and a limited number of parameters needed, which can be obtained from basic masonry tests or simplified homogenisation procedures. In simplified micro-models (or meso-models) properties of units and mortar are lumped in a spring layer with zero thickness connecting units that are expanded, including joint thickness. Recent improvements in computer performance allowed to reduce the degree of idealisation by representing masonry explicitly, unit-by-unit, in the so-called detailed micro-modelling approaches (Lourenço 2002). Finite Element Method (FEM) based approaches have been satisfactorily used at the micro (Petracca et al. 2017; Abdulla et al. 2017) and meso (Aref and Dolatshahi 2013; Giambanco et al. 2018) scale levels, but they cannot reproduce separation, recontact, and collapse. On the other hand, micro-modelling approaches based on the discrete methods (or discontinuous- Pulatsu et al. 2020a - where rigid or deformable units are connected through nonlinear springs) can reasonably capture the heterogeneous nature of masonry, representing its behaviour up to complete collapse (Karbassi and Nollet 2013; Keys and Clubley 2017; Malomo et al. 2020a), including the automatic detection of cracks and the simulation of their propagation.

Initially conceived for soil mechanics problems (Cundall and Strack 1979), discrete models proved to be particularly suitable for simulating a wide range of applications in different fields ranging from, geomechanics (Cheng et al. 2004; O'Sullivan 2008; Bandera et al. 2021) to fluid dynamics (Xu and Yu 1997), structural analysis (Lemos 1997), impact and blast (Keys and Clubley 2017). More recent applications of the discrete element method in structural analysis and assessment of unreinforced masonry structures (URM) (Lemos

2007) include modifications of this numerical approach such as the Rigid Body and Spring Models (RBSM) (Casolo and Peña 2007), and the Applied Element Method (AEM) (Meguro and Tagel-Din 2000). Other discrete approaches accounting for the discontinuity of the structure and based on the physics of contact and friction among blocks are the Discontinuous Deformation Analysis (DDA) and the Non Smooth Contact Dynamics (NSCD) (Moreau 1988). More recently, to overcome the problem of the high computational cost which related to the accuracy of discrete approaches, macro-discrete models have been developed for assessing the seismic response of URM structures in more reasonable timeframes (Pantò et al. 2017; Chácara et al. 2018; Malomo and DeJong 2021a, b).

This work presents a review of the main discrete approaches for the analysis of existing masonry structures. First, a brief overview on the mechanical behaviour of masonry and the most commonly employed mechanical models is presented. Then a review of the most commonly employed discrete methods is proposed based on their applications, limits, and advantages.

2.2 Masonry mechanical behaviour

Masonry is a heterogeneous material composed of units and mortar. Units are typically bricks (e.g. clay or calcium-silicate), blocks (e.g. hollow clay blocks) or irregular stone, whereas joints can be either mortar or dry. The quality of masonry components, the size and arrangement of the units (Malomo et al. 2019a), the joint width, and the quality of workmanship, construction and maintenance play a key role in the performance of the structural system when subjected to seismic action.

At the macro-scale, masonry behaviour and the occurrence of different failure modes depend on several aspects such as the level of vertical compression, aspect ratio (i.e. the ratio between height and length of the wall) and quality of mortar and units. Flexural and shear responses (or hybrid modes) govern the in-plane behaviour of walls, resulting in different lateral displacement, energy dissipation and strength capacities. The possible in-plane failure modes for a masonry wall are presented in Figure 2.2 and they are: (a) flexural failure with crack through mortar joints, (b) masonry crushing, (c) rigid overturning, (d) shear stepped cracks through both bed and head joints, (e) sliding along the bed joints, f) shear failure with cracks through units. Flexural failures (Figure 2.2a,b,c) usually occur in slender panels, whereas squat walls are more likely affected by shear failure modes (Figure 2.2d, e, f). A low level of compression can be related to horizontal flexural cracking (Figure 2.2a) or sliding along bed joints (Figure 2.2e), whereas higher vertical stress might cause flexural/rocking behaviour with toe-crushing (Figure 2.2b) or diagonal shear cracks (Figure 2.2d,f). The properties of masonry components also affect the occurrence of one failure mode or the others. Depending on the relative strength of units to mortar different types of failure can occur; shear stepped cracks through joints in the case of strong units and weak mortar, or shear failure with cracks through units in the case of strong mortar and weak units. A low tensile strength favours the development of horizontal flexural cracks through joints, whereas a low compressive strength causes the failure at the compressed toe in the case of flexural/rocking mechanism.

Out-of-plane (OOP) failures are also important causes of the structural collapse in unreinforced masonry buildings subjected to seismic actions (Graziotti et al. 2019). Depending on the boundary conditions, the OOP failure modes can be one (Figure 2.2g) or two-way bending (Figure 2.2h). The first type of failure occurs in longer walls and walls without side supports, whereas the two-way bending occurs in walls with at least one vertical edge supported.
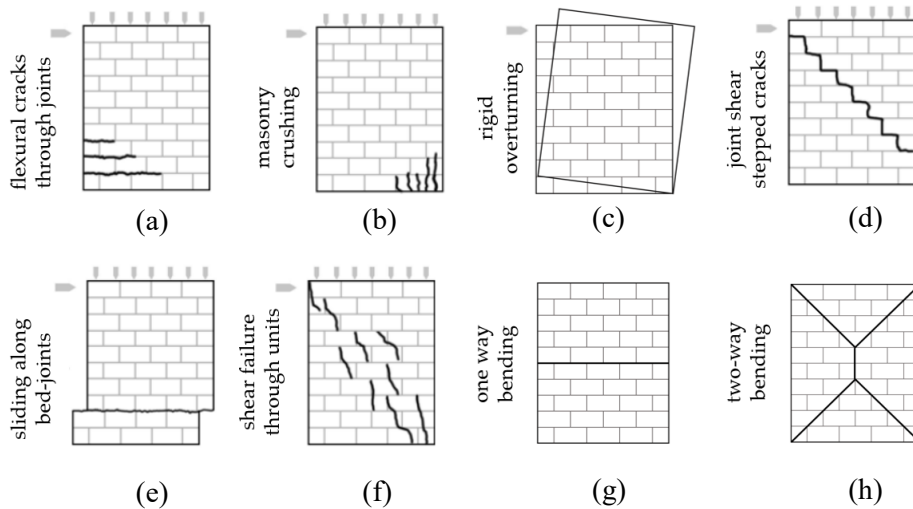
Figure 2.2 In-plane failure mode of a URM panel: a) flexural failure mode with cracks through bed joints, b) masonry crushing in compression, c) rigid overturning, d) diagonal shear failure with stepped cracks through joints, e) sliding along bed joints, and f) diagonal shear failure with cracks through bricks. (adapted from Malomo et al. (2018a)). Out of plane failure mode of a URM panel: g) one-way bending, and h) two-way bending.

Similar to what is seen at the macro-scale, masonry failure can be represented by five failure types at the micro-scale level (as shown in Figure 2.3): a) joint debonding, b) sliding along bed joints or head joints, c) cracking of bricks under direct tension, d) diagonal tensile cracking of bricks under shear-compression and e) crushing.
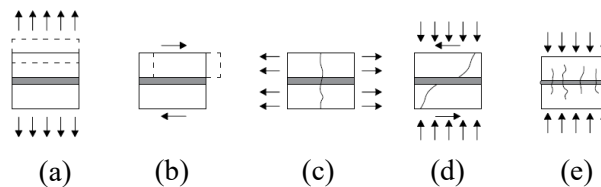
Figure 2.3 Masonry failure mechanisms: a) joint debonding, b) sliding along joints, c) unit direct tension cracking, d) shear-compression cracking of unit and e) crushing

For tensile, (Figure 2.3a,c), compressive, (Figure 2.3e), and shear, (Figure 2.3b,d), failures, masonry exhibits a softening behaviour with the progressive deterioration of strength and stiffness with increasing strain. This is an important feature of quasi-brittle materials such as mortar, brick, stone, and concrete, which must be accounted for by the adopted

constitutive model. Softening is mainly caused by the progressive growth of internal cracks (Angelillo et al. 2014), and it causes energy dissipation, represented by the area below the stress-strain curve in Figure 2.4a), known as fracture energy (G_f, in tension, failure mode I), and compressive fracture energy, G_c (Figure 2.4b) (van der Pluijm 1997). In the case of shear deformation under lateral loading, mode II, the related dissipated energy is identified as the integral of the stress-strain curve in the absence of normal stress (failure mode II fracture energy, G_f^{II}, Figure 2.4c). Moreover, the lateral deformation in a shear test is often accompanied by a volumetric expansion due to the roughness (i.e. the asperity) of the cracked surface. This phenomenon, experimentally observed by several researchers (van der Pluijm 1993; Andreotti et al. 2018; Sharma et al. 2021), is accounted for by the dilatancy angle Ψ, describing the relation between the shear and the normal displacement.
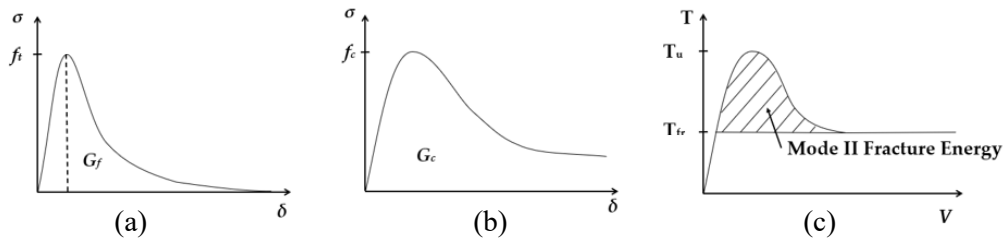
Figure 2.4 Masonry softening in a) tension, b) compression (adapted from (Angelillo et al. 2014)) and c) shear (adapted from van der Pluijm (1993))

Modelling the mechanical behaviour of masonry to represent its heterogeneity with advanced numerical models requires the characterisation of several parameters included in the tables below that should be inferred from experimental tests on masonry and its components (mortar and units) or derived from empirical and theoretical relations when experimental data are not available. Table 2.1 reports the most commonly-employed characterisation tests and the related mechanical parameters required by the more advanced constitutive laws.

Table 2.1 Mechanical parameter and related characterisation tests for masonry

Compressive strength	Young's modulus	Tensile strength	Cohesion	Friction coefficient
f_m	E_m	$f_{t,m}$	c	μ
Uniaxial compression test	Uniaxial compression test	Diagonal compression test	Triplet test with Mann and Müller (1982) correction[*]	Triplet test with Mann and Müller (1982) correction[*]
	Direct, homogenisation (Mayorca and Meguro 2003; Malomo et al.2018b) or empirical relations			

[*]The Mann and Müller correction accounts for the presence of head joints in the transition from the local to the global strength criterion

The parameters listed in Table 2.1 can be used to describe the mechanical behaviour of masonry in continuum macro-models, where the heterogeneity of this material is neglected, as equivalent homogenised properties are assumed. Table 2.2 and Table 2.3 reported mortar and unit properties required in more detailed modelling approaches. These parameters could be used to explicitly describe the behaviour of mortar and units or to derive the equivalent properties of micro-model elements interfaces.

Table 2.2 Mechanical parameter and related characterisation tests for mortar

Compressive strength	Young's modulus	Tensile strength	Cohesion
f_{mo}	E_{mo}	$f_{t,mo}$	c^{**}
Uniaxial compressive test on mortar cube or prism	Uniaxial compressive test on mortar cube or prism	Flexural tensile strength test on mortar prisms	Triplet test
	Theoretical or empirical formulae (U.B.C. 1991; Matysek and Janowski 1996; Brooks and Baker 1998; Ciesielski 1999)		
Friction coefficient	Mode I fracture energy	Mode II fracture energy	Dilatancy angle
μ^{**}	G_{fI}^{**}	G_{fI}^{**}	Ψ^{**}
Triplet test	Couplet tensile test	Triplet test	Triplet test

**These parameters are related to joints

Table 2.3 Mechanical parameter and related characterisation tests for units

Compressive strength	Young's modulus	Tensile strength	Mode I fracture energy
f_u	E_u	$f_{t,u}$	G_{fI}
Uniaxial compressive test on brick unit	Uniaxial compressive test on brick unit	Flexural strength test on brick units or splitting test	Tensile test
	Theoretical or empirical formulae (Jäger et al. 2004; Kaushik et al. 2007)		

2.3 Constitutive models for masonry

Constitutive models represent the mathematical description of the materials' mechanical behaviour and they are required to represent the structural response in numerical models. Different levels of detail and, consequently, different levels of approximation, can be adopted nowadays to model masonry structures. When considering the macro-scale level,

masonry failure modes are usually represented by strength criteria assigned to the macroelement (e.g. Gambarotta and Lagomarsino 1997; Lourenço et al. 1998; Bracchi and Penna 2021; Bracchi et al. 2021). On the other hand, micro-modelling approaches can represent the mutual interaction between masonry components accounting for the failure modes at the micro-scale level, as shown in Figure 2.3. Constitutive models for masonry are usually developed with a phenomenological approach in which the observed mechanism is represented to have consistency between simulation and experiments (Lourenço et al. 1995). A brief overview of the most commonly employed mathematical description for discrete models is presented in the following.

The multi-surface cap model originally proposed by Lourenço and Rots (1997) and presented in Figure 2.5, is one of the most commonly adopted in discrete models. This model combines the compression cap with Coulomb's friction law and a tension cut-off accounts for joint failure modes (a)-(b) and (e) in Figure 2.3, which involve both mortar and units. Each failure mode is associated with a yielding surface in the plasticity model. Cohesion, involved in the sliding mode (Figure 2.3b), and bond tensile strength (Figure 2.3c), are constant until the stress reaches the yielding surface. After that, an exponential equation accounting for the softening deterioration of both cohesion and tensile strength is defined. For the cap model, an ellipsoid interface model is adopted.
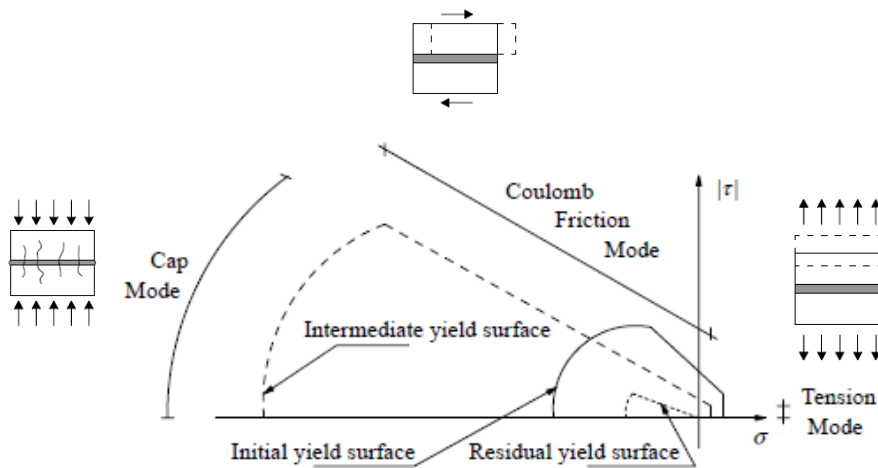
Figure 2.5 Interface cap constitutive model (adapted from Lourenço (1996))

Several numerical tools implement variations of this original formulation, often assuming further simplifications (e.g. Pandey and Meguro 2004). An example is the linearised version of the multi-surface cap model, adopted by Mayorca and Meguro (2003). This revision simplifies the tension cut off and Coulomb's friction law from exponential to linear softening equations. Some applications of the Applied Element Method (AEM) set cohesion and tensile strength to zero after the attainment of the peak (Malomo et al. 2018b). A similar concept is proposed by the damage model for mortar joints introduced by Gambarotta and Lagomarsino (1997). This model considers mortar damage and mortar-

brick interface decohesion introducing a damage variable governing the damage evolution associated with the extension of cracks and sliding of mortar joints.

Constitutive models developed for quasi-brittle materials are usually assumed to represent the behaviour of masonry units (e.g. Khoo and Hendry 1973; Lee and Fenves 1998). The behaviour of masonry in compression is conceptually similar to the concrete one, with hardening and softening branches before and after the peak strength, and consequently, constitutive models originally developed for this material are often adopted (e.g. Lee and Fenves 1998; Maekawa and El-Kashif 2004), Figure 2.6.
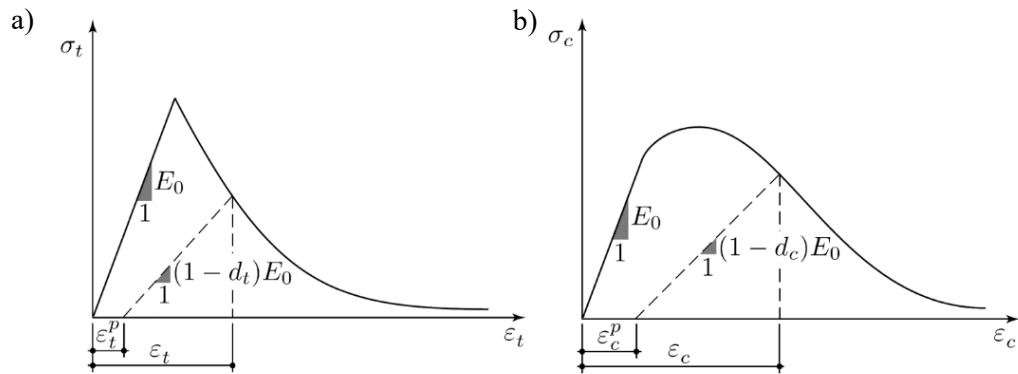
Figure 2.6 Plastic-damaging behaviour of blocks: a) tension and b) compression (adapted from D'Altri et al. (2019))

2.4 Discrete modelling approaches

A wide range of models is now available for the simulation of the mechanical behaviour of masonry, from the more advanced detailed micro-models to the wide-spread simplified macro-modelling approaches. This section presents an overview of the most commonly employed approaches for representing masonry behaviour at a small-scale level, focusing on discrete models.

Micro-modelling approaches are the most advanced tools capable of reproducing masonry's complex behaviour in detail. The most accurate micro-modelling techniques allow the explicit representation of masonry components, mortar and units, and their interaction without needing any interpretation of failure modes and with the direct evaluation of the mechanical parameters from small characterisation tests. These approaches are typically developed in the finite element (FE) or the discrete element method (DEM) framework. In the framework of FEM, with explicitly modelled units and mortar, phenomena such as the volumetric expansion of units under compression or dilatancy can be captured.

In Figure 2.7, several small-scale applications of detailed FEM micro-models are presented. Based on continuum mechanics, FEM approaches cannot simulate strong discontinuities between blocks. To overcome this problem, joint interface elements can be

included in the FE mesh to model the response of discontinuities, corresponding to the cracking of masonry, block separation, rotation, or frictional sliding. This evolution is commonly included in the hybrid FEM-DEM models. Due to their high computational cost, FEM or hybrid FEM-DEM models are typically used for small scale research problems, such as those presented in Figure 2.7. In discrete models, units are modelled as either rigid or deformable elements, expanded to include mortar joint thickness and connected by spring interfaces accounting for mortar and mortar-unit interaction. These approaches are usually included in the "simplified micro-models" or "meso-models" (Lourenço 2002) and lead to accurate results even in large deformation fields, with lower computational effort compared to FEM. Cundall (1971) initially proposed the Discrete Element Method (DEM) for soil mechanics applications to describe discontinuous phenomena in large deformation and dynamics. Later extended to other applications, this approach was successfully used to analyse masonry structures (Lemos 2007; Malomo et al. 2019b).
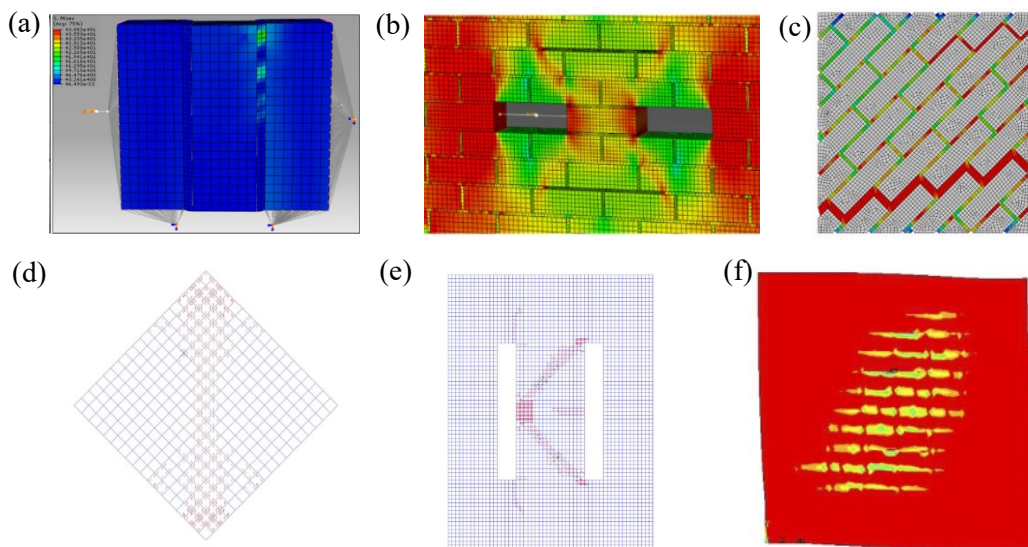
Figure 2.7 Applications of FEM micro-models: a,b) simulation of triplet and shove tests using FEM to investigate the effect of dilatancy (Andreotti et al. 2018), c) FE model employed to determine the limit surface for biaxial compression-tension tests considering different orientations of the bed joints (Kowalewski and Gajewski 2015) d,e) FE models are used to simulate diagonal-compression and Sheppard tests for calibrating a new numerical procedure f) simulation of a diagonal-compression test used to study the behaviour of hollow brick masonry under predominant shear stress (Gabor et al. 2006)

In the framework of discrete methods, different numerical tools are available in literature such as Non-Smooth Contact Dynamics (NSCD), Discontinuous Deformation Analysis (DDA), combined Finite-Discrete Element Method (FDEM, FE-DEM), Applied Element Method (AEM) or Rigid Body and Spring Model (RBSM). These approaches differ for the contact type, contact behaviour, the use of deformable or rigid units, and the numerical procedure's implementation. In Figure 2.8, the schematic representation of masonry

idealisation in RBSM (Figure 2.8a), DEM (Figure 2.8b) and AEM (Figure 2.8c) is presented.
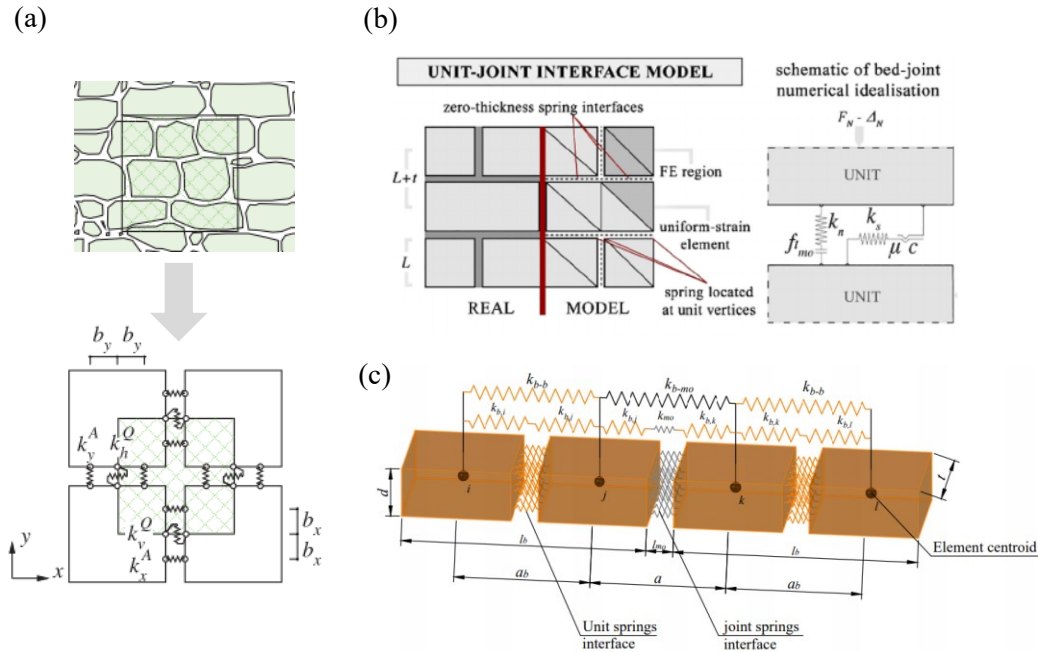
Figure 2.8 Scheme of modelling representation in a) RBSM (Casolo and Peña 2007), b) DEM (Malomo et al. 2019b) and c) AEM (Morandini et al. 2022)

2.4.1 Distinct Element Method (DEM)

Contrary to the FE approach, where masonry is idealised as a continuum interrupted by joints, in DEM masonry is represented as an assemblage of units interacting at their boundaries through contact surfaces between distinct elements. According to Lemos (2007), DEM can be classified as block DEM and particle DEM.

The first consists of an assemblage of polygonal or polyhedral bodies, whereas particle DEM, using circular and spherical particles, represents material at a small scale. A fine line separates FEM (and FEM-DEM), and DEM approaches as the first can include joint elements, whereas the latter may have an internal FE mesh. Nonetheless, a set of common features characterise DE approaches (Lemos 2007).

-   The material is considered a discontinuous system where blocks can be rigid, concentrating the system deformability into joints.
-   A set of contact points or edge-to-edge contacts represent the interaction between blocks, and the stress distribution is discontinuous through the contact surface.
-   The complete separation of blocks is possible with automatic contact detection.
-   This approach allows representing the strongly nonlinear behaviour of masonry, including joint sliding and total separation in large displacement with geometry

and connectivity variations. These characteristics make DEM particularly suitable for analysing structural failure in a quasi-static or dynamic process in the context of safety assessment.

In DEM, units and joints are usually explicitly modelled. Units are represented by polyhedral shapes and can be rigid blocks, with deformations concentrated at the joints, or deformable, typically modelled with an internal finite element mesh. Regarding constitutive models, a simple Coulomb model is usually adopted, considering normal and shear stiffness and friction angle, while finite tensile and cohesion are sometimes considered along with the post-peak softening branch, to provide fracture energy and avoid numerical problems which a sudden bond failure may cause.

Contacts between blocks occur in point contacts without any interface (as per AEM) or joint element (as per FEM). DEM approaches are more suitable for large displacement where contact points (orientation, type, location and connectivity) have been updated. The stress at a contact point is a function of the relative displacement between two blocks at that point. Contact points are typically placed at vertex-face or edge-edge interactions. DEM allows the vertex-edge contact (impossible in FEM), and blocks can be meshed independently without needing to match nodal points. The drawback is the need for a large number of contact points, and thus a great computation effort, to have an accurate distribution of stress, which is usually accurate with joint elements in FE codes. The accuracy of DEM is strongly dependent on the number of contact points, thus requiring a great computational cost. To improve the representation of stress distribution, several codes implement an edge-edge formulation to represent contacts (Munjiza et al. 1995). In 3D there are several possibilities for contact representation, one of the most popular is the use of edge-edge and vertex-face contact types. Each contact force is a function of the relative block displacement at that point, and the joint constitutive models are typically formulated in terms of stress and relative displacements.

According to DEM, contact between blocks can be either rigid or deformable. In the first case, the condition of no overlapping is adopted, and in the latter, a small overlap is allowed, and the contact stiffness is defined in both normal and shear directions. In DEM, deformable contacts are usually implemented with penalty coefficients, which allow the definition of a threshold overlap size and define normal and shear stiffness. Automatic contact detection involves that there is no need to define the system connectivity.

Rigid blocks are usually used for seismic analyses rather than deformable blocks with FE mesh because of the lower computational cost, particularly in explicit time-step algorithms, which are usually adopted by DE codes. Cundall (1971) adopted the explicit central difference algorithm for the time-integration of the equation of motion of rigid blocks. The same algorithm is also used for static problems by introducing a high damping value, allowing the convergence of static equilibrium. Rayleigh damping, which considers a mass and stiffness proportional contribute is often adopted. The consideration of damping in dynamic problems solved with an explicit algorithm requires a small time-step for numerical stability (Lemos 2007). When an internal FE mesh is considered, the equations

of motion are integrated at each block nodal point, assuming lumped masses. However, implicit time-integration schemes are also implemented, given their capability to use larger time-steps. Implicit algorithms are indeed unconditionally stable but require the solution of a system of equations at each time step, with a larger run time. Explicit methods require a greater number of time-step but need a lower computational time for each one.

2.4.2 Rigid Body and Spring Models (RBSM)

Conceptually similar to the DEM, the RBSM was originally proposed by Kawai (1978). The RBSM represents masonry as an assemble of rigid blocks connected by springs, where the contact properties are obtained through a homogenisation procedure, and units do not necessarily represent masonry units (Casolo 2000). The model proposed by Casolo and Pena (2007) defines a macroscopic unit cell by four quadrilateral rigid elements (Figure 2.8a) with a size equal to or larger than the minimum representative volume (REV) of the heterogeneous material. The rigid units are connected by three normal and shear springs at each side, and their mechanical behaviour is defined based on phenomenological consideration of the in-plane damage mechanisms described at the meso-scale.

The RBSM proposed by Casolo (Casolo 2000; Casolo and Uva 2013), specifically conceived to represent the OOP response of masonry façades, is based on flexural-torsional kinematics where in-plane rigidity is assumed. This approach is suitable for slender walls where the membrane effect is negligible. Rigid elements are connected by spherical elasto-plastic hinges located at connection points placed at the midpoint of any edge, where bending and twisting rotations are allowed. The energy dissipation is modelled with a constant viscous matrix proportional to the mass matrix. The time integration is performed through the implicit Newmark scheme. The mesoscale damage mechanisms and the post-elastic response of masonry piers are described considering three failure mechanisms: rocking, shear cracking and sliding.

2.4.3 Applied Element Method (AEM)

Among the discrete approaches, Applied Element Method (AEM) based models are among the most employed numerical tools for analysing extreme loading conditions (seismic assessment, demolition, and explosion), and they can be classified as RBSM. In the AEM the structure is divided into small elements connected by springs accounting for the material nonlinearity, deformations and failures (Meguro and Tagel-Din 2000, 2001; Mayorca and Meguro 2003; Pandey and Meguro 2004). The AEM elements are connected through springs placed on the entire surface, representing stress, strain, and connectivity between them. Contrary to FE models, this allows the partial connectivity between blocks and avoids the need for transition elements between large and small mesh sizes. In AEM, masonry behaviour is described by a Mohr-Coulomb yielding criterion. Cohesion can be set to zero right after reaching the maximum shear strength or can go to zero with a softening branch. A cut-off criterion is employed for the spring tensile failure. A simplified version of the elasto-plastic fracture model, originally developed by Maekawa and El-Kashif (2004) is commonly used to simulate the cyclic cumulative damage of masonry elements subjected to uniaxial compression.

The damping matrix takes into account the sources of damping that are not implicitly considered, such as cracking, energy dissipation due to different loading/unloading stiffnesses of compression springs, energy dissipation due to the opening and closure of cracks, friction between elements during the contact, collision and rebounding (Tagel-Din and Meguro 2002). The other sources of damping can be accounted for in a damping matrix that is proportional to the mass matrix and is calculated based on the first mode deformation. Collisions and recontact are considered in the AEM through the definition of collision springs added where contact between elements occur. When springs between two elements in touch attain the separation strain, they are removed, and these elements behave as two separate rigid bodies. Normal and shear springs are added at the contact point when a collision occurs. The normal spring direction is the one of the line connecting the two elements centroid, while the shear spring direction is tangent to the circular elements. Collision springs exist when elements are in contact and are removed after separation. The collision is checked only between near elements to reduce the computational time. The element shape is assumed to be circular to simplify the collision check procedure. The energy dissipated in the collision is taken into account, assuming different loading and unloading stiffnesses. The kinetic energy lost in the collision is considered through the rebound factor, which is the ratio between the element velocity before and after the collision. The analysis is reliable until the complete collapse of the structure.

2.4.4 Non-Smooth Contact Dynamics (NSCD)

Initially developed to study the dynamics of granular materials (Moreau 1988; Jean 1999), the NSCD involves a finite number of degrees of freedom and unilateral constraints. The NSCD method implements Signorini's impenetrability condition and Coulomb's law for dry friction for the contact model with an implicit time integration solver. With the use of rigid blocks and accounting for the non-smooth nature of dynamic contacts (blocks can slide or impact together), this approach is particularly suitable for analysing dynamic problems, as the seismic assessment of masonry structures. The assumption of perfectly plastic impacts without bounces determines a null value of the restitution coefficient in Newton's law. This simplified modelling of the impacts limits the computational complexity of the problem. The energy dissipation is related to the material damage and cracking after the collision, and the friction determines it. In this model, friction also provides numerical stability. This is an important feature of this modelling approach as damping effects, which are essential for the continuum models, are neglected.

2.4.5 Discontinuous Deformation Analysis (DDA)

Originally proposed by Shi (1992), DDA assume deformable blocks and a uniform state of strain and stress for each of them. The hard contact type is adopted with no overlaps allowed. The time-stepping algorithm is based on a global stiffness matrix, solved using the simplified penalty method. Due to its capability to model discontinuities, also simulating the more or less constant layer of mortar using numerical contact parameters (impenetrability, friction, cohesion), the DDA is well suited to simulate masonry behaviour (Bravo and Pérez-Aparicio 2007). However its application is still mostly limited to rock mechanics and engineering geology.

2.5 Discrete modelling applications

This section presents a brief overview of discrete models application, ranging from small-scale tests to more complex structural systems.

2.5.1 Small-scale tests and sub-structures: analysis of in-plane mechanisms

Small scale component tests are usually simulated to calibrate the mechanical parameters of discrete models. Unlike the explicit FEM, a homogenisation procedure is usually required to determine the properties of the interfaces accounting for both mortar joints mortar-bricks interaction.

In Figure 2.9, some applications of discrete approaches for the simulation of small scale tests are presented. Figure 2.9a,b shows the simulation of tests on small-scale masonry specimens for the calibration of a damaging block-based model (D'Altri et al. 2019).
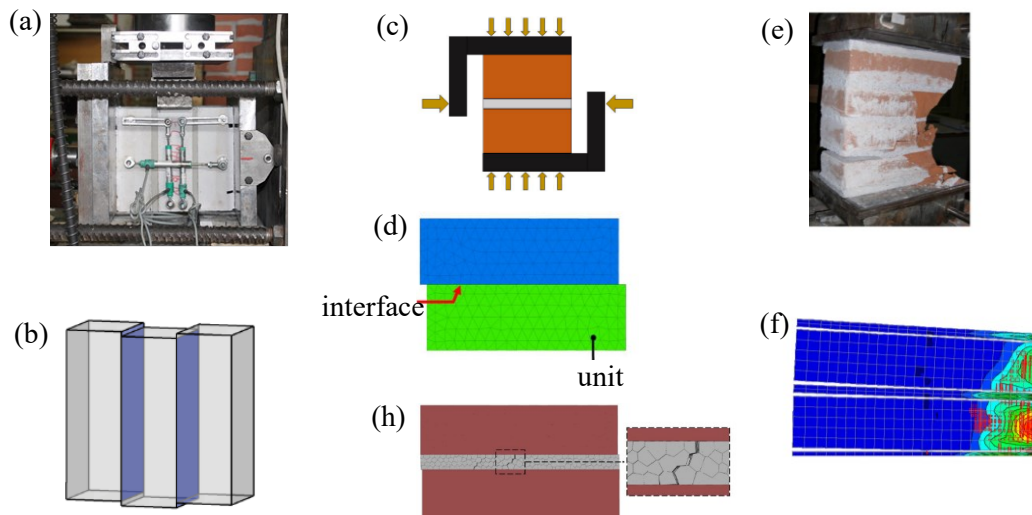
Figure 2.9 Simulation of small-scale tests using discrete approaches: a,b) experimental and numerical (block-based model (D'Altri et al. 2019)) triplet test, c,d,h) experimental and numerical (DEM (Pulatsu et al. 2020a)) couplet test, e,f) FE-DEM application to study the effect of load eccentricity (Adam et al. 2010)

Masonry is idealised in solid 3D finite elements governed by a plastic-damage constitutive law in tension and compression, while a cohesive-frictional contact-based formulation is adopted to simulate their cyclic interaction. In Figure 2.9c-e a DEM model to analyse brickwork masonry considering the units and/or the mortar explicitly as a group of 3D polyhedral blocks (referred to as meso-model), interacting along their boundaries is proposed (Pulatsu et al. 2020a). Elastic-softening tension and shear contact models describe the mechanical interaction among the distinct blocks. Using the proposed contact models, it is possible to capture the complete macro behaviour of masonry together with the corresponding deformation. In Figure 2.9e,f the application of a FE model to the study of the micromechanics of solid brickwork subjected to eccentric loads is presented (Adam et

al. 2010). Bricks and mortar have been modelled explicitly, assuming nonlinear constitutive models and the brick-mortar interface where the detachment is located.

Discrete modelling approaches are widely used for research aims or to simulate tests at the component level (Pulatsu et al. 2016, 2020b, a; Bui et al. 2017; Malomo et al. 2018a, b; D'Altri et al. 2019), given their capability to account for the interaction between mortar and units and for several aspects of masonry micro-structure that affect its response. In Figure 2.10, the application of AEM (Figure 2.10a), DEM (Figure 2.10b) and NSCD (Figure 2.10d) to the problem of analysing the in-plane behaviour of masonry are presented. Due to their low degree of approximation, discrete approaches are suitable for studying the effect of different bond patterns (Malomo et al. 2019a), irregular distribution of openings (Malomo et al. 2019b) or other irregularities. On the other hand, despite the accuracy of the predictions obtained with discrete approaches, these methods are usually computationally expensive, and their applications are often limited to research problems. A Macro-Distinct Element Model (M-DEM) (Malomo and DeJong 2021b) was recently proposed to overcome this issue. This hybrid approach employs a new macroelement consisting of an assembly of FE macro-blocks, with internal tetrahedral mesh connected by nonlinear springs. This new macroelement (Figure 2.10c) proved to be able to reproduce both shear and flexure responses of walls as well as the associated damage propagation.

a) AEM	b) DEM	c) M-DEM	d) NSCD
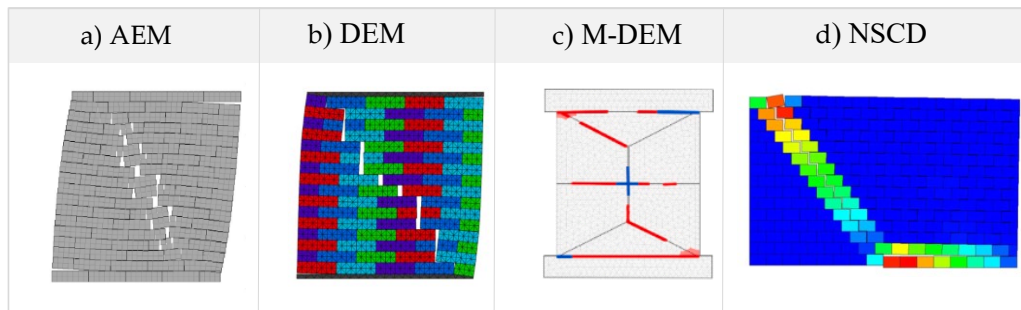
Figure 2.10 Simulation of in-plane component tests using discrete modelling approaches a) (Mayorca and Meguro 2003) AEM b) (Pulatsu et al. 2020b) c) M-DEM (Malomo and DeJong 2021b) d) NSCD (Chetouane et al. 2005)

2.5.2 Sub-structures: analysis of out-of-plane mechanisms

Out-of-plane (OOP) failure modes are among the most frequent causes of collapse for URM structures that lack an adequate connection between orthogonal walls and diaphragm, as confirmed by recent and past earthquakes (Penna et al. 2014). Indeed, these mechanisms prevent the development of the global structural capacity associated with the so-called box behaviour. Despite the importance of investigation and prevention of such mechanisms to avoid premature collapses of URM structures, some of the most widespread numerical modelling approaches neglect the OOP contribution (e.g. Equivalent-frame models - Lagomarsino et al. 2013; Addessi et al. 2015; Raka et al. 2015-) and storey-mechanism based approaches -Tomazevic 1978-). Although some recent applications have tried to overcome such limitations (Vanin et al. 2020; Malomo and DeJong 2021a), block-based

modelling strategies are still the most suitable for analysing masonry's OOP response. Among these, the Rigid Body and Spring Model (RBSM) and the Discrete Element Method (DEM), as well as the more efficient Applied Element Method (AEM), are particularly suitable to represent the OOP response of masonry. Thanks to its capability to explicitly represent units separation, DEM has been successfully used to investigate local out-of-plane mechanisms of blocky assemblies (de Felice and Giannini 2001; Peña et al. 2006; de Felice 2011; Shawa et al. 2012; Pulatsu et al. 2016; Godio and Beyer 2019) and URM structures with dry joints (Bui et al. 2017), as well as to reproduce experimentally-observed out-of-plane collapses of unreinforced masonry specimen (Galvez et al. 2018) or to predict the possible failure (Godio and Beyer 2019).

Some applications of various discrete models to the simulation problem of the out of plane response of masonry sub-structures are presented in Figure 2.11. Figure 2.11a presents the rigid block model used in the limit analyses formulated by Orduña and Lourenço (2005). In this model, rigid blocks interact through quadrilateral interfaces without tensile strength and cohesion. Figure 2.11b shows an application of the rigid block model proposed by Portioli (2020), which adopts a constitutive model with a no tension frictional behaviour and infinite compressive strength, whereas Figure 2.11c presents the simulation of an out-of-plane test with the damaging block-based model proposed by D'Altri (2019). In Figure 2.11d, DEM was used to simulate the response of a real stone structure, considering units shape and arrangement (Lemos 2019) and in Figure 2.11 the hybrid M-DEM model proposed by Malomo and DeJong (2021a) for the simulation of the OOP behaviour of a masonry panel is shown.
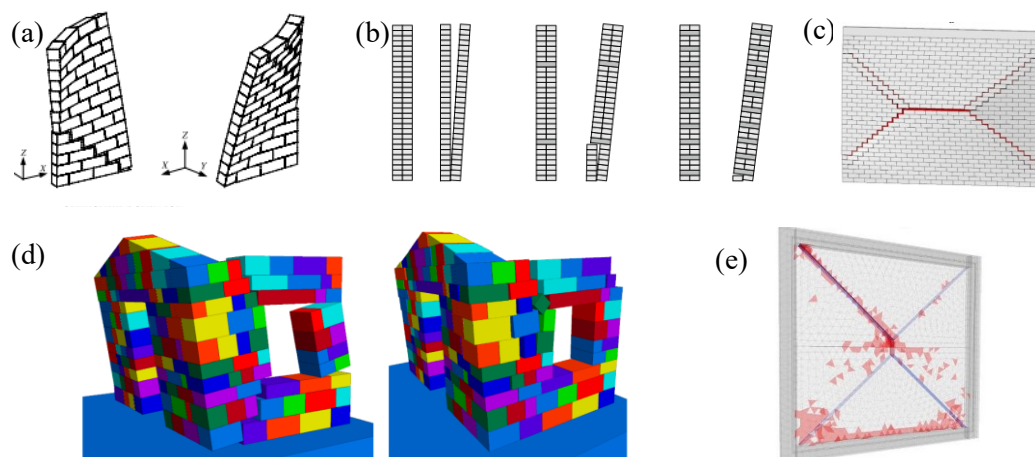
Figure 2.11 a) DEM for limit analysis (Orduña and Lourenço 2005) b) Rigid block-based model (Portioli 2020),c) block-based model (D'Altri et al. 2019), d) DE model of real stone sub-structure (Lemos 2019) e) M-DEM (Malomo and DeJong 2021a)

2.5.3 Masonry arches and bridges

DEM was also successfully employed to investigate the influence of backfill on masonry arch bridge and their interaction. Since masonry often consists of strong units (typically

stone) where deformations are concentrated at the joints in these applications, rigid blocks are usually assumed for dynamic analyses to reduce the computational time (Sarhosis et al. 2014, DeJong et al. 2015). In Figure 2.12, different examples of the application of DEM approaches to the assessment of masonry arch bridges are presented. In Figure 2.12a the Rigid Block, DE and FE models employed to assess the load-carrying capacity of stone masonry arch bridge are presented. The responses of the bridge under its weight and incremental vertical forces to represent the static loading of a standard vehicle, obtained with the three modelling approaches, were compared with consistent results between the three strategies (Costa et al. 2015). In Figure 2.12b, the DE model used to investigate the behaviour of Donim bridge and the influence of soil characteristics is presented (Pulatsu et al. 2019). Several arch bridge models (Figure 2.13c) were developed, and simulations were compared with experimental results. The comparison highlighted the capability to represent with a good approximation experimental failure mode and crack initiation and propagation (Sarhosis et al. 2019). In Figure 2.12d the NSCD model used to analyse the behaviour of an arch masonry bridge under both static and dynamic loads assuming deformable or rigid blocks, is presented. The assumption of rigid blocks required lower time for the analysis than the deformable one but was less realistic (Chetouane et al. 2005).

2.5.4 Complex structural systems

The use of advanced numerical tools to analyse complex structural systems is made difficult by the computational effort required by the great number of elements and contacts involved. Technological advancement and DEM strategies reduced the time needed for the analyses, allowing numerical investigation of complex structures under dynamic load (i.e. earthquake, impact, blast). In Figure 2.13, some applications of discrete approaches to studying complex masonry structures are presented. Figure 2.13a shows the DEM model used to assess an adobe church's seismic performance (Kuño Tambo church through pushover analyses, Perù). The irregular unit arrangement was modelled using a regular pattern based on the units' real dimension, comparing results obtained adopting rigid and deformable blocks and different assumptions on wall connections. In this case, the assumption of rigid or deformable units did not significantly affect the building response (Mendes et al. 2020). In Figure 2.13 b the DEM model of the Mustafa Pasha Mosque is presented (Çaktı et al. 2016). In this study, blocks were assumed rigid, and only the mass proportional Rayleigh damping component was used to reduce computational time, as deformable blocks and stiffness-proportional damping contribute requires shorter time steps. The comparison of the dynamic behaviour of the numerical model with the experimental response observed in a shake-table test showed a good performance of DEM. Nevertheless, despite the modelling assumption to reduce the time step, the computational effort was prohibitive in view of applying this approach to more complex structural systems.
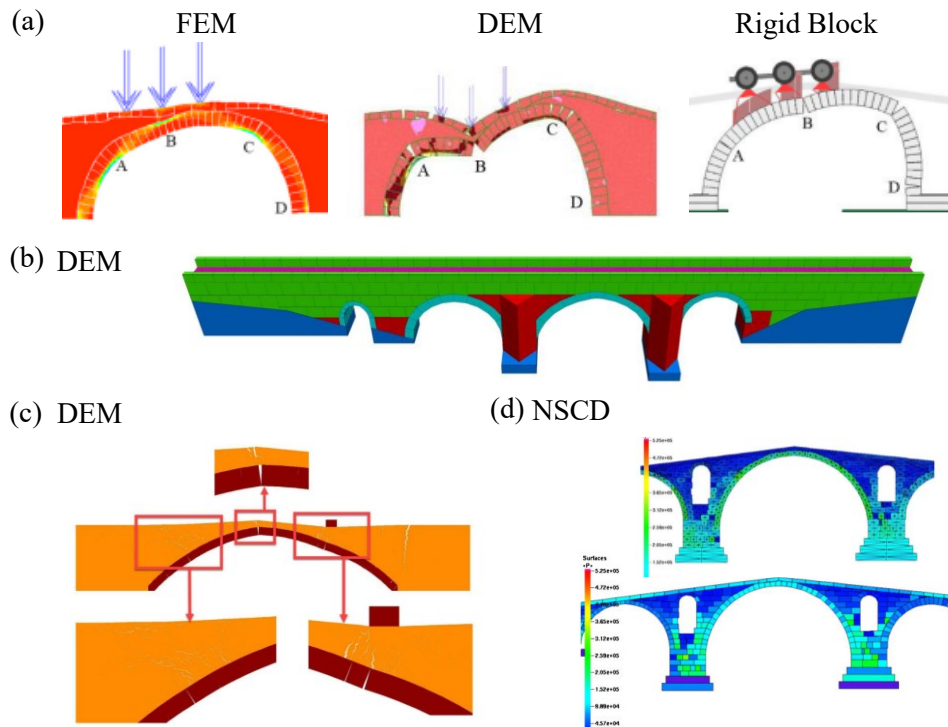
Figure 2.12 Discrete model of arch masonry bridges a)FEM, DEM and Rigid Block model (Costa et al. 2015), b) DEM (Pulatsu et al. 2019), c) DEM (Sarhosis et al. 2019), d) NSCD (Chetouane et al. 2005)

The macro-model and the block-based micro-model presented in Figure 2.13c were used to perform pushover analyses comparing the results obtained with the experimental dynamic counterpart of a masonry specimen tested in a shake-table test. In this case, both models led to results consistent with the experimental outcomes (Cannizzaro and Lourenço 2017). In Figure 2.13d the NSCD model of Pomposa Abbey (Codigoro, Italy) is shown. Under three main simple assumptions (rigid block, simple contact laws between blocks and absence of any damping), the response of the abbey model is influenced only by the friction coefficient (Ferrante et al. 2020). Since the determination of mechanical parameters in existing masonry buildings is often critical, having a single significant parameter represents an important feature of this model. In Figure 2.13e, f two macroelement based models are presented. The first was employed to reproduce the in-plane quasi-static behaviour of a masonry façade (Caliò et al. 2012), whereas the second Macro-Distinct Element Model was used to predict the dynamic response of a shake-table test by comparing experimental backbone and numerical pushover (Tomić et al. 2020). In both cases, the employment of these simplified modelling strategies allows reducing the computational cost without affecting the accuracy of the results. Figure 2.13g shows the NSCD model used to simulate dynamic analyses on two ancient masonry manufactures, the 'Nîmes arena and Arles aqueduct in France, to assess their seismic vulnerability (Rafiee et al. 2008).In these studies, the NSCD approach was selected for its ability to account for the interaction of many elements.

Despite the technological advancement and the significant improvement of the numerical strategies to reduce the computational time, this aspect is still the biggest issue to be overcome. Rigid blocks often allow larger time steps, so they are frequently applied in dynamic analysis, as also discussed in this section. DEM often requires small time steps for dynamic analyses due to numerical stability. When the stiffness-proportional component of Rayleigh damping is used, this condition may be particularly severe, with demanding run times for large or complex models (Lemos 2019). To overcome this issue, the AEM considers only the mass-proportional component of Rayleigh damping, which is, however, rarely applied as this approach directly considers almost all damping sources (e.g. material nonlinearity, rebound effects), as discussed in Section 2.4.3. This approach allows the use of larger time steps. The NSCD employed a different approach as dissipated energy is accounted for with the involvement of friction (Ferrante et al. 2020).

(a) DEM   (b) DEM   (c) DEM

(d) NSCD

(e) M-DEM   (f) M-DEM
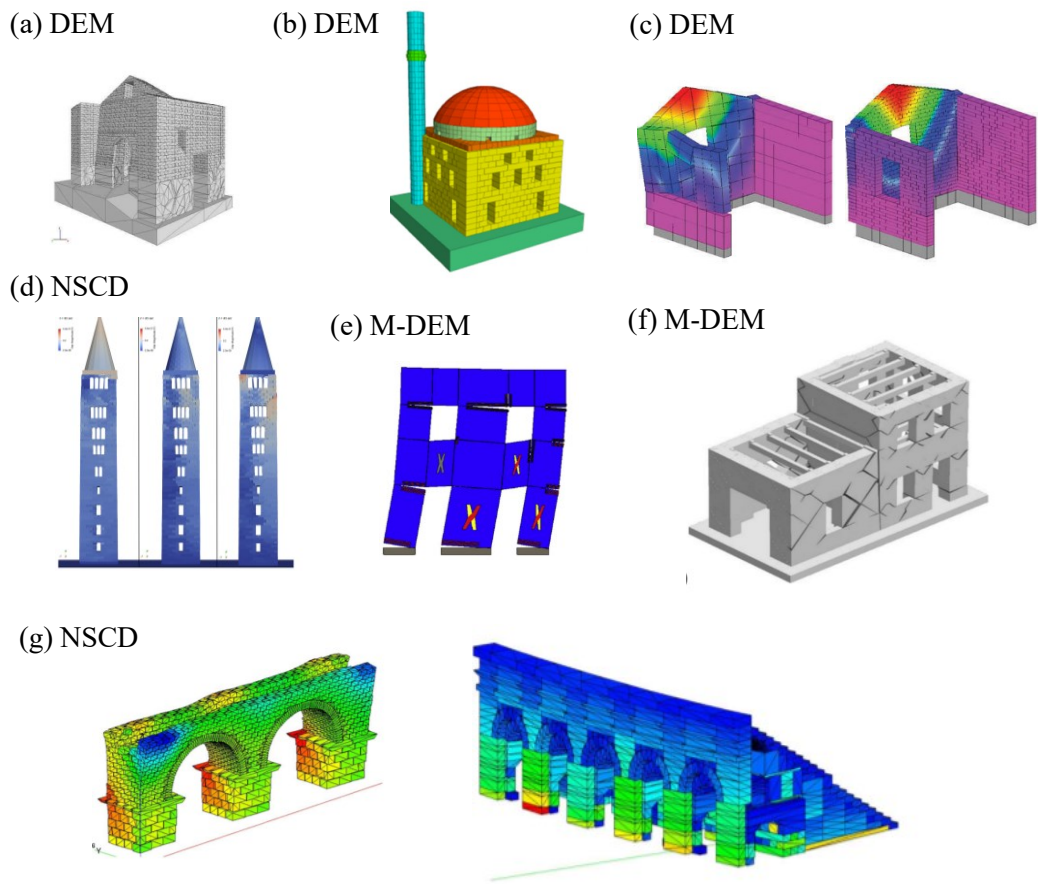
(g) NSCD

Figure 2.13 a) DEM (Mendes et al. 2020), b) DEM (Çaktı et al. 2016) c) macro and block-based micro-model (Cannizzaro and Lourenço 2017) d) NSCD (Ferrante et al. 2020) e) M-DEM (Caliò et al. 2012) f) M-DEM (Tomić et al. 2020)g) NSCD (Rafiee et al. 2008)

2.5.5 Collapse

Thanks to its computational efficiency and its reliability in large displacement fields, the AEM is one of the most used discrete approacches to simulate extreme loading conditions such as explosion or earthquake up to the complete collapse of the structure. In Figure 2.14 and Figure 2.15 some examples of the application of DEM and AEM models to collapse analyses are presented.

(a) DEM

(b) AEM

(c) AEM

(d) DEM

(e) AEM
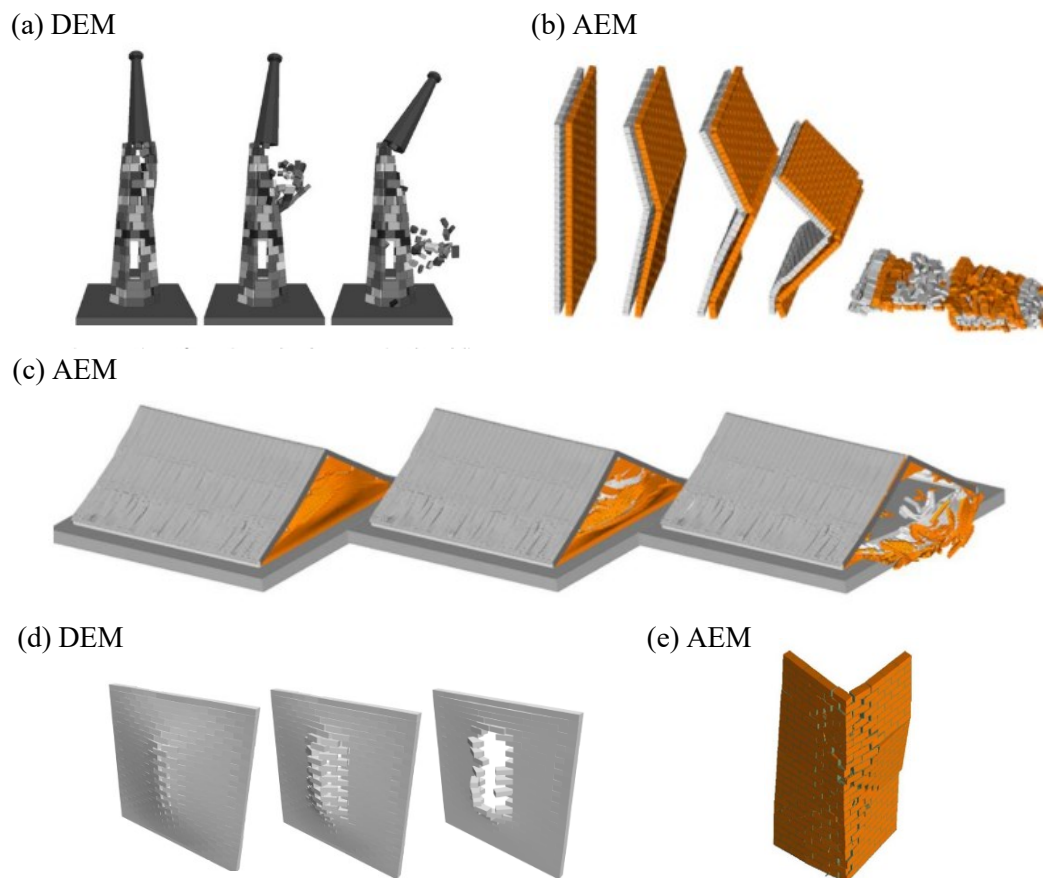
Figure 2.14 a) progressive collapse of the spire under impulse loading using DEM (DeJong and Vibert 2012) b) AEM for the simulation of one-way-bending response of cavity walls (Malomo et al. 2020b) c) AEM of a roof substructure (Malomo et al. 2020) d) DEM masonry panels subjected to blast loading (Masi et al. 2019) e) AEM of masonry wall subjected to blast loading (Keys and Clubley 2017)

The DEM model presented in Figure 2.14a was used to analyse the dynamics of a stone spire to study the collapse under constant horizontal acceleration, impulse base motion, and earthquake ground motion (DeJong and Vibert 2012). In Figure 2.14d the DE models employed for analysing the dynamic response of masonry subjected to blast loads are presented (Masi et al. 2019). In this last study, the rigid block model gave sufficiently accurate predictions for the failure (strength) of the masonry structure subjected to blast

loads, reducing the computational time up to 60%. In Figure 2.14e the AEM model used to reproduce the experimental test on panels subjected to blast loading is presented. The AEM model reproduced with a good agreement the experimental test also in terms of debris distribution. In Figure 2.15a,b,c AEM and DEM models used to simulate experimental shake-table tests up the collapse are presented. The model used to simulate the progressive collapse of the Polcevera viaduct in Genoa is shown in Figure 2.15d (Calvi et al. 2019).
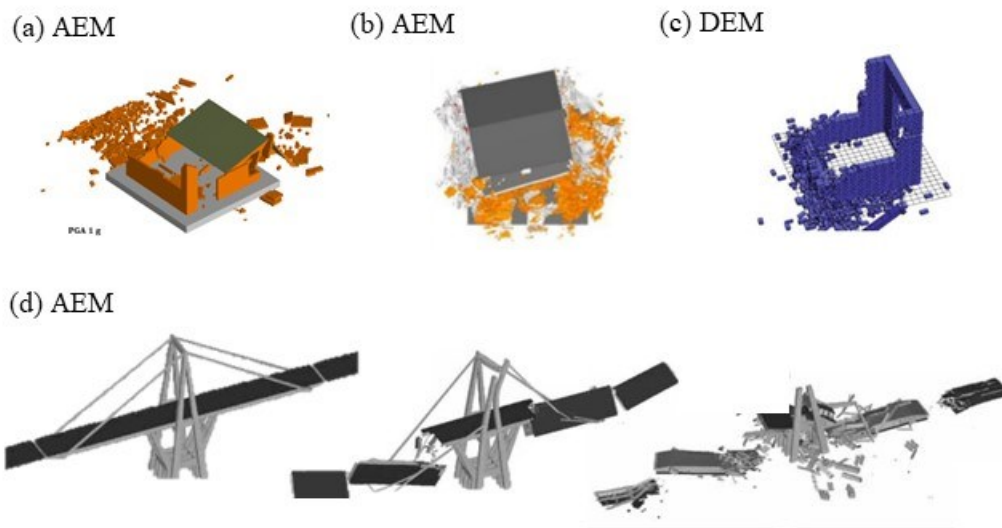
Figure 2.15 Collapse analyses using AEM a) (Domaneschi et al. 2018) b) (Malomo et al. 2021c) d) (Calvi et al. 2019) and c) DEM (Nakagawa et al. 2012)

2.5.6 Final remarks

Discrete models provide adequate solutions for the structural analysis and the seismic assessment of URM, being particularly suitable for representing the heterogeneous nature of masonry. However, their employment has been limited by the computational cost and by the need of expert users and a large set of mechanical parameters often not available from characterisation tests. The recent development of computational tools allowed more widespread use of discrete modelling approaches, which have become more commonly employed in research and engineering practice. A practice-oriented overview of the currently available discrete models is proposed in this chapter, discussing their main characteristics and differences. The main limitations that led to the AEM's choice are summarised in the following.

In NSCD-based models, the assumption of perfectly plastic impact provides numerical stability and simplifies the problem. On the other hand, the energy dissipation is only accounted for by friction. Cracking, energy dissipation due to different loading/unloading stiffnesses of compression springs or due to the opening and closure of cracks, collision and rebounding are not explicitly considered, as is the case of the AEM.

In DDA-based models as well, the interactions between blocks are determined by contacts and friction. Moreover, this approach is not as widely applied as AEM or DEM to simulate masonry structures' behaviour.

The Rigid Body and Spring Models (RBSM) represent masonry as rigid blocks and contact springs, but the discretisation is based on a homogenisation procedure, and they do not explicitly account for the unit arrangement. Moreover, the Poisson effect is considered by introducing additional diagonal springs. The AEM, an efficient implementation of the RBSM, can account for the Poisson's effect without any additional spring and adopt a brick-based block arrangement (Tateo and Casolo 2021). Contrary to the AEM, other RBSM do not consider the recontact between neighbour elements, and the analyses up to the complete collapse are unattainable (Furukawa et al. 2012).

In DEM codes, the analysis of static problems is often computationally inefficient, requiring the calibration of a damping factor for the dynamic relations scheme (Malomo et al. 2018b). Moreover, DEM represents contact surfaces with a series of contact elements whose amount and properties are important for the accuracy of the approach. However, a greater amount of contact elements requires greater computational power. Similarly, the accuracy of the AEM depends on the size of the elements, but it is independent of the number of springs located at the element's interfaces, decreasing the computational time and power necessary (Meguro and Tagel-Din 1998).

This thesis employed a discrete modelling approach based on the Applied Element Method. In addition to the above motivations, the AEM was chosen for its capability of reproducing the response of large-scale systems up to complete failure in a reasonable time, also allowing the evaluation of the amount and the extent of debris.

References

Abdulla KF, Cunningham LS, Gillie M (2017) Simulating masonry wall behaviour using a simplified micro-model approach. Eng Struct 151:349–365. https://doi.org/10.1016/j.engstruct.2017.08.021.

Adam JM, Brencich A, Hughes TG, Jefferson T (2010) Micromodelling of eccentrically loaded brickwork: Study of masonry wallettes. Eng Struct 32:1244–1251. https://doi.org/10.1016/j.engstruct.2009.12.050.

Addessi D, Liberatore D, Masiani R (2015) Force-based beam finite element (FE) for the pushover analysis of masonry buildings. Int J Archit Herit 9:231–243.

Andreotti G, Graziotti F, Magenes G (2018) Detailed micro-modelling of the direct shear tests of brick masonry specimens: The role of dilatancy. Eng Struct 168:929–949. https://doi.org/10.1016/j.engstruct.2018.05.019.

Angelillo M, Lourenço PB, Milani G (2014) Masory behaviour and modelling. Mech Mason Struct 551:. https://doi.org/10.1007/978-3-7091-1774-3_1.

Aref AJ, Dolatshahi KM (2013) A three-dimensional cyclic meso-scale numerical procedure for simulation of unreinforced masonry structures. Comput Struct 120:9–

23. https://doi.org/10.1016/J.COMPSTRUC.2013.01.012.

Bandera S, Sullivan CO, Tangney P, Angioletti Uberti S (2021) Computers and Geotechnics Coarse-grained molecular dynamics simulations of clay compression. Comput Geotech 138:104333. https://doi.org/10.1016/j.compgeo.2021.104333.

Bracchi S, Galasco A, Penna A (2021) A novel macroelement model for the nonlinear analysis of masonry buildings . Part 1 : Axial and flexural behavior. Earthq Eng Sructural Dyn 50:2233–2252. https://doi.org/10.1002/eqe.3445.

Bracchi S, Penna A (2021) A novel macroelement model for the nonlinear analysis of masonry buildings. Part 2: Shear behavior. Earthq Eng Struct Dyn 50:2212–2232. https://doi.org/10.1002/eqe.3444.

Bravo R, Pérez-Aparicio JL (2007) Discontinuous Numerical Analysis of Masonry Vaults. Solid Mech its Appl 3:365–380. https://doi.org/10.1007/978-1-4020-6405-0_23.

Brooks JJ, Baker A (1998) Modulus of Elasticity of Masonry. Mason Int 12:58–63.

Bui TT, Limam A, Sarhosis V, Hjiaj M (2017) Discrete element modelling of the in-plane and out-of-plane behaviour of dry-joint masonry wall constructions. Eng Struct 136:277–294.

Çaktı E, Saygılı Ö, Lemos J V., Oliveira CS (2016) Discrete element modeling of a scaled masonry structure and its validation. Eng Struct 126:224–236. https://doi.org/10.1016/j.engstruct.2016.07.044.

Caliò I, Marletta M, Pantò B (2012) A new discrete element model for the evaluation of the seismic behaviour of unreinforced masonry buildings. Eng Struct. https://doi.org/10.1016/j.engstruct.2012.02.039.

Calvi GM, Moratti M, O'Reilly GJ, et al (2019) Once upon a Time in Italy: The Tale of the Morandi Bridge. Struct Eng Int 29:198–217. https://doi.org/10.1080/10168664.2018.1558033.

Cannizzaro F, Lourenço PB (2017) Simulation of Shake Table Tests on Out-of-Plane Masonry Buildings. Part (VI): Discrete Element Approach. Int J Archit Herit 11:125–142. https://doi.org/10.1080/15583058.2016.1238973.

Casolo S (2000) Modelling the out-of-plane seismic behaviour of masonry walls by rigid elements. Earthq Eng Struct Dyn 29:1797–1813. https://doi.org/10.1002/1096-9845(200012)29:12<1797::AID-EQE987>3.0.CO;2-D.

Casolo S, Peña F (2007) Rigid element model for in-plane dynamics of masonry walls considering hysteretic behaviour and damage. Earthq Eng Struct Dyn 36:1029–1048.

Casolo S, Uva G (2013) Nonlinear analysis of out-of-plane masonry façades: Full dynamic versus pushover methods by rigid body and spring model. Earthq Eng Struct Dyn 42:499–521. https://doi.org/10.1002/eqe.2224.

Chácara C, Cannizzaro F, Pantò B, et al (2018) Assessment of the dynamic response of unreinforced masonry structures using a macroelement modeling approach. Earthq Eng Struct Dyn 47:2426–2446. https://doi.org/10.1002/eqe.3091.

Chen S-Y, Moon FL, Yi T (2008) A macroelement for the nonlinear analysis of in-plane unreinforced masonry piers. Eng Struct 30:2242–2252.

Cheng YP, Bolton MD, Nakata Y (2004) Crushing and plastic deformation of soils simulated using DEM. Geotechnique 54:131–141. https://doi.org/10.1680/geot.2004.54.2.131.

Chetouane B, Dubois F, Vinches M, Bohatier C (2005) NSCD discrete element method for modelling masonry structures. Int J Numer Methods Eng 64:65–94.

Ciesielski R (1999) The dynamic module of elasticity of brick walls. In:Proceedings of the Conference of the Committee of Civil Engineering PZITB: Lublin, Poland.

Coburn A, Spence R (2003) Earthquake protection. Second edition. Ed. John Wiley & Sons, Ltd. ISBN: 0-471-49614-6.

Costa C, Arêde A, Morais M, Aníbal A (2015) Detailed FE and de Modelling of Stone Masonry Arch Bridges for the Assessment of Load-carrying Capacity. Procedia Eng 114:854–861. https://doi.org/10.1016/j.proeng.2015.08.039.

Cundall PA (1971) A computer model for simulating progressive large scale movements in blocky rock systems. In: Proceedings of the Symposio of the International Society of Rock Mechanics (ISRM), Nancy.

Cundall PA, Strack ODL (1979) A discrete numerical model for granular assemblies. Géotechnique 29:47–65. https://doi.org/10.1680/geot.1979.29.1.47.

D'Altri AM, Messali F, Rots J, et al (2019) A damaging block-based model for the analysis of the cyclic behaviour of full-scale masonry structures. Eng Fract Mech 209:423–448. https://doi.org/10.1016/j.engfracmech.2018.11.046.

D'Altri AM, Sarhosis V, Milani G, et al (2020) Modeling Strategies for the Computational Analysis of Unreinforced Masonry Structures: Review and Classification. Arch Comput Methods Eng 27:1153–1185. https://doi.org/10.1007/s11831-019-09351-x.

de Felice G, Giannini R (2001) Out-of-plane seismic resistance of masonry walls. J Earthq Eng 5:253–271. https://doi.org/10.1080/13632460109350394.

de Felice G (2011) Out-of-plane seismic capacity of masonry depending on wall section morphology. Int J Archit Herit 5:466–482. https://doi.org/10.1080/15583058.2010.530339.

DeJong MJ, Vibert C (2012) Seismic response of stone masonry spires: Computational and experimental modeling. Eng Struct 40:566–574.

DeJong MJ, Giardina G, Plunkett W, Ochsendorf JA (2015) Seismic design of a stone vault. In: Proceedings of the Society for Earthquake and Civil Engineering Dynamics Conference. Cambridge, United Kingdom.

D.M. 17/01/2018 (2018) Norme Tecniche per le Costruzioni (NTC2018), Gazzetta Ufficiale, n. 42 del 20/ 02/2018- Supplemento ordinario n.8 (in Italian).

Domaneschi M, Scutiero G, Marasco S, et al (2018) A methodology to quantify debris generation after a seismic event. In: Proceedings of the 16th European Conference on

Earthquake Engineering. Thessaloniki, Greece.

Ferrante A, Clementi F, Milani G (2020) Advanced numerical analyses by the Non-Smooth Contact Dynamics method of an ancient masonry bell tower. Math Methods Appl Sci 43:7706–7725. https://doi.org/10.1002/mma.6113.

Furukawa A, Kiyono J, Toki K (2012) Numerical simulation of the failure propagation of masonry buildings during an earthquake. J Nat Disaster Sci 33:11–36.

Gabor A, Ferrier E, Jacquelin E, Hamelin P (2006) Analysis and modelling of the in-plane shear behaviour of hollow brick masonry panels. Constr Build Mater 20:308–321. https://doi.org/10.1016/j.conbuildmat.2005.01.032.

Galvez F, Giaretton M, Abeling S, et al (2018) Discrete Element modelling of a two-storey unreinforced masonry scaled model. In: Proceedings of the 16th European Conference on Earthquake Engineering. Thessaloniki, Greece.

Gambarotta L, Lagomarsino S (1997) Damage models for the seismic response of brick masonry shear walls. Part I: The mortar joint model and its applications. Earthq Eng Struct Dyn 26:423–439. https://doi.org/10.1002/(SICI)1096-9845(199704)26:4<423.

Giambanco G, La Malfa Ribolla E, Spada A (2018) Meshless meso-modeling of masonry in the computational homogenization framework. Meccanica 53:1673–1697. https://doi.org/10.1007/s11012-017-0664-7.

Godio M, Beyer K (2019) Evaluation of force-based and displacement-based out-of-plane seismic assessment methods for unreinforced masonry walls through refined model simulations. Earthq Eng Struct Dyn 48:454–475. https://doi.org/10.1002/eqe.3144.

Heyman J (1966) The stone skeleton. Int J Solids Struct 2:249-279.

Jäger W, Irmschler HJ, Schubert P (2004) Mauerwerk-Kalender 2004. Ernst & Sohn Verlag für Architektur und technische Wissenschaften.

Jean M (1999) The non-smooth contact dynamics method. Comput Methods Appl Mech Eng 177:235–257.

Karbassi A, Nollet M-J (2013) Performance-based seismic vulnerability evaluation of masonry buildings using applied element method in a nonlinear dynamic-based analytical procedure. Earthq Spectra 29:399–426. https://doi.org/10.1193/1.4000148.

Kaushik HB, Rai DC, Jain SK (2007) Stress-strain characteristics of clay brick masonry under uniaxial compression. J Mater Civ Eng 19:728–739.

Kawai T (1978) New discrete models and their application to seismic response analysis of structures. Nucl Eng Des 48:207–229. https://doi.org/10.1016/0029-5493(78)90217-0.

Keys R a, Clubley SK, Engineering C (2013) Modelling Debris Distribution of Masonry Panels Subject to Blast Loads using Experimental & Applied Element Methods. In: Proceedings of the15th Int Symp Interact Eff munitions with Struct 1–10.

Keys RA, Clubley SK (2017) Establishing a predictive method for blast induced masonry debris distribution using experimental and numerical methods. Eng Fail Anal 82:82–

91. https://doi.org/10.1016/j.engfailanal.2017.07.017.

Khoo CL, Hendry AW (1973) Strength tests on brick and mortar under complex stresses for the development of a failure criterion for brickwork in compression. In: Proceedings of the British Ceramic Society. pp 51–66.

Kowalewski Ł, Gajewski M (2015) Determination of failure modes in brick walls using cohesive elements approach. Procedia Eng 111:454–461. https://doi.org/10.1016/j.proeng.2015.07.116.

Lagomarsino S, Penna A, Galasco A, Cattari S (2013) TREMURI program: An equivalent frame model for the nonlinear seismic analysis of masonry buildings. Eng Struct 56:1787–1799. https://doi.org/10.1016/j.engstruct.2013.08.002.

Lagomarsino S, Cattari S (2015) PERPETUATE guidelines for seismic performance-based assessment of cultural heritage masonry structures. Bull Earthq Eng 13:13–47. https://doi.org/10.1007/s10518-014-9674-1.

Lee J, Fenves GL (1998) Plastic-Damage Model for Cyclic Loading of Concrete Structures. J Eng Mech 124:892–900. https://doi.org/10.1061/(asce)0733-9399(1998)124:8(892).

Lemos J V (1997) Discrete element modelling of the seismic behaviour of stone masonry arches. In: Proceedings of the 4th International Symposium on Numerical Methods in Structural Masonry. E & FN SPON, Florence, Italy, pp 220–227.

Lemos J V (2007) Discrete element modeling of masonry structures. Int J Archit Herit 1:190–213. https://doi.org/10.1080/15583050601176868.

Lemos J V. (2019) Discrete element modeling of the seismic behavior of masonry construction. Buildings:. https://doi.org/10.3390/buildings9020043.

Lourenço PB, Rots JGJG, Blaauwendraad J (1995) Two approaches for the analysis of masonry structures - micro and macro-modeling. Res Artic HERON - Delft Univ Technol (Delft, Netherlands) 40:313–340.

Lourenço PB (1996) Computational strategies for masonry structures. PhD Thesis. Delft University of Technology, Delft, The Netherlands.

Lourenço PB, Rots JG (1997) Multisurface Interface Model for Analysis of Masonry Structures. J Eng Mech 123:660–668. https://doi.org/10.1061/(ASCE)0733-9399(1997)123:7(660).

Lourenço PB, Rots J, Blaauwendraad J (1998) Continuum Model for Masonry: Parameter Estimation and Validation. J Struct Eng 124:642–652. https://doi.org/10.1061/(ASCE)0733-9445(1998)124:6(642).

Lourenço PB (2002) Computations on historic masonry structures. Prog Struct Eng Mater 4:301–319. https://doi.org/10.1002/pse.120.

Maekawa K, El-Kashif KF (2004) Cyclic cumulative damaging of reinforced concrete in post-peak regions. J Adv Concr Technol 2:257–271.

Magenes G, Penna A, Senaldi IE, et al (2014) Shaking table test of a strengthened full-

scale stone masonry building with flexible diaphragms. Int J Archit Herit 8:349–375. https://doi.org/10.1080/15583058.2013.826299.

Malomo D, DeJong MJ, Penna A (2018a) Distinct Element modelling of the in-plane cyclic response of URM piers subjected to shear-compression. Earthq Eng Sructural Dyn 48:1322–1344.

Malomo D, Pinho R, Penna A (2018b) Using the applied element method for modelling calcium silicate brick masonry subjected to in-plane cyclic loading. Earthq Eng Struct Dyn 47:1610–1630. https://doi.org/10.1002/eqe.3032.

Malomo D, DeJong MJ, Penna A (2019a) Influence of Bond Pattern on the in-plane Behavior of URM Piers. Int J Archit Herit 00:1–20. https://doi.org/10.1080/15583058.2019.1702738.

Malomo D, DeJong MJ, Penna A (2019b) Distinct element modelling of the in-plane cyclic response of URM walls subjected to shear-compression. Earthq Eng Struct Dyn 48:1322–1344. https://doi.org/10.1002/eqe.3178.

Malomo D, Morandini C, Penna A, Dejong MJ (2019c) Assessing the reliability of the equivalent-frame idealisation of URM façades with irregular opening layouts by comparison with the discrete micro-models. In: Proceedings of SECED 2019 Conference. Greenwich, London.

Malomo D, Pinho R, Penna A (2020a) Simulating the shake table response of unreinforced masonry cavity wall structures tested to collapse or near-collapse conditions. Earthq Spectra 36:554–578. https://doi.org/10.1177/8755293019891715.

Malomo D, Pinho R, Penna A (2020b) Numerical modelling of the out-of-plane response of full-scale brick masonry prototypes subjected to incremental dynamic shake-table tests. Eng Struct 209:110298. https://doi.org/10.1016/j.engstruct.2020.110298.

Malomo D, DeJong MJ (2021a) A Macro-Distinct Element Model (M-DEM) for out-of-plane analysis of unreinforced masonry structures. Eng Struct 244:112754. https://doi.org/10.1016/j.engstruct.2021.112754.

Malomo D, DeJong MJ (2021b) A Macro-Distinct Element Model (M-DEM) for simulating the in-plane cyclic behavior of URM structures. Eng Struct 227:111428. https://doi.org/10.1016/j.engstruct.2020.111428.

Malomo D, Morandini C, Crowley H, et al (2021c) Impact of ground floor openings percentage on the dynamic response of typical Dutch URM cavity wall structures. Bull Earthq Eng 19:403–428. https://doi.org/10.1007/s10518-020-00976-z.

Mann W, Müller H (1982) Failure of shear-stressed masonry: an enlarged theory, tests and application to shear walls. Proc Br Ceram Soc 223–235.

Masi F, Stefanou I, Vannucci P, Maffi-Berthier V (2019) A discrete element method approach for the preservation of the architectural heritage against explosions. 12th HSTAM Int Congr Mech 10–16.

Matysek P, Janowski Z (1996) Analysis of factors affecting the modulus of elasticity of the walls. In: Proceedings of the Conference of the Committee of Civil Engineering

PZITB: Lublin, Poland.

Mayorca P, Meguro K (2003) Modeling Masonry Structures using the Applied Element Method. Seisan Kenkyu,j 55:581–584.

Meguro K, Tagel-Din H (1998) A New Simplified and Efficient Technique for Fracture Behavior Analysis of Concrete Structures. In: Proceedings of the Third International Conference on Fracture Mechanics of Concrete and Concrete Structures (FRAMCOS-3) 2:911–920.

Meguro K, Tagel-Din H (2000) Applied element method for structural analysis: Theory and application for linear materials. Struct Eng Eng 17:21–35.

Meguro K, Tagel-Din H (2001) Applied Element Simulation of RC Structures under Cyclic Loading. J Struct Eng 127:1295–1305. https://doi.org/10.1061/(ASCE)0733-9445(2001)127:11(1295).

Mendes N, Zanotti S, Lemos J V. (2020) Seismic Performance of Historical Buildings Based on Discrete Element Method: An Adobe Church. J Earthq Eng 24:1270–1289. https://doi.org/10.1080/13632469.2018.1463879.

Morandini C, Malomo D, Penna A (2022) Equivalent frame discretisation for URM façades with irregular opening layouts. Bull Earthq Eng 20: 2589-2618 https://doi.org/10.1007/s10518-022-01315-0.

Moreau JJ (1988) Unilateral contact and dry friction in finite freedom dynamics. In: Nonsmooth mechanics and Applications. Springer, pp 1–82.

Munjiza A, Owen DRJ, Bicanic N (1995) A combined finite-discrete element method in transient dynamics of fracturing solids. Eng Comput 12:145–174. https://doi.org/10.1108/02644409510799532.

Nakagawa T, Narafu T, Imai H, et al (2012) Collapse behavior of a brick masonry house using a shaking table and numerical simulation based on the extended distinct element method. Bull Earthq Eng 10:269–283. https://doi.org/10.1007/s10518-011-9288-9.

O'Sullivan C (2008) Particle-based discrete element modelling: A geomechanics overview. In: Proceedings of the 12th International Conference on Computer Methods and Advances in Geomechanics 2008 1:498–505.

Orduña A, Lourenço PB (2005) Three-dimensional limit analysis of rigid blocks assemblages. Part II: Load-path following solution procedure and validation. Int J Solids Struct 42:5161–5180. https://doi.org/10.1016/j.ijsolstr.2005.02.011.

Pandey BH, Meguro K (2004) Simulation of brick masonry wall behavior under in-plane lateral loading using applied element method. In: Proceedings of the 13th World Conf Earthq Eng Vancouver, BC, Canada, August 1–6.

Pantò B, Cannizzaro F, Caliò I, Lourenço PB (2017) Numerical and experimental validation of a 3D macro-model for the in-plane and out-of-plane behavior of unreinforced masonry walls. Int J Archit Herit 11:946–964.

Peña F, Prieto F, Lourenço PB, et al (2006) Dynamical Behaviour of Rigid Block Structures Subjected to Earthquake Motion. Struct Anal Hist Constr 2:707–714.

Penna A, Morandi P, Rota M, et al (2014) Performance of masonry buildings during the Emilia 2012 earthquake. Bull Earthq Eng 12:2255–2273. https://doi.org/10.1007/s10518-013-9496-6.

Petracca M, Pelà L, Rossi R, et al (2017) Micro-scale continuous and discrete numerical models for nonlinear analysis of masonry shear walls. Constr Build Mater 149:296–314. https://doi.org/10.1016/j.conbuildmat.2017.05.130.

Portioli F (2020) Rigid block modelling of historic masonry structures using mathematical programming: a unified formulation for non-linear time history, static pushover and limit equilibrium analysis. Bull Earthq Eng 18:211–239. https://doi.org/10.1007/s10518-019-00722-0.

Pulatsu B, Bretas EM, Lourenço PB (2016) Discrete element modeling of masonry structures: Validation and application. Earthquakes Struct 11:563–582. https://doi.org/10.12989/eas.2016.11.4.563.

Pulatsu B, Erdogmus E, Lourenço PB (2019) Simulation of Masonry Arch Bridges Using 3D Discrete Element Modeling. RILEM Bookseries 18:871–880. https://doi.org/10.1007/978-3-319-99441-3_94.

Pulatsu B, Erdogmus E, Lourenço PB, et al (2020a) Discontinuum analysis of the fracture mechanism in masonry prisms and wallettes via discrete element method. Meccanica 55:505–523. https://doi.org/10.1007/s11012-020-01133-1.

Pulatsu B, Erdogmus E, Lourenço PB, et al (2020b) Simulation of the in-plane structural behavior of unreinforced masonry walls and buildings using DEM. Structures 27:2274–2287. https://doi.org/10.1016/j.istruc.2020.08.026.

Rafiee A, Vinches M, Bohatier C (2008) Modelling and analysis of the Nìmes arena and the Arles aqueduct subjected to a seismic loading using the Non-Smooth Contact Dynamics method. Eng Struct 30:3457–3467. https://doi.org/10.1016/j.engstruct.2008.05.018.

Raka E, Spacone E, Sepe V, Camata G (2015) Advanced frame element for seismic analysis of masonry structures: model formulation and validation. Earthq Eng Struct Dyn 44:2489–2506.

Roca P, Cervera M, Gariup G, Pela' L (2010) Structural analysis of masonry historical constructions. Classical and advanced approaches. Arch Comput Methods Eng 17:299–325. https://doi.org/10.1007/s11831-010-9046-1.

Sarhosis V, Oliveira D V, Lemos J V, Lourenco PB (2014) The effect of skew angle on the mechanical behaviour of masonry arches. Mech Res Commun 61:53–59. https://doi.org/10.1016/j.mechrescom.2014.07.008.

Sarhosis V, Forgács T, Lemos J V. (2019) A discrete approach for modelling backfill material in masonry arch bridges. Comput Struct 224:. https://doi.org/https://doi.org/10.1016/j.compstruc.2019.106108.

Sharma S, Graziotti F, Magenes G (2021) Torsional shear strength of unreinforced brick masonry bed joints. Constr Build Mater 275:122053. https://doi.org/10.1016/j.conbuildmat.2020.122053.

Shawa O A, de Felice G, Mauro A, Sorrentino L (2012) Out-of-plane seismic behaviour of rocking masonry walls. Earthq Eng Struct Dyn 41:949–968. https://doi.org/10.1002/eqe.1168.

Shi G (1992) Discontinuous deformation analysis: A new numerical model for the statics and dynamics of deformable block structures. Eng Comput 9:157–168. https://doi.org/10.1108/eb023855.

Tagel-Din H, Meguro K (2002) Applied Element Method Used for Large Displacement Structural Analysis. J Nat disaster Sci 24:25–34.

Tateo V, Casolo S (2021) Explicit dynamic analysis by a rigid body-spring model of impact loads of artillery on middle age fortifications. Buildings 11:607. https://doi.org/10.3390/buildings11120607.

Tomazevic M (1978) The computer program POR. Report ZRMK. Inst Test Res Mater Struct Ljubljana.

Tomić I, Penna A, Dejong M, et al (2020) Blind predictions of shake table testing of aggregate masonry buildings. In: Proceedings of the 17th World Conference on Earthquake Engineering, 17WCEE Sendai, Japan.

U.B.C. (1991) International Conference of Building Officials. Uniform Building Code. In: International conference of building officials, USA. Whittier, USA.

van der Pluijm R (1993) Shear behavior of bed joints. 6th North Am Mason Conf 125–136.

van der Pluijm R (1997) Non-linear behaviour of masonry under tension. Heron 42:25–48.

Vanin F, Penna A, Beyer K (2020) A three-dimensional macroelement for modelling the in-plane and out-of-plane response of masonry walls. Earthq Eng Struct Dyn 49:1365–1387. https://doi.org/10.1002/eqe.3277.

Xu BH, Yu AB (1997) Numerical simulation of the gas-solid flow in a fluidized bed by combining discrete particle method with computational fluid dynamics. Chem Eng Sci 52:2785–2809. https://doi.org/10.1016/S0009-2509(97)00081-X.

Yagoda-Biran G, Hatzor YH (2016) Benchmarking the numerical Discontinuous Deformation Analysis method. Comput Geotech 71:30–46. https://doi.org/10.1016/j.compgeo.2015.08.003.

3. Improving the realiability of Equivalent Frame Models of URM façades with irregular opening layouts

Abstract

Researchers and practitioners widely employ simplified Equivalent Frame Models (EFM) for reproducing the in-plane governed response of unreinforced brick masonry (URM) structures, as they typically represent an acceptable compromise between numerical accuracy and computational cost. However, when considering URM structural systems with irregular opening distribution, the definition of the effective height and length of deformable components (i.e. pier and spandrel elements) still represents an open challenge. In this work, the influence of irregular distribution of openings on the predicted lateral response of full-scale URM façades was investigated. To this end, several geometrical combinations characterised by various degrees of irregularity were considered and idealised according to commonly employed EF discretisation approaches. Then, after a preliminary calibration process against experimental tests on both individual piers and a full-scale building façade, EFM results were compared with micro-modelling predictions, carried out within the framework of the Applied Element Method (AEM) and used as a benchmark. Although in specific irregular configurations using some discretisation approaches, macro and micro-models converge to similar results, non-negligible differences in terms of initial lateral stiffness, base-shear and damage distribution were observed with other EF schemes or opening layouts, thus indicating that a careful selection of appropriate criteria is indeed needed when performing in-plane analyses of URM systems with irregular opening distributions. Finally, building on inferred simulated data, potential solutions are given to overcome typical EF discretisation issues and better approximate micro-modelling outcomes.

Keywords: unreinforced masonry, in-plane, irregular opening layouts, Equivalent Frame model, micro-modelling, Applied Element Method

3.1 Introduction

To simulate the in-plane (IP) behaviour of unreinforced masonry (URM) structures under seismic loading, several different modelling methods are presently available in the literature, ranging from advanced micro-modelling to the more simplified macro-modelling approaches (Lourenço, 2002, Roca et al. 2010, D'Altri et al. 2020). The selection of the

modelling scale and refinement level is unavoidably related to the specific structure and mechanical phenomenon under investigation. A low degree of idealisation typically characterises micro-modelling approaches (D'Altri et al. 2020), according to which the actual masonry texture is explicitly reproduced, unit-by-unit.

In this context, discrete models, initially conceived to analyse soil mechanics problems, proved to be particularly suitable for simulating IP-governed responses of URM components and building sub-systems (Malomo et al. 2019a, Pulatsu et al. 2020). Building on previous advancements (e.g. Kawai 1978, Meguro and Hakuno 1989, Casolo and Peña 2007), a recent effort to increase the computational efficiency of discrete methods was made by Meguro and Tagel-Din (2000), developing an innovative rigid body and spring modelling technique, the Applied Element Method (AEM). In the AEM, masonry members are represented as an assembly of rigid elements connected by nonlinear springs interfaces, where material properties are lumped and failure occurs. This efficient tool proved to be suitable to model the heterogeneous nature of URM structures, also enabling the possibility of representing their behaviour up to complete collapse (Karbassi and Nollet 2013, Keys and Clubley 2017, Malomo et al. 2020).

Nonetheless, and despite recent upgrades to these initial schemes (Malomo and DeJong 2021a), the high computational cost and number of material parameters entailed by the abovementioned approaches often make their application prohibitively expensive for professional aims and for e.g. numerically-based seismic risk studies, where a large suite of simulated responses is needed. To decrease computational burden, simplified methods, ranging from the application of limit analysis (Block et al. 2006, Milani et al.2006) to story mechanism models (Braga and Dolce 1982, Tomaževič 1978) and equivalent single-degree-of-freedom systems (Graziotti et al.2016, Snoj and Dolšek 2020), have been used over the years to study the structural behaviour of low-rise and regular masonry constructions subjected to either quasi-static or dynamic IP loading. Amongst others, Equivalent Frame Model (EFM)-based approaches demonstrated to represent an acceptable solution for simulating the IP nonlinear response of large-scale URM buildings. EFM are currently widely employed by both practitioners and researchers, and their use is endorsed by several codes (e.g. Italian code, NTC 2008).

This simplified modelling strategy idealises masonry into an assembly of deformable elements (i.e. spandrels and piers), connected by rigid regions, building a frame of macroelements and nodes. Thanks to its simple approach, the EFM has a limited computational cost, allowing it to be employed for professional aims without losing accuracy. The EFM has proven to be a reliable tool to assess URM building governed by in-plane mechanisms (Magenes 2000, Belmouden and Lestuzzi 2009, Costa et al. 2011, Raka et al. 2015, Penna et al. 2016, Cattari et al. 2018,2021, Kallioras et al. 2019, Peruch et al. 2019, Vanin et al. 2020a, Malomo and DeJong 2021b). Its application has been recently extended to include the out-of-plane response (Vanin et al. 2020b, Malomo and DeJong 2021a).

Although several codes allow the use of the EF approach, they do not provide clear indications on the discretisation criterion for the frame geometry definition. Discretisation criteria and other modelling choices can lead to a dispersion of results, especially when irregular opening distributions are present, being also a source of uncertainty (Parisi and Augenti 2013, Bracchi et al. 2015, Berti et al. 2017).

In the EFM, piers are the main loadbearing elements, carrying vertical loads and providing resistance towards horizontal actions. Spandrels couple the response of those vertical elements affecting their boundary conditions, lateral capacity and crack propagation. Based on these considerations, the first simplified frame approaches defined piers effective height, assuming two limit conditions on spandrels contribute, as suggested by FEMA 356 (2000). The first condition assumes strong spandrels and weak piers (SSWP) and represents the most logical choice for new buildings with rigid diaphragms. This hypothesis assumes that piers crack first, assuming infinitely rigid spandrels and perfect coupling between piers, which are in a fixed-fixed condition with any rotation allowed (storey-mechanism, POR method, Tomazevic 1978). The opposite hypothesis requires uncoupled piers in a cantilever condition, WSSP, weak spandrels and strong piers. In this case, the assumption is that spandrels crack first and represents a more realistic choice when flexible floors provide at the most coupled horizontal displacement for vertical elements (Lagomarsino et al. 2013). However, those upper and lower bounds often are not representative of the actual building's response.

Based on the results of a full-scale test (Yi et al. 2006), Moon et al. (2006) proposed a method defining the effective height as the height over which a compression strut is likely to develop. According to this criterion, the compressive strut is defined assuming that cracks can propagate at 45° or horizontally, offering the minimum lateral resistance (with the steepest possible angle). A similar criterion was formulated by Augenti (2006), and it was based on post-earthquake observation. According to Augenti, the effective height of a pier should be the height of the opening following the pier in the direction of seismic load. These criteria lead to different discretisation depending on the direction of the applied load in the presence of irregular openings. Nonetheless, the use of the EF approach for dynamic analyses requires a unique model.

Dolce (1991) proposed a more complex criterion for the definition of the effective height of piers in a storey-mechanism approach, and it was based on FEM analyses on pier-spandrels sub-systems accounting for the pier stiffness, and the elastic rotational and translational restrains provided by spandrels. This criterion assumed the equivalent effective height of the pier equal to the distance of midpoints of the line connecting two consecutive opening corners further incremented by a contribution proportional to the difference between such distance and the inter-storey height. A limit of 30° was assumed for the inclination of the line connecting consecutive opening corners. The criterion was calibrated by Dolce, comparing the statistical evaluation of the equivalent stiffness obtained with FEM and the elastic stiffness of a pier calculated considering the classical relation for a Timoshenko's beam. The criterion proposed by Lagomarsino (2013) and

currently implemented in the TREMURI computer program is similar to the one of Dolce, without any limit on the inclination of cracks.

The problem of the reliability of EFM in the presence of irregular opening distribution (Siano et al. 2017; Quagliarini et al. 2017) and the definition of the discretisation criteria was discussed by several authors (Calderoni et al. 2017; Camilletti et al. 2018), but a commonly accepted criterion is still missing. The most employed rules come from empirical observation of earthquake damage (Augenti 2006), simplified numerical simulations (Dolce 1991) or assumptions on crack propagation. However, their employment choice is delegated to engineering judgment for the lack of general indication in the presence of irregularities. Several authors investigated the problem of the reliability of the EFM in the presence of irregular openings considering a single discretisation criterion (Parisi and Augenti 2013; Pagani et al. 2017; Berti et al. 2017). On the other hand, many studies analysed the effect of different EFM discretisation criteria (Bracchi et al. 2015), in some cases using continuum FEM as a reference (Calderoni et al. 2017, Siano et al. 2017, Camilletti et al. 2018, Cattari et al. 2021) to compare EFM results.

Since the coupling effect provided by spandrels is also affected by the presence of lintels, adjoining walls, floor connection, and brick arrangement that influences crack propagation, the idealisation of masonry as a continuum is not suitable to account for such contributes. The comparison with a numerical approach that accounts for such features is needed to extend the validity of the EFM to URM buildings with irregular opening distributions providing a general discretisation criterion.

In this work, a discrete modelling approach was considered as a reference solution to evaluate the reliability of EFM, discretised adopting different criteria. Contrary to previous research, which commonly adopted a phenomenological description of masonry, the macroelement considered in this work has the main advantage of relating the structural behaviour to quantities measured experimentally, such as mechanical properties, using mechanically based relationships and applying strength criteria having a solid scientific basis. Moreover, both EF and discrete models were validated against experimental tests, thus providing reliable results for the comparison. The problem of the EF discretisation criterion was scrutinised in this study. To this end, a set of irregular opening layouts were analysed to investigate whether different criteria lead to significantly different results. Then, the lateral response of a few selected irregular configurations, discretised with different criteria, was compared with micro-modelling predictions, used here as a benchmark to evaluate the accuracy of EF results. Finally, some critical situations were discussed.

3.2 Selected numerical modelling strategies

In this section, the employed modelling strategies are presented, and their idealisation approach to URM buildings is discussed.

3.2.1 Equivalent Frame Model (EFM)

According to the EFM, masonry structures are ideally subdivided into rigid nodes and deformable elements (i.e. spandrels and piers), as depicted in Figure 3.1a. This assumption is based on experimental outcomes and post-earthquake observations indicating that deformations are located in recurrent areas while others work as rigid parts. In this work, the research version of TREMURI software (Lagomarsino et al. 2013) was used, considering the macroelement model initially proposed by Penna et al. (2014) and then further improved by Bracchi et al. (2021). A macroelement is a two-node element with eight degrees of freedom (DOFs), and it consists of three main parts: a central body where only shear deformations are allowed and where two internal DOFs are placed, and two zero-thickness spring interfaces governing the axial-flexural behaviour, where six DOFs are located. A no-tension model with the bilinear law in compression proposed by Bracchi et al. (2021) is assigned to the zero-thickness springs, whereas the shear damage model is based on the one proposed by Gambarotta and Lagomarsino (1997). Shear failure is predicted by multiple shear strength criteria implemented in the macroelement by Bracchi and Penna (2021).

In this work, the strength criterion was selected to be representative of the expected failure mode (i.e. diagonal shear failure). The selected strength criterion is the one proposed by Mann and Müller (1982), accounting for the brick tensile failure, f_{bt}. Originally formulated as a local criterion, it was converted into a global strength criterion (3.1) by Magenes and Calvi (1997), introducing the correction to consider the influence of the shear span ratio.

$$V = \frac{f_{bt}lt}{2.3(1 + \alpha_v)}\sqrt{\frac{N}{f_{bt}lt} + 1} \tag{3.1}$$

Where α_v is the shear span ratio, and it is equal to h_0/l. h_0 is the distance between the section with zero moment and the section with the maximum moment, and l is the wall length.
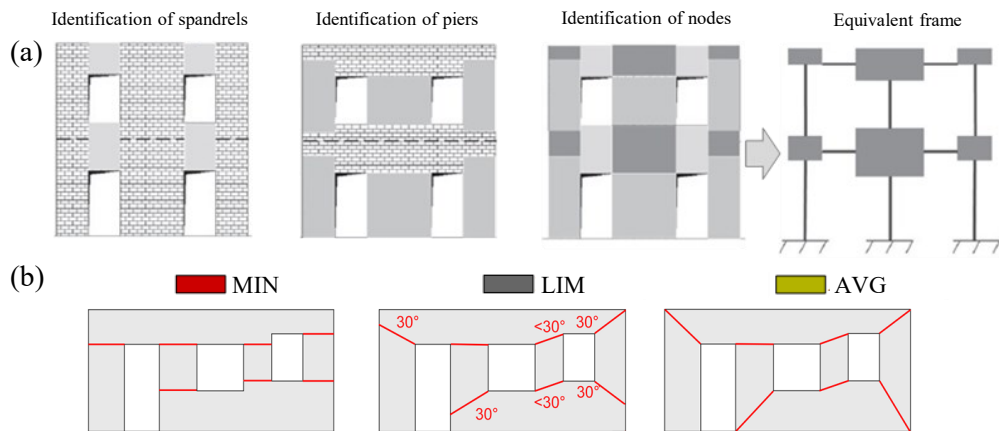
Figure 3.1 a) EFM idealisation (adapted from Lagomarsino et al. 2013), b) selected criteria for the identification of the effective height of piers in EF wall discretisation

Mechanical properties considered in the macroelement model are: density ρ, Young modulus E, shear modulus G, compressive strength f_m, brick tensile failure, f_{bt}, cohesion c, friction coefficient μ. Two phenomenological parameters govern the nonlinear shear response: Gc_t, controlling macroelement inelastic shear deformability, and β, which influences the slope of the post-peak softening branch.

The identification of rigid nodes and deformable elements (i.e. spandrels and piers) is often a challenging process, especially when considering irregular opening distributions, a common feature of pre-code existing URM buildings. Moreover, the selection of effective height of deformable elements might be affected by several aspects, influencing e.g. the direction of crack propagation (as the presence of lintels or other irregularities which can lead to local weaknesses), and it might vary depending on the direction of the lateral load, leading to a different failure mode. In practice, in the presence of regular opening distribution, spandrels are identified as the elements between two aligned vertical openings, and piers are defined according to a discretisation criterion among the available in the literature. Rigid nodes are the portions delimited by these deformable elements. Several discretisation approaches define geometrical rules for piers effective height identification, mostly based on experimental (Yi et al. 2006) or post-earthquake observation (Augenti 2006) and on the assumption of the expected failure mode and the inclination of cracks, which delimits the deformable parts of the structure. Although some criteria (e.g. Augenti 2006, and Moon et al. 2006) lead to different discretisation depending on the direction of the applied load, the use of the EF approach for dynamic analyses requires a unique model (e.g. Lagomarsino et al. 2013).

In this work, three discretisation criteria were chosen according to the most common assumptions (Rota et al. 2014, Bracchi et al. 2015), generating a single EF discretisation for both loading directions. The first criterion (MIN) assumes piers effective height as the masonry wall's minimum clear height between two consecutive openings. The second approach (LIM) assumes the effective height of piers as the distance between midpoints of the segments connecting two corners of adjacent openings, with a limit of 30° for the inclination of that line. Where the hypothesis to limit to 30° the maximum cracks inclination is derived from the criterion proposed by Dolce (1991) for the definition of pier effective height in models based on storey mechanisms (POR). The third criterion (AVG) is equal to the second one without limiting the ideal corner connecting line's maximum inclination. This last criterion, which was also adopted for spandrels element, is the criterion implemented in 3Muri, the commercial version of the TREMURI computer program (Lagomarsino et al. 2013). The three criteria are graphically represented in Figure 3.1b): MIN, LIM and AVG from left to right.

3.2.2 Applied Element Method (AEM)

The AEM was selected in this work as a reference model to evaluate the EFM predictions. It can be classified as a rigid body and spring model. Its application to masonry structures modelling consists of the ideal representation of this material as an assembly of rigid elements connected by zero-thickness springs interfaces, where material properties are lumped. This discrete approach is naturally suitable for modelling heterogeneous material,

and it explicitly represents the actual brick arrangement (Figure 3.2a). The material model in compression is the one originally developed by El-Kashif and Maekawa (2004) with a tension cut-off without any softening branch. Sliding along mortar joints is represented by Coulomb's friction model. Each spring interface is characterised by a normal and a shear stiffness evaluated through equation (3.2)-(3.5), where the nomenclature can be found in Figure 3.2b. Springs placed between bricks units and representing mortar-brick interaction are here named brick-mortar springs. Their normal ($k_{n,b\text{-}mo}$) and shear ($k_{s,b\text{-}mo}$) stiffnesses are evaluated considering mortar and brick springs in series by equations (3.2) and (3.3). In order to capture the possible cracking through brick, units are further divided into two elements connected by brick-brick springs interfaces, evaluating their stiffnesses ($k_{n,b\text{-}b}$ and $k_{s,b\text{-}b}$) by equation (3.4) and (3.5). Where E_b, G_b, E_{mo} and G_{mo} are the unit and mortar Young's and shear moduli, respectively.

$$\frac{1}{k_{n,b-mo}} = \frac{a - l_{mo}}{E_b \, d \, t} + \frac{l_{mo}}{E_{mo} \, d \, t} \qquad (3.2) \qquad \frac{1}{k_{s,b-mo}} = \frac{a - l_{mo}}{G_b \, d \, t} + \frac{l_{mo}}{G_{mo} \, d \, t} \qquad (3.3)$$

$$\frac{1}{k_{n,b-b}} = \frac{a_b}{E_b \, d \, t} \qquad (3.4) \qquad \frac{1}{k_{s,b-b}} = \frac{a_b}{G_b \, d \, t} \qquad (3.5)$$
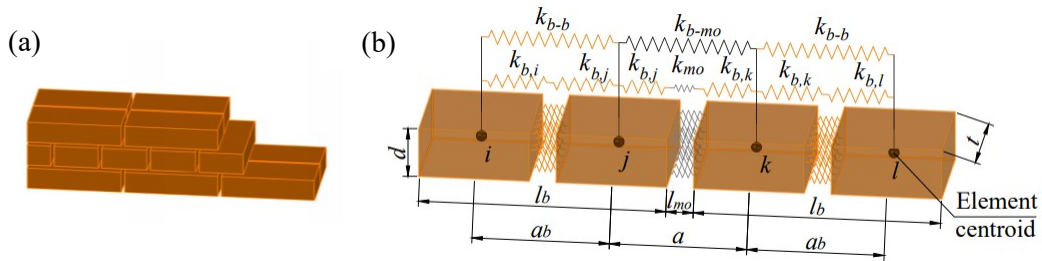
Figure 3.2 a) Brick based arrangement, b) masonry discretisation

3.3 Model validation against experimental data

The models material properties employed in this work were calibrated by simulating the experimental shear-compression tests on two masonry panels tested at the Joint Research Centre (Ispra, Italy) by Anthoine et al. (1995). Both AEM and EFM were then validated on a full-scale in-plane cyclic test of a building façade tested at the University of Pavia (Italy) by Magenes et al. (1995). The first simulations are discussed in section 3.1, whereas the latter, which allowed the EFM spandrel mechanical parameters refinement, is presented in section 3.2.

3.3.1 Simulation of shear compression test on single components

Two solid bricks two-wythe walls with an English bond pattern arrangement were tested at the Joint Research Centre of Ispra under a compression level of 0.6 MPa and double-fixed boundary conditions. A horizontal displacement history was applied in a quasi-static test to the top beam performing two or three cycles at each amplitude. The two walls, named

Highsta and Lowsta, were 0.25 m thick and 1 m in length, with different height/length ratios of 2 and 1.35. The squat wall (i.e. Lowsta) exhibited a shear failure with diagonal cracking and a peak shear force of 84 kN, which was reached at 2.8 mm of horizontal displacement, corresponding to a 0.2% drift, with a strength degradation from this point on. The slender wall (i.e. Highsta) was characterised by a flexural behaviour with horizontal cracks at the top and bottom due to the partialisation of the panel section, without any strength degradation. The peak shear force of 72 kN was reached at a drift level of 0.6% (12.7 mm). The EFM parameters, calibrated through the shear compression tests on these two walls, are presented in Table 3.1.

Table 3.1 Macroelement mechanical parameters (EFM)

ρ [kg/m^3]	E [MPa]	G [MPa]	f_m [MPa]	f_{bt} [MPa]	Gc_t [-]	β [-]
1800	2300	800	6.20	1	1.80	0.38

Compressive strength, f_m, and density, ρ, were obtained by characterisation test. Elastic and shear moduli, E and G, as well as the brick tensile strength, f_{bt}, were initially derived by component tests and further refined through the comparison with the experimental shear-compression tests on piers. The shear model parameters (i.e. the shear deformation parameter c_t and the softening parameter β) were calibrated through the presented numerical simulations. As discussed in section 3.2, the macroelement here adopted for pier elements assumed an equivalent Mohr-Coulomb criterion, automatically evaluating the equivalent cohesion and friction coefficient for the selected shear strength criterion, as presented by Bracchi and Penna (2021). The macroelement proposed by Penna et al. (2014) was adopted for spandrel elements. A preliminary sensitivity analysis (whose results are not reported here for space constraints) was carried out to set optimal convergence parameters.

The AEM Young's and shear moduli of brick-mortar springs were first estimated and further calibrated, comparing numerical and experimental results of the two shear-compression tests considered, as discussed in section 3.2.2. The other material parameters were assumed according to the characterisation test results and further refined simulating the shear-compression tests on individual piers. In Table 3.2, material properties of the AEM model are presented, identified for brick-brick (subscript b) and mortar-brick (subscript b-mo) interfaces. A brick based discretisation was adopted, and, as the failure modes involved cracks passing through bricks, the units were further separated into two parts connected by brick-brick springs.

Table 3.2 Material properties of AEM model

ρ [kg/m^3]	E_b [MPa]	G_b [MPa]	f_{bt} [MPa]	c_b [MPa]	μ_b	f_m [MPa]
1800	2400	960	1.25	4.42	0.80	15.6
$E_{b\text{-}mo}$ [MPa]	$G_{b\text{-}mo}$ [MPa]	$f_{t\,b\text{-}mo}$ [MPa]	$c_{b\text{-}mo}$ [MPa]	$\mu_{b\text{-}mo}$		
1550	540	0.23	0.23	0.80		

E_b, G_b, f_{bt}, c_b and μ_b are elastic and shear moduli, tensile strength, cohesion and friction coefficient of brick. $E_{b\text{-}mo}$, $G_{b\text{-}mo}$, $f_{t\,b\text{-}mo}$, $c_{b\text{-}mo}$ and $\mu_{b\text{-}mo}$, are the elastic and shear moduli, tensile strength, cohesion and friction coefficient of mortar-brick interfaces. E_b, f_{bt}, $f_{t\,b\text{-}mo}$ and $c_{b\text{-}mo}$ were derived from characterisation tests (Binda et al. 1996a,b). The compressive strength f_m was assumed equal to the brick one for both brick-brick and mortar-brick interfaces to avoid premature failure, as already suggested by other researchers (Mayorca and Meguro 2003, Malomo et al. 2018). G_b and $G_{b\text{-}mo}$ were evaluated assuming $G=0.35E$. c_b was derived analytically assuming a Mohr-Coulomb criterion. $\mu_{b\text{-}mo}$ and μ_b were refined in the calibration process.

The comparison in terms of hysteretic curves of the two numerical models and the experimental tests on both squat and slender walls is presented in Figure 3.3.
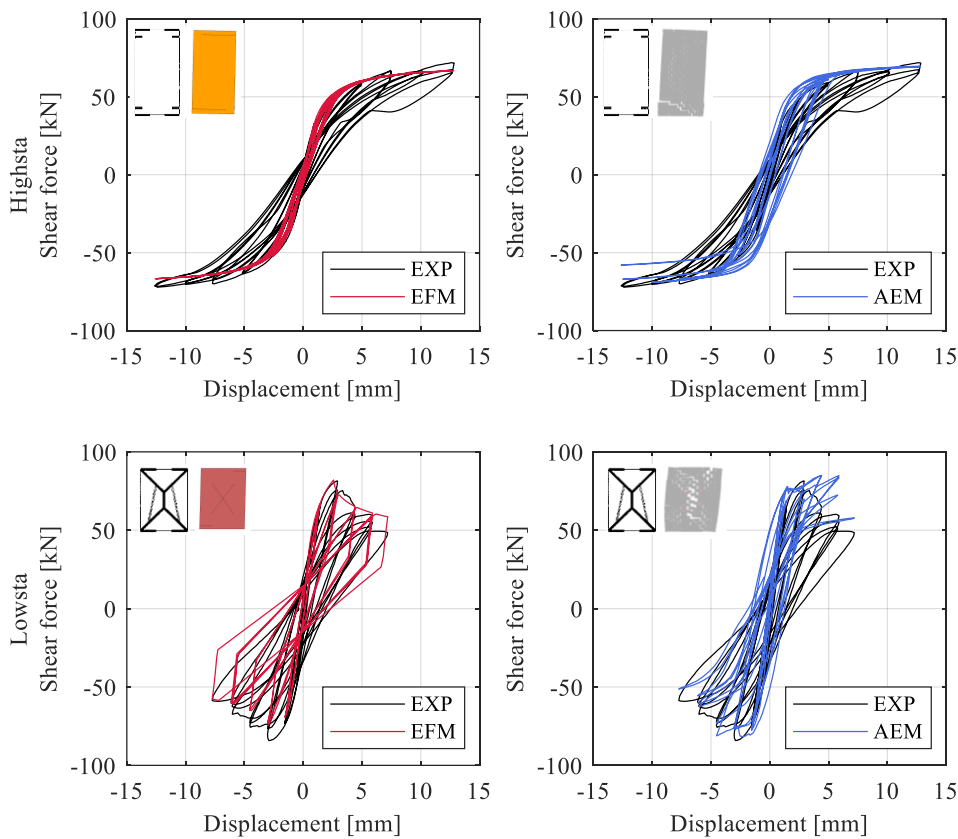
Figure 3.3 Experimental (adapted from Anthoine et al. 1995) vs numerical force-displacement hysteresis of Highsta and Lowsta obtained with the EFM and AEM models

Both numerical models satisfactorily captured the Highsta wall behaviour. The EF macroelement showed flexural cracks at the top and bottom sections, showing a good

agreement in peak base shear capacity and initial lateral stiffness (Figure 3.3), with differences around 7% and 5%, respectively, while energy dissipation is slightly underestimated (Figure 3.4). The AEM showed a flexural-rocking behaviour with cracks developed at the top and bottom sections and then propagated through the first courses. A good agreement was found in initial lateral stiffness and shear force (Figure 3.3), with differences lower than 5%, while stiffness deterioration was underestimated.

Regarding the squat wall, Lowsta, both models captured initial lateral stiffness (differences <10%) and post-peak deterioration, predicting a diagonal shear failure mechanism. The EFM predicted almost the exact value of the peak base shear in the positive direction and a difference around 10% in the negative, with a good agreement in energy dissipated. The AEM showed few brick failures at the top and bottom corners and at the centre of the panel. The energy dissipated was slightly overestimated in the central cycles due to the brick failures, and it was underestimated in the last, while minor differences were found in peak base shear (<5%), reached at 0.4% of drift ratio (where the experimental peak was at 0.2% of drift ratio). These differences found in the AEM response of Lowsta model are consistent with what was already found by other researchers using discrete approaches and allowing only a single failure surface into brick elements (Miglietta et al. 2017, Malomo and DeJong 2021a). Despite these differences, the AEM predicts the strength deterioration with a good agreement, with differences around 20% with respect to the experimental decreasing, whereas a difference of 30% was found in EFM. The cumulative energy dissipated is reported in Figure 3.4, normalised with respect to the total experimental energy dissipated.
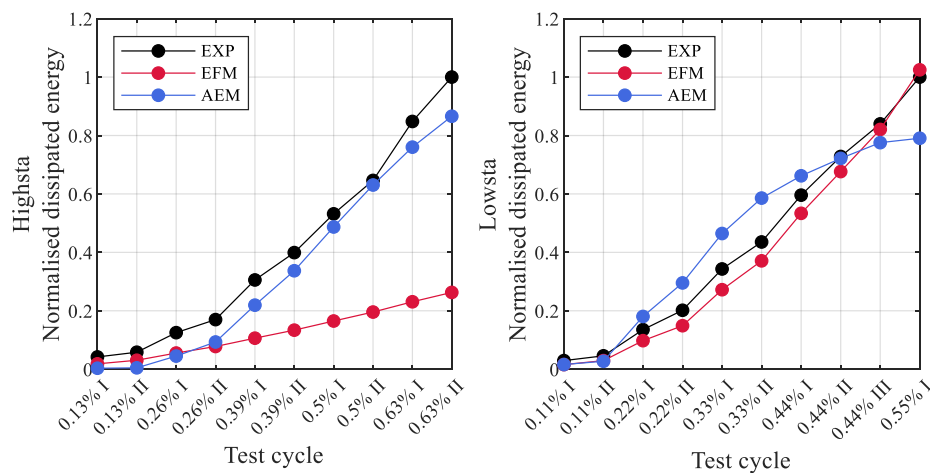
Figure 3.4 Experimental (EXP) vs numerical (AEM, EFM) cumulative dissipated energy, normalised with respect to the total experimental value, of Highsta and Lowsta

As the cyclic behaviour obtained with the two modelling approaches is in good agreement with the experimental ones, in this work, the attention was focused on the effect of the irregularity on the monotonic response.

3.3.2 Simulation of a quasi-static test on a full-scale URM prototype

The prototype considered in this work is a two-storey URM masonry building consisting of four two-wythe walls of solid bricks arranged in an English bond pattern. The structure had a regular opening distribution, and flexible diaphragms consisted of a series of isolated steel beams where the vertical load of 10 kN/m^2 was applied at both floor levels. One of the two longitudinal walls, named Door Wall, was disconnected from the transversal walls, and it was here referred to as a regular baseline for the following study. The full-scale prototype was tested at the University of Pavia in 1995 under a quasi-static cyclic test. Horizontal forces were applied in displacement control through actuators placed at each level of the longitudinal façades, keeping a constant ratio between the applied loads. Three EF models of the independent wall, Door Wall, were built assuming the three discretisation criteria considered. Material properties adopted in EFM are reported in Table 3.3, while the AEM ones are the same implemented in the component tests Table 3.2. In both AEM and EFM models, the steel trusses placed at each floor level and used to apply the horizontal loads were explicitly modelled considering the actual cross-section and providing axial and flexural stiffness. No additional restraints were necessary at the floor level. Regarding the AEM, units are placed in a brick-based arrangement (i.e. two-wythe), and forces were applied through a system of trusses and steel beams with the aim to obtain equal forces at each floor level.

Two in-plane monotonic static analyses (i.e. in both positive and negative directions) were performed with the four models (i.e. AEM and the three EFM), and results are compared in terms of damage, initial lateral stiffness and peak base shear. Out-of-plane displacements were restrained in the AEM model, whereas the EF 2D model allowed IP analyses.

Table 3.3 Material properties of EFM piers for MIN, AVG and LIM criteria

	ρ [kg/m^3]	E [MPa]	G [MPa]	f_m [MPa]	f_{bt} [MPa]	Gc_t [-]	β [-]
MIN	1800	1570	600	6.20	0.80	1.90	0.30
LIM	1800	2300	800	6.20	0.83	3.30	0.30
AVG	1800	2300	800	6.20	0.83	4.00	0.30

First cracks developed through spandrels in the experimental cyclic test, with minor flexural damage at piers edges. Then, with the loss of the coupling effect of spandrels, the central ground-level pier developed a diagonal shear mechanism, and external ground-level piers failed in shear (Figure 3.5a). Both AEM and EFM predicted an in-plane response mainly governed by ground-level piers, as experienced by the experimental prototype.

In the AEM, first cracks developed through spandrels and piers edges due to flexural mechanisms, then the ground-level central pier showed diagonal cracks. The external ground-level pier on the compressed side exhibited diagonal cracks due to a shear mechanism at large displacements (corresponding to a drift of 0.4%), whereas only flexural cracks at top and bottom edges occurred for lower displacements (Figure 3.5c). As monotonic static analyses were performed, the ground-level pier subjected to a lower

compression (i.e. in the negative side for positive pushover and vice versa) showed only flexural cracks at both edges. Minor flexural damage was detected in piers at the first level, as shown in (Figure 3.5b).
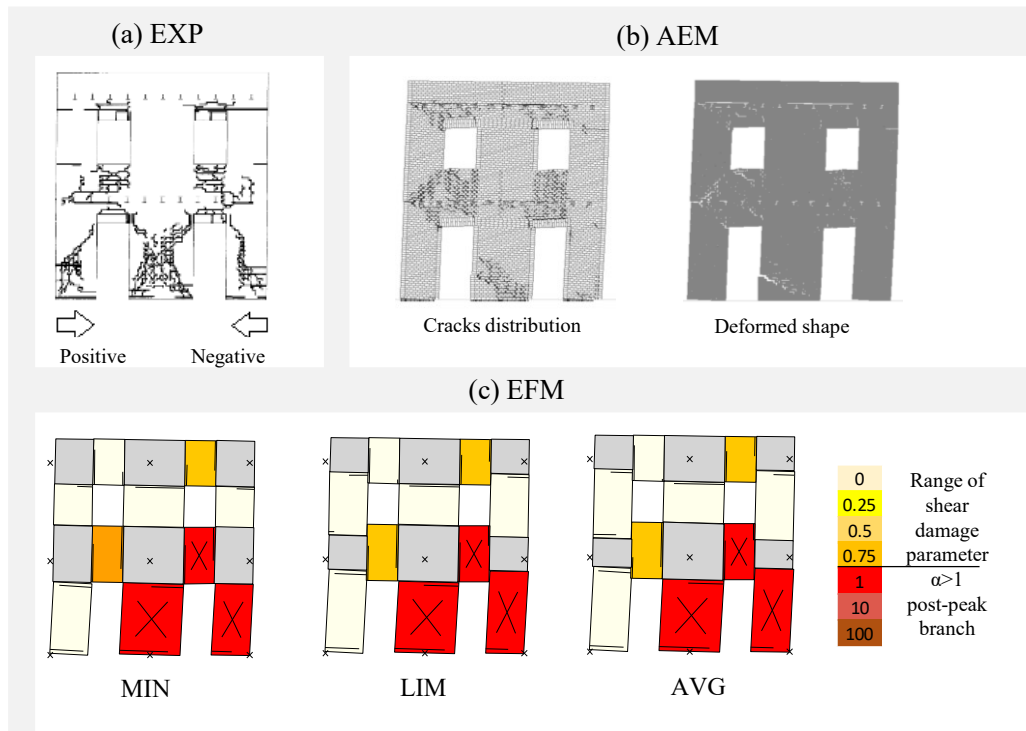
Figure 3.5 a) Experimental (adapted from Magenes et al. 1995), b) AEM and c) EFM damage patterns

A good agreement was found between numerical and experimental results in terms of initial lateral stiffness, peak and residual base shear (V_b), with differences under 15% and 10%, respectively, compared to the experimental backbone (Figure 3.6). Moreover, the AEM showed a slightly higher base shear than the experimental counterpart. This result was somehow expected, given that cyclic degradation experienced by the experimental specimen could not occur in a monotonic test. The EFM initially showed damage located at spandrels, more significant in the one at the more compressed side. Then, according to what exhibited by AEM and by the experimental specimen, a shear failure mechanism developed in the central pier and the external one at the compressed side. In Figure 3.5c, the EFM damage pattern obtained with the three criteria is presented. The shear damage parameter α>1 represents the attainment of the maximum shear strength of the macroelement.
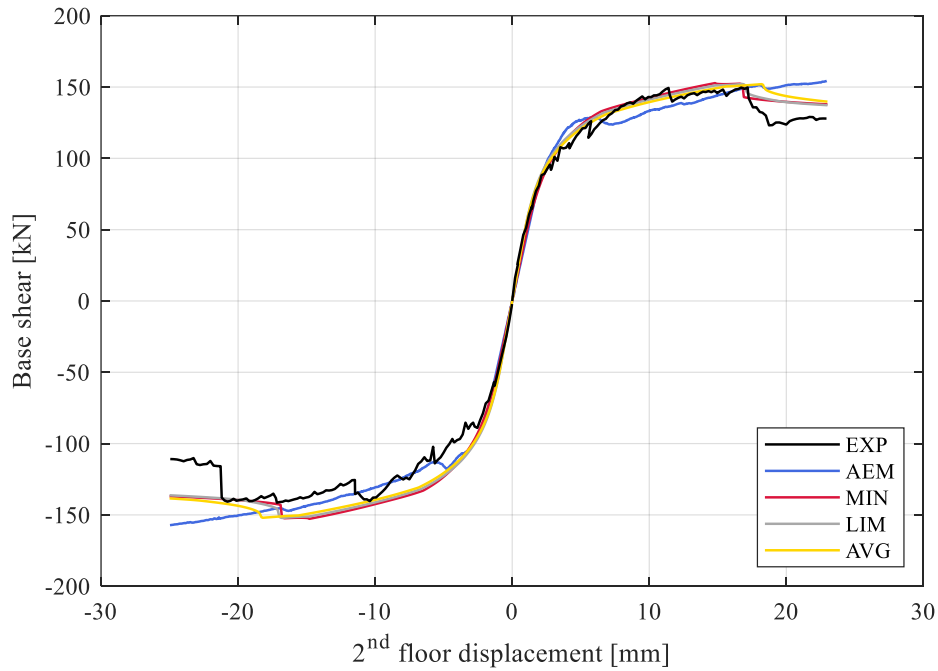
Figure 3.6 Experimental versus numerical IP monotonic pushover curves

3.4 EFM vs AEM numerical outcomes

This work aims to evaluate the effect of different discretisation criteria on the predicted EFM response to formulate suggestions on the use of this modelling approach when the distribution of the openings is irregular. To this end, a set of façades (Figure 3.7) characterised by various irregularities on the opening distribution, selected according to the classification proposed by Parisi and Augenti (2013), and including vertical and horizontal misalignments and different opening sizes, was chosen starting from the regular layout (i.e. Door Wall, configuration 1). Fourteen EF models were created applying the selected discretisation criteria, i.e. MIN, LIM and AVG.
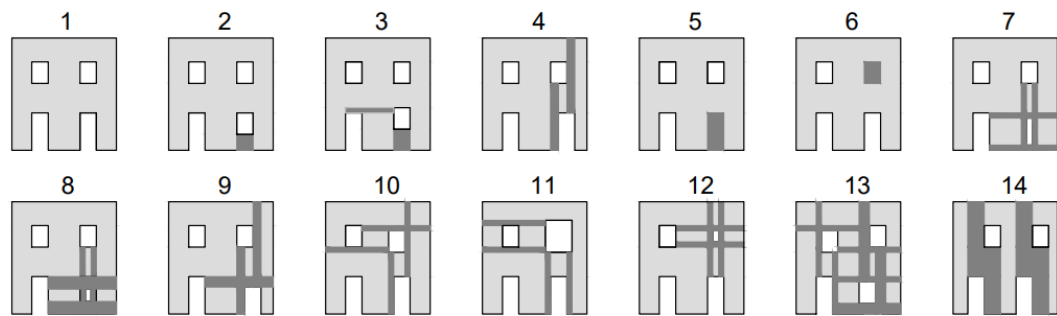
Figure 3.7 Selected layouts

Monotonic static analyses in displacement control were performed in both directions with EFM, and their results were compared for each configuration in terms of initial lateral stiffness (ILS) and peak base shear (V_{bp}), Figure 3.8.

Figure 3.8 Results in terms of initial lateral stiffness (ILS_n) and peak base shear ($V_{b,np}$), normalised with respect to the experimental value of the regular configuration (i.e. 1)

As discussed in section 3.3.1, in the EFM local drift limits, corresponding to a sudden drop of the lateral capacity, were not explicitly introduced as the post-peak deterioration was adequately predicted by the macroelement shear model. Monotonic static analyses were also performed with the AEM models, which were assumed as a benchmark. As constructing AEM models is time-consuming, only the relevant configurations were analysed using this modelling approach. The selection was based on the larger differences found between the three EFM results in terms of lateral strength and stiffness. Figure 3.8 compares the results obtained with the three EF discretisation criteria on the fourteen configurations in peak base shear (V_{bp}) and initial lateral stiffness (ILS_n), normalised with respect to the experimental values of the regular configuration, whereas Figure 3.9 and Figure 3.10 present the damage pattern predicted by EFM and AEM models. The ILS was computed considering the inclination of the line connecting the points that correspond to the 15% and the 30% of the V_{bp}. The three criteria showed a good agreement in configurations 4,6,9,10,11,12, and 14, with almost equal values of V_{bp} and variability of ILS under 20%.

On the contrary, more significant differences were found in the other layouts. Among the considered set of irregular configurations, a selection of case study was analysed using the AEM approach, and it comprised configurations 1,2,5,6,7,8 and 13. The selection was driven by the need to analyse further the configurations where the EF geometrical identification is more challenging, leading to different discretisations and lateral responses. Among the considered layouts analysed with the AEM approach, more significant differences were found when a reduced or missing opening was considered, with differences up to 80% in terms of ILS and up to 30% in V_{bp}.

When loaded in the positive direction, all the considered configurations showed the initial cracking of first and second floor spandrels and the partialisation of piers at ground level due to flexural mechanisms. Then, increasing the horizontal applied load, piers and spandrels at ground level exhibited shear damage up to the attainment of their shear strength. AEM models first showed the extensive diagonal cracking of the central pier at ground level, followed by the downwind pier. In contrast, the external pier with the lower compression level (i.e. on the left side) exhibited flexural cracks. Consistently, EFM presented a shear mechanism on the elements at the compressed side, with the attainment of their maximum lateral strength, which corresponds to the peak base shear of the façade. Typically, MIN discretisation reached its lateral strength at lower displacement than LIM and AVG in both positive and negative loading directions. EF and AEM models predicted similar responses when façades were loaded in the negative direction, with the initial development of flexural cracks, followed by extensive shear damage on the elements at the compressed side. Generally, EFM resulted in a higher value of V_{bp} and ILS, even greater when the MIN criterion is considered.
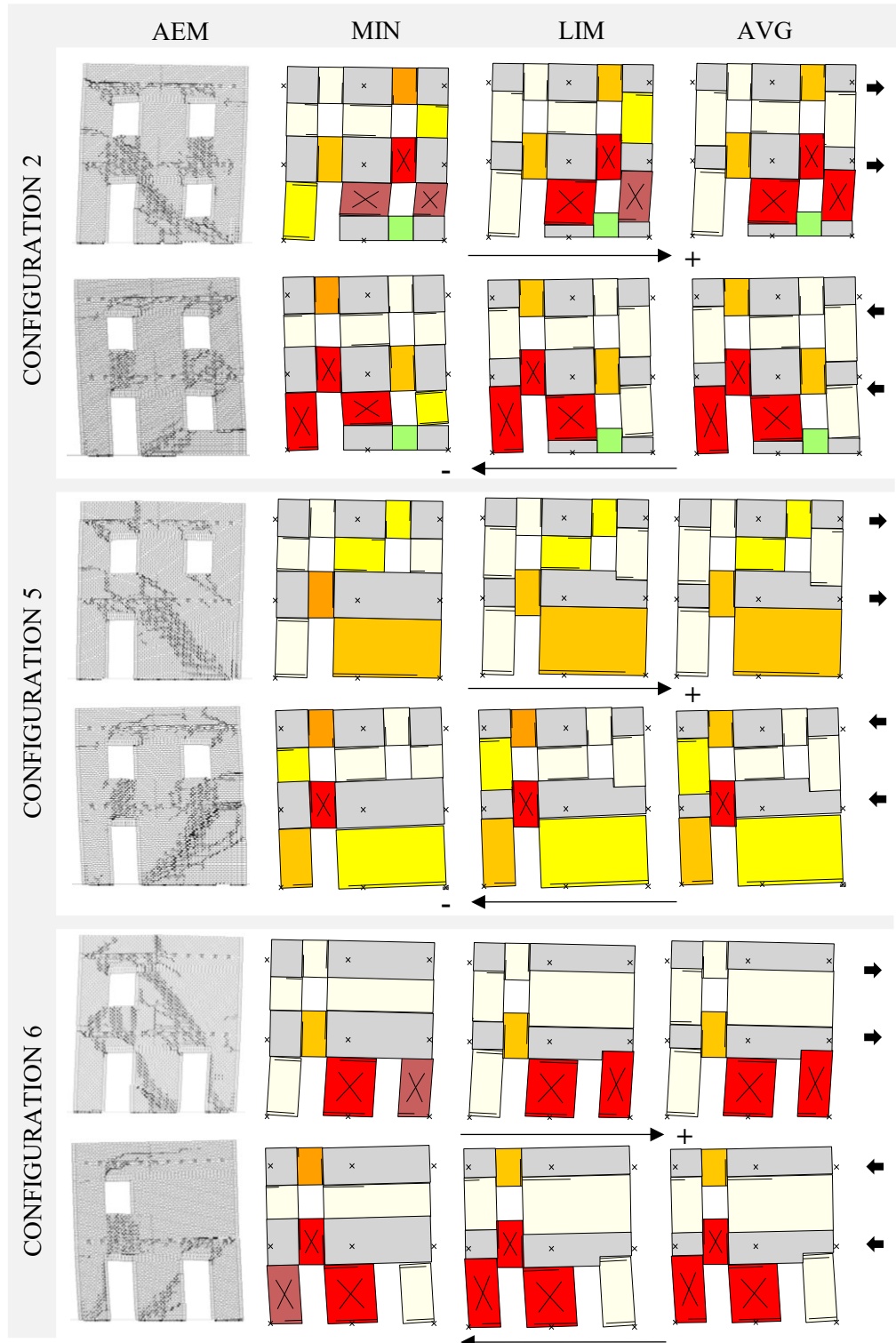
Figure 3.9 Deformed shape and damage of AEM and EFM of configuration 2 (C2), C5 and C6 at 25 mm of top displacement -refer to Figure 3.5c for the color legend-.
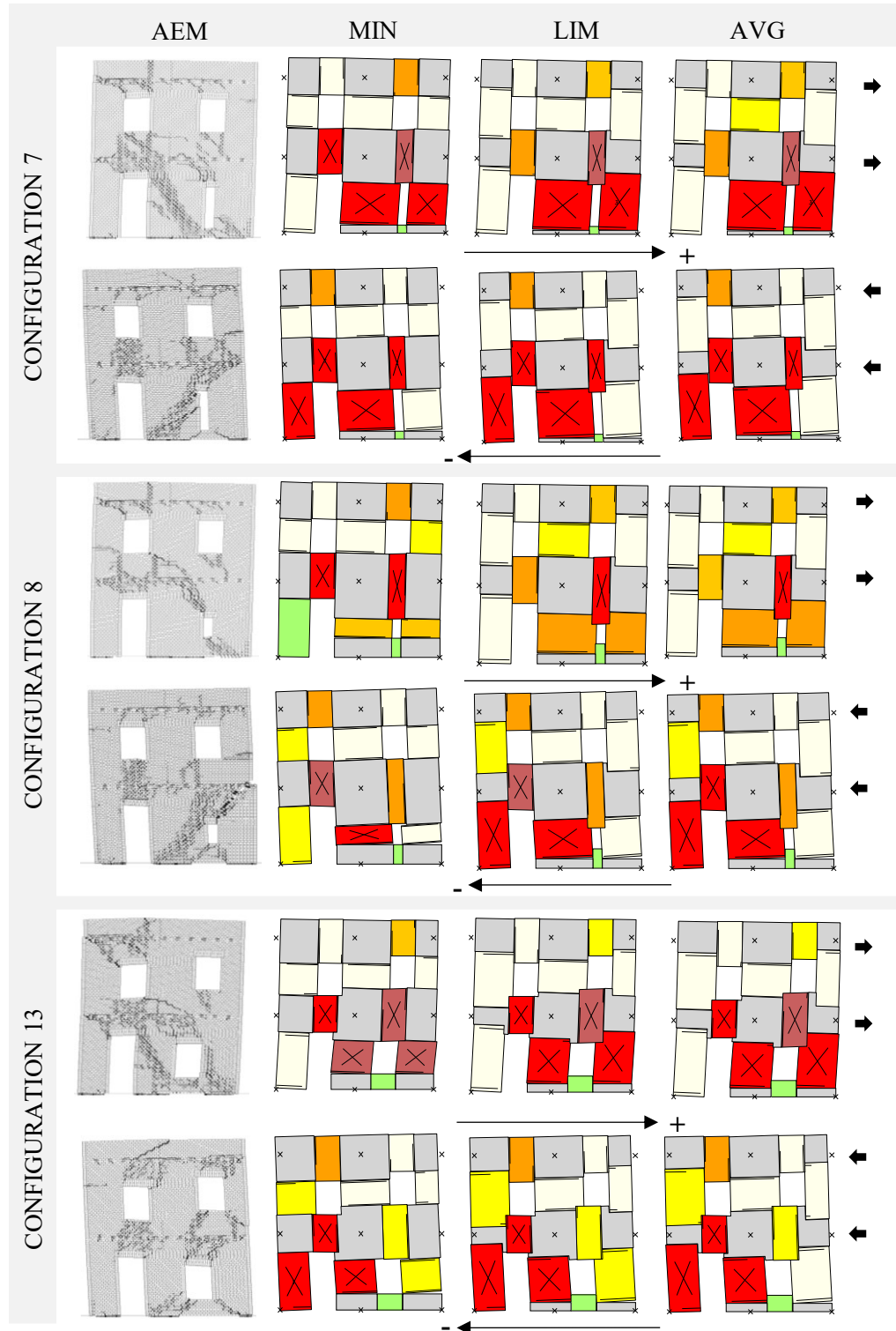
Figure 3.10 Deformed shape and damage of AEM and EFM of C7, C8 and C13 at 25 mm of top displacement (15 mm for C8 in positive direction) -refer to Figure 3.5c for the color legend-.

Due to the presence of different irregularities or discretisations, some differences were found with respect to the above presented general response:

- In the positive direction, the AEM models of configurations 2, 5, 7 and 8 experienced a sudden decrease of the global base shear after the opening of the diagonal crack on the central pier, then configurations 5,7 and 8 exhibited a brittle failure due to the stress concentration caused by the application of the horizontal load through the second floor trusses, accompanied by the diagonal cracking of central pier at first level in configuration 7 and 8. The analyses were interrupted when a brittle failure occurred at 15 mm of top displacement in configurations 5 and 8. EFM did not present this phenomenon.
- EFM of configuration 5 predicted flexural damage in spandrels and piers, followed by light shear damage at ground level. This configuration showed a global cantilever behaviour of the whole façade without attaining the peak shear strength in any element. A similar response was detected when EFM of configuration 5 were loaded in the negative direction. On the contrary, the AEM model lateral response was governed by the diagonal shear mechanism on the squat pier when the load was applied in the positive direction. In contrast, the predicted failure mechanisms of the two modelling approaches were consistent in the negative direction.
- In configuration 6, EFM showed almost the same damage pattern of configuration 1 at ground level, whereas the squat pier at first level was substantially undamaged, as well as, naturally, the large rigid nodes. On the contrary, the squat pier at the first level was interested by the development of diagonal cracks when the AEM model was pushed in the positive direction.
- In the positive direction, the AEM model of configuration 8 predicted a lateral response governed by the diagonal cracking passing through the small window at ground level. EFM predicted slight shear damage on the downwind piers at the ground level, with a global response consistent with the one predicted by EFM in configuration 5.

3.5 Analysis and interpretation of results

The crack pattern predicted by AEM models, concentrated in recurring areas, suggests that it is still possible to idealise a structure as an assemble of deformable and rigid portions even when the distribution of the openings is irregular. On the other hand, some differences were found in the geometry of EFM deformable elements and the AEM regions interested by crack propagation. Moreover, generally, EFM tend to predict higher initial lateral stiffness (ILS) than the AEM models. This can be attributed to the larger rigid nodes, compared to the portions not affected by cracks in the AEM. The authors already noted this phenomenon, as in previous works discrete models predicted lower initial stiffness with respect to the EF approach (Malomo et al. 2019b). The MIN discretisation, which led to larger rigid portions, often predicted higher lateral stiffness than AEM and the other discretisation criteria.

In contrast, AVG and LIM seem to represent better the deformable regions identified by the cracks in the AEM models, and consequently, the lateral stiffness. Moreover, the MIN

criterion led to a stiffer response despite the lower value of E and G compared to the other criteria, as the effective height of piers more influenced the lateral stiffness than the material properties. For this reason, in the configurations where discretisation criteria led to similar rigid portions (e.g. 4,6,14), MIN resulted in a lower ILS (see Figure 3.8). In terms of peak base shear ($V_{b,p}$), good agreement was found between AEM and AVG and LIM models in configuration 2,6,7 and 13 (<10%) in the positive direction, whereas higher differences were found in terms of ILS. The MIN criterion showed greater $V_{b,p}$ and ILS differences in configurations with a reduced opening at the ground level (i.e. 2,5,7 and 8). This last aspect was further scrutinised in the following (section 6).

In order to compare the influence of the selected discretisation criteria on the EFM reliability, the lateral response of the irregular configurations was further analysed comparing the equivalent bilinear curves obtained from the EFM and AEM force-displacement curves. Where the equivalent lateral stiffness was obtained considering the secant stiffness at the 70% of the maximum base shear (as proposed by several codes like NTC 2008) and the yielding force, F_y, was found by equating the areas below the curves between the origin and the ultimate displacement (which was limited to the maximum displacement of the experimental test on configuration 1). The comparison between the bilinear curves obtained from the EFM and the AEM pushover curves is reported in Figure 3.11. Contrary to other discrete approaches, which proved to be a suitable reference for the identification of the ultimate displacement capacity (Malomo et al. 2019), the AEM reliability has not been demonstrated. For this reason, the ultimate displacement of the considered façades was limited to the maximum displacement attained in the experimental test. No drift limits, needed to identify the ultimate capacity in the EFM, were imposed.

Piers at ground level governed the IP response of the irregular façades, consistently with what experimentally found in the regular configuration. This led to the different response of the EFM defined with the three criteria when the irregularity was located at the ground level, as the discretisation approach affected the effective height of piers at ground level, which mostly influenced the lateral response. Consistently, the equivalent bilinear curves obtained with the EFM in configurations 4,9,10,11,12 and 14 were almost superimposable (see Figure 3.11). These configurations were not further analysed with the AEM model, as the three adopted discretisation criteria led to equivalent results. Configuration 3 (C3) showed noticeable differences between the bilinear curves obtained with the three EFM. Nevertheless, as this layout was generated by introducing a horizontal misalignment on the ground level window of C2, and the EFM of C2 and C3 resulted in comparable responses, only C2 was modelled and analysed with the AEM.

Regarding the configurations analysed with the micro-modelling approach, i.e. 1,2,5,6,7,8 and 13, the comparison between the yielding force, F_y, obtained by the bilinearisation process is presented in Figure 3.12, and it is expressed in terms of percent difference with respect to the AEM value. The MIN criterion generally led to significant differences with respect to the AEM model in both directions, whereas AVG and LIM resulted more consistent with the value of F_y obtained with the micro-models. When considering C5, no differences were found between the three EFM, which predicted significant differences

compared to AEM. Two modified discretisation layouts were proposed for C5 to overcome this problem, and they are discussed in the following (3.5.2).
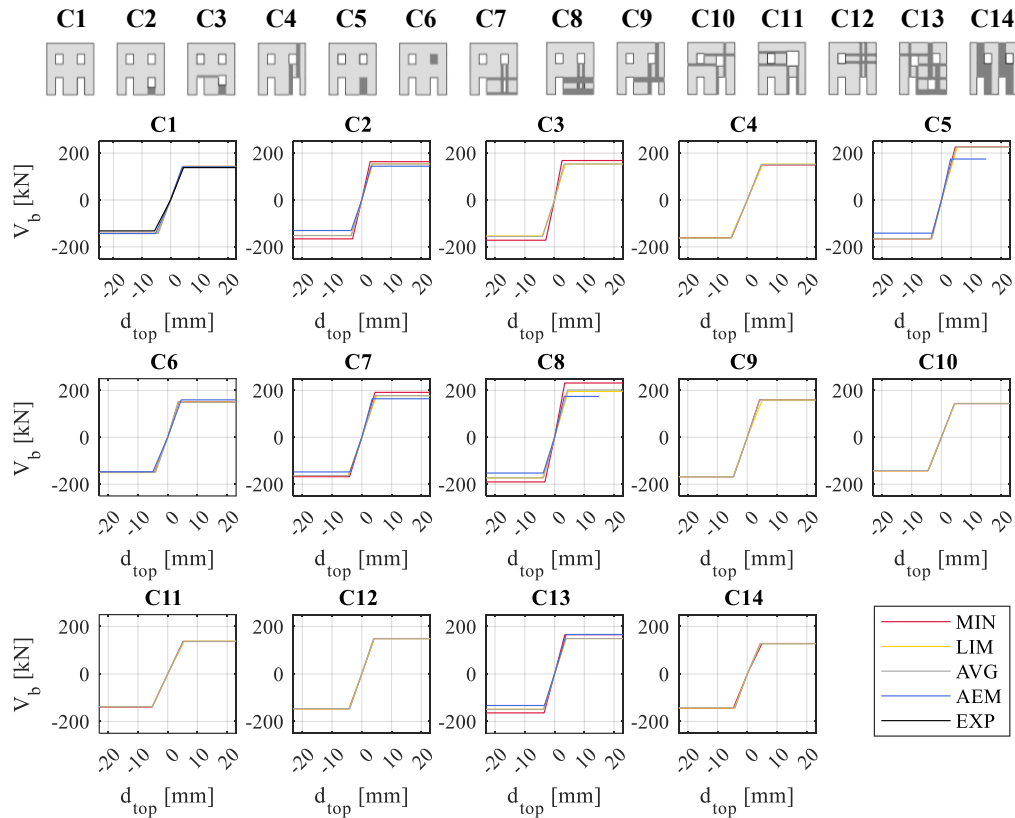
Figure 3.11 Comparison between the equivalent bilinear curves obtained from the EFM and AEM pushover curves
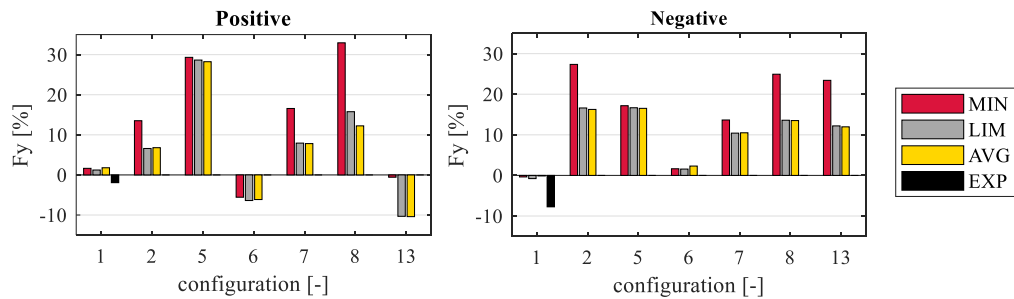
Figure 3.12 Comparison between the equivalent yielding force obtained with EFM and AEM models

The lateral stiffness of EFM was computed and compared for each configuration considering the secant line passing through the origin and the point corresponding to a different percentage of the peak base shear: 40%, 50%, 60% and 70%. This last, $k_{,70}$, was

considered in the bilinearisation process. The stiffness degradation predicted by EFM and AEM models was compared in Figure 3.13. The more significant differences in lateral stiffness between AEM and EFM were found when the MIN criterion was adopted. Indeed, LIM and AVG predicted a higher initial lateral stiffness which converged to the AEM values when the secant stiffness, $k_{,70}$, was considered. On the contrary, in C2 and C8, MIN predicted a stiffer response even considering the secant value of $k_{,70}$. The results obtained by comparing configurations 1,2,5,6,7,8, and 13 EFM responses with those of AEM models are summarised in Table 3.4. The qualitative assessment in terms of damage pattern and failure mechanism is reported as G, M and S, which mean good agreement, moderate differences, and significant differences. The comparison in terms of yielding force and lateral stiffness of the bilinear curve with respect to the AEM model is expressed in percentage form for MIN (M), LIM (L) and AVG (A) criteria.
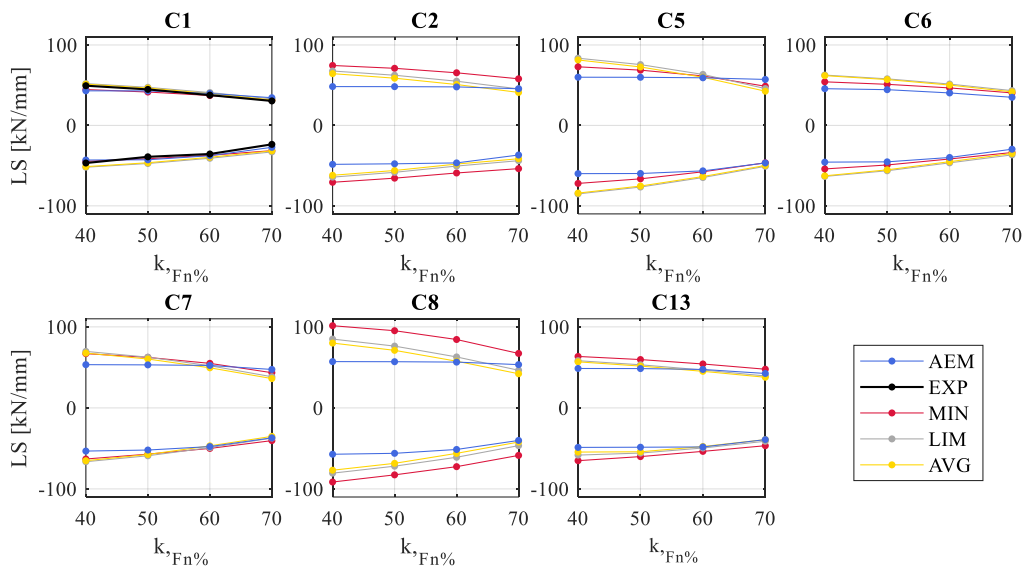
Figure 3.13 Degradation of the lateral stiffness of EFM and AEM model

Although a general tendency to overestimate the size of rigid nodes was found, interesting regions undamaged in the AEM counterpart, the EFM was still generally capable of representing the damage pattern and the failure mechanism, even in the presence of an irregular opening distribution. This tendency can be related to the need of a single model for both loading directions, leading to a compromise that overestimated the size of the nodes in the presence of small openings. AVG and LIM criteria generally predicted a good agreement in F_y and $k_{,70}$ compared to the AEM model. Whereas MIN led to higher values of both $k_{,70}$ and F_y, suggesting AVG and LIM criteria should be preferred. On the other hand, further investigation on C5 and C8 seems needed as the EFM predicted different damage patterns and, in C5, a different failure mechanism.

		C1		C2		C5		C6		C7		C8		C13	
		+	-	+	-	+	-	+	-	+	-	+	-	+	-
Failure mechanism	MIN	G	G	G	G	S	S	G	G	G	G	G	G	G	G
	LIM	G	G	G	G	S	S	G	G	G	G	G	G	G	G
	AVG	G	G	G	G	S	S	G	G	G	G	G	G	G	G
Damage Pattern	MIN	G	G	M	M	S	S	M	G	M	M	S	S	M	M
	LIM	G	G	G	G	S	S	M	G	G	G	G	G	G	G
	AVG	G	G	G	G	S	S	M	G	G	G	G	G	G	G
F_y	MIN	2%	<1%	13%	27%	30%	17%	5%	2%	17%	15%	33%	25%	<1%	13%
	LIM	1%	<1%	7%	17%	29%	17%	6%	2%	8%	10%	16%	14%	10%	12%
	AVG	2%	<1%	7%	17%	28%	17%	6%	2%	8%	10%	12%	14%	10%	12%
$k_{,70}$	MIN	9%	15%	27%	46%	15%	<1%	16%	14%	8%	9%	25%	46%	12%	19%
	LIM	4%	20%	<1%	19%	20%	10%	24%	24%	19%	<1%	13%	15%	7%	5%
	AVG	8%	15%	10%	12%	26%	6%	20%	18%	23%	5%	21%	5%	11%	<1%

Table 3.4 Summary of the results

3.5.1 Influence of the opening size

Further considerations are discussed below to overcome the issues on EF discretisation of C5 and C8. Considering configurations 1,2,7,8, and 5 in this order, we could compare the lateral response predicted by the models when reducing the size of one of the two openings at the ground level.

As shown in Figure 3.14, ILS and $V_{,bp}$ of both AVG and LIM increased with reducing the irregular opening at the ground level. AEM predicted increasing $V_{,bp}$ and ILS when reducing the opening size, consistently with AVG and LIM. On the contrary, MIN predicted greater ILS and $V_{,bp}$ in configuration 8, even compared to C5, where one opening is missing.

Figure 3.15 compares AEM and EFM pushover curves of C7 and C8 with C5, which should represent a higher limit for both ILS and $V_{,bp}$. Both C5 and C8 exhibited a lower displacement capacity in the positive direction, compared to the other configurations considered. This was due to a brittle mechanism caused by the stress concentration on the second floor where the steel trusses applied the horizontal load. In the presence of small openings (e.g. C8), AEM cracks propagation (Figure 3.10), and stress distribution (Figure 3.16) suggested the activation of a single strut when stress propagation was not disturbed by the presence of the opening, as already noted by (Camilletti et al. 2018). On the contrary, in the EFM, two deformable portions surrounding the opening were considered, leading to different predictions of the façade response by the two modelling approaches. As shown in Figure 3.16, for small displacement (<5 mm) in the positive direction, C7 and C8 showed two compressed struts through the central squat pier and the slender one at the compressed side. Whereas C5 developed only a single strut crossing the squat pier. C8 had an intermediate stress distribution, disturbed by the presence of the small opening. Once diagonal cracks developed through the squat ground pier of C5, stress distribution became analogous to C8. The pushover curve of C5 experienced a drop, reaching a residual base shear closer to C8.
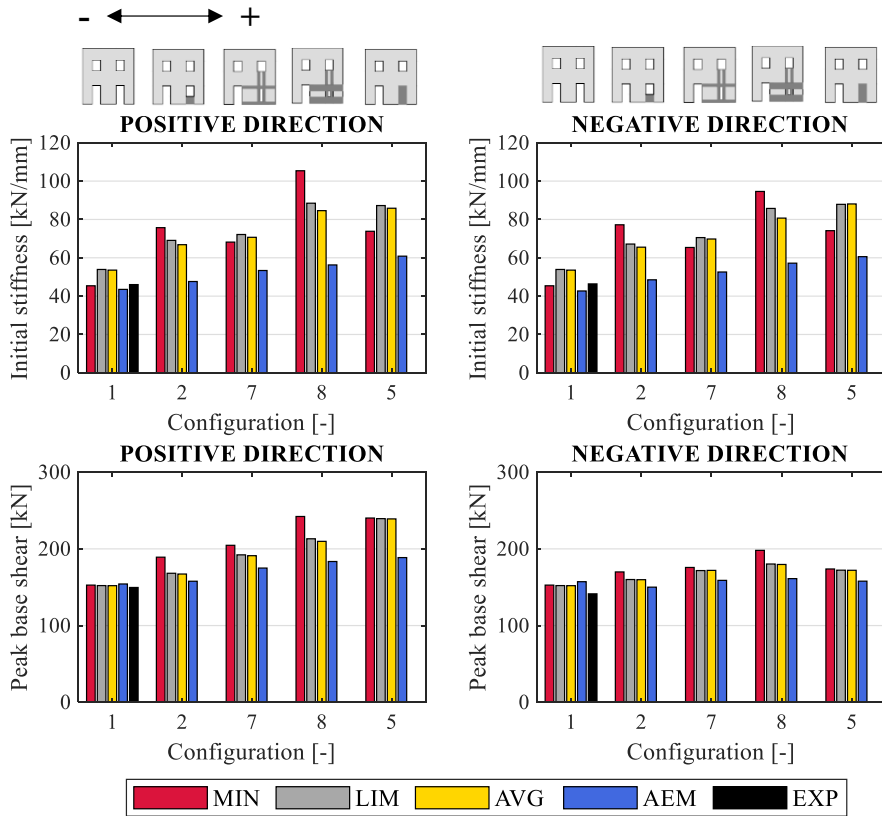
Figure 3.14 Parametric analysis on opening size: comparison between configurations 1,2,5,7,8 in terms of initial stiffness (ILS) and peak base shear ($V_{,bp}$)
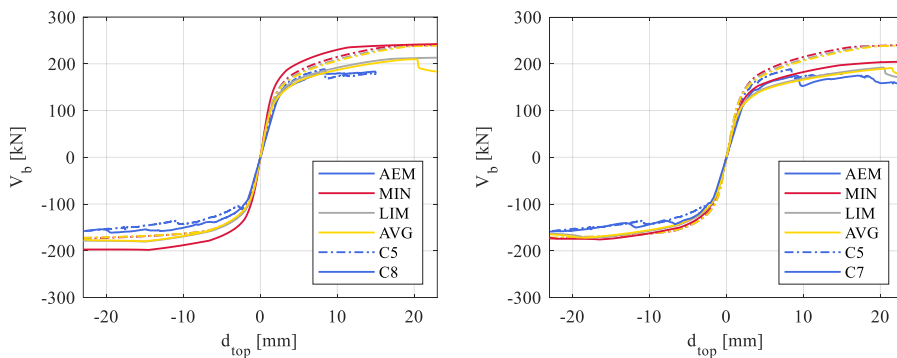
Figure 3.15 Comparison between configurations 5-8 (left) and 5-7 (right) pushover curves obtained with AEM and EFM
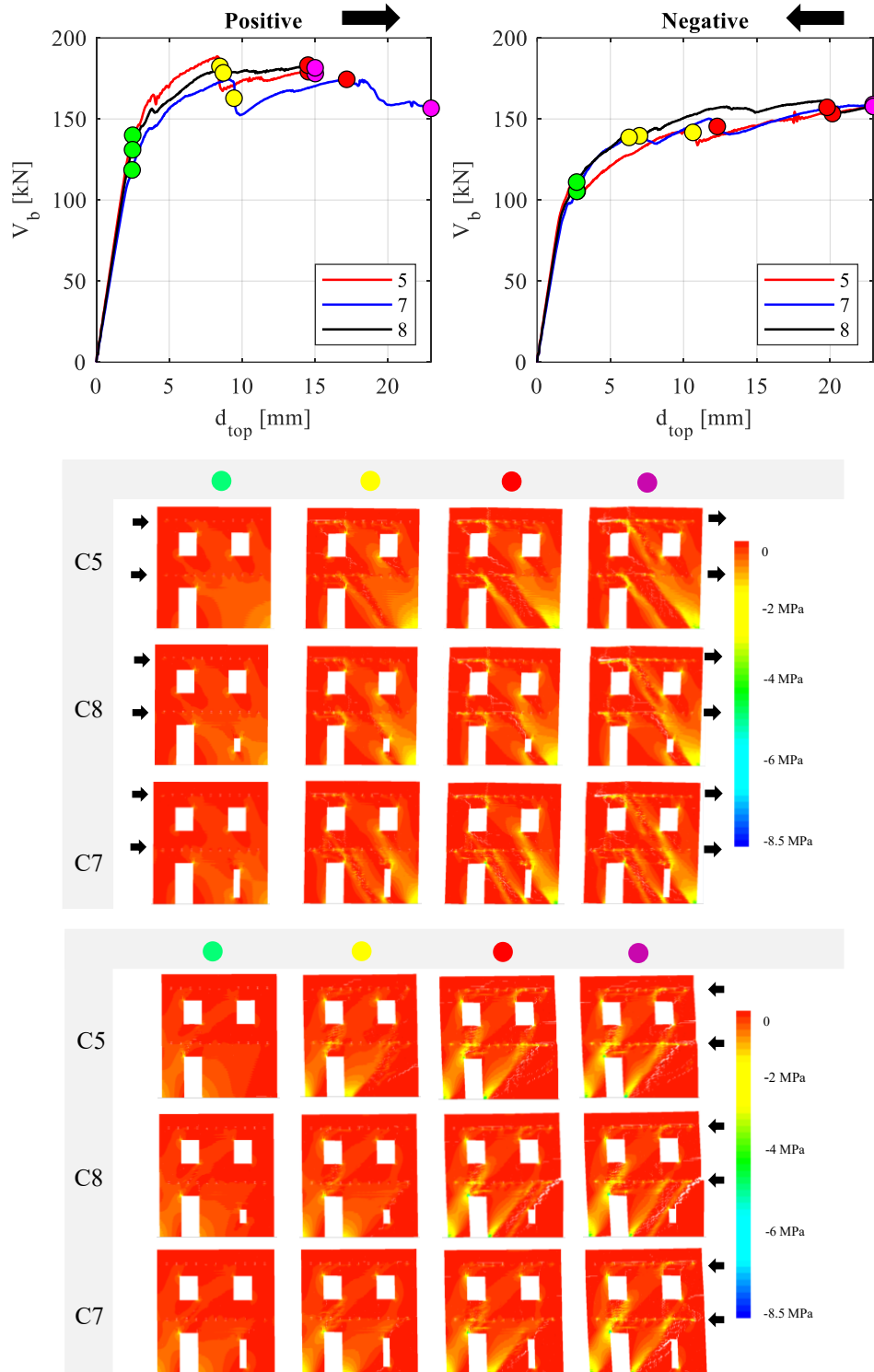
Figure 3.16 Stress distribution of configurations 5,7 and 8

Indeed, from this point on, the two façades showed the same response, with a brittle failure occurred at the same displacement, as shown in Figure 3.15. The three configurations (i.e. 5,7, and 8) developed the same stress distribution when loaded in the negative direction, with two main compressed struts through the slender and the squat piers at ground level. This observation is consistent with what found comparing the $V_{,bp}$, as the three configurations had almost the same lateral resistance in the negative direction, whereas more significant differences were found in terms of stiffness.

The stress distribution reported in Figure 3.16 suggests that the small opening can be neglected when the stress propagation is not disturbed by its presence. In this case, the small opening of both C7 and C8 can be neglected. Indeed, the C5 capacity curve (Figure 3.15) is very close to the C7 and C8 in the negative direction. In the positive direction, the small opening of C7 should be considered, as it affected the location of the diagonal cracks on the central squat pier at ground level. Considering C8, the presence of the small opening allowed diagonal cracking at the same location of C5 at ground level. Crack propagation seems to be favoured by the presence of that small opening, but not modified, suggesting its presence can be neglected. Moreover, comparing stress distribution and crack propagation in the AEM model of C5 with EFM discretisations and damage patterns, a different elements geometry seems needed, as the two modelling approaches led to different damage location and global behaviour.

Once C5 was loaded in the positive direction, the diagonal shear cracks experienced by the AEM around 8 mm of top displacement caused the development of two compressed struts at ground level. The façade was still able to carry vertical and lateral loads, and the static analyses could continue with lower shear capacity due to the separation of the two struts. This effect cannot be reproduced by the EFM, as the squat pier was modelled as a single element. To account for this phenomenon, two solutions for the EF discretisation were proposed and discussed in section 3.5.2.

3.5.2 Numerically-calibrated EFM layouts

To overcome the problem of the EF discretisation of C5, two different solutions were proposed. The first model, named C5M2, considered to reduce the shear strength of the squat pier at ground level, according to the actual portion interested by the stress distribution. The inclination of stress direction of propagation was assumed 45°; then, we considered the pier length equal to its height. It was possible to evaluate an equivalent value of f_{bt}, reducing the shear strength accounting for the "effective" pier length, according to equation (1), without affecting the lateral stiffness. It is worth noting that this approach allowed maintaining the discretisation based on simple geometrical rules, modifying the local value of f_{bt}. The same consideration can be adopted even if the criterion based on the shear failure due to the attainment of tensile strength of masonry is considered (Turnšek and Sheppard 1980).

As the crack propagation produced the separation of two struts in AEM, the second model, named C5M3, assumed to separate the squat pier into two elements. This assumption has to be carefully chosen as it causes the reduction of the lateral stiffness. This effect could be

eventually balanced considering the minimum effective height of the new piers. Moreover, the different aspect ratios of the two piers might lead to a different mechanism. Deformed shape and pushover curves of the new discretisations C5M2 and C5M3 are shown in Figure 3.17.
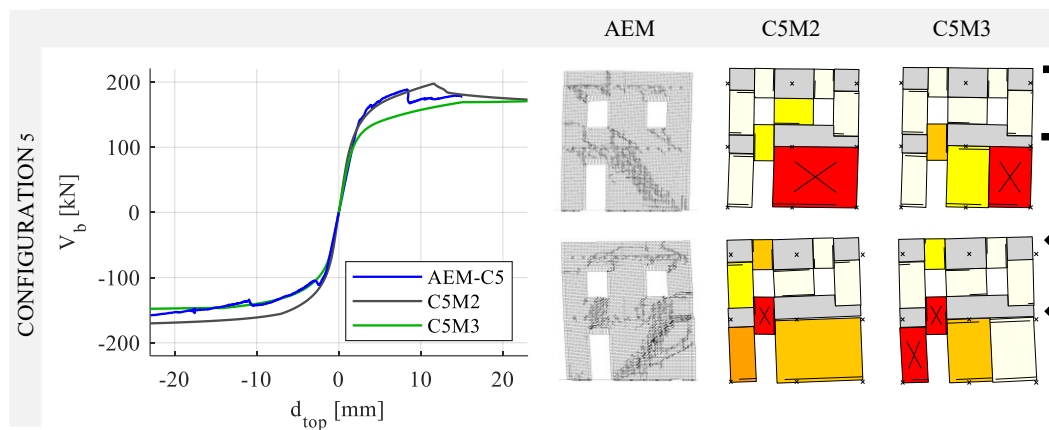
Figure 3.17 Configuration 5: pushover curves, deformed shape and damage of AEM and EFM (C5M2 and C5M3)

In both models, the AVG mechanical parameters were assumed. Compared to the original discretisations, the new models better represented the lateral response of configuration 5 in terms of failure mechanism, $V_{,bp}$ and damage pattern. C5M3 predicted ILS closer to the AEM (+10%), whereas C5M2 was more consistent with the standard discretisations obtained with AVG and LIM (+40%). In the positive direction, C5M2 and C5M3 predicted with a good agreement the $V_{,bp}$ with respect to what was exhibited by the AEM, with differences around 10%, whereas the three models converged to the same residual lateral strength. In C5M2, the squat pier at the ground level attained its peak shear strength at 12 mm of top displacement, 4 mm later than the AEM. The shift of the maximum base shear is related to the parameter Gc_t, which was calibrated on the experimental test on the Door Wall. On the contrary, C5M3 predicted a significant stiffness degradation for intermediate displacement. The residual base shear and damage of C5M3 were consistent with those predicted by AEM and C5M2, with the attainment of the peak shear strength by the external pier at ground level. Both C5M2 and C5M3 predicted flexural mechanism with light shear damage and flexural partialisation at ground-level piers edges when loaded in the negative direction. In C5M3, the slender downwind pier attained its peak shear strength. C5M2 predicted higher $V_{,bp}$ (+10%) and ILS (+40%) with respect to the AEM. The two EF proposed models (C5M2 and C5M3) predicted a lateral response of configuration 5 more consistent with the AEM than the original discretisation (i.e. AVG, LIM and MIN), as also shown by Table 3.5, where damage pattern, failure mechanism, F_y and $k_{,70}$ obtained with the different discretisations are compared with the AEM benchmark.

These preliminary results suggest that modifying the EF discretisation according to the development of compressed struts, assuming the inclination of stress propagation, might

help to improve the EFM capacity to simulate the lateral response of irregular walls in the presence of small or absent openings and squat piers.

Table 3.5 Summary of the results obtained with different discretisations for configuration 5

	C5-MIN		C5-LIM		C5-AVG		C5M2		C5M3	
	+	-	+	-	+	-	+	-	+	-
Failure mechanism	S	S	S	S	S	S	G	G	G	G
Damage pattern	S	S	S	S	S	S	G	G	G	G
F_y	30%	17%	29%	17%	28%	17%	1%	19%	3%	4%
$k_{,70}$	15%	<1%	20%	10%	26%	6%	10%	25%	6%	23%

3.6 Conclusions

Equivalent Frame Models are widely employed in the seismic assessment of the in-plane governed behaviour of unreinforced masonry buildings, representing a good compromise between accuracy and computational burden when performing large-scale nonlinear analyses. However, the selection of the most appropriate discretisation criterion, i.e. the definition of frame topology and effective length/height of the structural members, is still challenging because of the irregular distribution of openings. An inaccurate definition of deformable and rigid elements may significantly affect the numerical predictions. In this work, three commonly employed discretisation criteria (i.e. minimum, MIN, limited, LIM and average, AVG, effective height criteria), based on simple geometrical rules, were selected. Their effectiveness was analysed in a study investigating the differences in terms of predicted in-plane behaviour of multiple opening configurations derived from a baseline model, i.e. an experimentally tested building façade. The EFM results were compared with the benchmark predictions by detailed micro-models developed using the Applied Element Method (AEM), where each brick is modelled separately.

First, AEM and EF models were calibrated against cyclic quasi-static tests on two individual URM piers and a full-scale regular URM building façade. Then pushover analyses were performed on a set of irregular configurations, obtained from the regular one combining horizontal and vertical misalignments and variations of the opening size. The lateral response of models was discussed and compared for the selected configurations. Although only minor differences were found between EFM and AEM in some cases, results were scattered in others, especially in terms of peak base shear and initial lateral stiffness, mostly when the irregularity consisted of an opening with a reduced size. Forcing the EF discretisation in case of very little openings multiple small-size deformable and non-deformable regions are created, even in regions affected by cracks in the AEM analyses, leading to a stiffer response and a higher base shear resistance prediction, especially when the MIN criterion was considered. The presence of small openings only marginally affected the lateral response predicted by the AEM models, suggesting that only openings with a minimum dimension should be accounted for in the EF discretisation, unless their presence significantly alter the stress distribution. Noticeable differences were also found where the absence of an opening (or the presence of a very small one) produced a pier with a small aspect ratio (height/length). In this case, the stress distribution obtained from the AEM models allowed identifying the development of a single diagonal strut affecting only a part of such a pier, hence producing an element with a reduced effective length. A correction of

the shear strength of the resulting squat piers proportional to the ratio of effective and nominal lengths solved the inconsistent overprediction of lateral strength in the EF model.

Results also showed that EFM tends to overestimate the initial lateral stiffness with respect to AEM. However, this difference becomes generally minor when considering the secant stiffness adopted for the bilinear approximation of the pushover curves.

Despite the differences between EFM and AEM results discussed above, this research indicates that even in the presence of irregular opening distributions, it is still possible to identify recurring uncracked regions and portions of the structure where damage is concentrated. In general, it was observed that simple geometrical rules as AVG or LIM resulted in very similar predictions of lateral response compatible with those by detailed micro-models. Moreover, no significant differences were found between these two criteria, suggesting the two are equally valid even in the presence of the considered irregularities. Although this study was limited only to some of the many possible irregular opening layouts, it suggests that considering the actual stress distribution and the development of compressed struts based on simple geometrical rules can improve standard EFM discretisation strategies. When the application of such improved techniques is not feasible, the AVG or the LIM criteria should be adopted. The use of MIN criterion should be recommended, however, when the presence of strong lintels extended into the masonry well beyond the opening width would not allow the formation of inclined cracks starting from the opening corners, hence limiting the effective height of piers (e.g. Penna et al. 2016).

Acknowledgements

References

Anthoine A, Magonette G, Magenes G (1995) Shear-compression testing and analysis of brick masonry walls. Proceedings of the lOth European Conference on Earthquake Engineering. Vienna, Austria.

Applied Technology Council (ATC) (2000). Pre-standard and commentary for the seismic rehabilitation of buildings. FEMA 356. Washington DC, USA.

Augenti N (2006) Seismic behaviour of irregular masonry walls. Proceedings of the 1st European conference on earthquake engineering and seismology. Geneva, Switzerland.

Belmouden Y, Lestuzzi P (2009) An equivalent frame model for seismic analysis of masonry and reinforced concrete buildings. Constr. Build. Mater. 23:40–53.

Berti M, Salvatori L, Orlando M, Spinelli P (2017) Unreinforced masonry walls with irregular opening layouts : reliability of equivalent-frame modelling for seismic vulnerability assessment. Bull Earthq Eng 15:1213–1239. https://doi.org/10.1007/s10518-016-9985-5.

Binda L, Tiraboschi C, Mirabella Roberti G, et al (1996a) Experimental and numerical investigation on a brick masonry building prototype - 5.2 - Measuring masonry material properties: detailed results from an extensive experimental research: Tests on masonry specimens.

Binda L, Tiraboschi C, Mirabella Roberti G, et al (1996b) Experimental and numerical investigation on a brick masonry building prototype - 5.1 - Measuring masonry material properties: detailed results from an extensive experimental research: Tests on masonry components.

Block P, Ciblac T, Ochsendorf J (2006) Real-time limit analysis of vaulted masonry buildings. Comput Struct 84:1841–1852.

Bracchi S, Rota M, Penna A, Magenes G (2015) Consideration of modelling uncertainties in the seismic assessment of masonry buildings by equivalent-frame approach. Bull Earthq Eng 13:3423–3448. https://doi.org/10.1007/s10518-015-9760-z.

Bracchi S, Galasco A, Penna A (2021) A novel macroelement model for the nonlinear analysis of masonry buildings . Part 1 : Axial and flexural behavior. Earthq Eng Struct Dyn 50:2233–2252. https://doi.org/10.1002/eqe.3445.

Bracchi S, Penna A (2021) A novel macroelement model for the nonlinear analysis of masonry buildings. Part 2: Shear behavior. Earthq Eng Struct Dyn 50:2212–2232. https://doi.org/10.1002/eqe.3444.

Braga F, Dolce M (1982) A method for the analysis of antiseismic multi-storey masonry buildings (In Italian). Proceedings of the 6th International Brick Masonry Conference. Rome, Italy, pp 1089–1099.

Calderoni B, Cordasco EA, Musella C, Sandoli A (2017) La modellazione delle pareti murarie in relazione alle irregolarità geometriche : problemi aperti. Proceedings of 17th ANIDIS Conference. Pistoia, Italy.

Camilletti D, Cattari S, Lagomarsino S (2018) In plane seismic response of irregular URM walls through equivalent frame and finite element models. Proceedings of the 16th European Conference on Earthquake Engineering. Thessaloniki, Greece, pp 1–12

Casolo S, Peña F (2007) Rigid element model for in-plane dynamics of masonry walls considering hysteretic behaviour and damage. Earthq Eng Struct Dyn 36:1029–1048. https://doi.org/10.1002/eqe.670.

Cattari S, Camilletti D, Lagomarsino S, et al (2018) Masonry italian code-conforming buildings. Part 2: nonlinear modelling and time-history analysis. J Earthq Eng 22(sup2):2010–2040. https://doi.org/10.1080/13632469.2018.1541030.

Cattari S, Camilletti D, D'Altri AM, Lagomarsino S. (2021) On the use of continuum finite

element and equivalent frame models for the seismic assessment of masonry walls. J Build Eng 43:102519. https://doi.org/10.1016/j.jobe.2021.102519.

Costa AA, Penna A, Magenes G (2011) Seismic performance of Autoclaved Aerated Concrete (AAC) masonry: From experimental testing of the in-plane capacity of walls to building response simulation. J Earthq Eng 15:1–31. https://doi.org/10.1080/13632461003642413.

D'Altri AM, Sarhosis V, Milani G, et al (2020) Modeling strategies for the computational analysis of unreinforced masonry structures: review and classification. Arch Computat Methods Eng 27(4):1153–1185. https://doi.org/10.1007/s11831-019-09351-x.

Dolce M (1991) Schematizzazione e modellazione degli edifici in muratura soggetti ad azioni sismiche. L'industria delle costruzioni 25(242): 44–57 [in italian]

El-Kashif KF, Maekawa K (2004) Time-dependent nonlinearity of compression softening in concrete. J Adv Concr Technol 2:233–247.

Gambarotta L, Lagomarsino S (1997) Damage models for the seismic response of brick masonry shear walls. Part II: the continuum model and Its applications. Earthq Eng Struct Dyn 26(4):441–462. https://doi.org/10.1002/(SICI)1096-9845(199704)26:4<441::AID-EQE651>3.0.CO;2-0.

Graziotti F, Penna A, Magenes G (2016) A nonlinear SDOF model for the simplified evaluation of the displacement demand of low-rise URM buildings. Bull Earthq Eng 14:1589–1612. https://doi.org/10.1007/s10518-016-9896-5.

Kallioras S, Graziotti F, Penna A (2019) Numerical assessment of the dynamic response of a URM terraced house exposed to induced seismicity. Bull Earthq Eng 17:1521–1552. https://doi.org/10.1007/s10518-018-0495-5.

Karbassi A, Nollet MJ (2013) Performance-based seismic vulnerability evaluation of masonry buildings using applied element method in a nonlinear dynamic-based analytical procedure. Earthq Spectra 29(2):399–426. http://dx.doi.org/10.1193/1.4000148.

Kawai T (1978) New discrete models and their application to seismic response analysis of structures. Nucl Eng Des 48:207–229. https://doi.org/10.1016/0029-5493(78)90217-0.

Keys RA, Clubley SK (2017) Establishing a predictive method for blast induced masonry debris distribution using experimental and numerical methods. Eng Fail Anal. 82:82-91 https://doi.org/10.1016/j.engfailanal.2017.07.017.

Meguro K, Hakuno M (1989) Fracture analyses of RC structure by modified distinct element method. Struct Eng Eng 6(2):283s–294s

Lagomarsino S, Penna A, Galasco A, Cattari S (2013) TREMURI program: An equivalent frame model for the nonlinear seismic analysis of masonry buildings. Eng Struct 56:1787–1799. https://doi.org/10.1016/j.engstruct.2013.08.002.

Lourenço PB (2002) Computations on historic masonry structures. Prog Struct Eng Mater 4(3):301–319. https://doi.org/10.1002/pse.120.

Magenes G (2000) A method for pushover analysis in seismic assessment of masonry

buildings. Proceedings of the 12th World Conference on Earthquake Engineering. pp 1–8

Magenes G, Calvi GM, Kingsley GR (1995) Seismic testing of a full-scale , Two-story masonry building : Test procedure and measured experimental response. Consiglio nazionale delle ricerche, gruppo nazionale per la difesa dai terremoti, Pavia, Italy.

Magenes G, Calvi GM (1997) In-plane seismic response of brick masonry walls. Earthq Eng Struct Dyn 26:1091–1112.

Malomo D, Pinho R, Penna A (2018) Using the applied element method for modelling calcium silicate brick masonry subjected to in-plane cyclic loading. Earthq Eng Struct Dyn 47(7):1610–1630. https://doi.org/10.1002/eqe.3032.

Malomo D, DeJong MJ, Penna A (2019a) Distinct element modelling of the in-plane cyclic response of URM walls subjected to shear-compression. Earthq Eng Struct Dyn.48:1322-1344. https://doi.org/10.1002/eqe.3178.

Malomo D, Morandini C, Penna A, Dejong MJ (2019b) Assessing the reliability of the equivalent-frame idealisation of URM façades with irregular opening layouts by comparison with the discrete micro-models. Proceedings of SECED 2019 Conference. Greenwich, London

Malomo D, Pinho R, Penna A (2020) Simulating the shake table response of unreinforced masonry cavity wall structures tested to collapse or near-collapse conditions. Earthq Spectra 36(2):554–578. https://doi.org/10.1177/8755293019891715.

Malomo D, DeJong MJ (2021a) A Macro-Distinct Element Model (M-DEM) for simulating the in-plane cyclic behavior of URM structures. Eng Struct 227:111428. https://doi.org/10.1016/j.engstruct.2020.111428.

Malomo D, DeJong MJ (2021b) A Macro-Distinct Element Model (M-DEM) for out-of-plane analysis of unreinforced masonry structures. Eng Struct 244:112754. https://doi.org/10.1016/j.engstruct.2021.112754.

Mann W, Müller H (1982) Failure of shear-stressed masonry: an enlarged theory, tests and application to shear walls. Proc Br Ceram Soc 223–235

Mayorca P, Meguro K (2003) Modeling masonry structures using the Applied element method. Seisan Kenkyu, 55(6):581–584. https://doi.org/10.11188/seisankenkyu.55.581.

Meguro K, Tagel-Din H (2000) Applied Element Method for structural analysis: theory and application for linear materials. JSCE Struct Eng Earthq Eng. 17(1):21–35.

Miglietta PC, Bentz EC, Grasselli G (2017) Finite/discrete element modelling of reversed cyclic tests on unreinforced masonry structures. Eng Struct 138:159–169. https://doi.org/10.1016/j.engstruct.2017.02.019.

Milani G, Lourenço PB, Tralli A (2006) Homogenised limit analysis of masonry walls, Part I: failure surfaces. Comput Struct 84:166–180. https://doi.org/10.1016/j.compstruc.2005.09.005.

Moon FL, Yi T, Leon RT, Kahn LF (2006) Recommendations for seismic evaluation and retrofit of low-rise URM structures. J Struct Eng 132(5):663–672.

https://doi.org/10.1061/(asce)0733-9445(2006)132:5(663).

NTC 2008 (2008) Nuove Norme Tecniche per le Costruzioni, G.U. n. 29, 4 Febbraio 2008, S.O. n. 30. D.M. del Ministero delle Infrastrutture e dei Trasporti 14 Gennaio 2008.

Pagani C, Salvatori L, Orlando M, Spinelli P (2017) Irregular opening layouts in unreinforced masonry walls : equivalent frame and finite element simulations. Proceedings of the 17° ANIDIS Conference,:Pistoia, Italy.

Parisi F, Augenti N (2013) Seismic capacity of irregular unreinforced masonry walls with openings. Earthq Eng Sructural Dyn 42(1):101–121. https://doi.org/10.1002/eqe.2195.

Penna A, Lagomarsino S, Galasco A (2014) A nonlinear macroelement model for the seismic analysis of masonry buildings. Earthq Eng Struct Dyn 43:159–179. https://doi.org/10.1002/eqe.2335.

Penna A, Senaldi IE, Galasco A, Magenes G (2016) Numerical simulation of shaking table tests on full-scale stone masonry buildings. Int J Archit Herit 10(2-3):146–163. https://doi.org/10.1080/15583058.2015.1113338.

Peruch M, Spacone E, Camata G (2019) Nonlinear analysis of masonry structures using fiber - section line elements. Earthq Eng Sructural Dyn 48(12):1345–1364. https://doi.org/10.1002/eqe.3188.

Pulatsu B, Erdogmus E, Lourenço PB, et al (2020) Discontinuum analysis of the fracture mechanism in masonry prisms and wallettes via discrete element method. Meccanica 55:505–523. https://doi.org/10.1007/s11012-020-01133-1.

Quagliarini E, Maracchini G, Clementi F (2017) Uses and limits of the equivalent frame model on existing unreinforced masonry buildings for assessing their seismic risk: A review. J Build Eng 10:166–182. https://doi.org/10.1016/j.jobe.2017.03.004.

Raka E, Spacone E, Sepe V, Camata G (2015) Advanced frame element for seismic analysis of masonry structures: model formulation and validation. Earthq Eng Struct Dyn 44:2489–2506. https://doi.org/10.1002/eqe.2594.

Roca P, Cervera M, Gariup G, et al. (2010) Structural analysis of masonry historical constructions. Classical and advanced approaches. Arch Comput Methods Eng 17:299–325. https://doi.org/10.1007/s11831-010-9046-1.

Rota M, Penna A, Magenes G (2014) A framework for the seismic assessment of existing masonry buildings accounting for different sources of uncertainty. Earthq Eng Sructural Dyn 43(7):1045–1066. https://doi.org/10.1002/eqe.2386.

Siano R, Sepe V, Camata G, et al (2017) Analysis of the performance in the linear field of equivalent-frame models for regular and irregular masonry walls. Eng Struct 145:190–210. https://doi.org/10.1016/j.engstruct.2017.05.017.

Snoj J, Dolšek M (2020) Pushover-based seismic risk assessment and loss estimation of masonry buildings. Earthq Eng Struct Dyn 49:567–588. https://doi.org/10.1002/eqe.3254.

Tomazevic M (1978) The computer program POR. Report ZRMK. Inst Test Res Mater Struct Ljubljana.

Turnšek V, Sheppard P (1980) Shear and flexural resistance of masonry walls. Proceedings of the international research conference on earthquake engineering. Skopje, Macedonia, pp 517–573.

Vanin F, Penna A, Beyer K (2020a) Equivalent-frame modeling of two shaking table tests of masonry buildings accounting for their out-of-plane response. Front Built Environ 6:42. https://doi.org/10.3389/fbuil.2020.00042.

Vanin F, Penna A, Beyer K (2020b) A three-dimensional macroelement for modelling the in-plane and out-of-plane response of masonry walls. Earthq Eng Struct Dyn 49:1365–1387. https://doi.org/10.1002/eqe.3277.

Yi T, Moon FL, Leon RT, Kahn LF (2006) Lateral load tests on a two-story unreinforced masonry building. J Struct Eng Eng 132(5):643–652.

4. Assessment of the seismic response of Dutch URM cavity wall structures with different openings percentage

Abstract

Unreinforced masonry (URM) buildings with cavity walls, typically constituted by the assembly of a loadbearing inner leaf weakly coupled to an outer veneer with no structural functions, are widely present in a number of regions exposed to tectonic or induced seismicity, including the Groningen province (The Netherlands), which has lately experienced low-intensity ground shaking due to natural gas extraction. Recently, experimental evidence has shown that the lack of seismic details, and, above all, the presence of large ground floor openings, makes these structures particularly vulnerable towards horizontal actions. In this endeavour, advanced discrete element models, developed within the framework of the Applied Element Method (AEM), are employed to investigate numerically the impact of ground floor openings percentage on the dynamic behaviour of cavity wall systems representative of the typical Dutch terraced houses construction, namely low-rise residential URM buildings with rigid floor diaphragms and timber roof. Firstly, the model is validated through comparison with a shake-table test of a full-scale building specimen, tested up to near-collapse. Then, a comprehensive numerical study, which featured several combinations of ground-floor openings and the application of various acceleration time-histories up to complete collapse, is undertaken. The ensuing results allowed a comparison of the fragility associated with each of the considered openings layouts, showing how the presence of large ground floor openings may significantly increase the seismic vulnerability of typical URM Dutch terraced houses.

Keywords: unreinforced masonry, cavity wall systems, openings, shake-table, Applied Element Method

4.1 Introduction

The cavity wall construction technique is typical of Central and Northern European regions (though it is now widely seen also in a number of other countries around the world, such e.g. China, USA, New Zealand (Dizhur et al. 2013; Zhang et al. 2016; Desai 2017), including the Groningen province in The Netherlands, where it usually consists of an assembly of a loadbearing inner unreinforced masonry (URM) calcium-silicate (CS) brick panels plus an external clay (CL) brick building envelope aimed at providing protection

against atmospheric agents and thermal insulation in addition to the characteristic aesthetic appearance. These two masonry wythes are typically weakly coupled by metal connectors (or tie elements). Because of the intrinsic vulnerability of URM cavity wall systems, they became in recent years the focus of various experimental (e.g. Dizhur et al. 2017; Derakhshan et al. 2018; Graziotti et al. 2019a) and numerical (e.g. Tomassetti et al. 2018; Kallioras et al. 2019; D'Altri et al. 2019a; Malomo et al. 2020a) research endeavours. In this framework, of particular interest is the situation of the Groningen region, not historically-prone to tectonic earthquakes but now exposed to low-intensity ground motions due to natural gas extraction. Indeed, a relevant part of the Groningen building stock is constituted by URM cavity wall structures (see Figure 4.1, where one of the end units – usually taken as a reference for the design of full-scale building specimens, as discussed in the following – is highlighted in red), which typically come in the form of contiguous low-rise constructions (hereinafter referred to as terraced houses) characterised by large ground floor openings, rigid floor diaphragms and timber roof. Despite the need for detailed numerical analyses of the collapse response of cavity wall terraced house buildings for supporting the development seismic risk models (e.g. van Elk 2019) in regions where these structural types are most widespread, they were not readily available in the literature. Indeed, their validation required shake-table tests on complete structural systems that only now have become available, through the experimental campaign cited above. Further, since the local interaction among in-plane and out-of-plane (OOP) loaded components often influences the global response of cavity wall systems, the use of simplified models (e.g. Penna et al. 2014; Raka et al. 2015; Sangirardi et al. 2019), which often neglect the contribution of OOP-loaded members, seems to be not generally applicable.
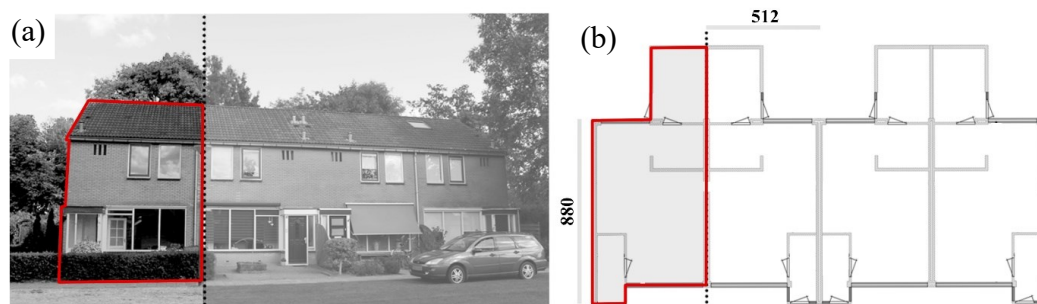
Figure 4.1 a) Front and b) plan views of a typical Dutch URM terraced house (adapted from Graziotti et al. 2017) – the red envelopes indicate the right-side end unit

Similarly, as extensively discussed in Grunwald et al. (2018), the application of most of the typically-employed continuum-based advanced numerical approaches (e.g. the Finite Element Method, FEM) to the collapse simulation of complex structures might lead to inadequate results. This notwithstanding, satisfactory results have been obtained using FEM micro (Petracca et al. 2017; Abdulla et al. 2017) and meso-scale (Aref and Dolatshahi 2013; Giambanco et al. 2018) modelling strategies for the analysis of pre-collapse damage states, as comprehensively discussed in (D'Altri et al. 2019b). On the other hand, several applications (Pulatsu et al. 2016; Galvez et al. 2018b; Godio and Beyer 2019; Portioli 2019;

Masi et al. 2020) have shown that e.g. Distinct Element (DEM) and Rigid Body and Spring models (RBSM) (see Lemos 2007), being able to account explicitly for the discrete nature of masonry, are capable of duly representing the mutual interaction among various bodies, as well as separation, impact and frictional phenomena. However, although some promising hybrid modelling strategies have been recently proposed (e.g. Pantò et al. 2017; Chácara et al. 2018; Malomo et al. 2019a), obtaining results in a reasonable timeframe is still an open challenge. A similar but more computationally efficient numerical technique is the Applied Element Method (AEM), initially conceived by Meguro and Tagel-Din (2000) for simulating controlled demolition and collapse of steel and reinforced concrete (RC) structures (e.g. Salem et al. 2016; Calvi et al. 2019). As most of the RBSM, the AEM is based on the mechanical interaction among rigid blocks connected by nonlinear spring layers, carrying only mass and damping of the system. However, unlike RBSM (see Furukawa et al. 2012), the recontact between neighbouring elements initially not in contact is allowed. This is an essential feature for collapse analysis, which enabled various researchers to develop AEM-based models capable of satisfactorily reproducing the response of large-scale systems up to complete failure (e.g. Karbassi and Nollet 2013; Domaneschi et al. 2019; Malomo et al. 2020c).

As a result of all of the above, the AEM was employed in this work for investigating numerically the influence of ground floor openings percentage on the dynamic behaviour and collapse capacity of full-scale terraced house structures with cavity walls, rigid diaphragms and timber roof. To this end, leverage was made on the comprehensive experimental campaign described by Graziotti et al. (2019a), which featured, in addition to static/dynamic testing of cavity wall components (Graziotti et al. 2016b, a, 2019b) and sub-structures (Tomassetti et al. 2019a, b), also the shake-table testing of two full-scale cavity wall two-story building prototypes representative of the end-unit of a set of typical Dutch terraced houses; EUC-BUILD1 (Graziotti et al. 2017) and EUC-BUILD6 (Miglietta et al. 2021); the main distinction between such test specimens was in the size of their ground-floor openings, which were purposely wider in the case of EUC-BUILD6. Taking also advantage of the findings in Malomo et al. (2020b), where adequate agreement among experimental outcomes and numerical counterparts of shake-table-tested cavity wall building specimens (including EUC-BUILD1) has been found, a refined AEM model of EUC-BUILD6 was herein developed and preliminarily calibrated through comparison against the available experimental results. Given the encouraging results obtained, analogous assumptions were also considered for the development of a number of models in which, parametrically, the area of ground floor openings was varied. For each configuration, the predicted damage distribution, failure modes and collapse capacities, as well as the inferred total base shear, significantly differed from one to another, underlining the impact that the extent of ground floor openings can have on the dynamic performance of cavity wall buildings. Finally, leveraging upon the results of the abovementioned analyses, a comparative assessment of the effect that the openings configuration has on the fragility of the considered case-study was also undertaken.

4.2 Applied Element Modelling of URM cavity wall systems

Within the AEM framework, three-dimensional elements are idealised as an assembly of rigid bodies, characterised by six degrees of freedom. Connection is provided by zero-thickness nonlinear interface springs (with normal (k_{ni}) and shear (k_{si}) stiffness, Eqs. (4.1)-(4.2) uniformly distributed along the contact surfaces, in which the mechanical properties of the system are lumped. Interface forces among adjacent units are inferred by multiplying the local stiffness matrix with the displacement vector terms (or vice-versa, in the case of displacement-controlled problems). As shown in e.g. Malomo et al. (2018), to which interested readers are referred for further details, global stiffness matrix of the whole structure can be obtained by assembling the matrices referred to each couple of units in the considered directions.

The actual masonry texture of CS/CL cavity wall members (which usually feature a standard running bond pattern) can be explicitly represented using such a simplified micro-modelling approach, as depicted in Figure 4.2a. From the latter, where E_u, G_u, E_{mo} and G_{mo} are the unit and mortar Young's and shear moduli respectively, while j and d stand for the spring number along y and z-direction respectively, it can be gathered that k_{ni} and k_{si} are computed assuming unit and mortar springs arranged in series. The interface stiffnesses k_{nu} and k_{su} of unit-to-unit spring layers, instead, can be inferred using Eqs. (4.3)-(4.4). It is however noted that since the effect of brick failures was not particularly predominant in the response of EUC-BUILD6, bricks were herein modelled as fully-rigid, without any internal subdivision (see Figure 4.2a).

$$k_{ni} = \sum_{i=1}^{j}\left(\frac{l_u - t_{mo}}{E_u\, d\left(\frac{t_u}{j}\right)} + \frac{t_{mo}}{E_{mo}\, d\left(\frac{t_u}{j}\right)}\right)^{-1} \quad (4.1) \qquad k_{si} = \sum_{i=1}^{j}\left(\frac{l_u - t_{mo}}{G_u\, d\left(\frac{t_u}{j}\right)} + \frac{t_{mo}}{G_{mo}\, d\left(\frac{t_u}{j}\right)}\right)^{-1} \quad (4.2)$$

$$k_{nu} = \sum_{i=1}^{j}\left(\frac{E_u\, d\left(\frac{t_u}{j}\right)}{l_e}\right) \qquad (4.3) \qquad k_{su} = \sum_{i=1}^{j}\left(\frac{G_u\, d\left(\frac{t_u}{j}\right)}{l_e}\right) \qquad (4.4)$$

In the nonlinear range, a simplified version of the elastic-perfectly-plastic fracture model conceived by El-Kashif and Maekawa (2004) is typically used for representing the effect of cyclic damage due to uniaxial compression loading (see Figure 4.2b). A tension cut-off criterion (with no softening branch) characterises the spring response in tension/flexure, while shear-governed behaviours are reproduced using a Mohr-Coulomb-like model, where cohesion is set to zero right after reaching the maximum shear strength, as shown in Figure 4.2c.

To reproduce joint-level failure modes, the mechanical properties of each masonry component needs to be determined, selected, and assigned to the associated normal/shear interface springs. However, experimental campaigns rarely include all the necessary tests for characterising the response of mortar and units separately. Therefore, as suggested by Malomo et al. (2019b), a number of empirical (i.e. Jäger et al. 2004; Kaushik et al. 2007) and theoretical (i.e. Brooks and Baker 1998; Ciesielski 1999; Matysek and Janowski 1996;

U.B.C. 1991) formulae were employed to obtain first estimates of the required material parameters where direct experimental values were not available. Then, the ensuing average is considered for modelling purposes and the associated shear moduli are obtained assuming material isotropy (these values will be given in the next sections). Using this simplified procedure, whose effectiveness has been already extensively investigated by the authors in the context of the same experimental campaign and with respect to the modelling of both static and dynamic tests on small-scale samples, in-plane and OOP-loaded components (Malomo et al. 2020b), and full-scale building specimens with cavity walls (Malomo et al. 2020a), a reasonable approximation (i.e. 0.178 s) of the undamaged state period associated to the 1st mode (i.e. 0.170 s) of EUC-BUILD6 was obtained.
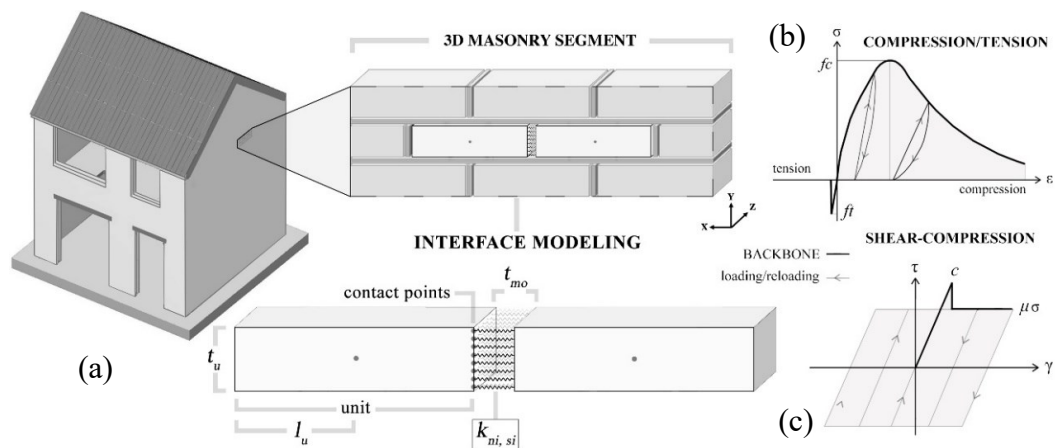
Figure 4.2 (a) Adopted AEM discretisation of a masonry cell and spring interface stiffnesses, (b) compression/tension and (c) shear-compression joint models (adapted from Malomo et al. 2020a)

During the analysis, no external dynamic relaxation schemes were introduced, meaning that the only source of damping in the proposed numerical models is the energy dissipation due to difference in loading and unloading paths of compression springs, as well as that induced by the process of crack closure/opening. Recent applications (e.g. (Papantonopoulos et al. 2002; Calvi et al. 2019) shown that this usually provides adequate results when considering the collapse modelling of both reduced and large-scale systems. Interested readers may refer to Tagel-Din (1998) for additional details. The AEM formulation also readily allows the assignment of equivalent mechanical properties to interface springs to describe the actual behaviour of a wide range of connection types (e.g. nailed, friction, etc.) present in the EUC-BUILD6 building specimen, whose test results were used in this work as a reference for calibrating the AEM models considered in the numerical study presented in the following sections. Since experimental evidence has shown that the latter may influence significantly the dynamic response of cavity wall systems (see Graziotti et al. 2017; Tomassetti et al. 2019a, b), most of these details, as summarised below and illustrated in Figure 4.3, were duly reproduced in the numerical models:

- During the construction of EUC-BUILD6, the mortared connections among the underneath of the 1st floor RC slab (herein modelled as fully rigid, since no damage was observed experimentally) and the top edge of the CS longitudinal façades were filled only after the attainment of gravity loads, which thus acted only on the transversal CS façades. Consequently, the frictional resistance provided by these mortar layers is likely to be limited due to lack of vertical compression; similarly, their compressive strength might be also likely affected by shrinkage phenomena. To account for these aspects, reduced flexural and shear stiffnesses have been allotted to the corresponding interface springs (see Figure 4.3a). Further, for reproducing the experimental conditions in the static range, the top course of bricks of the transversal façades was deleted – and then restored – after the application of gravity loads.

- Tie connectors (i.e. 3mm-diameter and 200mm-long steel bars weakly coupling the response of CS and CL panels) and L-shaped anchors (employed during the considered test for preventing early OOP failure of roof-gable assemblies) were idealised as elastic-perfectly-plastic beam elements; their numerical distribution faithfully replicates the actual one (i.e. 1 tie/m^2). In the AEM model, to avoid the explicit simulation of interpenetration phenomena (such as the pull-out) between ties and masonry leaves and reduce computational expense, the contact with masonry occurs only through the transverse section of the ties (see Figure 4.3b). Since they typically failed within the CL mortar bonds, a strain-softening bilinear constitutive law (with pull-out strength equal to the experimentally inferred one, i.e. 2.3 kN, see Messali et al. 2016) was assigned to the CL wall-tie interfaces. Contrarily, on the CS wall side, a linear elastic connection, characterised by the CS mortar flexural stiffness, was used.

- The roof structure of EUC-BUILD6 consisted of an assembly of timber joists and planks covered by ceramic tiles (see Figure 4.3d), whose nonlinear response was mainly governed by the mechanical contribution of nailed connections. While timber members have been explicitly modelled as elastic elements for representing URM walls-ties, the system nonlinearity was accounted for by equivalent interface springs with initial and post-peak rotational stiffnesses (i.e. $k_{\varphi 0}$ and $k_{\varphi 1}$, determined according to Gattesco and Macorini 2014, assumed as 1773 and 77 kNmm/rad respectively), in which the system nonlinearity is lumped, and characterised by a strain-hardening bilinear constitutive law, as described by Foschi (1974). In practice, through the definition of F_{max}, namely the maximum lateral capacity (equal to 1.3 kN) experimentally-inferred by Dolan and Madsen (1992), the value of $k_{\varphi 0}$ automatically changes into $k_{\varphi 1}$ right after reaching F_{max}.
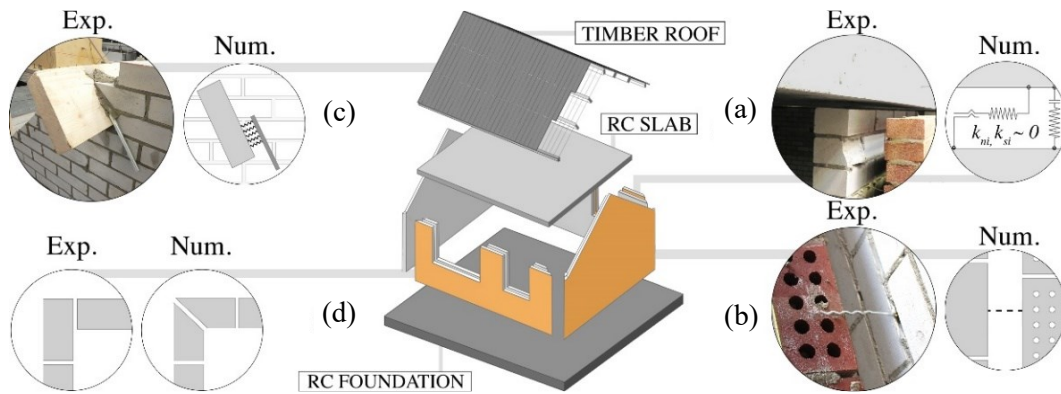
Figure 4.3 Experimental vs. numerical construction details of terraced house test specimen (adapted from Malomo et al. 2020a)

4.3 Simulation of the shake-table behaviour of a cavity wall building specimen

The EUC-BUILD6 building prototype (see Figure 4.4) was tested at the shake-table of Eucentre and, as extensively discussed in (Miglietta et al. 2021), and consisted of a two-storey URM structure with asymmetrically-distributed large openings (particularly at the ground floor), RC diaphragms, timber roof and cavity walls. It was 5.94 m large, 5.58 m wide and 7.83 m-height, with a total mass of 47.2 tons. Considering the definition reported in the Groningen Exposure Database by Arup (2019a), according to which the opening percentage can be computed as the ratio between the width of the openings and the width of the façade, the longitudinal ground floor walls of EUC-BUILD6 are characterised by 80% (West) and 50% (East) opening percentages, while the South façade was built as a blind wall, since the specimen was meant to represent the end-unit of a set of terraced house systems.
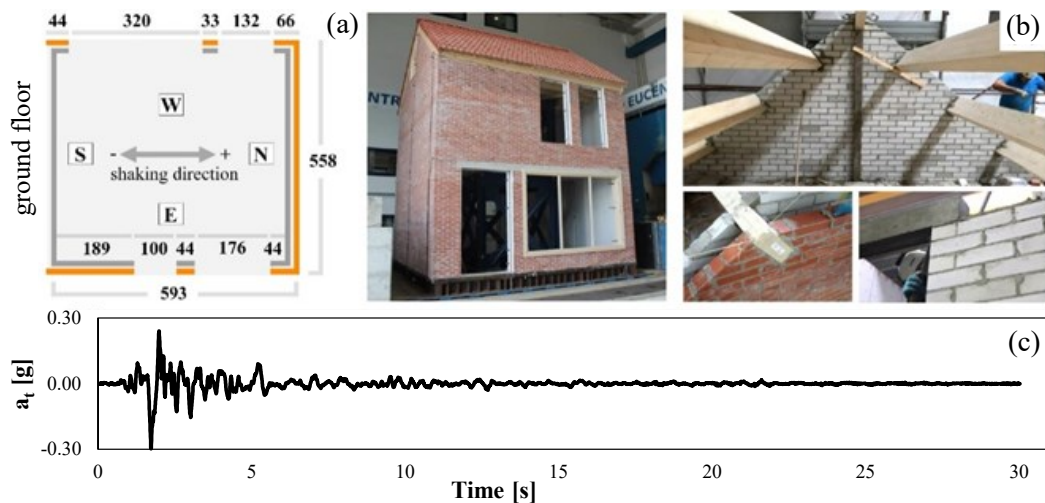
Figure 4.4 a) Ground floor plan (in cm), b) EUC-BUILD6 and roof construction details (Miglietta et al. 2021) and c) unscaled acceleration time-history (i.e. EQ-100%, plotted as table acceleration-a_t vs time)

The building prototype was fixed to the shake-table and the acceleration time-history depicted in Figure 4.4c, scaled according to the uniaxial loading protocol reported in Table 4.1 (where PTA is peak table acceleration), together with the damage limit states identified by Miglietta et al. (2021), was incrementally applied until reaching near-collapse condition. In Table 4.2, the main masonry material properties (i.e. compressive strength of masonry f_m, flexural bond strength f_w, cohesion c and friction coefficient μ), obtained either using the analytical formulae mentioned above or through characterisation tests and directly implemented in the model, are summarised.

Table 4.1 Test loading protocol, damage and limit states of EUC-BUILD6 (Miglietta et al. 2021)

Test ID	PTA [g]	Damage limit states [-]	Test ID	PTA [g]	Damage limit states [-]
EQ-20%	0.06	DL_1 – no visible damage	EQ-85%	0.26	DL_2 – minor str. damage
EQ-33%	0.16	DL_1 – no visible damage	EQ-100%(a)	0.31	DL_2 – minor str. damage
EQ-50%	0.16	DL_1 – no visible damage	EQ-100%(b)	0.30	DL_3 – damage in all the CS piers
EQ-66%	0.25	DL_2 – minor str. damage	EQ-133%	0.39	DL_4 – near-collapse conditions

Table 4.2 Actual and analytically-inferred masonry material properties of EUC-BUILD6

	f_{cm}	f_{cu}	f_w	E_m	c	μ	^1E_u	$^2E_{mo}$
CS - density $\delta m = 1837$ [kg/m3]								
Avg [MPa]	10.1	19.8	0.28	6593	0.6	0.7	7029	1438
C.o.V. [%]	0.06	0.18	0.32	0.09	-	-	0.4	-
CL - density $\delta m = 1967$ [kg/m3]								
Avg [MPa]	11.6	50.0	0.24	4436	0.3	0.6	9000	1126
C.o.V. [%]	0.29	0.10	0.52	0.29	-	-	0.2	-

[1] derived analytically using the equations proposed by Jäger et al. (2004) and Kaushik et al. (2007)
[2] inferred according to Brooks and Baker (1998), Ciesielski (1999), Matysek and Janowski (1996) and U.B.C. 1991

With respect to the observed response of the specimen, it should be noted that flexural/rocking mechanisms were predominant, as exhaustively discussed in Miglietta et al. (2021), with the first significant cracks detected at EQ-50% in the longitudinal CS panels/spandrels. No damage was observed at this stage in the CL walls. After EQ-85%, where both CS and CL transverse walls developed some cracks at the first floor due to the activation of an OOP mechanism, extensive damage was detected at EQ-100% due to increase in the width of pre-existing cracks and the activation of OOP two-way bending mechanisms in the first-floor transversal walls. Only moderate damage was experienced, instead, by the CL façades. The test was stopped right after EQ-133%, where the majority of the previous cracks substantially increased their extension/width, i.e. when the specimen reached near-collapse condition (determined by visual inspection).

It is noted that the latter was considered as a collapse-prevention threshold, characterised by heavy global structural damage, after which the repair of a house in similar conditions may not be convenient. From a numerical viewpoint, the analysis was interrupted right after the end of the last experimentally-performed shaking sequence. In Figure 4.5a, a comparison between actual and numerical floor and roof displacements, expressed in the form of interstorey drift ratios $\delta^{1st}, \delta^{2nd}, \delta^{roof}$ (computed as the relative displacement of the considered floor/roof diaphragm divided by the storey/roof height underneath), whose maximum values (starting from EQ-50%, i.e. when nonlinear response became predominant) are also summarised in Figure 4.5b, is proposed.

The model captured satisfactorily the experimentally-observed displacement demand at both floor and roof levels, although minor differences were predicted especially in the final test phases, where the model marginally overestimated and underestimated the 2nd floor and roof deformation capacities along positive and negative direction respectively. In the same figure, the factors *rBSc* and *rδ* are reported in table form. They are defined as the ratio between actual and predicted base shear coefficient BSc (calculated as the ratio between the absolute maximum recorded overall base shear and the weight of the specimen) and floor/roof interstorey drift ratios, indicate whether the model is under (red colour)-or over (light blue colour)-estimating the actual response. The general positive impression regarding the model performance is further confirmed from the hysteresis curves shown in Figure 4.5c, where adequate agreement was found also in terms of dissipated energy and total base shear.

As may also be gathered from Figure 4.6, actual and numerical final crack patterns are comparable (only numerical cracks with width > 1 mm were displayed), even if the model slightly underpredicted the damage propagation in the spandrel elements and the OOP-loaded transversal CS walls, particularly in the gables, where an overturning failure mechanism (more pronounced than its experimental counterpart) was obtained numerically. Similarly, probably because of the simplified modelling strategy presented in Section 2, the extent of horizontal cracks in the CS walls (which are may be due to the dynamic interaction among masonry and embedded tie connectors) were not adequately captured by the model. As observed experimentally, flexure/rocking failure mechanisms were predominant, with most of the damage concentred at the base/top joints of longitudinal piers, as well as in the CS transversal walls under two-way bending OOP actions. Further, it is worth noting that the crack localisation experienced by the specimen at the intersection between West and North façades due to the local sliding mechanism of the second floor was explicitly represented by the model. This damage was caused by the OOP response of the North wall, which was pushed by the flexible diaphragm that also prevented the engagement of the West squat wall.

For future comparisons, it is worth mentioning that performing the whole incremental dynamic analysis took 10–12 h (CPU: Intel Core i7 7820x, RAM: 64 GB DDR4, SSD: 250 GB M2-960-EVO), which seems reasonable especially if compared with other micro-modelling approaches (e.g. Çaktı et al. 2016; Galvez et al. 2018a).

Test ID	BSc exp.	BSc num.	rBSc -	δ^{1st} exp.	δ^{1st} num.	$r\delta^{1st}$ -	δ^{2nd} exp.	δ^{2nd} num.	$r\delta^{2nd}$ -	δ^{roof} exp.	δ^{roof} num.	$r\delta^{roof}$ -
EQ-50%	0.15	0.13	1.13	0.06	0.08	0.71	0.13	0.10	1.24	0.23	0.30	0.76
EQ-85%	0.21	0.19	1.10	0.24	0.17	1.37	0.71	1.10	0.64	0.53	0.49	1.08
EQ-100(a)%	0.19	0.21	0.90	0.45	0.37	1.22	2.23	2.33	0.96	0.50	0.53	0.95
EQ-133%	0.24	0.20	1.24	0.69	0.74	0.93	3.01	2.71	1.11	0.42	0.54	0.78

(b)
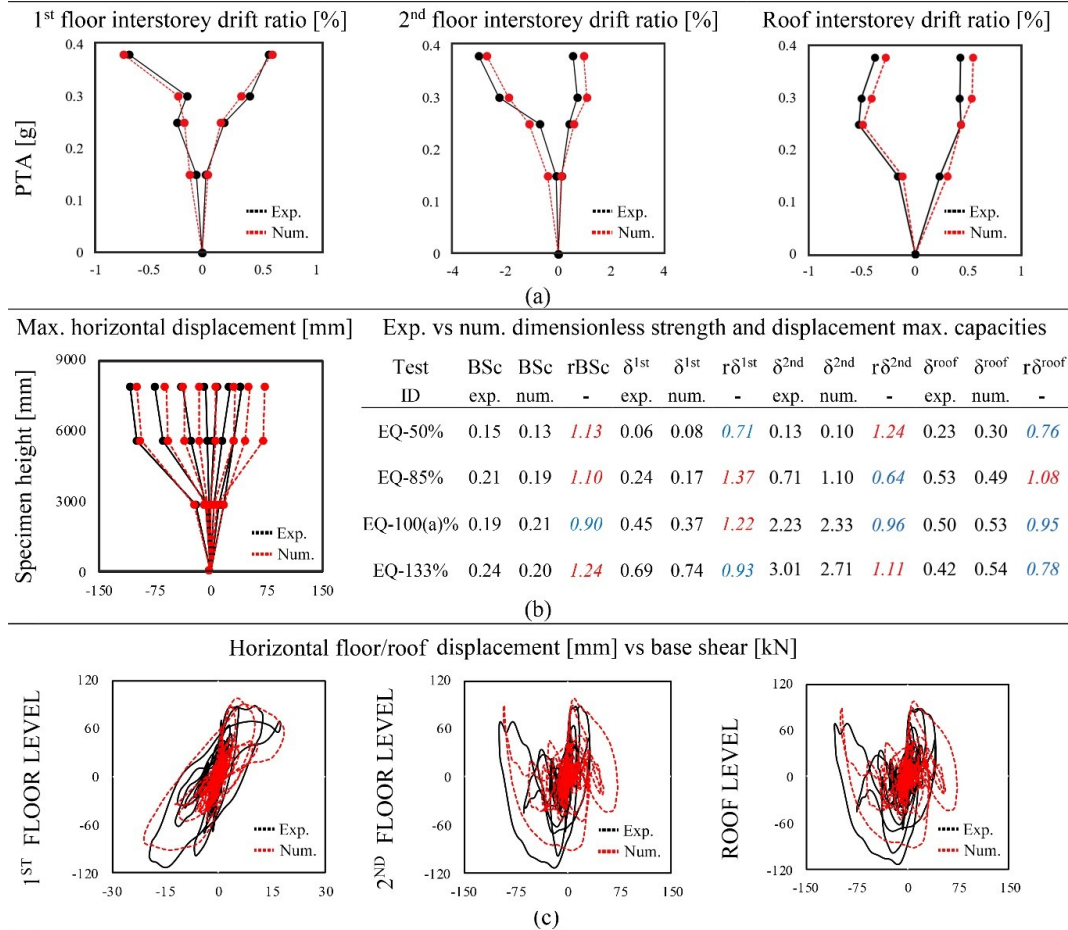
Figure 4.5 Experimental vs numerical comparisons in terms of a) interstorey drift ratio curves, b) building displacement profile and dimensionless strength-displacement absolute max. capacities, c) total floor/roof displacement vs total base shear hysteretic curves

4.4 Influence of ground floor openings percentage on dynamic response

In this section, a numerical study on the influence of ground floor openings percentage (it is recalled that the latter is herein defined as the ratio between the width of the openings and the length of the façade) on the seismic response of a cavity wall URM structure such as the tested house (i.e. EUC-BUILD6), is proposed. To this end, the calibrated EUC-BUILD6 model previously described (which featured 80% and 50% ground floor openings percentage in the West and East direction respectively) was geometrically modified to consider different configurations, characterised by various ground opening layouts (it is noted that the lower- and upper-bound opening percentages derive from the Groningen building exposure data reported in Arup (2019a)). In the first sub-section, the same incremental dynamic loading protocol employed in the test (which was again applied consecutively, i.e. accounting for the effect of damage accumulation) of EUC-BUILD6 was considered, as well as the same modelling assumptions. Finally, taking advantage from the findings of the latter modelling exercise, a number of triaxial acceleration time-histories

(selected to cover a range of intensities, as discussed in the following) were imposed to the model (each record was herein applied individually), thus enabling a broader and more realistic investigation of the effect that the ground floor opening percentage may have, also in terms of collapse capacity.
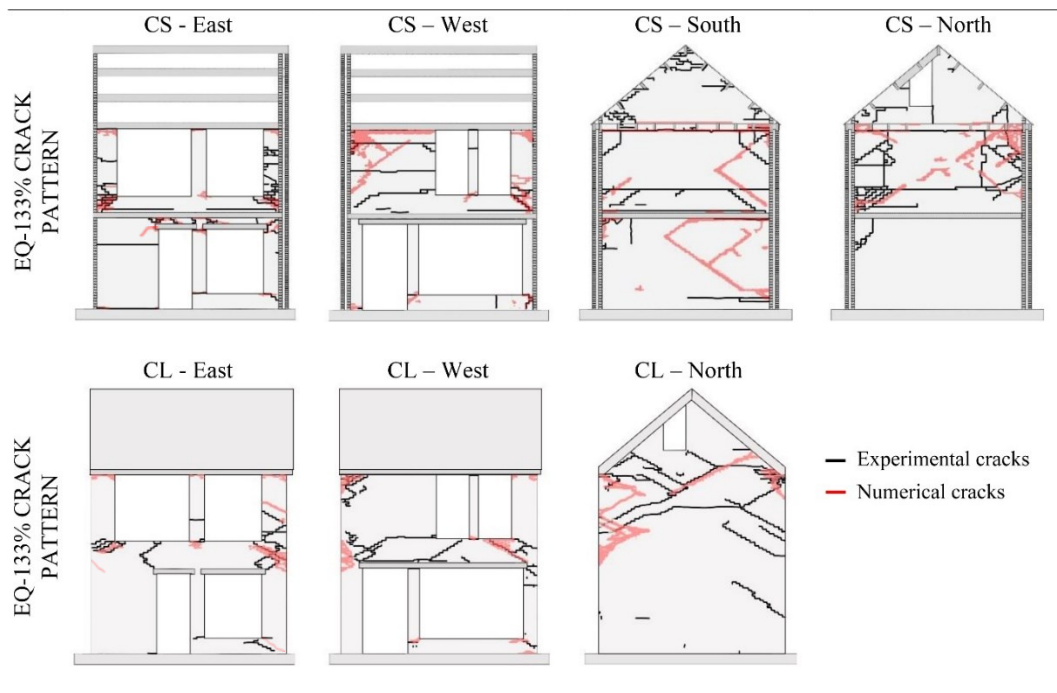
Figure 4.6 Experimental vs numerical final crack pattern (predicted cracks with width > 1mm coloured in red)

4.4.1 Experimentally employed incremental uniaxial acceleration time-histories

Two geometrical configurations, which can be deemed as representative of a lower and upper bound with reference to the extent of ground floor openings of the shake-table tested prototype, as described below in more detail and graphically represented in Figure 4.7, are considered in this sub-section. The obtained numerical results are compared to those experimentally inferred from the shake-table test of EUC-BUILD6 (hereinafter referred to as GFO80). It is noted that the ratio between the openings percentage of West and East façades was kept, in as much as possible, in the range of the one of EUC-BUILD6, i.e. approximately 1.6. The considered configurations are:

- Configuration GFO50 – in this case, rather than increasing the openings percentage of the initial structure, these were initially decreased to the following values: 50% for the West façade and 30% for the East façade.
- Configuration GFO90 – keeping again constant the ratio between the openings percentage of West and East façade, the openings percentage was increased up to 90% and 60% for West and East façade respectively.
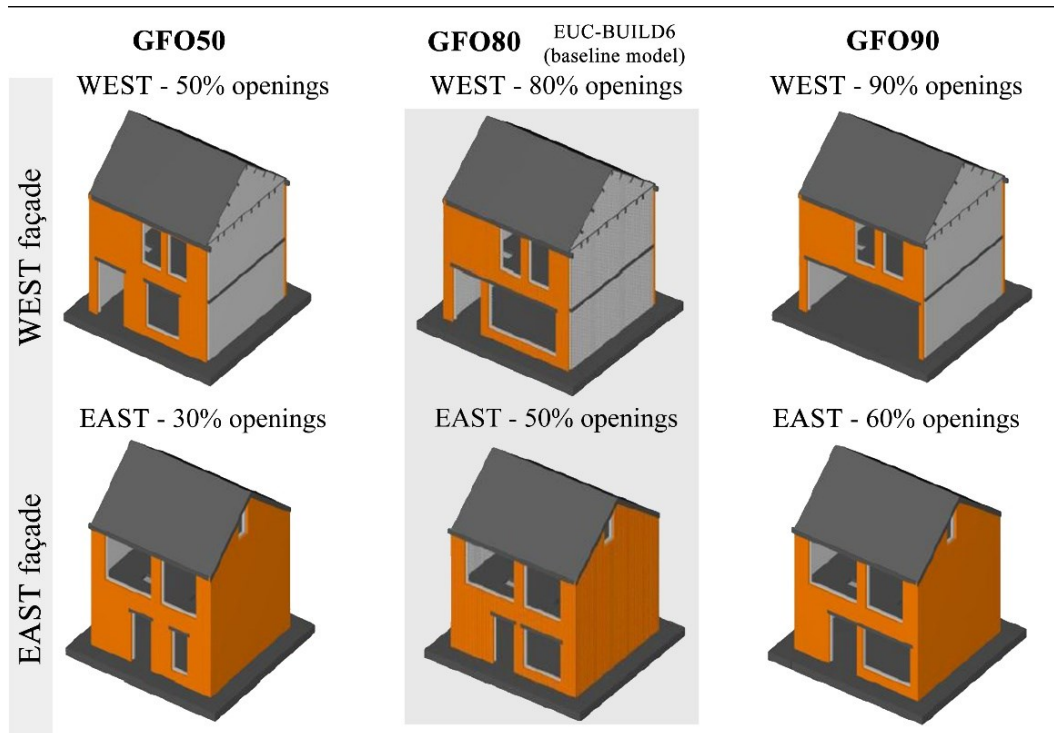
Figure 4.7 Screenshot of the models subjected to the experimentally-employed incremental uniaxial acceleration time-histories

In what follows, predicted responses for the two configurations described above are compared to each other, as well as to the experimental outcomes of the baseline structure (i.e. GFO80), allowing one to readily gather the impact that modifying the façade layout varying percentage of openings has on the response of the building prototype. As shown in Figure 4.8a,b,c, the lateral drift capacity of the various models markedly decreases with increasing openings percentage. Indeed, in the case of GFO50, where the ground floor openings percentage has been reduced, the predicted first floor displacement along the negative direction of loading (i.e. South, where the CL transversal wall is not present) is almost 5 times smaller than the one of the baseline model and more than 15 times lower with respect to that predicted in the case of GFO90 Figure 4.8a. The second floor and roof displacements for the various configurations considered, instead, appear comparable (albeit differences ranging from 20% for the second floor to 30% for the roof level were observed among e.g. GFO80 and GFO50 model). This is because the models experienced different failure modes, somehow counter-balancing the expected dissimilarities. As can be gathered from Figure 4.9, where the predicted damage propagation for all the configurations are compared, and further discussed in the following, the much more flexible characteristics of the ground floor level of GFO90 inevitably transformed the significantly stiffer response of the latter into that of a first-floor soft-storey type. Contrarily, in the cases of GFO80 and the GFO50 model, the stiffer response of the ground floor resulted in a damage localisation at the second-floor, thus this time inducing a second-floor soft-storey mechanism.
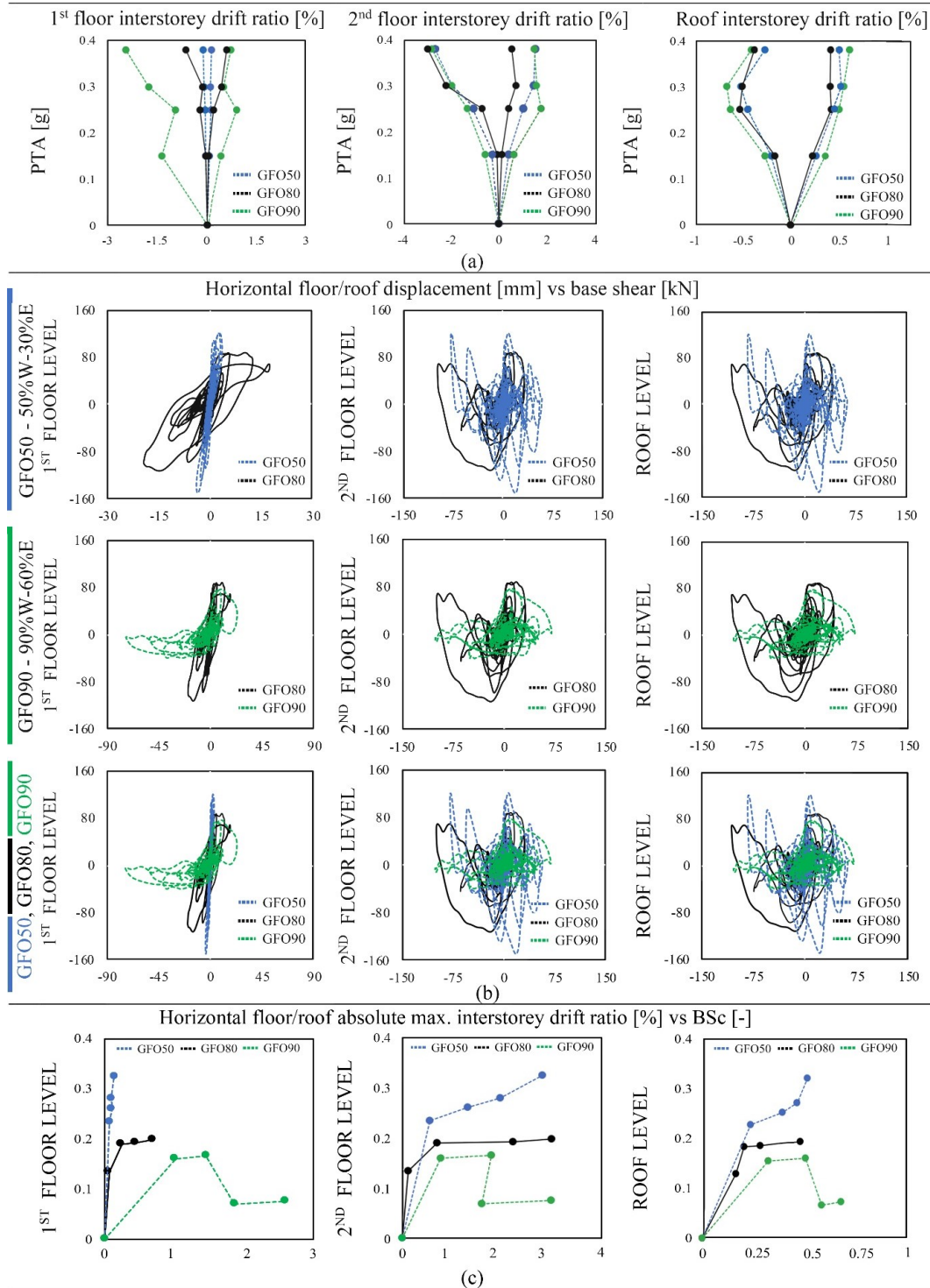
Figure 4.8 Experimental vs numerical results for each geometrical configuration in terms of a) interstorey drift ratio curves, b) floor/roof displacement vs total base shear hysteretic curves and c) total horizontal floor/roof absolute max. interstorey drift ratio vs BSc for each intensity level

	CS – North-West	CS – South-East	CL – North-West	CL – South-East
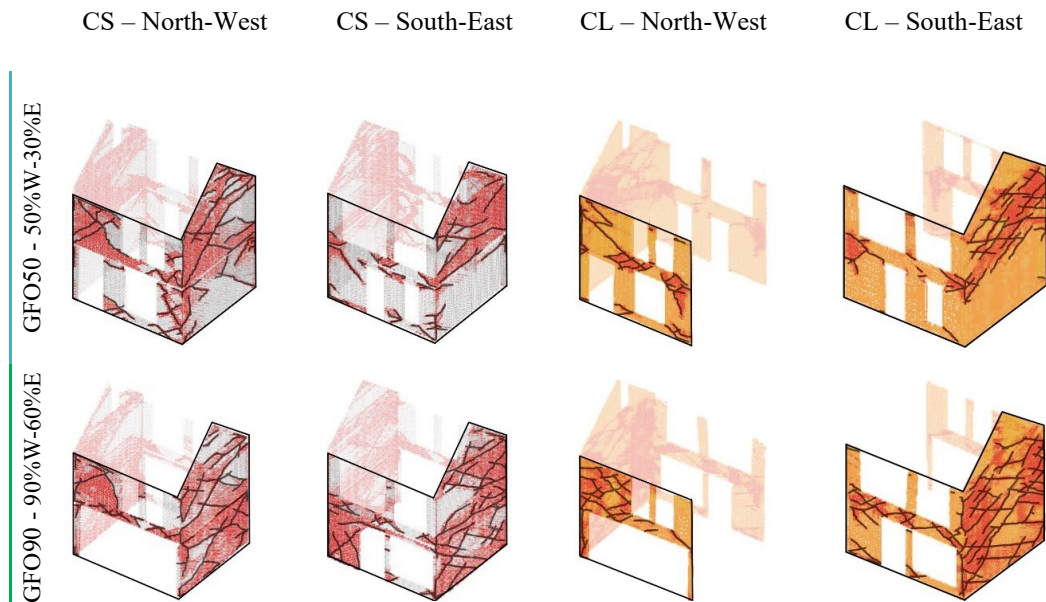
Figure 4.9 Numerical final crack patterns for all the configurations (cracks with width > 1mm highlighted in black colour)

From the hysteresis curves depicted in Figure 4.8b, as for the drift capacities, it is also evident that the overall strength capacity of the specimens would tend to decrease with increasing openings percentage. Such considerations are well epitomised by the plot in Figure 4.8c, where absolute maximum floor/roof interstorey drifts for each intensity level are plotted against the corresponding dimensionless BSc, and confirm that the extent of ground floor openings may affect significantly the dynamic performance of this specific type of URM cavity wall buildings. Finally, in Figure 4.9, the crack patterns at the end of the analyses are given (for the sake of clarity, cracks with width >1 mm are highlighted in black colour), confirming the first and second floor soft-storey types of response for GFO90 and GFO50, respectively. Indeed, the latter only suffered limited cracks at the ground floor, particularly for what concerns OOP damage in the CS transverse walls, which is close to negligible. For the cases of GFO90 a higher concentration of damage at the ground floor, instead, was observed, with several and diffuse cracks propagating on both in-plane and OOP-loaded CS/CL façades.

4.4.2 Triaxial acceleration time-histories

This section focuses on the undertaking of nonlinear dynamic analyses using the 11 triaxial "training records" (see Arup, 2017) employed in the fragility functions development by Crowley et al (2019a,b). As shown in Figure 4.10, four different combinations of opening layouts were considered; an additional configuration, i.e. GFO65, with a percentage of openings of 65% (West) and 45% (East), was introduced so as to allow a more evenly spread variation of the openings percentage (it is recalled that the lower- and upper-bound opening percentages derive from the Groningen building exposure data reported in Arup (2019a)). As before, the ratio between the openings percentage of West and East façades

was kept in the range of the one of GFO80, i.e. 1.6. In addition to GFO65, the following configurations were thus also selected:

- Configuration GFO50 – As for the previous sub-section, the openings percentage of the baseline model were decreased to 50% and 30% for West and East façade respectively.
- Configuration GFO80 – As in the case of EUC-BUILD6 building specimen, a percentage of openings of 80% and 50% were considered on the West and East side respectively.
- Configuration GFO90 – As for the previous sub-section, in this case the openings percentage was increased up to 90% and 60% for West and East façade respectively.
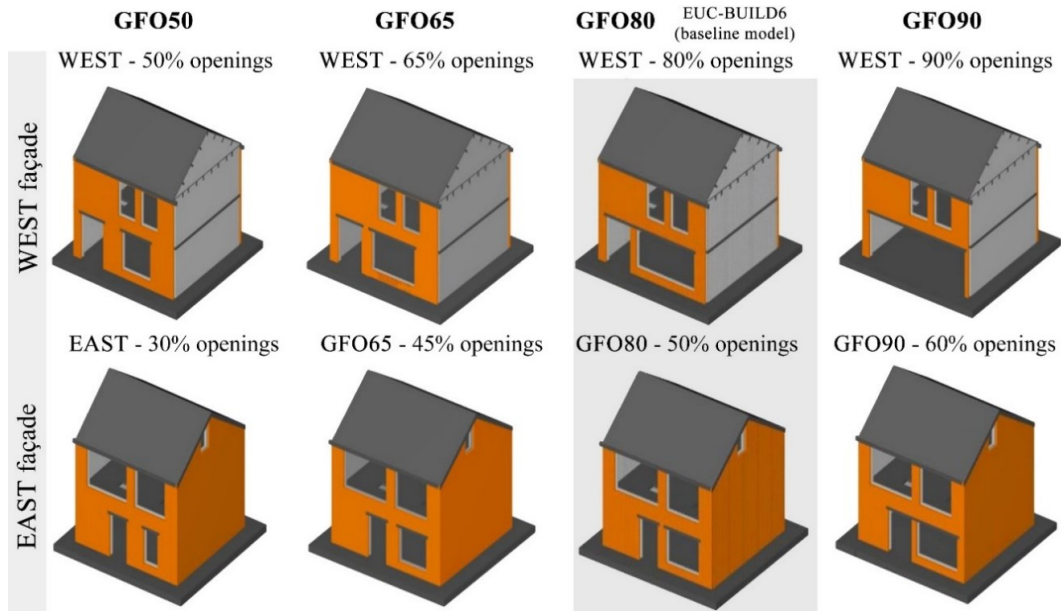
Figure 4.10 Screenshot of the models subjected to incremental triaxial acceleration time-histories

As already mentioned, in this case, 11 different triaxial ground motions of increasing intensity (Arup, 2019b), summarised in Table 4.3, have been applied to all models presented above. These acceleration time-histories have been selected to cover a range of intensities, herein expressed in terms of average spectral acceleration (avgSa, defined as the geometric mean of spectral accelerations from 0.01 to 1 seconds (step of 0.1 s), X direction), PGA and spectral acceleration at 0.1 seconds Sa(0.1s) along X direction (i.e. the longitudinal one, see Figure 4.3a). The horizontal components (with peak ground acceleration X_PGA) reported in Table 4.3 have been applied in the weak direction of each model (which has been identified a-priori as the longitudinal one, i.e. along the X-axis, as also confirmed by experimental outcomes), as that which is expected to have the lowest strength (i.e. lowest base shear capacity). The other two components along the Y and Z directions, characterised by Y_PGA and Z_PGA respectively, have also been applied to all

models. In the following sub-sections, for the sake of clarity, the ground motions will be indicated by using the time-history numbers reported in Table 4.3 (i.e. 1-11).

Table 4.3 Main properties of the employed triaxial ground motions (Arup, 2019b)

Time-history			avgSa	Sa(0.1s)	X_PGA	Y_PGA	Z_PGA
TH no.	label	colour	[g]	[g]	[g]	[g]	[g]
1	N_00356L		0.1	0.11	0.09	0.06	0.03
2	E_00137_EW		0.25	0.44	0.19	0.32	0.10
3	N_00694T		0.34	0.38	0.23	0.24	0.08
4	N_00616T		0.41	0.49	0.24	0.14	0.18
5	N_00147T		0.48	0.67	0.25	0.19	0.17
6	N_00250L		0.71	0.87	0.88	0.41	0.32
7	E_17167_EW		0.79	0.72	0.53	0.50	0.30
8	N_00415L		1.03	1.02	0.78	1.02	0.40
9	N_00569T		1.05	0.68	0.52	0.40	0.46
10	N_00407L		1.11	1.26	0.82	0.42	0.50
11	N_00451T		1.53	1.49	1.25	0.71	0.39

The AEM models predicted, depending on the considered geometrical configuration and type of imposed ground motion, a wide range of different responses, as depicted in Figure 4.12 and Figure 4.12 (it is noted that the roof hystereses were herein not included, given that, as shown in previous sections (see e.g. Figure 4.5 and Figure 4.7), roof deformation is essentially negligible). With reference to GFO50, in several cases (e.g. records 1-2-3-4-5), giving its reduced percentage of ground floor openings, a second floor soft-storey mechanism often governed the overall behaviour, inducing significant damage localisations particularly at the first floor level. Nonetheless, although the model subjected to input 10 suffered extensive damage, also exhibiting partial collapse, only two global collapses, induced by the application accelerograms 9 and 11, were observed. The magnitude of the predicted base shear ranged from 49 (record 1) to 225 kN (record 11), corresponding to a maximum absolute 2nd floor displacement of 1.4 and 97 mm respectively. As for the case of GFO50, the numerical results obtained for GFO65 seem to indicate that a second floor soft-storey mechanism was the predominant failure mode, especially for the models subjected to the first set of ground motions (i.e. from record 1 to 5). For the remaining records, on the other hand, which are characterised by a higher value of ground acceleration, damage also propagated beneath the level of the first-floor diaphragm. Similarly to GFO50, while partial collapse was observed when imposing accelerogram 10, global failures were predicted for ground motions 9 and 11. In the latter run, it is worth noting that lower displacements, with respect to GFO50, were inferred. This might be attributable to the fact that, unlike GFO50, the failure mechanism of GFO65 also included OOP modes, which undoubtedly contributed to decreasing its displacement

capacity, resulting in an early combined IP-OOP collapse (see Figure 4.13). In general, lower base shear capacities were recorded, this time ranging from 52 to 173 kN.
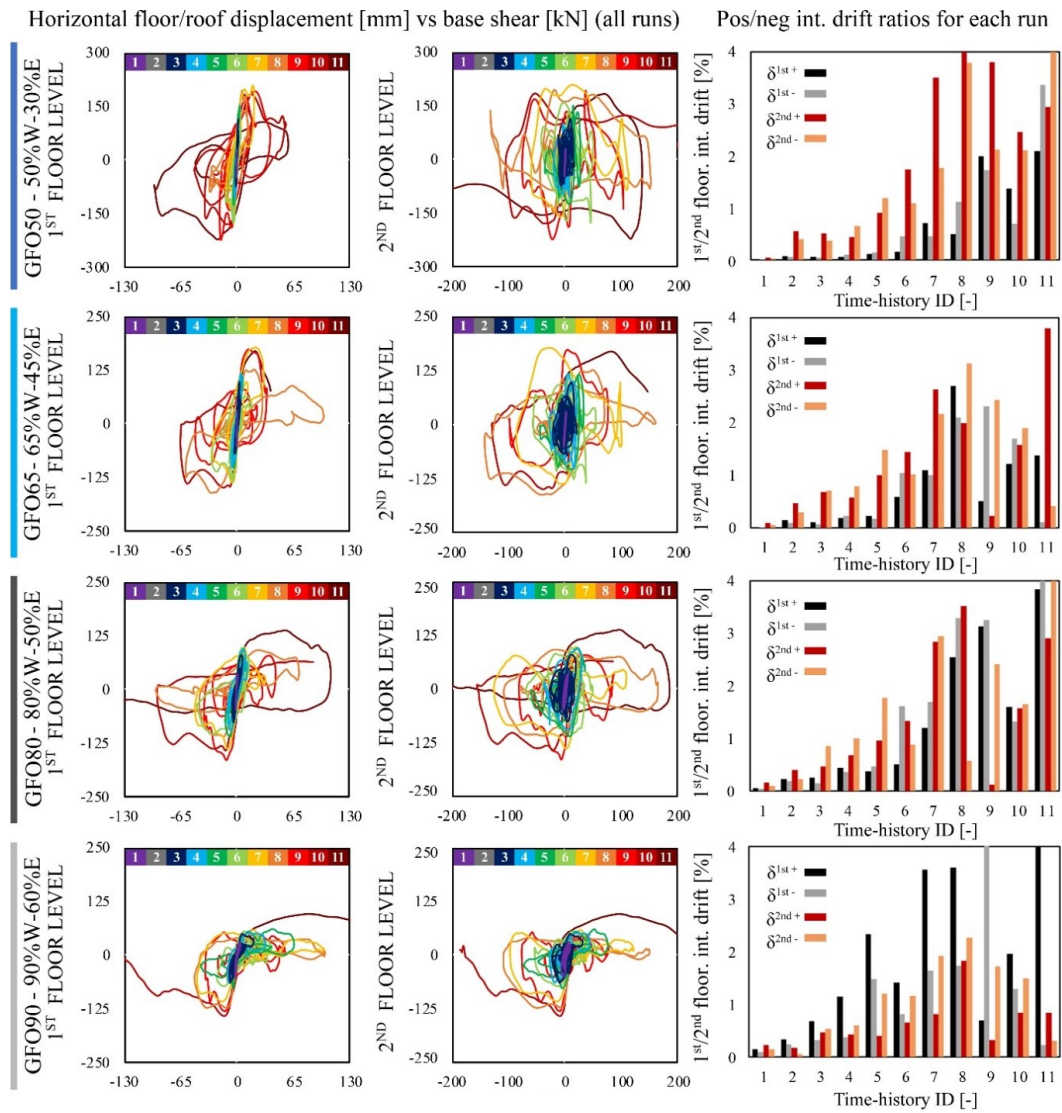
Figure 4.11 Numerical results for each geometrical configuration in terms of a) total floor displacement vs. total base shear hysteretic curves and 1st/2nd interstorey drift ratios b) BSc of GFO80 vs BSc of GFO50/GFO65/GFO90
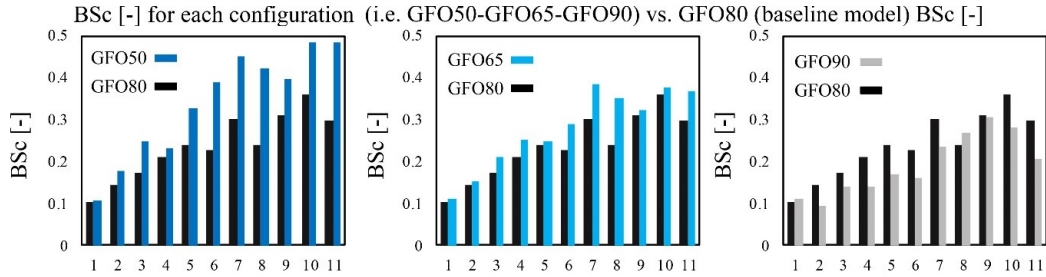
Figure 4.12 Numerical results for each geometrical configuration in terms of BSc of GFO80 vs BSc of GFO50/GFO65/GFO90
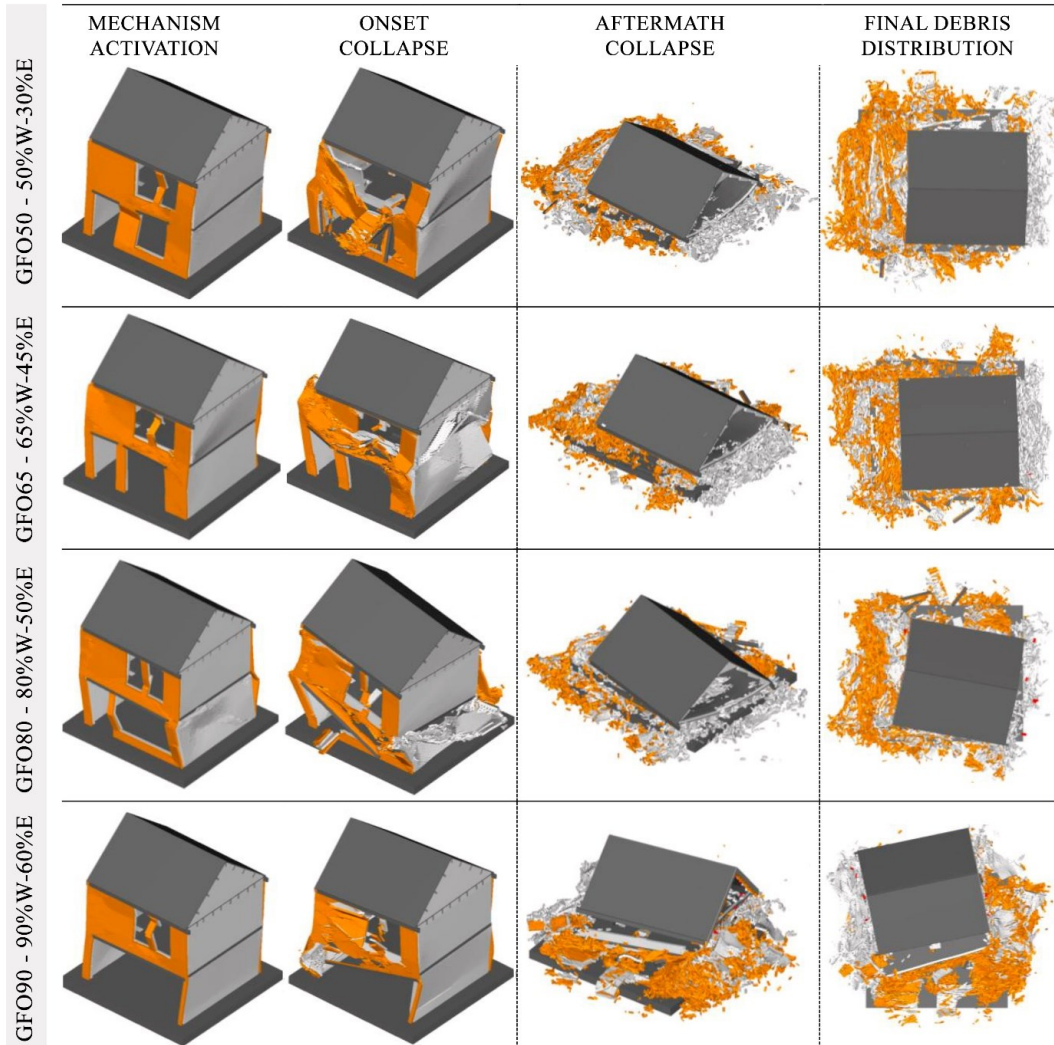
Figure 4.13 Selected screenshots of the most representative failure mechanisms, collapse modes and debris distribution from the considered geometrical configurations subjected to triaxial acceleration time-histories

Unlike EUC-BUILD6 (characterised by an analogous openings percentage at the ground floor of GFO80, i.e. 80% West and 50% East), the GFO80 models subjected to triaxial ground motions predicted first floor storey failure mechanisms in most of the cases. However, similarly to what has been experimentally observed in the case of EUC-BUILD6, a torsional mechanism (which also appears to be more pronounced with increasing opening percentage, as depicted in Figure 4.12), induced by the asymmetrical distribution of the large ground floor openings and causing the early failure of the CS OOP-loaded South party wall, was observed (see Figure 4.13). Further, it is noted that with respect to both GFO50 and GFO65, the extent of horizontal displacement predicted at the first floor level substantially increased, leading to a higher number of models which predicted near-collapse condition damage states and partial collapses, while the ground motions causing global collapses (i.e. record 9 and 11) and their number remained unchanged.

In the extreme case of a 90% openings percentage at the West ground floor façade, as expected, a larger number of global collapses (i.e. from record 8 to 11) was predicted, with the model exhibiting a torsion-governed first floor soft-storey mechanism. With respect to all the previous configurations, a clear increase in terms of detected damage was found, even considering the first set of runs. In general, while the maximum absolute predicted base shear was significantly lower (from 44 to 130 kN), larger first and second floor displacements were observed. With a view to investigate the relationship between the extent of ground floor openings and damage level, for each analysis the latter was thus classified in the following categories (also graphically represented in Figure 4.14):

- Slight to moderate damage (S-MD): negligible or minor damage (maximum residual crack opening lower than 1 mm, as suggested in Baggio et al. 2007), easily repairable and for which the structure could be considered as fully operational.
- Moderate to heavy damage (M-HD): maximum residual crack opening higher than 1mm. At this stage, which could be considered as a life safety limit state, the damage might be considered as relevant but still repairable.
- Near collapse conditions (NC): collapse-prevention threshold, characterised by heavy and widespread structural damage.
- Partial collapse (PC): when the collapse of one or more members or entire sub-structures occurs, associated with heavy and widespread structural damage
- Global collapse (GC): when the entire structure experiences global failure (for the sake of clarity it should be noted that in the examples shown in Figure 4.14 the onset of collapse, rather than the global collapse, is depicted).

In Figure 4.14, the average range of first floor interstorey drift ratio δ^{1st} associated to each of the adopted damage limit state is also reported. It is noted that a good agreement was found with experimentally-derived drift limits for analogous structures (see e.g. Graziotti et al. 2017). As shown in in the same Figure, it seems that there is a direct relationship between the geometry of these URM cavity wall configurations, characterised by different percentages of openings at the ground floor, and their vulnerability. For what concerns the first records (i.e. 1-5), while either S-M or M-H damage was detected when considering GFO50 and GFO65, GFO80 and GFO90 also experienced near-collapse conditions. On the

other hand, focusing on the last set of records 6-11, it can be gathered that a higher number of partial and global collapses were observed in the models characterised by larger ground floor opening percentages.
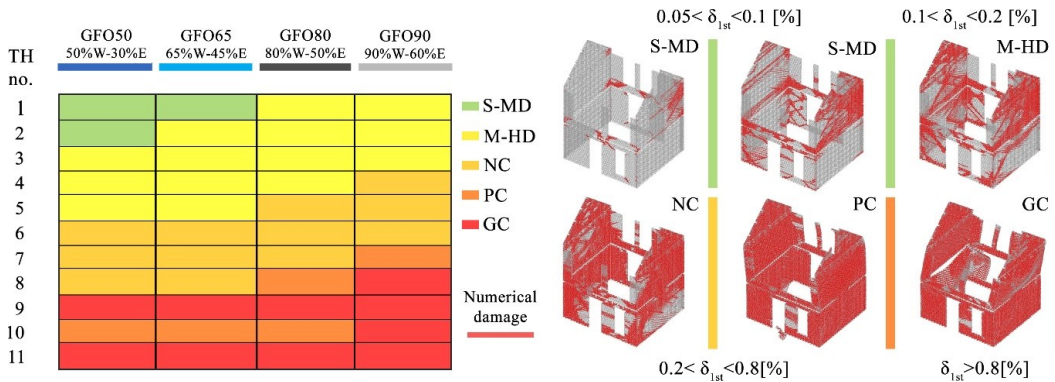
Figure 4.14 Numerically-inferred damage limit states for each configuration and applied acceleration time-history, examples of crack-based identification of the proposed damage limit states

4.5 Influence of ground floor openings percentage on fragility functions

In this section, for the four different configurations considered in the previous section (i.e. GFO50, GFO65, GFO80, GFO90) subjected to triaxial acceleration time-histories, fragility functions (which describe the probability of reaching/exceeding a given damage or collapse state under increasing levels of ground shaking intensity) were developed according to the procedure proposed by Crowley et al. (2019a,b). To start with, this required the definition, for each structural configuration, of a simplified single-degree-of-freedom (SDOF) system whose hysteretic response is capable of reproducing the displacement estimates that were obtained with the multi-degree-of-freedom (MDOF) AEM models under the 11 training records.

To reproduce the dynamic response using SDOF models, use was made of the software SeismoStruct (Seismosoft 2019) and the 'multi_lin' response curve by Sivaselvan and Reinhorn (1999) implemented therein. The latter features a polygonal hysteresis loop that can account for both stiffness and strength cyclic degradation (an example is shown in Figure 4.15a). The maximum 1st floor displacement of each of the four MDOF case-studies, under each triaxial training record, was thus converted to its equivalent SDOF counterpart (see Crowley et al., 2019a,b) and then compared with that obtained employing the SeismoStruct SDOF model. The latter was then iteratively adapted until attainment of adequate agreement between equivalent SDOF and SeismoStruct SDOF displacements Sd. In Figure 4.15b, such comparison, as a function of average spectral accelerations $avgSa$, for one of the structural models is depicted.

The final adopted properties for each of the four SDOF systems are reported in Table 4.4. The sixteen parameters of the *multi_lin* hysteretic model are defined as follows: EI is the initial stiffness (kN/m), PCP and PCN are the positive and negative "cracking" force (kN), PYP and PYN are the positive and negative yield force (kN), UYP and UYN are the positive

and negative yield displacement (m), *UUP* and *UUN* are the positive and negative ultimate displacement (m), *EI3P* and *EI3N* are the positive and negative post-yield stiffness as percent of elastic, *HC* is the stiffness degrading parameter, *HBD* is the ductility-based strength decay parameter, *HBE* is the hysteretic energy-based strength decay parameter, *HS* is the slip parameter, and *IBILINEAR* is a model parameter equal to 0 for trilinear model, 1 for bilinear model, and 2 for vertex-oriented model.
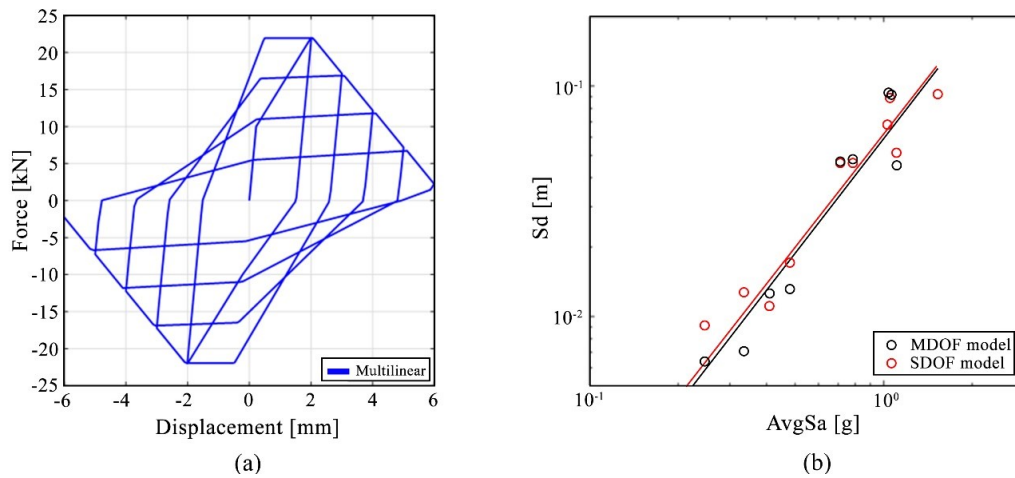
Figure 4.15 a) Example response curve for the multi_lin hysteretic model, and b) comparison of displacements from MDOF (transformed to SDOF) and corresponding SDOF from SeismoStruct model (with calibrated multi_lin hysteretic response curve)

Records compatible with the level of seismic hazard in the Groningen field at the time this study was carried out, computed with the use of the ground motion model by Bommer et al. (2017), were selected through disaggregation (mean magnitude and distance) at four different return periods (Tr = 500, 2500, 10k and 100k years) at one of the highest hazard locations in the field. The records were then selected from a large database, including European (Akkar et al., 2014) and NGA-West records (Chiou et al., 2008), and matched to spectra conditioned on four different levels of AvgSa (corresponding to the four return periods), i.e. 0.20g, 0.34g, 0.50g, 0.86g, using the ground motion selection procedure proposed by Baker and Lee (2018). The associated response spectra are depicted in Figure 4.16(a).

The cloud method (see Jalayer, 2003; Cornell et al., 2002) was then considered to derive the probabilistic relationship among ground motion intensity and nonlinear structural behaviour of the SDOF systems; once the maximum nonlinear dynamic displacement response of a given SDOF (S_{di}) is obtained from all ground-motion records, each response is plotted against a scalar/vector intensity measure ($\ln(AvgSa)$ herein) and the statistical parameters corresponding to a fitted lognormal distribution of $S_d \mid \ln(AvgSa)$ can be extracted. Specifically, the expected value, $E[\ln S_d \mid \ln(AvgSa)]$, is modelled by a linear regression equation (with the necessary censoring (Stafford, 2008) when the SDOF displacement response exceeds that associated with the ultimate deformation capacity obtained from the MDOF collapse analyses described earlier), whilst the standard deviation

or dispersion is estimated by the standard error of the regression (see Crowley et al. (2019) for the complete formulae employed).

Table 4.4 Final adopted properties implemented in the SDOF systems (note: *multi_lin* hysteretic model parameters are defined in base units of kN and m)

Property/Parameter	GFO50	GFO65	GFO80	GFO90
Mass (tonnes)	42	42	42	42
Period (s)	0.09	0.13	0.18	0.26
EI	200,000	100,000	50,000	25,000
PCP	100	50	50	50
PYP	160	125	125	100
UYP	0.004	0.005	0.01	0.05
UUP	0.048	0.069	0.093	0.078
EI3P	0.0046	0.008	1E-9	1E-9
PCN	100	50	50	50
PYN	160	125	125	100
UYN	0.004	0.005	0.01	0.05
UUN	0.048	0.069	0.093	0.078
EI3N	0.0046	0.008	1E-9	1E-9
HC	1	1	1	1
HBD	0.001	0.001	0.001	0.001
HBE	0.001	0.001	0.001	0.001
HS	1	1	1	1
IBLINEAR	0	0	0	0

The final collapse fragility functions inferred for the four opening configurations considered are shown in Figure 4.16b, confirming the observations made previously regarding the increase in seismic vulnerability of these structures when there is an enlargement of the ground-floor openings, especially accentuated when a value of 90% is reached for the ground-floor openings.

On the other hand, however, it can also be noticed that for the cases of 50%, 65% and 80% ground floor openings, the fragility remains relatively unchanged, which suggests that an openings percentage value in between 80% and 90% could possibly be used as a threshold for a change of fragility in this type of structures. It is underlined that, although not central to this study, where the focus is on the relative changes in fragility (as a function of ground-floor openings percentage), rather than on the absolute fragility values, the analysis of a single house unit allows a good approximation, albeit with a slight overestimation, of the seismic vulnerability of the whole terraced building, as shown in Kallioras et al. (2019).
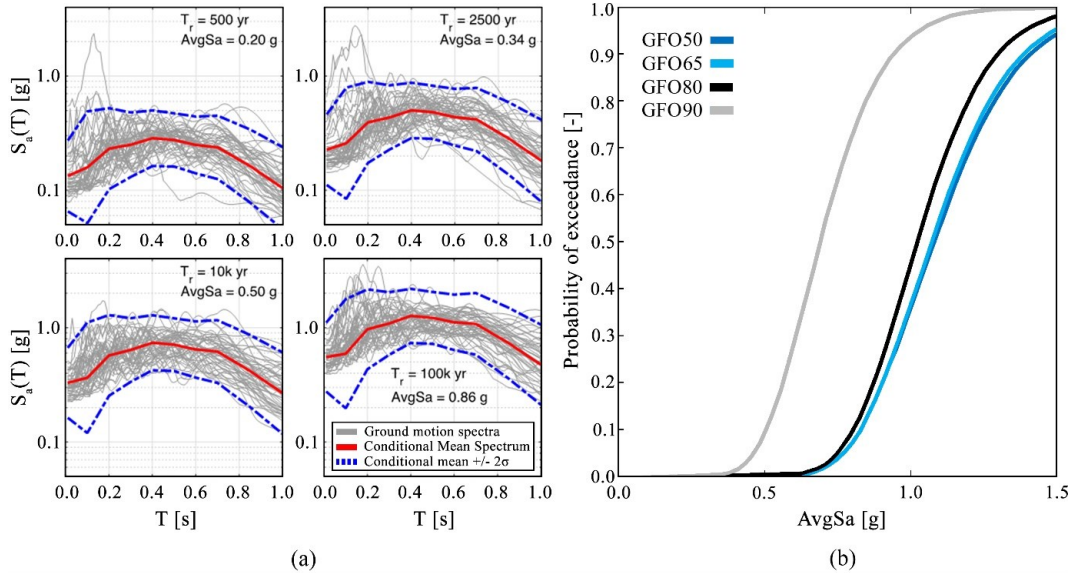
Figure 4.16 a) Spectra of selected records and the conditional spectra (herein represented with the mean and +/- 2σ) to which they have been matched; b) fragility functions inferred for each one of the four structural configurations

4.6 Conclusions

In this work, the impact of ground floor openings percentage on the response of URM cavity wall building systems was investigated using a discrete numerical approach, the Applied Element Method (AEM), whose unique features enabled a comprehensive numerical study to be carried out in a reasonable timeframe, also accounting for IP-OOP interaction and representing explicitly damage initiation and propagation until the complete collapse. After a preliminary calibration of the AEM model against experimental shake-table results of a full-scale cavity wall building specimen (i.e. EUC-BUILD6), where adequate agreement among actual and modelled dynamic behaviour was found, the response of a number of additional geometrical configurations, characterised by different ground floor opening percentages and subjected to various acceleration time-histories, was investigated.

The results from the first set of analyses, where the same incremental uniaxial loading protocol employed for EUC-BUILD6 was applied consecutively, i.e. accounting for the effect of damage accumulation, confirm that the extent of ground floor openings may affect significantly the dynamic performance of URM buildings, with the overall strength capacity of the latter decreasing with increasing openings percentage, which also causes deformations and failure mechanisms to concentrate on the ground floor. Similarly, when considering triaxial seismic excitation (this time without accounting for damage accumulation), it was found that the extent of damage is again proportional to the percentage of openings at the ground floor and, depending on the various selected geometrical configurations, different failure mechanisms were predicted, affecting both displacement and strength capacity. More specifically, it was observed that especially in the case of large openings percentage on the ground floor (i.e. > 80%) the overall response

was significantly affected by the presence of torsional mechanisms, which governed the collapse mode, thus further increasing the vulnerability of these structural typologies towards horizontal actions. The observed torsional behaviour could perhaps have been slightly emphasised by the limitation of the analysis only to the terminal unit of the terraced house.

Leveraging upon the results of the above nonlinear dynamic analysis of the AEM models, ensuing fragility functions were also developed, allowing a more readily appreciation of how the introduction of large ground floor openings (often pursued to increase the amount of natural lighting of the house) might lead to a non-negligible increase in the seismic vulnerability of structures of the type studied in the work. A repetition of this fragility study considering one or more models of actual terraced houses will undoubtedly constitute a good complement to the results obtained here for the EUC-BUILD6 model (which, on the other hand, featured the advantage of being validated with shake-table results).

References

Akkar S, Sandikkaya MA, Senyurt M, Azari Sisi A, Ay BO, Traversa P, Douglas J, Cotton F, Luzi L, Hernandez B, Godey S (2014) Reference database for seismic ground-motion in Europe (RESORCE), Bull Earthq Eng 12:311-339.

Arup (2017) Typology modelling: analysis results in support of fragility functions—2017 batch results, Tech Rep no 229746_031.0_REP2005, November 2017. Available at http://www.nam.nl/feiten-en-cijfers/onderzoeksrapporten.html.

Arup (2019a) Exposure Database v6, Tech Rep no 229746_031.0_REP2014, 28 June 2019. Available at http:// www.nam.nl/feiten-en-cijfers/onderzoeksrapporten.html.

Arup (2019b) Typology modelling: Analysis results in support of fragility functions – 2018-2019 batch results, Tech Rep no 229746_031.0_REP2015, June 2019. Available at http://www.nam.nl/feiten-en-cijfers/onderzoeksrapporten.html.

Abdulla KF, Cunningham LS, Gillie M (2017) Simulating masonry wall behaviour using a simplified micro-model approach. Eng Struct 151:349–365.

https://doi.org/10.1016/j.engstruct.2017.08.021.

Aref AJ, Dolatshahi KM (2013) A three-dimensional cyclic meso-scale numerical procedure for simulation of unreinforced masonry structures. Comput Struct 120:9–23. https://doi.org/10.1016/J.COMPSTRUC.2013.01.012.

Baggio C, Bernardini A, Colozza R, et al (2007) Field manual for post-earthquake damage and safety assessment and short term countermeasures (AeDES). Eur Comm Res Centre—Institute Prot Secur Citizen, EUR 22868.

Brooks JJ, Baker A (1998) Modulus of Elasticity of Masonry. Mason Int 12:58–63.

Çaktı E, Saygılı Ö, Lemos J V., Oliveira CS (2016) Discrete element modeling of a scaled masonry structure and its validation. Eng Struct 126:224–236. https://doi.org/10.1016/j.engstruct.2016.07.044.

Calvi GM, Moratti M, O'Reilly GJ, et al (2019) Once upon a Time in Italy: The Tale of the Morandi Bridge. Struct Eng Int 29:198–217. https://doi.org/10.1080/10168664.2018.1558033.

Chácara C, Cannizzaro F, Pantò B, et al (2018) Assessment of the dynamic response of unreinforced masonry structures using a macroelement modeling approach. Earthq Eng Struct Dyn 47:2426–2446. https://doi.org/10.1002/eqe.3091

Ciesielski R (1999) The dynamic module of elasticity of brick walls. In: Proceedings of the Conference of the Committee of Civil Engineering PZITB: Lublin, Poland.

Crowley H, Pinho R (2017) Report on the v5 fragility and consequence models for the Groningen field.

Crowley H, Pinho R, Cavalieri F (2019) Report on the v6 Fragility and Consequence Models for the Groningen Field. Report-Groningen F Seism Hazard Risk Assess Proj

Crowley H, Pinho R, van Elk J, Uilenreef J (2018) Probabilistic damage assessment of buildings due to induced seismicity. Bull Earthq Eng. https://doi.org/10.1007/s10518-018-0462-1.

Crowley H, Polidoro B, Pinho R, Van Elk J (2017) Framework for developing fragility and consequence models for local personal risk. Earthq Spectra 33:1325–1345. https://doi.org/10.1193/083116EQS140M.

D'Altri AM, Messali F, Rots J, et al (2019a) A damaging block-based model for the analysis of the cyclic behaviour of full-scale masonry structures. Eng Fract Mech 209:423–448. https://doi.org/10.1016/j.engfracmech.2018.11.046.

D'Altri AM, Sarhosis V, Milani G, et al (2019b) Modeling Strategies for the Computational Analysis of Unreinforced Masonry Structures: Review and Classification. Arch Comput Methods Eng. https://doi.org/10.1007/s11831-019-09351-x.

Derakhshan H, Lucas W, Visintin P, Griffith MC (2018) Out-of-plane Strength of Existing Two-way Spanning Solid and Cavity Unreinforced Masonry Walls. Structures 13:88–101. https://doi.org/10.1016/j.istruc.2017.11.002.

Desai N (2017) Evaluation of code provisions for design of medium rise buildings

supporting brick veneer wall systems under the effect of in-plane seismic loads. Eng Struct 138:260–269. https://doi.org/10.1016/j.engstruct.2017.02.022.

Dizhur D, Giaretton M, Giongo I, Ingham J (2017) Seismic retrofit of masonry walls using timber strong-backs. Struct Eng Soc J - SESOC 30:30–44.

Dizhur D, Moon L, Ingham J (2013) Observed performance of residential masonry veneer construction in the 2010/2011 canterbury earthquake sequence. Earthq Spectra 29:1255–1274. https://doi.org/10.1193/050912EQS185M.

Dolan JD, Madsen B (1992) Monotonic and cyclic nail connection tests. Can J Civ Eng 19:97–104.

Domaneschi M, Cimellaro GP, Scutiero G (2019) A simplified method to assess generation of seismic debris for masonry structures. Eng Struct 186:306–320. https://doi.org/10.1016/j.engstruct.2019.01.092.

El-Kashif KF, Maekawa K (2004) Time-dependent nonlinearity of compression softening in concrete. J Adv Concr Technol 2:233–247.

Foschi RO (1974) Load-slip characteristics of nails. J Wood Sci 7:69–76.

Furukawa A, Kiyono J, Toki K (2012) Numerical simulation of the failure propagation of masonry buildings during an earthquake. J Nat Disaster Sci 33:11–36.

Galvez F, Giaretton M, Abeling S, et al (2018a) Discrete Element modelling of a two-storey unreinforced masonry scaled model. In: 16th European Conference on Earthquake Engineering. Thessaloniki, Greece.

Galvez F, Segatta S, Giaretton M, et al (2018b) FE and DE modelling of out-of-plane two way bending behaviour of unreinforced masonry walls. In: 16th European Conference on Earthquake Engineering. Thessaloniki, Greece.

Gattesco N, Macorini L (2014) In-plane stiffening techniques with nail plates or CFRP strips for timber floors in historical masonry buildings. Constr Build Mater 58:64–76. https://doi.org/10.1016/j.conbuildmat.2014.02.010.

Giambanco G, La Malfa Ribolla E, Spada A (2018) Meshless meso-modeling of masonry in the computational homogenization framework. Meccanica 53:1673–1697. https://doi.org/10.1007/s11012-017-0664-7.

Godio M, Beyer K (2019) Evaluation of force-based and displacement-based out-of-plane seismic assessment methods for unreinforced masonry walls through refined model simulations. Earthq Eng Struct Dyn 48:454–475. https://doi.org/10.1002/eqe.3144.

Graziotti F, Rossi A, Mandirola M, et al (2016a) Experimental characterisation of calcium-silicate brick masonry for seismic assessment. In: International Brick and Block Masonry Conference. Padua, Italy, pp 1619–1628.

Graziotti F, Tomassetti U, Penna A, Magenes G (2016b) Out-of-plane shaking table tests on URM single leaf and cavity walls. Eng Struct 125:455–470.

Graziotti F, Tomassetti U, Kallioras S, et al (2017) Shaking table test on a full scale URM cavity wall building. Bull Earthq Eng 15:5329–5364. https://doi.org/10.1007/s10518-

017-0185-8.

Graziotti F, Penna A, Magenes G (2019a) A comprehensive in situ and laboratory testing programme supporting seismic risk analysis of URM buildings subjected to induced earthquakes. Bull Earthq Eng 17:4575–4599. https://doi.org/10.1007/s10518-018-0478-6

Graziotti F, Tomassetti U, Sharma S, et al (2019b) Experimental response of URM single leaf and cavity walls in out-of-plane two-way bending generated by seismic excitation. Constr Build Mater 195:650–670. https://doi.org/10.1016/j.conbuildmat.2018.10.076

Grunwald C, Khalil AA, Schaufelberger B, et al (2018) Reliability of collapse simulation – Comparing finite and applied element method at different levels. Eng Struct 176:265–278. https://doi.org/10.1016/j.engstruct.2018.08.068

Jäger W, Irmschler H, Schubert P (2004) Mauerwerk-Kalender 2004. Ernst & Sohn Verlag für Architektur und technische Wissenschaften

Kallioras S, Graziotti F, Penna A (2019) Numerical assessment of the dynamic response of a URM terraced house exposed to induced seismicity. Bull Earthq Eng 17:1521–1552. https://doi.org/10.1007/s10518-018-0495-5

Karbassi A, Nollet M-J (2013) Performance-based seismic vulnerability evaluation of masonry buildings using applied element method in a nonlinear dynamic-based analytical procedure. Earthq Spectra 29:399–426

Kaushik HB, Rai DC, Jain SK (2007) Stress-strain characteristics of clay brick masonry under uniaxial compression. J Mater Civ Eng 19:728–739

Lemos J V (2007) Discrete element modeling of masonry structures. Int J Archit Herit 1:190–213

Malomo, D., Pinho, R., and Penna, A. (2018). Using the applied element method for modelling calcium silicate brick masonry subjected to in-plane cyclic loading. Earthq Eng Struct Dyn 47(7):1610–1630.

Malomo D, DeJong MJ, Penna A (2019a) A Homogenized Distinct Macro-block (HDM) model for simulating the in-plane cyclic response of URM walls. In: 13th North American Masonry Conference. Salt Lake City, Utah, United States

Malomo D, DeJong MJ, Penna A (2019b) Distinct element modelling of the in-plane cyclic response of URM walls subjected to shear-compression. Earthq Eng Struct Dyn. https://doi.org/10.1002/eqe.3178

Malomo D, Pinho R, Penna A (2020a) Simulating the shake table response of unreinforced masonry cavity wall structures tested to collapse or near-collapse conditions. Earthq Spectra 36:554–578. https://doi.org/10.1177/8755293019891715

Malomo D, Pinho R, Penna A (2020b) Numerical modelling of the out-of-plane response of full-scale brick masonry prototypes subjected to incremental dynamic shake-table tests. Eng Struct 209:110298. https://doi.org/10.1016/j.engstruct.2020.110298

Malomo D, Scattarreggia N, Orgnoni A, et al (2020c) Numerical Study on the Collapse of

the Morandi Bridge. J Perform Constr Facil 34:04020044. https://doi.org/10.1061/(ASCE)CF.1943-5509.0001428

Masi F, Stefanou I, Maffi-Berthier V, Vannucci P (2020) A Discrete Element Method based-approach for arched masonry structures under blast loads. Eng Struct 216:110721. https://doi.org/10.1016/j.engstruct.2020.110721

Matysek P, Janowski Z (1996) Analysis of factors affecting the modulus of elasticity of the walls. In: Proceedings of the Conference of the Committee of Civil Engineering PZITB: Lublin, Poland

Meguro K, Tagel-Din H (2000) Applied element method for structural analysis: Theory and application for linear materials. Struct Eng Eng 17:

Messali F, Esposito R, Maragna M (2016) Pull-out strength of wall ties. Report, TU Delft, NL

Miglietta M, Damiani N, Guerrini G, Graziotti F (2021) Full-scale shake-table tests on two unreinforced masonry cavity-wall buildings: effect of an innovative timber retrofit. Bull Earthq Eng 2561–2596. https://doi.org/10.1007/s10518-021-01057-5

Pantò B, Cannizzaro F, Caliò I, Lourenço PB (2017) Numerical and Experimental Validation of a 3D Macro-Model for the In-Plane and Out-Of-Plane Behavior of Unreinforced Masonry Walls. Int J Archit Herit 11:946–964. https://doi.org/10.1080/15583058.2017.1325539

Papantonopoulos C, Psycharis IN, Papastamatiou DY, et al (2002) Numerical prediction of the earthquake response of classical columns using the distinct element method. Earthq Eng Struct Dyn 31:1699–1717. https://doi.org/10.1002/eqe.185

Penna A, Lagomarsino S, Galasco A (2014) A nonlinear macroelement model for the seismic analysis of masonry buildings. Earthq Eng Struct Dyn 43:159–179

Petracca M, Pelà L, Rossi R, et al (2017) Micro-scale continuous and discrete numerical models for nonlinear analysis of masonry shear walls. Constr Build Mater 149:296–314. https://doi.org/10.1016/j.conbuildmat.2017.05.130

Portioli FPA (2019) Rigid block modelling of historic masonry structures using mathematical programming: a unified formulation for non-linear time history, static pushover and limit equilibrium analysis. Bull Earthq Eng 1–29. https://doi.org/10.1007/s10518-019-00722-0

Pulatsu B, Bretas EM, Lourenço PB (2016) Discrete element modeling of masonry structures: Validation and application. Earthq Struct 11:563–582. https://doi.org/10.12989/eas.2016.11.4.563

Raka E, Spacone E, Sepe V, Camata G (2015) Advanced frame element for seismic analysis of masonry structures: model formulation and validation. Earthq Eng Struct Dyn 44:2489–2506

Salem H, Mohssen S, Nishikiori Y, Hosoda A (2016) Numerical Collapse Analysis of Tsuyagawa Bridge Damaged by Tohoku Tsunami. J Perform Constr Facil 30:04016065. https://doi.org/10.1061/(ASCE)CF.1943-5509.0000925

Sangirardi M, Liberatore D, Addessi D (2019) Equivalent Frame Modelling of Masonry Walls Based on Plasticity and Damage. Int J Archit Herit 13:1098–1109. https://doi.org/10.1080/15583058.2019.1645240

Seismosoft (2019) SeismoStruct– A computer program for static and dynamic nonlinear analysis of framed structures. available at: http://www.seismosoft.com

Tagel-Din H (1998) A new efficient method for nonlinear, large deformation and collapse analysis of structures. Dr Thesis, Univ Tokyo

Tomassetti U, Graziotti F, Penna A, Magenes G (2018) Modelling one-way out-of-plane response of single-leaf and cavity walls. Eng Struct 167:241–255. https://doi.org/10.1016/j.engstruct.2018.04.007

Tomassetti U, Correia AA, Candeias PX, et al (2019a) Two-way bending out-of-plane collapse of a full-scale URM building tested on a shake table. Bull Earthq Eng 17:2165–2198. https://doi.org/10.1007/s10518-018-0507-5

Tomassetti U, Correia AA, Graziotti F, Penna A (2019b) Vulnerability of roof systems combining URM gable walls and timber diaphragms. Earthq Eng Struct Dyn. https://doi.org/10.1002/eqe.3187

U.B.C. (1991) International Conference of Building Officials. Uniform Building Code. In: International conference of building officials, USA. Whittier, USA

Zhang W, Du H, Li X, et al (2016) In-Plane Seismic Performance of Chinese Traditional Rowlock Cavity Walls under Low-Cycle Loading. Int J Archit Herit 10:204–216. https://doi.org/10.1080/15583058.2015.1113334

5. Development and validation of a modelling strategy for the seismic assessment of a timber retrofitting solution for URM cavity wall buildings

Abstract

This work presents the results of a numerical investigation on the effect of light timber retrofit systems on the global response of URM cavity-wall buildings. The building object of the study is a two-storey cavity-wall terraced house, retrofitted with OSB panels and timber frames. The Applied Element Method, was chosen for the numerical analyses. Numerical models, calibrated on experimental data of both retrofitted and non-retrofitted walls, were validated through the simulation of a shake-table test of a full-scale retrofitted specimen. A parametric study was then conducted to investigate the influence of different retrofit layouts on the building's global seismic response.

Keywords: timber retrofit, Applied Element Method, cavity-wall systems, shake-table test

5.1 Introduction

The Groningen area has recently been subjected to induced seismicity phenomena due to natural gas extraction (van Elk et al., 2019). Within the framework of a wide test campaign endeavour aimed at experimentally characterising the seismic response and resistance of URM buildings in the region (Graziotti et al., 2019), a light yet effective timber retrofit system specifically conceived for terraced houses, a residential building typology that constitutes an important portion of the existing URM building stock in that area, was devised and tested (Damiani et al., 2019). These low-rise structures, often coming in the form of multiple contiguous units (see Figure 5.1, where one of the end units – usually taken as a reference for the design of full-scale building specimens, as discussed in the following – is highlighted), typically feature rigid reinforced concrete (RC) floor diaphragms and timber roof, large openings at the ground floor and cavity-walls, as discussed in e.g. Graziotti et al.(2017). The latter usually consists of an assembly of a loadbearing inner unreinforced masonry calcium-silicate (CS) brick panels plus an external clay (CL) brick building envelope aimed at providing protection against atmospheric agents and thermal insulation in addition to the characteristic aesthetic appearance. These two masonry leaves are typically weakly coupled by metal connectors (or tie elements).

The seismic vulnerability of this structural configuration makes the development of appropriate retrofitting measures of relevance. To this end, two shake-table tests on two identical two-storey full-scale URM building prototypes with analogous geometrical and mechanical characteristics, reproducing the end unit of typical Dutch URM terraced houses and named EUC-BUILD6 and EUC-BUILD7, respectively, were carried out by Miglietta et al. (2021) at the Eucentre laboratory (Pavia, Italy). The main difference between the two specimens is that EUC-BUILD7 was retrofitted using the light timber strengthening solution mentioned above to assess and quantify potential benefits experimentally in terms of seismic performance. The retrofit system consisted of vertical timber laths (or *strong-backs*), horizontal nogging elements and oriented strand board (OSB) panels connected to the loadbearing CS walls through steel connectors. The complete kit was applied to the walls parallel to the shaking direction (i.e. longitudinal walls of the terraced house), whereas timber strong-backs alone were used for the transverse walls, mainly loaded out of their plane. Strengthening and stiffening of the 2nd timber floor diaphragm were also introduced by means of nailed OSB panels. In addition, the spacing of the steel ties connections between CS inner and CL outer leaves was reduced from 1 tie/m^2 (EUC-BUILD6) to 5 ties/m^2 (EUC-BUILD7).

Figure 5.1 a) Front view of a typical Dutch URM terraced house and highlighted end unit and b) overview of the specimen after the construction (adapted from Damiani et al. (2019))

The implementation of the abovementioned retrofit system, consistently with the outcomes of recent investigations conducted by other researchers using similar solutions (Cassol et al., 2021; Dizhur et al., 2017; Giarretton et al., 2016; Giongo et al., 2017; Riccadonna et al., 2019; Smiroldo et al., 2020; Valluzzi et al., 2013), resulted in a noticeable increase in terms of both ultimate displacement and overall base shear capacities as reported in Miglietta et al. (2021). Notwithstanding the significance of the results obtained, however, they inevitably only refer to the specific layout of the timber retrofit system tested, i.e. with a priori-defined timber lath spacing, arrangement and cross-section. In this connection, therefore, the optimisation process of the retrofit design might benefit from reliable and validated numerical models capable of extending experimental outcomes and further enhancing its effectiveness.

Despite the fact that the use of simplified methods, including e.g. those based on Equivalent Frame (EFM) idealisations (e.g. Lagomarsino et al., 2013; Magenes and Della Fontana,

1998; Raka et al., 2015; Vanin et al., 2020) is endorsed by many international codes and often preferred by both practitioners and researchers to simulate the in-plane (IP)-governed seismic response of URM buildings, the application of this modelling approach to retrofitted cavity-wall systems may be challenging (even if recently the use of the EFM was successfully extended to the problem of modelling cavity-wall systems by Kallioras et al. (2019).

Similarly, as extensively discussed by Grunwald et al. (2018), the application of most of the traditional continuum-based advanced numerical approaches (e.g. the Finite Element Method, FEM) to the simulation of complex structures might lead to inadequate results, especially when heavy-damage is predicted (i.e. when the retrofit system is supposed to play a more significant role) and when considering responses where contact/recontact (as in the case of retrofit to masonry interaction) and collision phenomena (e.g. among collapsed bricks and other structural members) would take place. Nonetheless, satisfactory results have been obtained using FEM micro (Abdulla et al., 2017; Petracca et al., 2017) and meso-scale (Aref and Dolatshahi 2013; Giambanco et al. 2018) modelling strategies for the analysis of pre-collapse damage states, including those of retrofitted URM structures (e.g. Carozzi et al., 2014; El-Diasity et al., 2015; Lucchini et al., 2017; Luccioni and Rougier, 2011), as comprehensively discussed in D'Altri et al. (2019).

On the other hand, several applications (de Felice, 2011; DeJong andVibert, 2012; Galvez et al., 2018; Godio and Beyer, 2019; Masi et al., 2020; Portioli, 2020; Pulatsu et al., 2016; Tondelli et al., 2016) have shown that e.g. Distinct Element (DEM) and Rigid Body and Spring models (RBSM) (see Lemos, 2007), being able to account explicitly for the discrete nature of masonry, are capable of duly representing the mutual interaction among various bodies, as well as separation, impact and frictional phenomena. However, although some hybrid modelling strategies have been recently proposed (e.g. Chàcara et al., 2018; Malomo and DeJong, 2021), obtaining results in a reasonable timeframe is still an open challenge. A similar but more computationally efficient numerical technique is the Applied Element Method (AEM), a rigid body and spring model initially conceived by Meguro and Tagel-Din (2000) for simulating controlled demolition and collapse of steel and reinforced concrete (RC) structures (e.g. Calvi et al.,2019; Salem et al., 2016). As the most of the RBSM, the AEM is based on the mechanical interaction among rigid blocks connected by nonlinear spring layers. However, unlike RBSM (see Furukawa et al., 2012), the recontact between neighbouring elements initially not in contact is allowed. This is an essential feature for collapse analysis, which enabled various researchers to develop AEM-based models capable of satisfactorily reproducing the response of large-scale systems up to complete failure (e.g. Domaneschi et al.,2019; Karbassi and Nollet, 2013; Malomo et al., 2021), as well as for the simulation of the response of URM buildings retrofitted with timber systems– something that, as far as the authors are aware of – has not been previously done.

In this work, building on the unique AEM features and with the aim to contribute towards the optimisation and enhancement of the presently-available retrofitting solutions for URM cavity-wall systems, a parametric study on the influence of different retrofit schemes is

conducted. To this end, taking advantage of previous successful modelling exercises on similar structures (Malomo et al., 2020), including EUC-BUILD6 (Malomo et al., 2021), the geometrical and mechanical characteristics of EUC-BUILD7 were taken as a reference, and its experimental shake-table response, as well as the IP quasi-static behaviour of both standard and retrofitted isolated URM wall components tested in the same experimental campaign (Guerrini et al., 2020) - i.e. EUC-COMP1 – non-retrofitted, and EUC-COMP2 – retrofitted - employed for validation purposes.

5.2 Simplified micro-modelling of retrofitted URM cavity-wall structures

In this section, a brief description of the reference building specimen (i.e. EUC-BUILD7) is provided, along with the micro-modelling strategy employed to reproduce its shake-table response numerically.

EUC-BUILD7 was characterised by a footprint area of 5.94 m x 5.58 m, with the longer dimension along the shaking direction and a total height of 7.83 m. The North (transverse), East and West (longitudinal) walls were made of an inner loadbearing CS brick leaf connected to an outer CL brick veneer through metal ties (5 ties/m^2, i.e. +500% with respect to EUC-BUILD6) and separated by an air gap. The South façade, instead, consisted of a single CS leaf alone, representing an internal wall separating two consecutive units. The 1st floor diaphragm was an RC slab, whereas the 2nd one was a timber floor retrofitted with 18 mm thick OSB panels nailed to the planks. The retrofit solution applied to the inner longitudinal CS walls (subjected to IP actions according to the orientation of the specimen on the unidirectional shake-table) consisted of a frame made by the assembly of strong-backs (i.e. vertical elements) and horizontal nogging- elements with dimensions 80 mm x 60 mm and connected to each other by steel angles. The wood employed for beams was red solid fir and it belonged to the category S10/C24 according EN 14081-1 (CEN, 2016), while the OSB boards belonged to the category OSB/3, according to EN 310 (CEN, 2006). OSB panels were nailed to timber frames, as shown in Figure 5.2. The transverse OOP-loaded CS walls were instead retrofitted with strong-backs only. Both the retrofit systems were connected to the CS walls through steel angles anchored to the masonry with an epoxy adhesive. Interested readers may refer to Damiani et al. (2019) and Miglietta et al. (2021) for further details on building construction and retrofit solution.

An AEM-based simplified micro-model was employed to represent numerically such a complex structural system. In the AEM framework, masonry segments are idealised as an assembly of rigid units connected by nonlinear springs in which material properties of the brick-mortar interface are lumped. Using this approach, the actual masonry texture of CS/CL cavity-wall members (which usually feature a standard running bond pattern) can be explicitly reproduced. Interested readers may refer to section 4.2 for further details on the employed mechanical parameters.
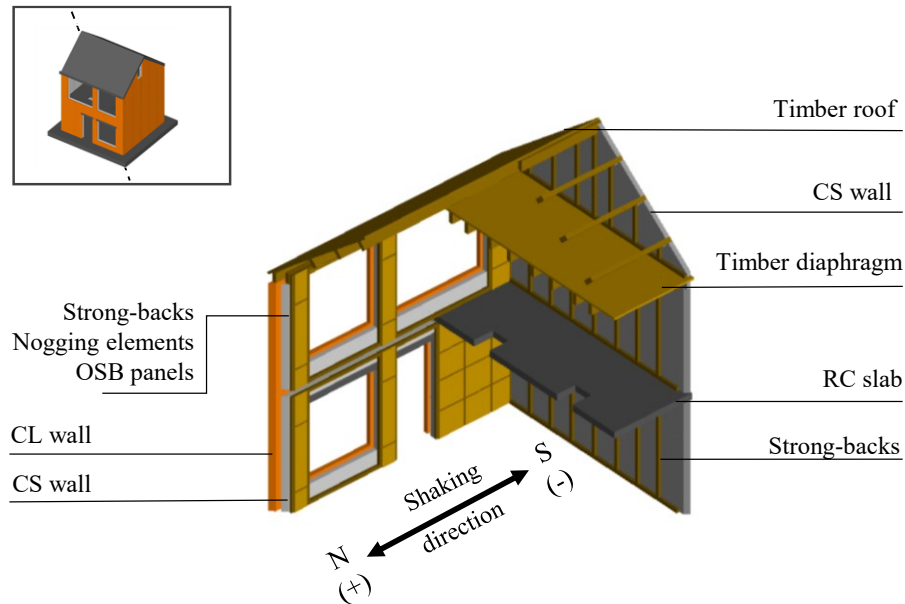
Figure 5.2 3D view of the retrofitted building specimen EUC-BUILD7

During the analysis, no external damping was introduced. Thus, the only source of damping in the proposed numerical models is the energy dissipation due to differences in loading and unloading stiffness of compression springs, and that induced by the process of crack closure/opening. Many applications (e.g. Calvi et al., 2019; Papantonopoulos et al., 2002) have shown that this approach usually provides adequate results when considering the collapse modelling of both reduced and large-scale systems.

The adopted modelling strategy for masonry and diaphragms was based on a previous work (Malomo et al., 2021), where the modelling of shake-table response EUC-BUILD6 was carried out, obtaining fairly accurate results, with the aim of accounting for the influence of the actual construction technique on the dynamic behaviour of EUC-BUILD7:

- Since the mortar layer beneath the 1st floor RC slab was filled only after the attainment of gravity load experimentally, the frictional resistance provided by these mortar layers was likely to be limited due to lack of vertical compression; similarly, their compressive strength might have been also likely affected by shrinkage phenomena. Thus, reduced compressive strength and stiffness have been allotted to the corresponding interface springs.
- The 1st floor RC slab was idealised as a rigid diaphragm, while 2nd timber floor and roof were modelled as bilinear membranes, whose material properties (i.e. stiffness, G, and yielding stress, f_y) were calibrated through the simulation of experimental tests on both strengthened and unstrengthened typical Dutch timber diaphragms (Ravenshorst and Mirra,2018), also accounting for the strengthening and stiffening of the 2nd floor diaphragm provided by nailed OSB panels.
- The tie-connectors (i.e. 3mm-diameter and 200mm-long steel bars) between CS and CL walls and the L-shaped anchors (which prevent the early OOP failure of the roof-

gable system) were idealised as bilinear beam elements (with pull-out strength equal to the experimentally inferred one, i.e. 2.3kN, as reported in Messali et al. (2016) placed according to their actual position in the real specimen.

As per the retrofit, both IP and OOP systems were explicitly modelled (see Figure 5.3) as discussed in the following, where details on the proposed numerical idealisations are given:

- Both strength and stiffness of the interface between outer and inner leaf spreader beams and 2nd floor were increased to introduce the improved connection made through a couple of screws, fixing the strengthened timber diaphragm to these elements.
- The retrofit system IP deformability was lumped into two main elements: strong-back-nogging element assembly and tie-down connections.
- Strong-backs and nogging elements were modelled as beam elements with cross-section comparable to their experimental counterparts and characterised by a bilinear model. The deformability of the strong-back and nogging elements assembly is provided by the introduction of equivalent yield stress f_{yw} =10 MPa, see Figure 5.3, which has been iteratively calibrated during the modelling of the IP response of EUC-COMP2 (i.e. the isolated retrofitted wall component modelled for validation purposes in the next section, together with its non-retrofitted counterpart, EUC-COMP1).
  - Strong-backs and nogging elements were rigidly connected to each other through underline interface 1. This assumption was based on the fact that only negligible damage was experimentally observed in the connection, which consisted of steel angles fastened to the timber elements.
  - Strong-backs and nogging elements were rigidly connected to small cuboids, fixed to the CS walls through interface 2. This enabled to simulate local damage propagation due to retrofit-wall interaction without modelling explicitly failures of the connections and interpenetration phenomena.
  - Tie-down connectors (i.e. metal L-shaped anchors connecting strong-backs to bottom/top timber beams) were represented by rigid elements fixed to the strong-backs (interface 5). Their deformability was lumped into spring interface 6, characterised by an elasto-plastic behaviour and by an equivalent Young modulus, iteratively calibrated through the modelling of EUC-COMP2.
  - The strong-backs were connected with the top/bottom timber beams through spring interface 4, which had zero tensile strength/cohesion to simulate dry contact.
  - The whole timber frame was connected to both foundation and/or timber roof through interface 7, which simulated a perfectly fixed connection.
  - OSB panels were modelled as bi-linear elastic equivalent membranes and connected through the linear spring interface 3 to strong-backs and nogging elements. The nailed connection between the timber frame and the OSB panels was represented through the equivalent cohesion and tensile strength of interface 3, evaluated according to the characteristic shear (2.5 kN) and pull-out (1 kN) strength.
  - For OOP retrofit, analogous assumptions were made; in the EUC-BUILD7 model, as in the actual test, no nogging elements were present in the transversal direction.
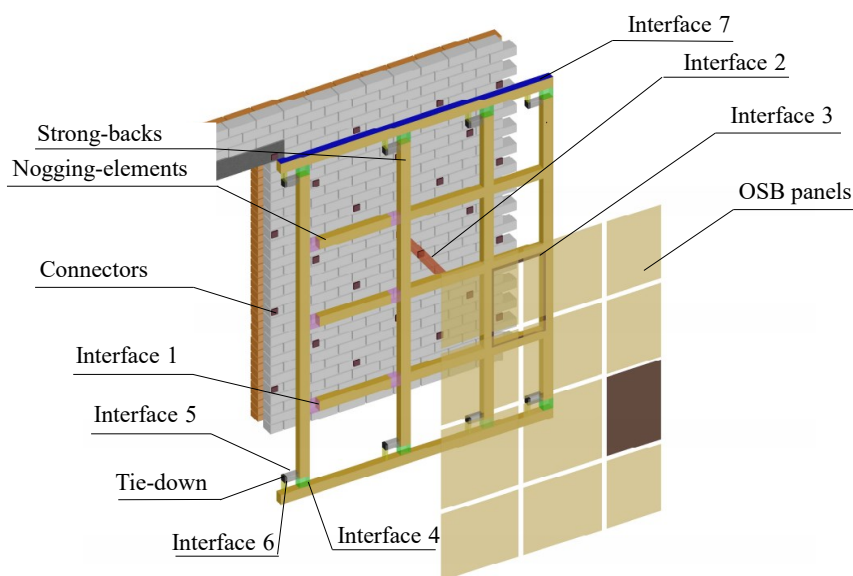
Figure 5.3 Construction details of retrofit solution and numerical idealisations

5.3 Calibration against a quasi-static in-plane test on URM wall components

In this section, the proposed AEM-based modelling strategy is preliminarily validated against experimental results from quasi-static IP cyclic tests on isolated CS wall components. The first specimen, EUC-COMP1, was deemed to be representative of the squat pier on the East side at the ground level of the EUC-BUILD6 building prototype, while the second specimen, EUC-COMP2, featured the same geometrical characteristics, but it was retrofitted using the same techniques employed for EUC-BUILD7 (Guerrini et al., 2020). Both walls were tested under double-fixed boundary conditions, constant vertical load (0.5 MPa) and the same horizontal displacement history (i.e. a total of 13 and 18 cycles – each of which including three sub-cycles – with increasing displacement magnitude up to 13.5 mm and 53.9 mm, for the URM and the retrofitted URM specimens, respectively), duly reproduced numerically. The experimental vs numerical results of the test performed on EUC-COMP1 are summarised in Figure 5.4.

Despite some noticeable differences with respect to the actual dissipated energy, Figure 5.4 (c), in the last cycles (which might be related to the fact that failure within brick was neglected – as gathered in Figure 5.4 b), the numerical model captured with reasonable accuracy the measured behaviour in terms of initial lateral stiffness (101 kN/mm vs 124 kN/mm), peak (78 kN vs 74 kN) and residual capacity (65 kN vs 59 kN), as depicted in Figure 5.4a. In the numerical model, each brick was discretised with a single element, neglecting internal brick failure. Although this simplified modelling strategy allowed to reduce the computational cost, it caused the main differences between the numerical and experimental damage patterns as the specimen EUC-COMP1 suffered some cracks passing through units in the first five brick courses due to the toe-crushing. Both the model and the specimen presented step-wise cracks due to the hybrid flexural-shear mechanism, whereas the horizontal crack at the top of the wall was more evident in the experimental test.

(a)   (b)

Experimental   Numerical

(c)
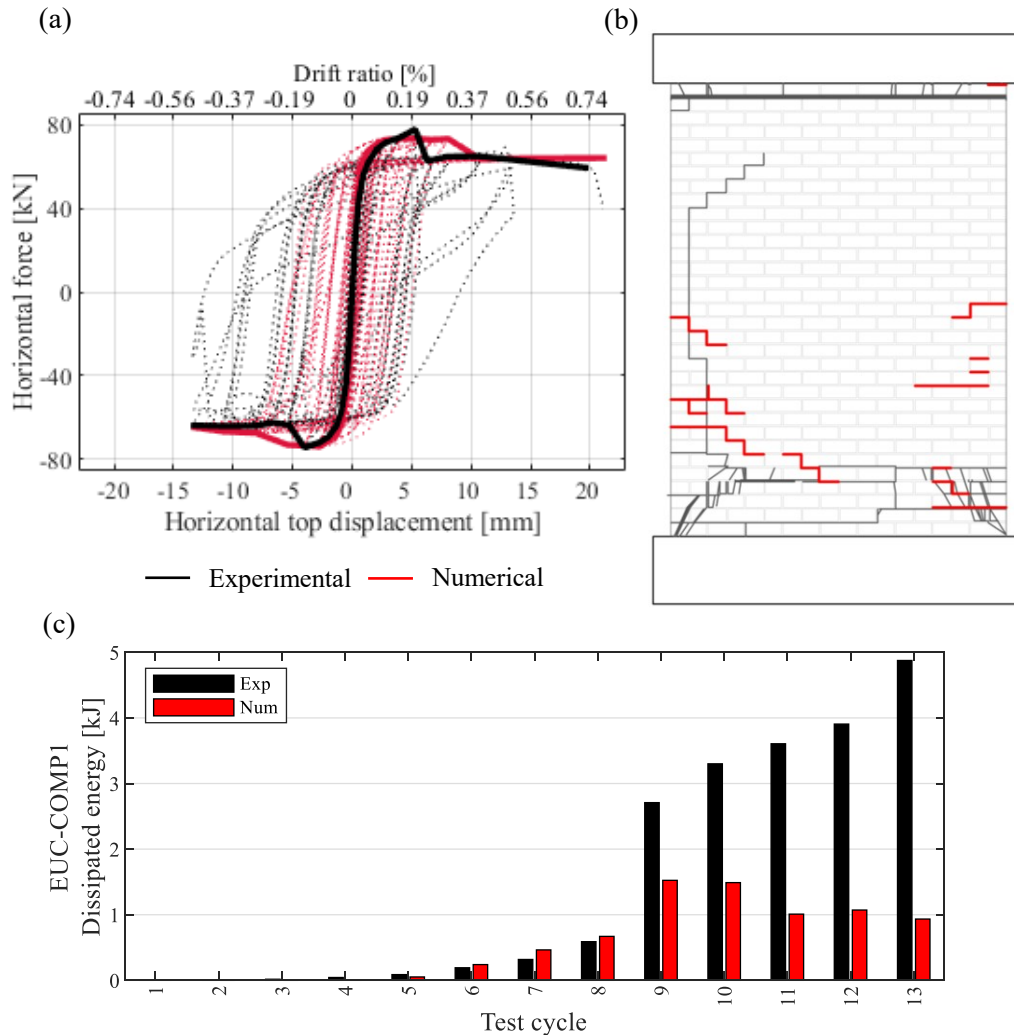
Figure 5.4 EUC-COMP1: experimental vs numerical a) hysteretic response (dotted lines) and backbone curves (continuous thick lines), b) damage pattern and c) dissipated energy

Similar results were also obtained for EUC-COMP2, where the timber retrofit was applied. Comparisons between experimental and numerical outcomes are shown in Figure 5.5. As it can be gathered from the experimental damage pattern (Figure 5.5b), masonry failed in flexure, whereas the timber retrofit presented only damage at the steel angles of tie-down connections, which buckled in compression after 0.6% of drift ratio. Both EUC-COMP1 and EUC-COMP2 presented a drop of strength at 0.2% of drift ratio after the extensive cracking of masonry.

Owing to the contribution of the retrofit system, EUC-COMP2 did not exhibit the above loss of strength, reaching higher displacement with respect to the non-retrofitted specimen. In the experimental test, the retrofitted wall reached its maximum shear strength of 105 kN at 0.8% of drift ratio, with a progressive degradation after this point and with a drop of

strength in the last set of cycles (up to 88 kN) due to the diagonal shear cracking of masonry, as depicted in Figure 5.5a. The AEM model adequately reproduced these aspects predicting peak and residual base shear of 109 kN and 100 kN, respectively. However, it was not capable of simulating the diagonal cracks developed in the wall in the very last cycles due to the shear deformations Figure 5.5b. Nevertheless, a remarkably good agreement has also been found here in terms of dissipated energy Figure 5.5c and reference to progressive stiffness and horizontal force degradation, Figure 5.5a. The comparison between numerical and experimental backbone curves parameters in the positive loading direction is presented in Table 5.1, indicating whether the model is under (red color)-or over (light blue color)-estimating the actual response. Where $K_{30\%}$ is the initial lateral stiffness evaluated in the first cycles, between the 15 and the 30% of the peak base shear, V_{max}, and V_{res} is the residual base shear.

(a)   (b)

(c)
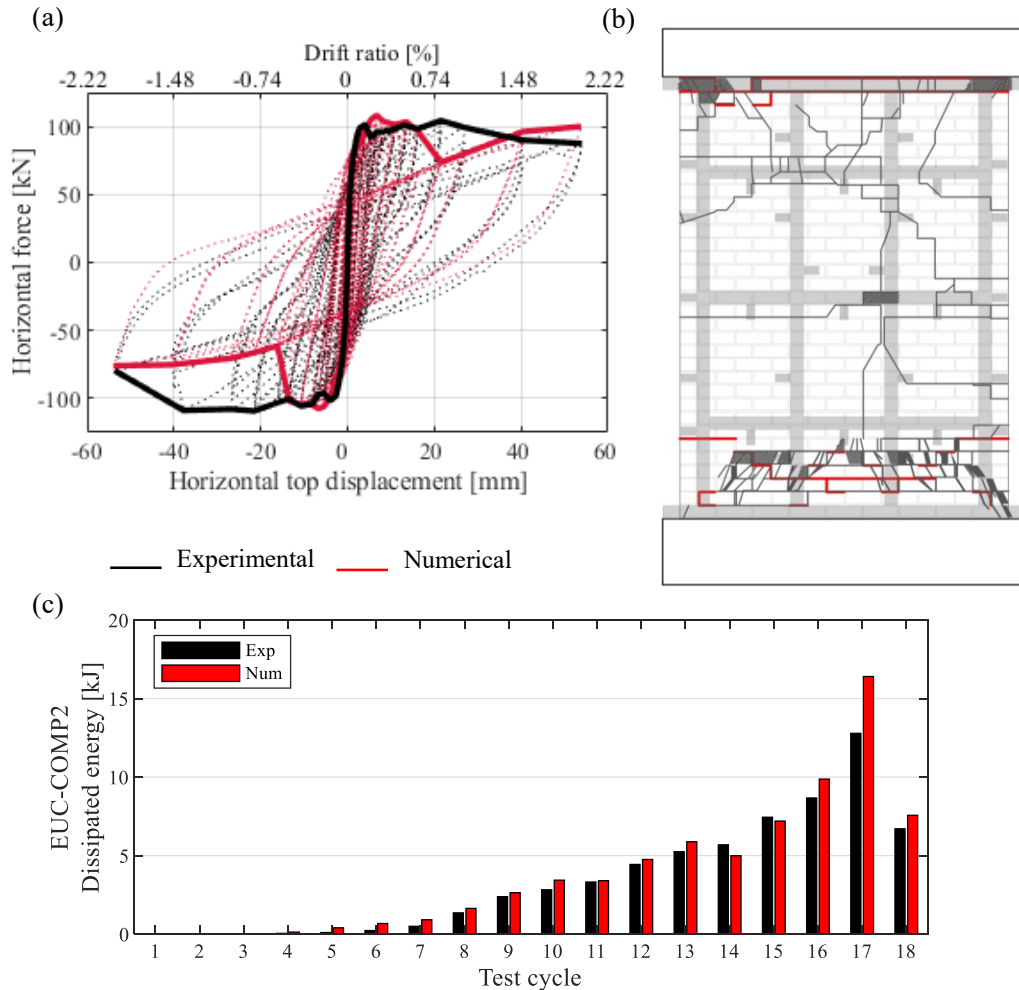
Figure 5.5 EUC-COMP2: experimental vs numerical a) hysteretic response (dotted lines) and backbone curves (continuous thick lines), b) damage pattern and c) dissipated energy

The experimentally measured and inferred material properties that were used in the AEM models are reported in Table 4.2. The material properties related to the retrofit are reported in Table 5.2, for timber elements $E_{0,mean}$ is the mean Young's modulus parallel to fibres, G_{mean} is average shear modulus, $f_{ms'}$ flexural resistance, $f_{t,0}$ tensile strength parallel to fibres, while E_w, G_w, f_{yw} the corresponding numerical value for Young's modulus, shear modulus and yield stress; for the OSB panels instead, E_0 Young's modulus parallel to fibres, E_{90} Young's modulus perpendicular to fibres, f_{90} flexural resistance perpendicular to fibres, f_0 flexural resistance parallel to fibres and E_{OSB}, G_{OSB}, f_{yOSB} the corresponding Young's modulus, shear modulus and yield stress, respectively.

Table 5.1 Comparison between experimental and numerical backbone curves parameters, positive loading direction

		$K_{30\%}^+$	V_{max}^+	V_{res}^+
	exp	101	78	59
EUC-COMP1	num	124	74	64
	ratio	0.81	1.06	0.92
	exp	114	105	88
EUC-COMP2	num	140	109	100
	ratio	0.81	0.96	0.88

Table 5.2 Experimental and inferred material properties

Timber	$E_{0,mean}$ [MPa]	G_{mean} [MPa]	$f_{ms'}$ [MPa]	$f_{t,0}$ [MPa]	E_w [MPa]	G_w [MPa]	f_{yw} [MPa]
	11000	690	24	14	6000	690	10
OSB	E_0 [MPa]	E_{90} [MPa]	f_{90} [MPa]	f_0 [MPa]	E_{OSB} [MPa]	G_{OSB} [MPa]	f_{yOSB} [MPa]
	3500	1400	10	20	1200	500	9

5.4 Simulation of the shake-table response of the retrofitted building specimen

The retrofitted building specimen was tested under a series of shake-table motions of increasing intensity, scaling the same acceleration time-history at eleven different levels of amplitude up to the attainment of near-collapse conditions (i.e. when the test was stopped), as depicted in Figure 5.6. The acceleration time-histories applied to the numerical model corresponded to the signals recorded at the base of the specimen during the shake-table test.

A soft storey mechanism governed the response of the specimen at the ground floor, characterised by the presence of large asymmetrical openings. As a consequence, the damage was mainly concentrated at the ground floor, whereas the first floor exhibited only minor damage due to the lower displacement demand. Damage at the ground level was widespread, with cracks propagated in longitudinal and transverse walls due to the IP shear response associated with the torsional effect caused by the significant difference in lateral stiffness between East and West façades. The slender piers of façades parallel to the shaking direction generally exhibited flexural/rocking behaviour with cracks propagated from the ends to the whole structural members due to the effect of the retrofit system. The

corner piers (especially the East-side one) were severely damaged due to the IP/OOP interaction and to the flange effect among perpendicular walls (as depicted in Figure 5.7). As per the gables, minor to moderate damage was detected between roof joists (South-side) and among the strong-backs (North-side).Transverse CS walls suffered significant IP shear damage at the ground floor, with diagonal cracks extending from edge to edge due to the global torsional response of the building. The first floor transverse walls suffered minor damage with a few horizontal cracks in the North wall and minor damage at the top East corner in the South wall. In the longitudinal CL façades, spandrels suffered relevant damage, particularly on the North-side, while the slender and squat ground-floor piers mainly exhibited rocking responses, characterised by localised damage at their extremities. Diffuse cracks were developed in the transversal direction, especially at the ground floor, and then propagated to the upper level. No relevant damage was detected in the timber retrofit at the end of the test. Further details on the experimental campaign can be found in Miglietta et al. (2021).

Test	PTA [g]
EQ@20%	0.06
EQ@33%	0.1
EQ@50%	0.17
EQ@66%	0.19
EQ@85%	0.25
EQ@100%	0.3
EQ@133%	0.41
EQ@133%-R	0.43
EQ@166%-R	0.51
EQ@200%-R	0.66
EQ@266%-R	0.78
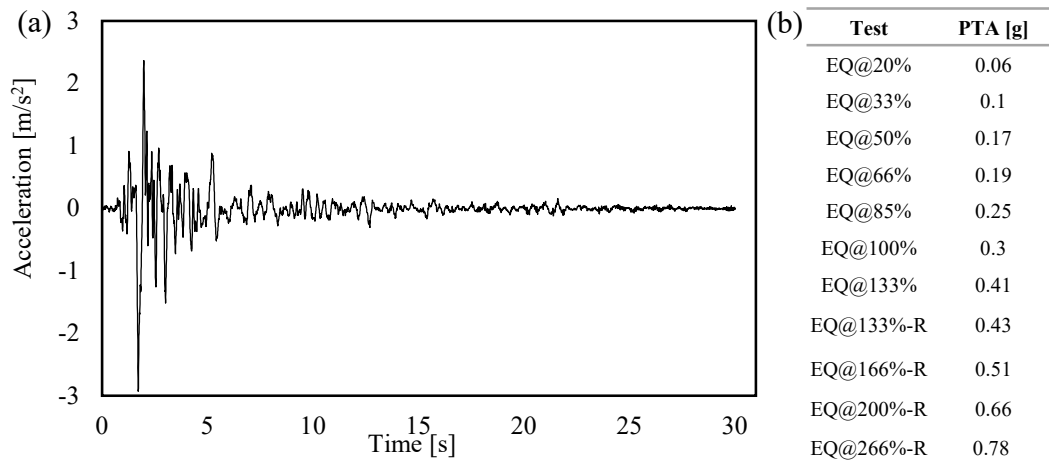
Figure 5.6 EQ@100% Horizontal seismic input a) and testing sequence b) of EUC-BUILD7. During the test, after EQ@133%, the retrofit system of the roof was activated, tightening the four steel rods connecting the ridge beam to the internal steel frame, as discussed in Miglietta et al. (2021)

In Figure 5.7, the damage obtained in the numerical model is superimposed to the actual one. For the CS walls, the model was capable of reproducing the overall final damage distribution, with most of the simulated cracks located at the ground floor. Although the observed OOP damage was slightly underestimated numerically, the one on the West and East side, and most noticeably that of the corner pier at the East-side, was effectively reproduced. Regarding CL walls, the numerical model predicted the partial collapse of CL West façade due to the sudden failure of the interface among the roof and the central slender pier located at the first floor, which did not occur experimentally. This last aspect might be related to the uncertainty on the experimentally-inferred tensile bond strength, whose value ranged from 0.04 and 0.33 MPa (i.e. C.o.V. 0.59), and to the fact that in the AEM model, an average value of 0.14 MPa was implemented.
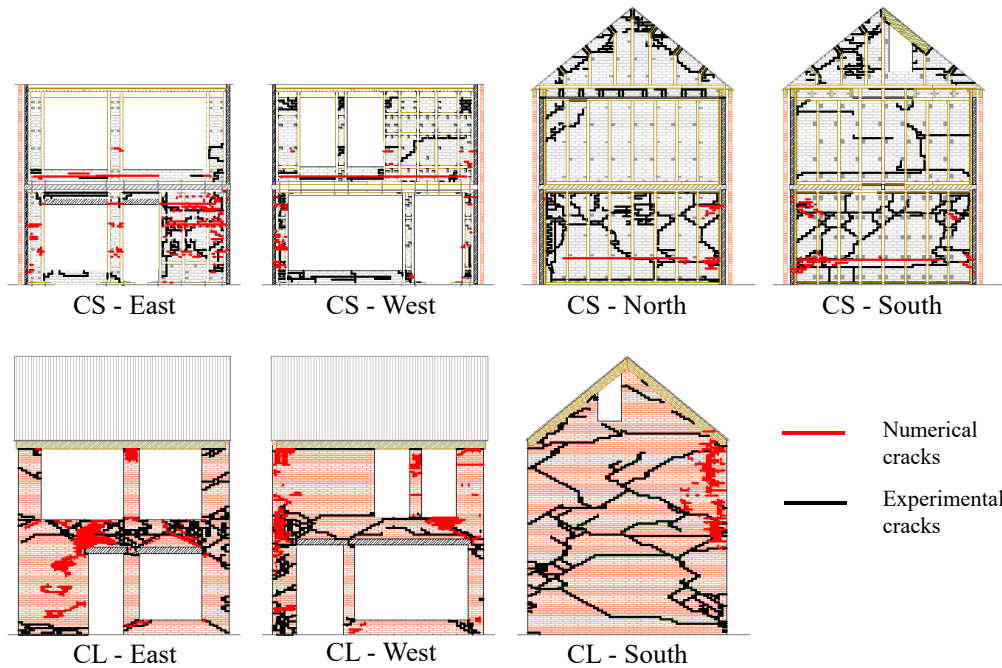
Figure 5.7 Comparison of experimental (black) and numerical (red) crack pattern in the CS inner leaf and CL outer leaf at the end of the testing sequence

Numerical and experimental outcomes can be compared in terms of base shear-displacement (Figure 5.8a) and PGA-interstorey drift (Figure 5.8b) of both 1st and 2nd floors through the simulated force-displacement hysteresis, which are referred to the whole testing sequence. Overall base shear was well predicted with minor differences in the central runs (i.e. from EQ@133% -0.41g- to EQ@166%-R -0.51g-) with an average absolute error of approximately 15%, as it can be gathered from Figure 5.8c, whereas its cyclic degradation and associated dissipated energy was satisfactorily reproduced. Compared in Figure 5.8c for each cycle, the BSc is computed by normalising the total base shear with respect to the total mass of the building.

Similarly, simulated displacements at 1st and 2nd floors appear comparable for each test phase, as shown in Figure 5.8a. In Figure 5.8c, experimental versus numerical base shear coefficients (BSc) are compared, whereas Figure 5.8d shows the comparison in terms of interstorey drift. From these figures, it can be gathered that the model significantly underestimated the timber roof displacement, particularly from run EQ@66% -0.19g- to run EQ@133%-R -0.43g-, before returning to acceptable values at the end of the test after the tightening of the steel cables connecting the ridge beam to the second-floor joists. A possible explanation might lie in the simplified modelling of the roof, numerically idealised as an equivalent nonlinear membrane, where the effect of cumulative plastic damage, as well as that of the joist-to-wall interaction, was neglected. The interstorey drifts are computed as the relative displacement of the considered floor/roof diaphragm divided by the storey/roof height underneath.
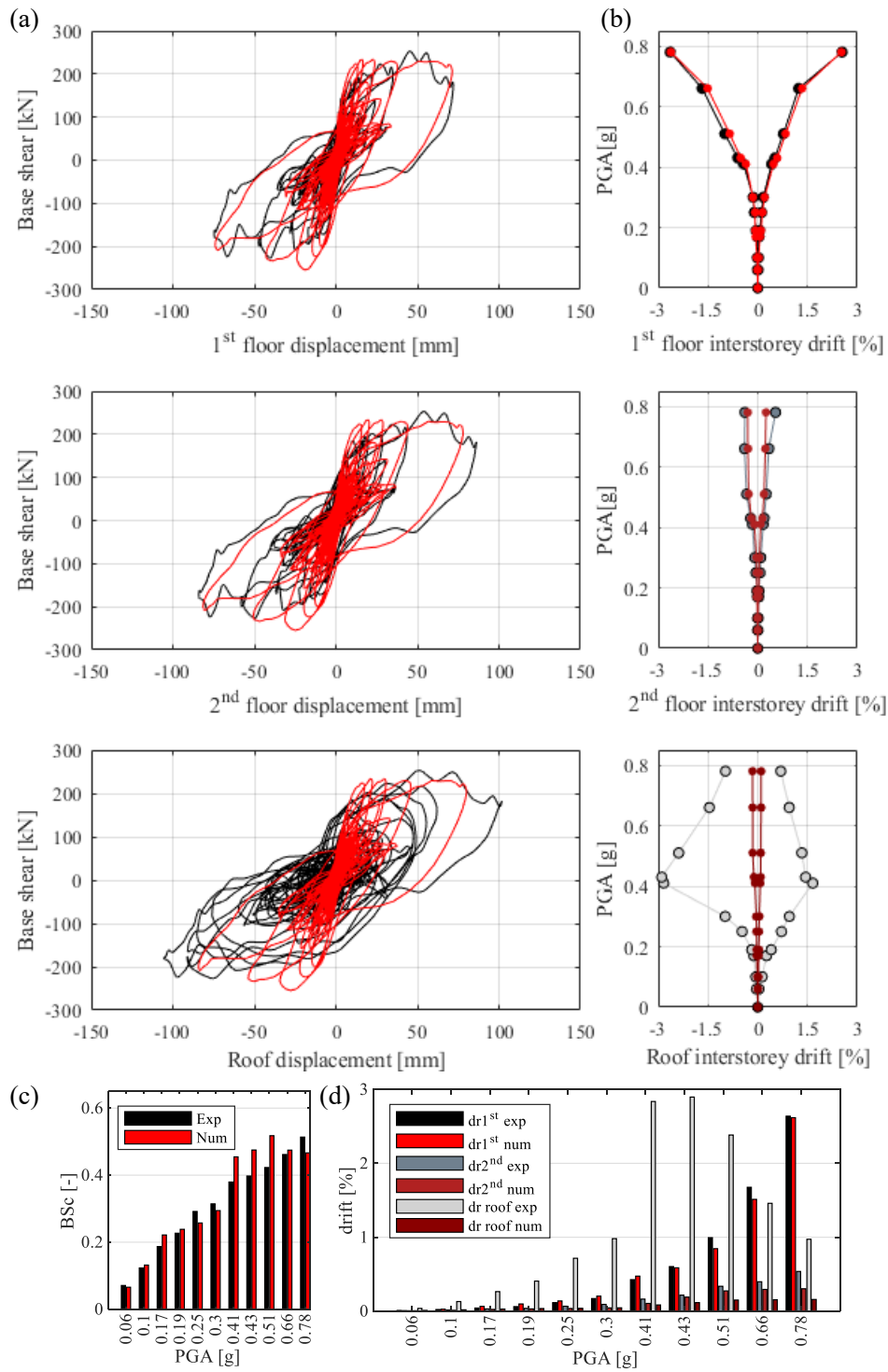
Figure 5.8 Experimental vs Numerical comparison in terms of: a) global hysteretic curves, b) interstorey drift at 1st and 2nd floor and roof, c) BSc and d) 1st, 2nd and roof interstorey drift.

In Figure 5.9, the comparison between numerical and experimental hysteretic behaviour during tests EQ@100%, EQ@133-R and EQ@266-R is also presented. The hysteretic behaviour and progressive stiffness degradation were reproduced with fairly good approximation.
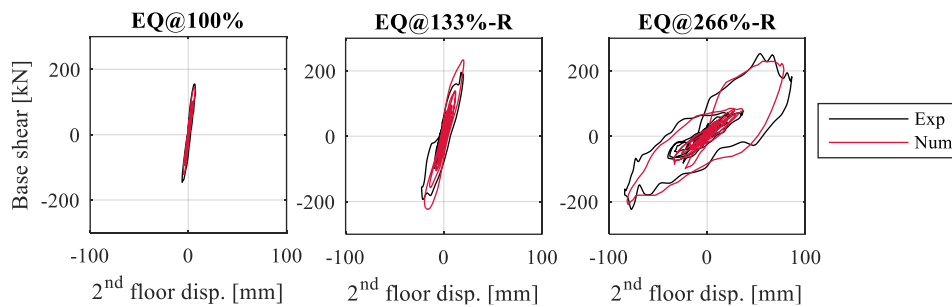
Figure 5.9 Comparison between numerical and experimental hysteretic curves (2nd floor displacement) of tests EQ@100%, EQ133%-R and EQ@266%-R

A reasonable approximation of the undamaged state period was obtained with the numerical model that predicted a first mode period of 0.178 s, whereas the period associated with the first mode was 0.17 s in the experimental test. As already noted by Miglietta et al. (2021), the introduction of the timber retrofitting system did not significantly affect the global mass and stiffness. As a consequence, the period associated with the first mode in the unreinforced building (i.e. EUC-BUILD6, see Malomo et al. 2021) and in the retrofitted version (i.e. EUC-BUILD7) were the same. Similarly, the same value was found for the different retrofit configurations presented in section 5.5.

5.5 Parametric study on the impact of different retrofit layouts

Given the encouraging results obtained when comparing the experimental results of EUC-BUILD7 with the ones obtained with the AEM model presented in the previous section, a new set of models, devised starting from the former (hereinafter referred to as baseline model, or simply BAS) and implementing different retrofit layouts, was created with the aim of extending the experimental findings, and numerically explore a potential enhancement of the retrofit solution tested in EUC-BUILD7. More specifically, four main configurations were selected and tested numerically under the same loading protocol considered during the actual shake-table test. The four configurations differ in terms of timber elements spacing (vertical and horizontal) and size used for the IP retrofit alone (Figure 5.10), whilst the OOP retrofit configuration was left unchanged. This decision is supported by the fact that the response of EUC-BUILD7 (as well as those of all the other Dutch two-storey cavity-wall building prototypes tested, see e.g. Graziotti et al. (2017)) was mainly governed by IP response, as also confirmed by the larger extent of damage in the longitudinal façades.
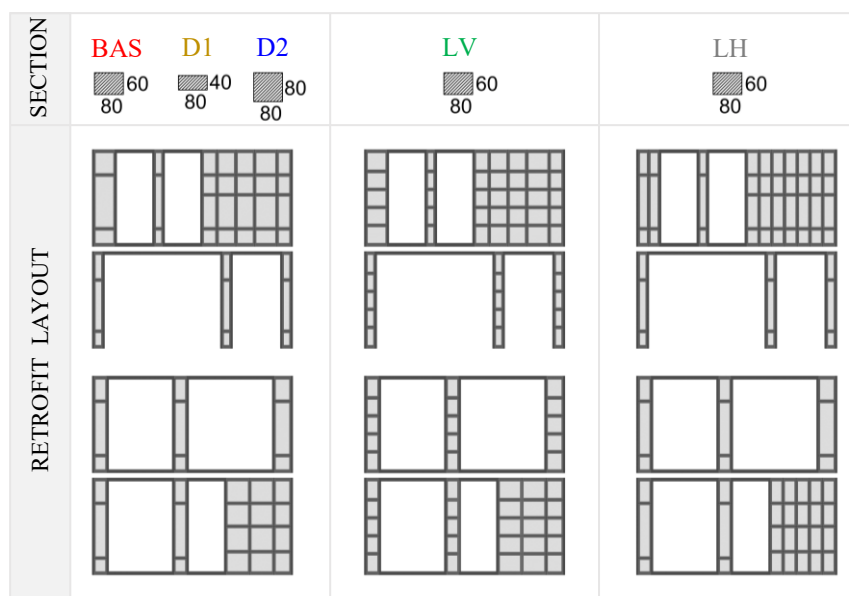
Figure 5.10 BAS, D1, D2, LH, LV configurations and strong-back size (BAS, D1 and D2 only differ for the strong-back cross-section)

Configurations LH and LV were obtained decreasing horizontal and vertical spacing of the timber frame. In both LH and LV configurations, the cross-section of the strong-back/nogging element is equal to that of BAS (i.e. 80x60mm). Configurations D1 and D2 were obtained decreasing and increasing the timber frame elements cross-section, respectively, acting on the dimension perpendicular to masonry wall (i.e. from 80x60mm to 80x40mm for D1 and 80x80mm for D2). As the contribution of the panels mainly depends on the OSB-frame connection (AWC, 2008) in all the cases, the thickness of the OSB panels remained constant and equal to that of the BAS model, i.e. 18mm. Due to the lack of characterisation tests on nails, the panel-frame interface properties of BAS model were refined through the comparison with the experimental test on EC-COMP2. For this reason, in the absence of any other experimental reference, the authors decided to keep constant that connection in the parametric study without introducing any variation on the nails dimension or spacing.

In Figure 5.11, a first comparison in terms of 1st floor displacement hysteretic response and 1st and 2nd floor interstorey drift is presented. As shown in Figure 5.11a,c, configurations LH, LV and D2, where horizontal (LH) or vertical (LV) frame spacing was reduced, or the frame section was increased (D2), would lead to a stiffer response with respect to BAS, with higher BSc values, lower displacements (as well as lower associated drift ratios, see Figure 5.11b,d computed as the relative displacement of the considered floor/roof diaphragm divided by the storey/roof height underneath), and thus minor damage, particularly at the ground level. On the contrary, in D1 the strong-back size reduction led to a more deformable response, with a significant increase in maximum displacement and damage at ground level up to the partial collapse of both inner and outer longitudinal facades.
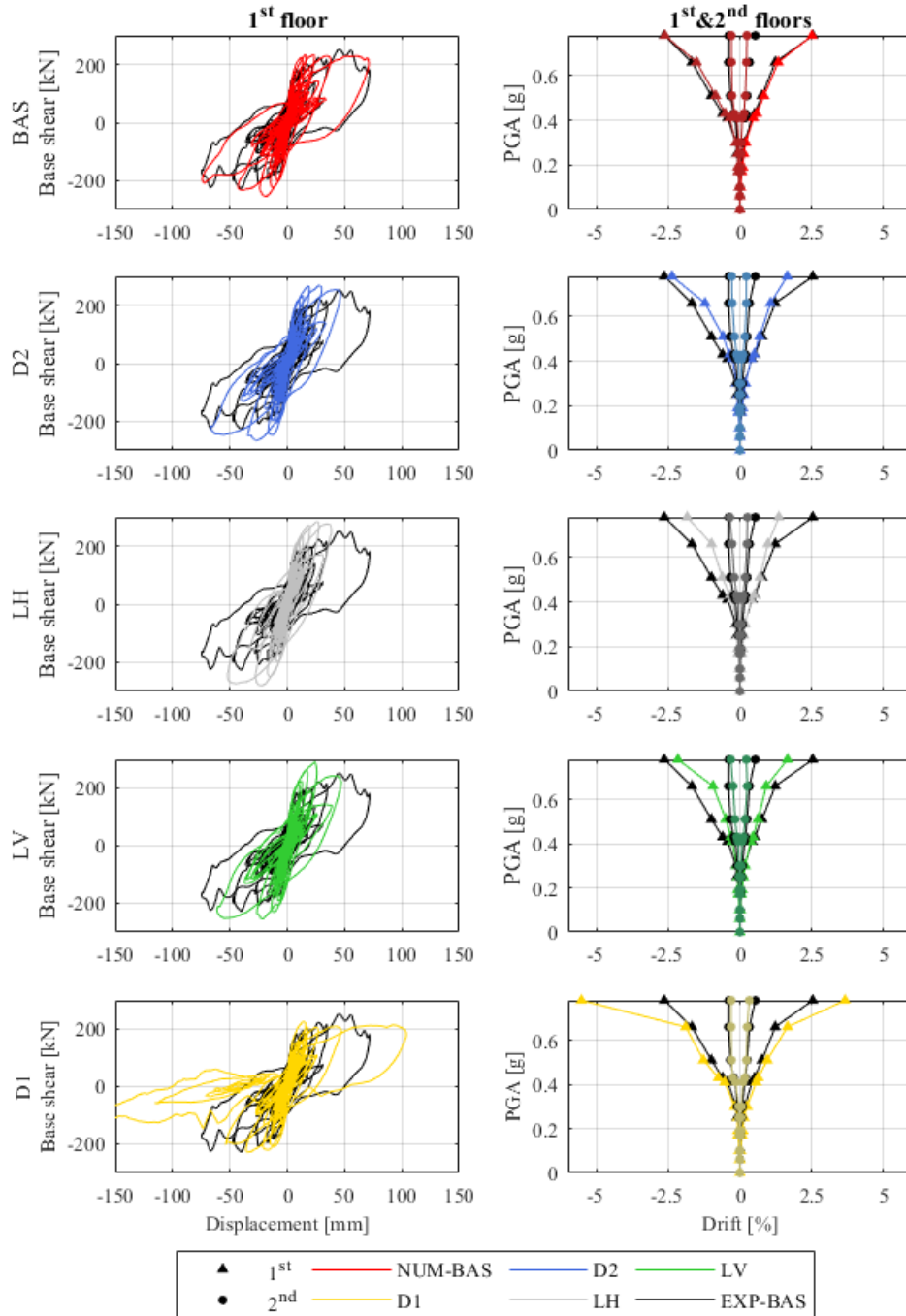
Figure 5.11 Comparisons between Numerical and Experimental (black) hysteresis curves (all runs) of 1st floor and interstorey drift curves of the considered retrofit configurations

In Figure 5.12a,b the influence of the vertical/horizontal retrofit frame elements spacing is analysed. Both LH and LV resulted in higher BSc and lower interstorey drift with respect to the BAS configuration. The greater differences between the three layouts were found in

the last runs (i.e. from EQ@166%, 0.51g), when the retrofit system's contribution was higher than in the initial runs (when instead it was the masonry that mostly contributed to the global response).

Similar results were obtained varying the size of frame elements section, as the effect of such modification was greater in the final runs when the retrofit system affected the most the global response. In Figure 5.12c,d the comparison between BAS and configurations D1 and D2 in terms of BSc and interstorey drift of ground and first floors are presented. D1, which was obtained reducing the frame members section, presented greater deformations, larger interstorey drift and lower BSc comparing to BAS, mostly in the last runs. Deformations were mostly concentrated at the ground floor, as reducing the retrofit contributed to emphasize the soft storey mechanism also experienced by BAS. Configuration D2, where the size of the frame elements was increased with respect to BAS, presented results analogous to LH and LV, with greater BSc and reduced interstorey drift in the last runs.

Figure 5.13 shows the final deformed shapes and associated numerical cracks pattern of both CS and CL leaves after the application of the whole loading protocol for all the configurations considered. It can be gathered that the greater the strong-back size (i.e. configuration D2), the lower the damage extent was. Similar results were obtained decreasing the horizontal (LH) frame spacing, whereas the vertical spacing reduction (LV) produced a stiffer frame with a minor deformation and damage in the longitudinal walls piers with respect to LH and BAS. On the contrary, configuration D1 led to more severe damage with the partial collapse of the East façade and the West CL leaf at the second-storey.

For future comparisons, it is worth mentioning that performing the whole incremental dynamic analysis for the selected configurations took around 16 h (CPU: Intel Core i7 8700k, RAM: 64 GB, SSD: 512 GB M2).

5.6 Conclusions

In this work, a modelling strategy based on the Applied Element Method (AEM) was used to investigate the sensitivity of a terraced building seismic performance to the geometrical configuration of a light timber retrofit system. Amongst other discrete approaches, the AEM was chosen for its computational effectiveness and its capability to represent the actual brick arrangement and masonry behaviour at the micro-scale. The retrofitting solution considered in this work is a light timber system designed to be sustainable, reversible and cost-effective, and applied to the inner load-bearing leaf of a cavity-wall building specimen, representative of an end unit of a Dutch terraced house tested at the Eucentre laboratory in Pavia.

First, the modelling strategy was validated simulating the two full-scale component tests on a retrofitted and a non-retrofitted calcium silicate walls, also allowing the calibration of some mechanical parameters not available from characterisation tests. Then, the mechanical parameters were implemented in the full-scale building model introducing IP

and OOP retrofit systems, floor strengthening, and other retrofitting details. Subsequently, the validated numerical building model was modified to obtain four different configurations with a view to investigate the sensitivity of the seismic performance to different retrofit layouts. This preliminary study showed a significant sensitivity to horizontal and vertical frame spacing variation and element size. Reducing retrofit frame spacing and increasing timber element size improved the seismic performance, reducing global deformation and damage. On the other hand, the reduction of timber frame elements size produced more significant displacement and damage, emphasising the soft storey mechanism experienced by the baseline specimen. It was also shown that, in order to optimise the retrofit effectiveness, it would be more efficient to vary horizontal or vertical frame elements spacing than to modify their dimensions, given that a greater section affects the retrofit footprint whereas a smaller one leads to a more deformable response.
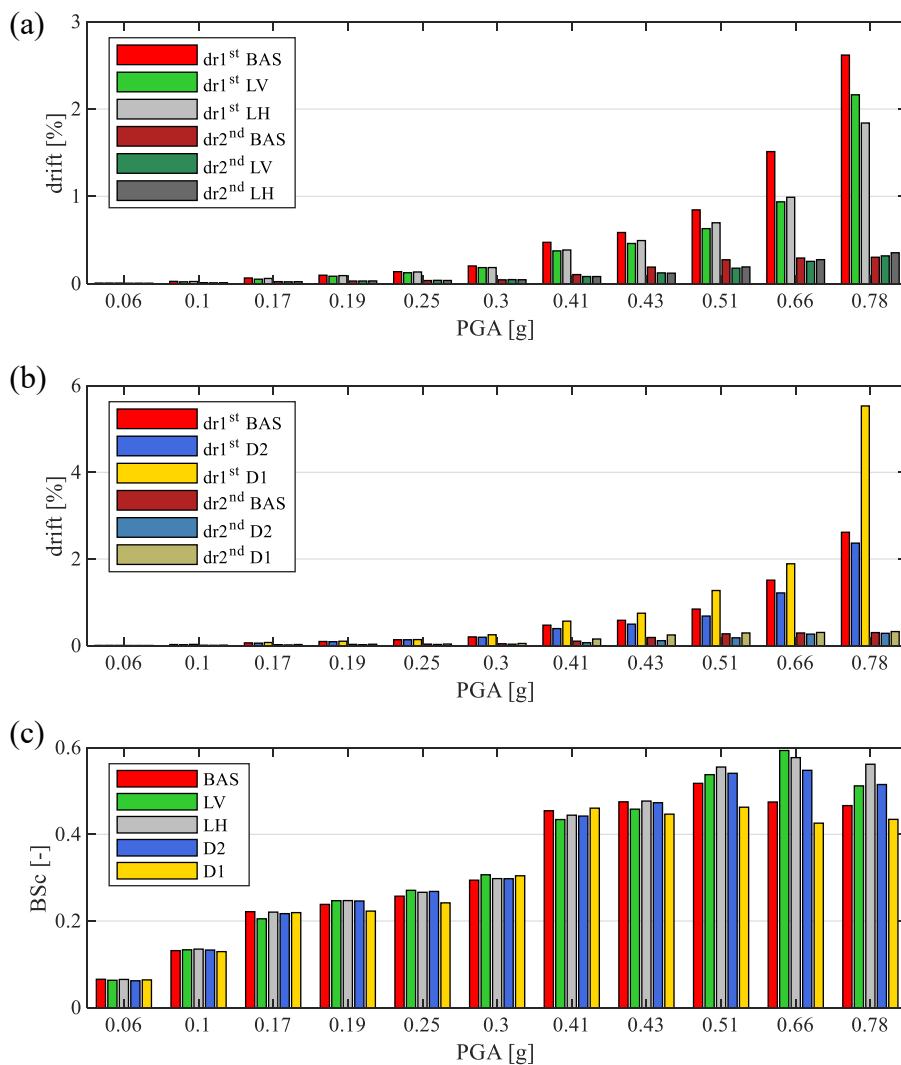
Figure 5.12 Parametric analyses results in terms of a) 1st and b) 2nd interstorey drift, and c) BSc

	CS	CL	Deformed shape
BAS Heavy structural			
D2 Heavy structural			
LH Heavy structural			
LV Heavy structural			
D1 Partial collapse			
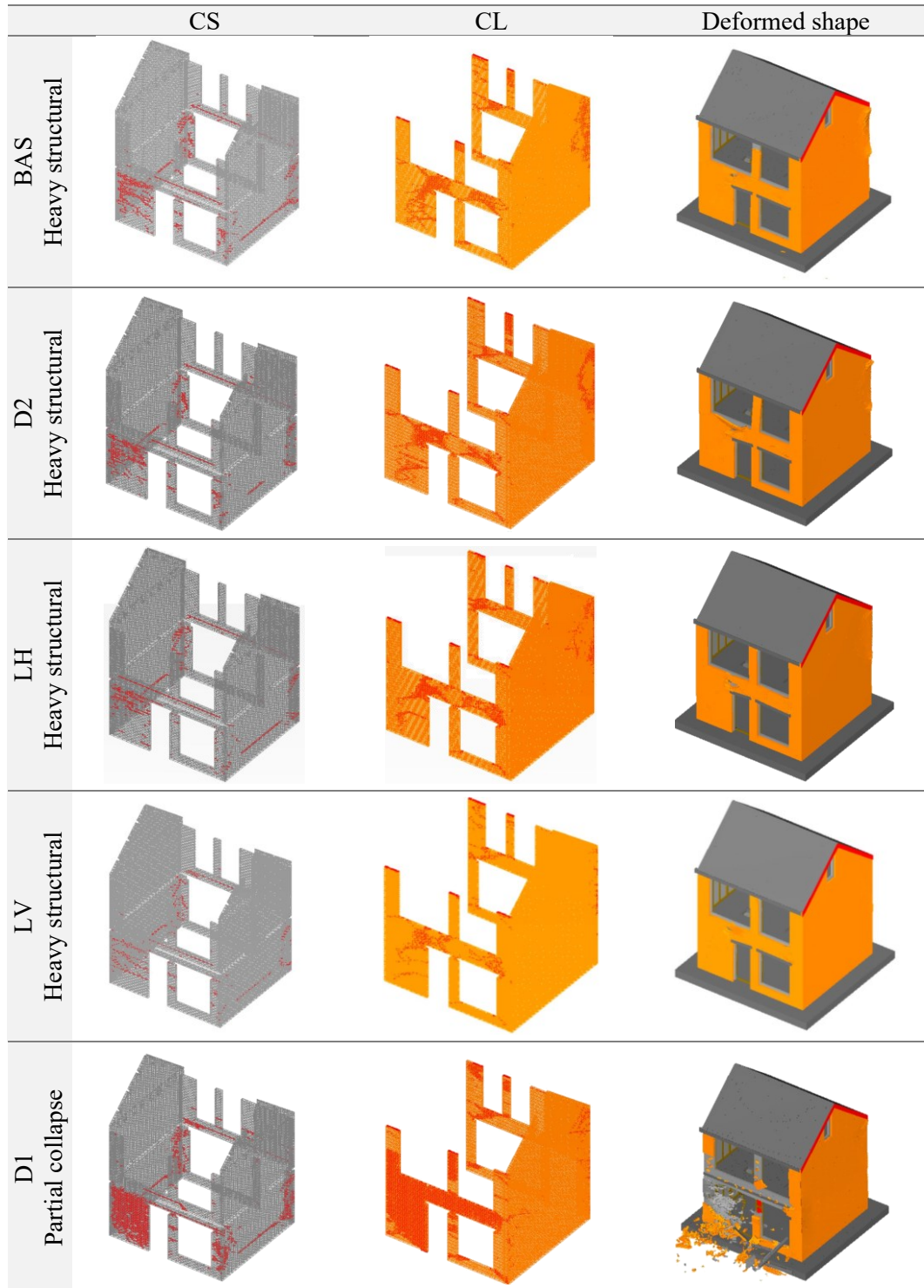
Figure 5.13 Deformed shape and numerical crack pattern of both CS and CL leaves at the end of the analysis for all the configurations considered

The results, obtained considering a typical Dutch house, can be generalised to the cavity-wall construction, widespread not only in the Central and Northern European regions but also in a number of other countries (such e.g. China, U.S.A, New Zealand). Moreover, the development of a validated modeling strategy for the retrofitting system may contribute to the extension of its application also to other masonry structures.

The AEM proved to be capable of reproducing the building specimen's response adequately, also enabling the investigation of the retrofit system sensitivity to the timber frame geometry and size. The development and validation of a modelling strategy suitable to simulate the effect of this strengthening technique represent the first step for the design of effective retrofitting interventions on existing masonry structures. This modelling exercise might also allow the development and/or calibration of more simplified numerical models, more suitable for engineering practice.

Acknowledgements

References

American Wood Council, (AWC), (2008). ANSI/AF&PA SDPWS-2008: Special design provisions for wind and seismic. Washington, DC.

American Wood Council (AWC). 2015. ANSI/AF&PA SDPWS-2015: Special design provisions for wind and seismic. Washington, DC.

Aref AJ, Dolatshahi KM (2013) A three-dimensional cyclic meso-scale numerical procedure for simulation of unreinforced masonry structures. Comput Struct 120:9–23. https://doi.org/10.1016/J.COMPSTRUC.2013.01.012.

Abdulla KF, Cunningham LS, Gillie M (2017) Simulating masonry wall behaviour using a simplified micro-model approach. Eng Struct 151:349–365. https://doi.org/10.1016/j.engstruct.2017.08.021.

Brooks JJ, Baker A (1998) Modulus of Elasticity of Masonry. Mason Int 12:58–63.

Calvi GM, Moratti M, O'Reilly GJ, et al (2019) Once upon a Time in Italy: The Tale of the Morandi Bridge. Struct Eng Int 29:198–217. https://doi.org/10.1080/10168664.2018.1558033.

Carozzi FG, Milani G, Poggi C (2014) Mechanical properties and numerical modeling of Fabric Reinforced Cementitious Matrix (FRCM) systems for strengthening of masonry structures. Compos Struct 107:711–725. https://doi.org/10.1016/j.compstruct.2013.08.026.

Cassol D, Giongo I, Ingham J, Dizhur D (2021) Seismic out-of-plane retrofit of URM walls

using timber strong-backs. Constr Build Mater 269:121237. https://doi.org/10.1016/j.conbuildmat.2020.121237.

Chácara C, Cannizzaro F, Pantò B, et al (2018) Assessment of the dynamic response of unreinforced masonry structures using a macroelement modeling approach. Earthq Eng Struct Dyn 47:2426–2446. https://doi.org/10.1002/eqe.3091.

Ciesielski R (1999) The dynamic module of elasticity of brick walls. In: Proceedings of the Conference of the Committee of Civil Engineering PZITB: Lublin, Poland.

Damiani N, Miglietta M, Mazzella L, et al (2019) Full-scale shaking table test on a Dutch URM cavity-wall terraced-house end unit – A retrofit solution with strong-backs and OSB boards – EUC-BUILD-7. Research report EUC052/2019U. Pavia, Italy Available online at: http://www.eucentre.it/nam-project.

De Felice G (2011) Out-of-plane seismic capacity of masonry depending on wall section morphology. Int J Archit Herit 5:466–482. https://doi.org/10.1080/15583058.2010.530339.

DeJong MJ, Vibert C (2012) Seismic response of stone masonry spires: Computational and experimental modeling. Eng Struct 40:566–574.

D'Altri AM, Messali F, Rots J, et al (2019) A damaging block-based model for the analysis of the cyclic behaviour of full-scale masonry structures. Eng Fract Mech 209:423–448. https://doi.org/10.1016/j.engfracmech.2018.11.046.

Dizhur D, Giaretton M, Giongo I, Ingham J (2017) Seismic retrofit of masonry walls using timber strong-backs. Struct Eng Soc J - SESOC 30:30–44.

Domaneschi M, Cimellaro GP, Scutiero G (2019) A simplified method to assess generation of seismic debris for masonry structures. Eng Struct 186:306–320. https://doi.org/10.1016/j.engstruct.2019.01.092.

El-Diasity M, Okail H, Kamal O, Said M (2015) Structural performance of confined masonry walls retrofitted using ferrocement and GFRP under in-plane cyclic loading. Eng Struct 94:54–69. https://doi.org/10.1016/j.engstruct.2015.03.035.

European Committee for Standardization (CEN); (2006) EN 300: Oriented Strand Boards (OSB)—defini- tions, classification and specifications.

European Committee for Standardization (CEN); (2016) European Committee for Standardization; EN 14081-1: timber structures. Strength graded structural timber with rectangular cross section. Part I: general requirements.

Furukawa A, Kiyono J, Toki K (2012) Numerical simulation of the failure propagation of masonry buildings during an earthquake. J Nat Disaster Sci 33:11–36.

Galvez F, Giaretton M, Abeling S, et al (2018) Discrete element modeling of a two storey unreinforced masonry scaled model. 16th Eur Conf Earthq Eng - ECEE 1–12.

Giambanco G, La Malfa Ribolla E, Spada A (2018) Meshless meso-modeling of masonry in the computational homogenization framework. Meccanica 53:1673–1697. https://doi.org/10.1007/s11012-017-0664-7.

Giaretton M, Dizhur D, Ingham JM (2016) Shaking table testing of as-built and retrofitted clay brick URM cavity-walls. Eng Struct 125:70–79. https://doi.org/10.1016/j.engstruct.2016.06.032.

Giongo I, Schiro G, Piazza M (2017) On the Use of Timber-Based Panels for the Seismic Retrofit of Masonry Structures. In: 3rd International Conference - Protection of historical constructions. Lisbon, Portugal.

Godio M, Beyer K (2019) Evaluation of force-based and displacement-based out-of-plane seismic assessment methods for unreinforced masonry walls through refined model simulations. Earthq Eng Struct Dyn 48:454–475. https://doi.org/10.1002/eqe.3144

Graziotti F, Penna A, Magenes G (2019) A comprehensive in situ and laboratory testing programme supporting seismic risk analysis of URM buildings subjected to induced earthquakes. Bull Earthq Eng 17:4575–4599. https://doi.org/10.1007/s10518-018-0478-6.

Graziotti F, Tomassetti U, Kallioras S, et al (2017) Shaking table test on a full scale URM cavity wall building. Bull Earthq Eng 15:5329–5364. https://doi.org/10.1007/s10518-017-0185-8.

Grunwald C, Khalil AA, Schaufelberger B, et al (2018) Reliability of collapse simulation – Comparing finite and applied element method at different levels. Eng Struct 176:265–278. https://doi.org/10.1016/j.engstruct.2018.08.068.

Guerrini G, Damiani N, Miglietta M, Graziotti F (2020) Cyclic response of masonry retrofitted with timber frames and boards. Struct Build 74:372–388. https://doi.org/10.1680/jstbu.19.00134.

Jäger W, Irmschler HJ, Schubert P (2004) Mauerwerk-Kalender 2004. Ernst & Sohn Verlag für Architektur und technische Wissenschaften.

Kallioras S, Graziotti F, Penna A (2019) Numerical assessment of the dynamic response of a URM terraced house exposed to induced seismicity. Bull Earthq Eng 17:1521–1552. https://doi.org/10.1007/s10518-018-0495-5.

Karbassi A, Nollet MJ (2013) Performance-based seismic vulnerability evaluation of masonry buildings using applied element method in a nonlinear dynamic-based analytical procedure. Earthq Spectra 29:399–426. https://doi.org/10.1193/1.4000148.

Kaushik HB, Rai DC, Jain SK (2007) Stress-strain characteristics of clay brick masonry under uniaxial compression. J Mater Civ Eng 19:728–739.

Lagomarsino S, Penna A, Galasco A, Cattari S (2013) TREMURI program: An equivalent frame model for the nonlinear seismic analysis of masonry buildings. Eng Struct 56:1787–1799. https://doi.org/10.1016/j.engstruct.2013.08.002.

Lemos J V. (2019) Discrete element modeling of the seismic behavior of masonry construction. Buildings 9:43. https://doi.org/10.3390/buildings9020043.

Lucchini S, Facconi L, Minelli F, Plizzari GA (2017) Numerical Study of a Full Scale Hollow Brick Masonry Building Strengthened with Steel Fiber Reinforced Mortar Coating. In: XVII ANIDIS.

Luccioni B, Rougier VC (2011) In-plane retrofitting of masonry panels with fibre reinforced composite materials. Constr Build Mater 25:1772–1788. https://doi.org/10.1016/j.conbuildmat.2010.11.088.

Maekawa K, El-Kashif KF (2004) Cyclic cumulative damaging of reinforced concrete in post-peak regions. J Adv Concr Technol 2:257–271.

Magenes G, Della Fontana A (1998) Siplified on-Linear Seismic Analysis of Masonry Buildings. In: Proceedings of the Fifth International Masonry Conference. London, United Kingdom, pp 1–313.

Malomo D, DeJong MJ (2021) A Macro-Distinct Element Model (M-DEM) for simulating the in-plane cyclic behavior of URM structures. Eng Struct 227:111428. https://doi.org/10.1016/j.engstruct.2020.111428.

Malomo D, Morandini C, Crowley H, et al (2021) Impact of ground floor openings percentage on the dynamic response of typical Dutch URM cavity wall structures. Bull Earthq Eng 19:403–428. https://doi.org/10.1007/s10518-020-00976-z.

Malomo D, Pinho R, Penna A (2018) Using the applied element method for modelling calcium silicate brick masonry subjected to in-plane cyclic loading. Earthq Eng Struct Dyn 47:1610–1630. https://doi.org/10.1002/eqe.3032.

Malomo D, Pinho R, Penna A (2020) Simulating the shake table response of unreinforced masonry cavity wall structures tested to collapse or near-collapse conditions. Earthq Spectra 36:554–578. https://doi.org/10.1177/8755293019891715.

Masi F, Stefanou I, Maffi-Berthier V, Vannucci P (2020) A Discrete Element Method based-approach for arched masonry structures under blast loads. Eng Struct 216:110721. https://doi.org/10.1016/j.engstruct.2020.110721.

Matysek P, Janowski Z (1996) Analysis of factors affecting the modulus of elasticity of the walls. In: Proceedings of the Conference of the Committee of Civil Engineering PZITB: Lublin, Poland.

Mayorca P, Meguro K (2003) Modeling masonry structures using the applied element method. Seisan Kenkyu 55:581–584.

Meguro K, Tagel-Din H (2000) Applied element method for structural analysis: Theory and application for linear materials. Struct Eng Eng 17:21–35.

Messali F, Esposito R, Maragna M (2016) Pull-out strength of wall ties. Report, TU Delft, NL.

Miglietta M, Damiani N, Guerrini G, Graziotti F (2021) Full-scale shake-table tests on two unreinforced masonry cavity-wall buildings: effect of an innovative timber retrofit. Bull Earthq Eng 2561–2596. https://doi.org/10.1007/s10518-021-01057-5.

Papantonopoulos C, Psycharis IN, Papastamatiou DY, et al (2002) Numerical prediction of the earthquake response of classical columns using the distinct element method. Earthq Eng Struct Dyn 31:1699–1717. https://doi.org/10.1002/eqe.185.

Petracca M, Pelà L, Rossi R, et al (2017) Micro-scale continuous and discrete numerical models for nonlinear analysis of masonry shear walls. Constr Build Mater 149:296–

314. https://doi.org/10.1016/j.conbuildmat.2017.05.130.

Portioli F (2020) Rigid block modelling of historic masonry structures using mathematical programming: a unified formulation for non-linear time history, static pushover and limit equilibrium analysis. Bull Earthq Eng 18:211–239. https://doi.org/10.1007/s10518-019-00722-0.

Pulatsu B, Bretas EM, Lourenço PB (2016) Discrete element modeling of masonry structures: Validation and application. Earthquakes Struct 11:563–582. https://doi.org/10.12989/eas.2016.11.4.563.

Raka E, Spacone E, Sepe V, Camata G (2015) Advanced frame element for seismic analysis of masonry structures : model formulation and validation. Earthq Eng Struct Dyn 44:2489–2506. https://doi.org/10.1002/eqe.

Ravenshorst, G.J.P. and Mirra, M. (2017). Test report on cyclic behaviour of replicated timber diaphragms representing a detached house. Report number C31B67WP4-7, version 1, 30 December 2017. Delft University of Technology.

Riccadonna D, Giongo I, Schiro G, et al (2019) Experimental shear testing of timber-masonry dry connections for the seismic retrofit of unreinforced masonry shear walls. Constr Build Mater. https://doi.org/10.1016/j.conbuildmat.2019.03.145.

Salem H, Mohssen S, Nishikiori Y, Hosoda A (2016) Numerical Collapse Analysis of Tsuyagawa Bridge Damaged by Tohoku Tsunami. J Perform Constr Facil 30:04016065. https://doi.org/10.1061/(ASCE)CF.1943-5509.0000925.

Smiroldo F, Giongo I, Piazza M (2020) Seismic retrofit of masonry infilled frames by using timber panels. In: 17th World Conference on Earthquake Engineering, 17WCEE. Sendai, Japan.

Tondelli M, Beyer K, DeJong MJ (2016) Influence of boundary conditions on the out-of-plane response of brick masonry walls in buildings with RC slabs. Earthq Eng Sructural Dyn 45:1337–1356. https://doi.org/10.1002/eqe.

U.B.C. (1991) International Conference of Building Officials. Uniform Building Code. In: International conference of building officials, USA. Whittier, USA.

Valluzzi MR, di Bella A, Garbin E (2013) Optimization of mechanical and acoustic performance of timber floors. Adv Mater Res 778:690–697. https://doi.org/10.4028/www.scientific.net/AMR.778.690.

van Elk JF, Bourne SJ, Oates SJ, et al (2019) A probabilistic model to evaluate options for mitigating induced seismic risk. Earthq Spectra 35:537–564. https://doi.org/10.1193/050918EQS118M.

Vanin F, Penna A, Beyer K (2020) Equivalent-Frame Modeling of Two Shaking Table Tests of Masonry Buildings Accounting for Their Out-Of-Plane Response. Front Built Environ 6:. https://doi.org/10.3389/fbuil.2020.00042.

6. A discrete modelling approach for URM walls with unfilled head joints

Abstract

The choice of the numerical approach for simulating the URM buildings response is usually guided by the analysis purpose, mostly in terms of time consumption and accuracy. Simplified approaches, such as the Equivalent Frame Model by macroelement, are widespread among practitioners thanks to their accuracy and limited computational cost. On the other hand, micro-modelling approaches are appreciated by researchers for their capacity to explicitly account for the interaction of the components following cracks propagation up to collapse. However, the significant computational time required for the analyses may prevent the application of these accurate modelling methods. In this study, a discrete modelling approach was applied to the simulation of in-plane shear-compression tests on masonry walls made by vertically hollowed "tongue and groove" clay units with thin webs/shells. The main purpose is to develop reliable models that can be used as a benchmark to improve simplified models and extend the test results, including loading conditions that are not explored experimentally.

6.1 Introduction

In the context of the development of energy efficiency and sustainability of buildings, good results can be achieved by adopting clay units with very thin webs and shells to improve the thermal and acoustic performance of masonry walls. However, clay units with thin webs and shells and a large percentage of voids may be a source of weakness and lead to a brittle behaviour when the wall is subjected to high values of vertical compression and to cyclic actions as in the case of seismic excitations (Tomaževič et al. 2006). For this reason, many codes in the past, such as the Italian masonry code D.M. 20/11/1987 (1987) and the Eurocode 8 (CEN 2005), introduced restrictions in the use of these units as load-bearing elements, prescribing a minimum thickness of web and shells and a limitation of the maximum void ratio. Nowadays, the NTC2018 (D.M. 17/01/2018) requires a minimum thickness of the webs and shells (7 and 10 mm, respectively) and limits the vertical void ratio to 55%. Moreover, when these units are intended to be used as structural elements in seismic areas, the void ratio is further limited to 45% and only units with continuous and

rectilinear webs parallel to the wall plane should be adopted. A minimum compressive strength for both mortar and units is also required, whereas the use of unfilled head joints is forbidden; in addition, the use of thin layer bed joints is restricted to seismic areas with low values of design peak ground acceleration depending on the number of storeys in the building.

In this context, a recent experimental campaign (Morandi et al., 2021) investigated the performance of masonry with thin web/shell clay units and unfilled head joints to evaluate the applicability of this solution in moderate seismicity areas. However, the experimental information is limited to the set of walls considered in the performed shear-compression tests and should be extended using numerical simulations. Therefore, a reliable numerical model is required, capable of representing the in-plane response of such masonry typology, including the cyclic behaviour of the unfilled vertical joints, with the possible separation and recontact between units.

Discrete models, initially conceived to analyse soil mechanics problems, proved to be particularly suitable for simulating in-plane-governed responses of URM components and building sub-systems (Pulatsu et al. 2016; Malomo et al. 2019). Building on previous advancements (e.g.Kawai 1978), a recent effort to increase the computational efficiency of discrete methods was made by Meguro and Tagel-Din (2000), developing an innovative rigid body and spring modelling technique, the Applied Element Method (AEM). In the AEM, masonry members are represented as an assembly of rigid elements connected by nonlinear springs interfaces, in which material properties are lumped and failures occur. This efficient tool proved to be suitable to model the heterogeneous nature of URM structures, also enabling the possibility of representing their behaviour up to complete collapse (Karbassi and Nollet 2013; Keys and Clubley 2017; Malomo et al. 2021), including separation and recontact between elements. For this reason, it is particularly suitable to model the masonry typology object of this work, including the behaviour of dry vertical joints and the complete separation of masonry wedges typical of the so-called "gaping" behaviour.

In this chapter, the capability of a discrete modelling approach, based on the Applied Element Method (AEM), was investigated to simulate the in-plane (IP) response of this innovative masonry. The discrete model has been validated through the simulation of the experimental shear-compression tests performed by (Morandi et al. 2021), with the purpose of applying this numerical tool in the study of the dynamic response of more complex structures and obtaining a reliable benchmark for the validation of simplified models. Moreover, the Equivalent Frame Model (EFM) was applied to the simulation of those shear-compression tests with the aim of validating a new strength criterion and constitutive law describing the lateral cyclic behaviour associated with the "gaping" mechanism developed by the URM walls with unfilled head joints. The results of EFM and AEM models were then compared with the experimental outcomes.

6.2 URM walls with thin shell/web clay units and unfilled head joints

In this work, the masonry typology called "MB", tested by Morandi et al. (2021), was considered. This masonry type consists of hollow clay "tongue and groove" units with thin web and shells, assembled with thin layer bed joints and unfilled head joints. Clay units had a percentage of voids of 55% and they can be classified into group 3 according to Eurocode 6 part 1-1 (CEN 2005). The properties of clay units are reported in Table 6.1. The actual Italian code requirements for clay units in a seismic zone are not satisfied as the void ratio is larger than 45% and web/shell thickness is lower than 7 and 10 mm respectively. The thin layer bed joints were made with a pre-batched mortar-glue, which contains fibres long enough to limit the penetration of the mortar in the holes of the units; the horizontal joints were laid with a special roll in order to have a constant thickness of about 1 mm. Head joints were unfilled, and the connection between two adjacent blocks was guaranteed only by the mechanical interlocking of the "tongue and groove" units (Figure 6.1a). Figure 6.1 shows the wall construction (Figure 6.1c) and the device used for the execution of the thin layer bed joints (Figure 6.1b).
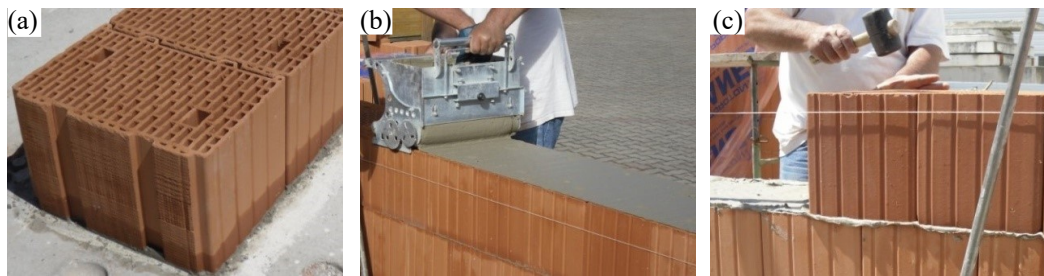
Figure 6.1 a) "tongue and groove" units, b) execution of the thin layer bed joints and c) construction of the wall masonry (adapted from Morandi et al. (2021))

Table 6.1 Characteristics of clay units

Length [mm]	230
Width [mm]	350
Height [mm]	235
Web/shell thickness [mm]	4-6
Gross dry density [kg/mc]	750

Characterisation tests on units, mortar and masonry assemblages were performed in the Department of Civil Engineering and Architecture laboratory of the University of Pavia. The results are summarised in Table 6.2, where f_b and f'_b are the vertical and lateral compressive strength of units (with the corresponding normalised values reported in brackets), while f_{fl} and f_m are the tensile (from flexural test) and compressive strength of mortar-glue. Concerning masonry properties, f and E are the vertical compressive strength and the elastic modulus, respectively, obtained from vertical compression tests on wallets, whereas the initial shear strength, f_{v0}, and the friction coefficient, μ, were evaluated through triplet tests at different levels of compression.

6.3 Experimental in-plane shear-compression tests

In-plane cyclic tests on walls with different aspect ratios and vertical compression levels were carried out at the Eucentre laboratory of Pavia. The tests were performed in double-fixed boundary conditions, and incremental displacements were applied in displacement control. At each displacement amplitude, three cycles have been performed up to the ultimate conditions. The experimental setup and loading protocol are presented in Figure 6.2. Five walls were tested, and their characteristics are summarised in Table 6.3, where l, t and h are the wall length, thickness and height, respectively, σ_v is the vertical compression applied at the top of the specimen, and the aspect ratio is evaluated as h/l. Finally, the experimental failure mode is reported.

Table 6.2 Mechanical properties

	Mean values [MPa]	St. deviation [MPa]	C.o.v. [%]
Vertical compressive strength of units, f_b	10.5 (12)	0.91	8.7
Lateral compressive strength of units, f'_b	1.7 (1.9)	0.42	24.7
Tensile (flexural) strength of mortar-glue, f_{fl}	4.1	0.49	11.8
Compressive strength of mortar glue, f_m	13.4	1.18	8.8
Compressive strength of masonry, f	6.2	0.60	9.7
Elastic modulus of masonry, E	6100	403	6.6
Initial shear strength (from triplet tests), f_{v0}	0.49	-	-
Friction coefficient (from triplet tests), μ	1.04	-	-
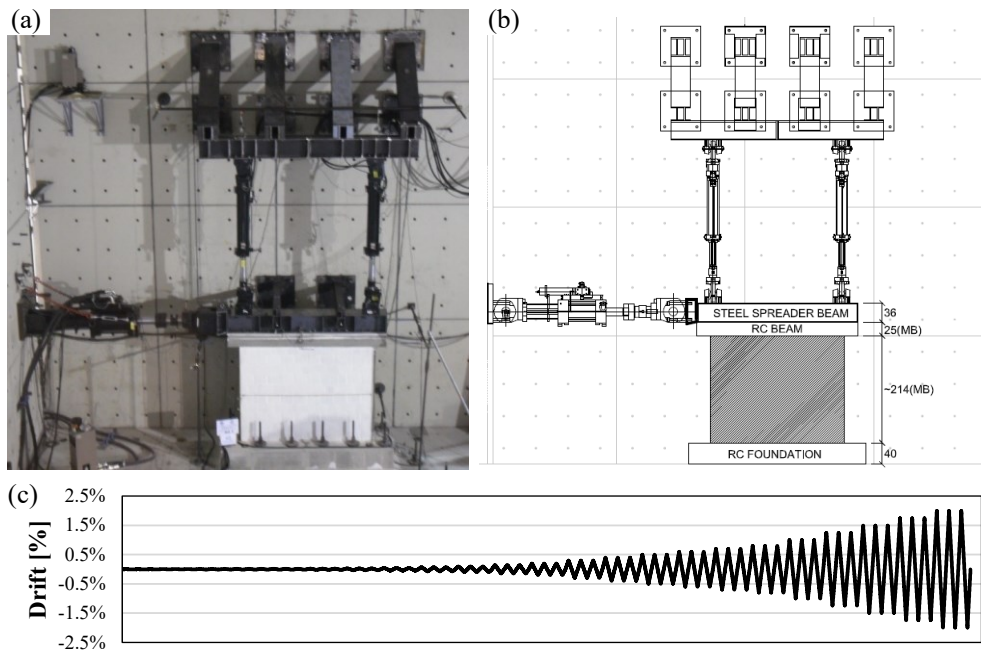
Figure 6.2 a,b) Experimental setup and c) loading protocol of the cyclic in-plane tests (adapted from Morandi et al. 2021)

The experimental results of the in-plane cyclic tests are reported in section 6.6, comparing both damage patterns and hysteretic curves with the numerical counterparts obtained with the AEM and EFM models described in sections 6.4 and 6.5.

Table 6.3 Properties of walls specimens

	l [mm]	Aspect ratio [-]	σ_v [MPa]	Failure mode
MB1	1350	1.6	0.15	"Gaping"-Flexural
MB2	1350	1.6	0.45	"Gaping"-Shear
MB3	1350	1.6	0.65	Shear
MB4	2700	0.8	0.45	"Gaping"
MB5	2700	0.8	0.65	"Gaping"-Shear

6.4 EFM models

In the Equivalent Frame Model (EFM), masonry structures are ideally subdivided into rigid nodes and deformable elements (i.e. spandrels and piers). This assumption is based on experimental and post-earthquake observations indicating that deformations are located in recurrent areas while others work as rigid parts. In this work, the research version of TREMURI software (Lagomarsino et al. 2013) was used, considering the macroelement model initially proposed by Penna et al. (2014) and then further improved by Bracchi et al. (2021). A macroelement (Figure 6.3a) is a two-node element consisting of three main parts: a central body where only shear deformations are allowed and two zero-thickness spring interfaces governing the axial-flexural behaviour. The no-tension model with the bilinear law in compression proposed by Bracchi et al. (2021) is assigned to the zero-thickness springs, whereas the shear damage model is based on the one proposed by Gambarotta and Lagomarsino (1997). Shear failure is predicted by multiple shear strength criteria implemented in the macroelement by Bracchi and Penna (2021).

In this work, the shear strength was calculated with equation (6.1) according to Bracchi and Penna (2021), referring to the compressed section after crack has developed. According to Eurocode 6-Part 1-1 (CEN 2005) in the case of unfilled head joints, the shear strength associated with the shear failure with cracks in the units, here named f_{vlt}, has to be equal to $0.045f_b$, which was further divided for 0.8 to obtain the mean value. However, the relation proposed by the Eurocode 6 for masonry with filled head joints (i.e. considering f_{vlt} equal to $0.065f_b$) seems to be more appropriate in this case. Indeed, using a lower value of f_{vlt} leads to closer lateral strength predicted by gaping and shear strength criteria, making the clear detection of the proper mechanism for the EFM model more complicated. f_b is the normalised compressive strength of the brick and α_v is the shear span ratio, equal to h_0/l. h_0 is the distance between the section with zero moment and the section with the maximum moment, and l is the wall length. The shear strength related to shear failure with sliding along bed joints of a cracked cross-section was evaluated with the equation proposed by Magenes and Calvi (1997) (6.2).

$$V_{sh,1} = \frac{1.5\, f_{vlt}\, lt N_0}{N_0 + 3 f_{vlt}\, \alpha_v lt} \tag{6.1}$$

$$V_{sh,2} = lt\, \frac{\left(1.5\, \bar{c} + \bar{\mu}\frac{N_0}{lt}\right)}{1 + 3\bar{c}\, \alpha_v / \left(\frac{N_0}{lt}\right)} \tag{6.2}$$

$$\begin{cases} \bar{\mu} = k\mu \\ \bar{c} = kc \end{cases} \qquad \text{where } k = \frac{1}{1 + \bar{\mu}\tan\theta} \tag{6.3}$$

$\bar{c}$ and $\bar{\mu}$ are the corrected cohesion and friction coefficient proposed by Mann and Müller (1982), which are obtained by correcting the experimental values of cohesion, c or initial shear strength f_{v0}, and friction coefficient, μ. According to Bracchi and Penna (2021) the correction was made with a factor k, which depends on the angle of the chord of the stepped crack with respect to the horizontal, θ, function of masonry pattern and unit dimensions. The macroelement mechanical parameters are reported in Table 6.4, where Gc_t and β govern the macroelemet inelastic shear deformability and the slope of the post-peak softening branch, respectively.

Table 6.4 Macroelement mechanical parameters

ρ [kg/m³]	E [MPa]	G [MPa]	f_b [MPa]	f_{vlt} [MPa]	c [MPa]	μ [-]	Gc_t [-]	B [-]
750	6100	1037	12	0.67	0.49	1.04	0.5	0.1

A new strength criterion was implemented in Tremuri software to account for the "gaping" mechanism. The shear strength is evaluated according to Jäger and Schöps (2008) with equation (6.4), and it is proportional to the axial force N and to the inclination of cracks (Figure 6.3) (*tanα*) which depends on the unit's dimensions.

$$V_{gap} = N \cdot \tan\alpha \tag{6.4}$$

(a)   (b)
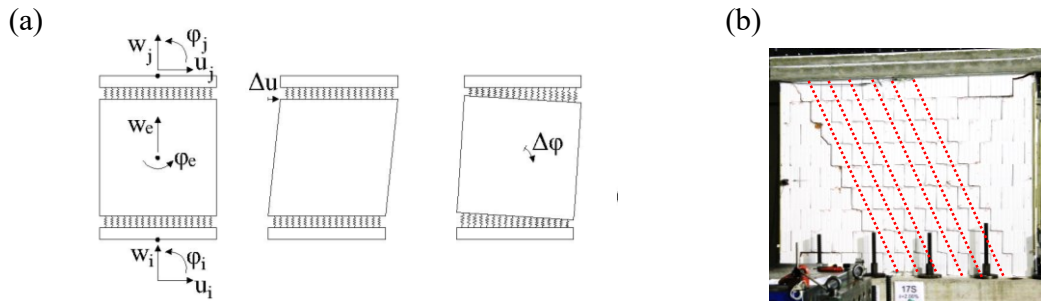
Figure 6.3 a) Macroelement (adapted from Penna et al. 2014) and b) separation of masonry wedges in the gaping behaviour

6.5 AEM models

According to the Applied Element Method (AEM), a structure is modelled as an assembly of rigid elements connected by zero-thickness springs interfaces where material properties are lumped and deformations and failures occur. As masonry is a heterogeneous material, two different spring interfaces are considered: unit springs, connecting rigid elements of the same unit, and joint springs, where the interaction between the mortar joint and the adjacent units are represented. Units springs stiffness was evaluated according to the original formulation of Meguro and Tagel-Din (2000), whereas the joint springs stiffness was calculated considering mortar joint and units as springs in series (Mayorca and Meguro 2003).

The material properties of AEM are reported in Table 6.5. Units are modelled as fully rigid, and their deformability was lumped in joint springs interfaces. Given the small thickness of the glue mortar, which might be influent with respect to masonry deformability, and the uncertain on the determination of the overlap area between thin-layer mortar and hollow brick units, a first estimation of the elastic modulus of mortar-units interface springs, E_m, was done assuming such value equal to the one obtained in the compression test on masonry assembly. The shear modulus of glue mortar, G_m, was estimated equal to the 30% of the elastic modulus. As already suggested by Mayorca and Meguro (2003), the elastic properties of joint springs needed to be further calibrated assuring they match with the experimental initial lateral stiffness. The value of tensile strength of joint material, f_{tm}, was assumed equal to 1/3 of the value obtained by flexural test and further reduced by 50% to account for the limited contact area due to the presence of holes on the surfaces of the units. The tensile strength of glue mortar was also evaluated analytically from triplet test results, assuming a Mohr-Coulomb criterion. The range for tensile strength obtained is 0.47-0.76 MPa, which is consistent with the adopted value of 0.7 MPa. Cohesion, c_{mg}, and friction coefficient, μ_m, of glue mortar were inferred by experimental triplet tests.

According to AEM, when a spring attains the defined strain limit (i.e. the separation strain), it is eliminated. When all springs are removed, adjacent units behave as detached. A brittle material with a low separation strain was chosen to represent the vertical unfilled joints to obtain premature failure and the elimination of such interface springs. As the top beam was cast directly on the specimen with the penetration of concrete in the unit's holes, elastic material with concrete elastic properties was assigned to the interface's springs between the masonry wall and the top beam. This assumption is justified by the absence of any sliding or damage in the top bed-joint. According to AEM formulation, the bottom interface properties were determined, assuming concrete, base mortar and units as stiffnesses arranged in series. Units were modelled as fully rigid, except for MB5 where a single failure surface was considered. In the last wall specimen, the unit-to-unit springs had compressive strength f_b derived from characterisation tests, elastic modulus E_b, assumed equal to 300 f_b according to (Kaushik et al. 2007) and tensile strength f_{bt} assumed equal to the 10% of the compressive one. A vertical separation surface was introduced only in MB5 to allow cracking through units, which was significant in that test. In Figure 6.4, the location of the different interfaces adopted in the discrete model is presented.

Table 6.5 Material properties of horizontal joint material in AEM

ρ [kg/m³]	E_m [MPa]	G_m [MPa]	f_m [MPa]	ft_m [MPa]	c_m [MPa]	μ_m [-]	E_b [MPa]	f_b [MPa]	f_{bt} [MPa]
750	6100	1830	13.4	0.7	0.49	1.04	3150	12	1.2
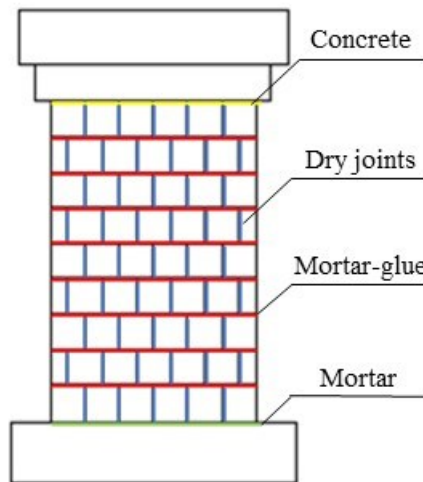
Figure 6.4 AEM model of MB1 with interfaces location

6.6 Simulation of the shear-compression tests

The shear-compression tests performed by Morandi et al. (2021) were simulated with the AEM and EFM models of the five walls, applying the same loading protocol. In the following, the numerical force-displacement curves and damage patterns were compared with the experimental outcomes.

6.6.1 MB1

The specimen MB1 showed the first light cracks in the bed joints at a level of drift of 0.15-0.2%, with a clear flexural behaviour and rotation points located at the base and in the upper corners. This behaviour was followed by developing a step-wise diagonal crack at a level of drift of 0.3%, with a second diagonal crack appearing in the opposite direction at 0.4% of drift ratio. At 0.8-1% of drift ratio, corner units showed diagonal cracks. The width of step-wise diagonal cracks increased with the top displacement, and the pier developed the characteristic gaping behaviour with sliding in the bed joints along the diagonal. At the ultimate drift (2%), corner units appeared significantly damaged with several cracks. The experimental hysteretic curve showed a peak of strength of 75 kN at 0.05-0.1% of drift ratio, and a strength deterioration up to a level of drift of 0.2-0.25% when the lateral strength reached the residual value of 42 kN, kept constant up to the end of the test. The peak of strength was related to the contribution of the mortar bed joints tensile strength, which was exceeded in the test's first stages, producing the settling of the lateral force at the residual wall capacity. The comparison between experimental and numerical force-displacement curves is presented in Figure 6.5.
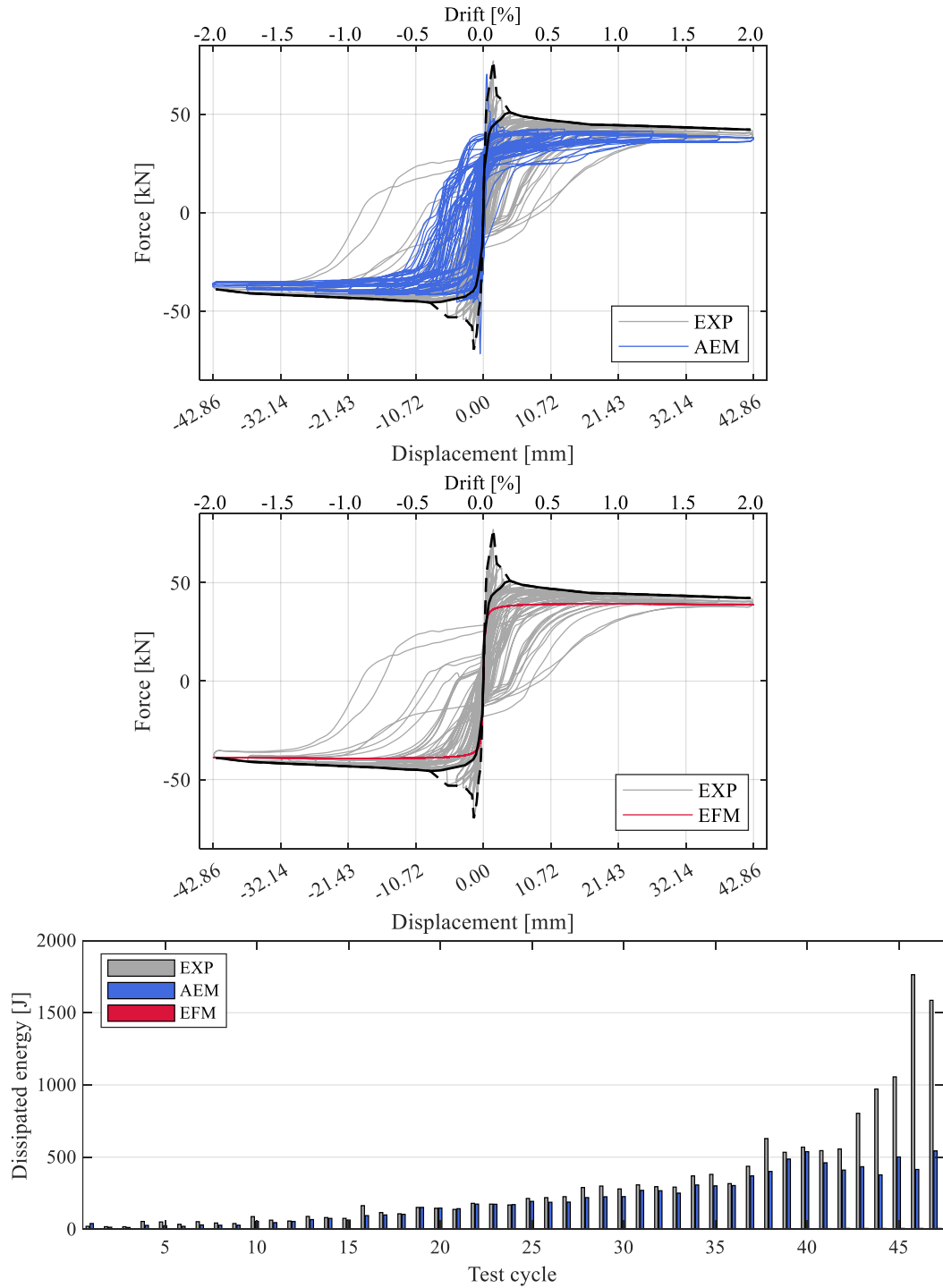
Figure 6.5 Experimental versus AEM and EFM force-displacement curves and dissipated energy for MB1

The AEM model predicted a peak of lateral strength of 71 kN at 0.04% of drift ratio, with strength deterioration after this point, corresponding to the attainment of the tensile strength in the glue mortar bed joints. The AEM model predicted a residual lateral strength of 38 kN, and a gaping behaviour, with the development of diagonal step-wise cracking with increasing displacement. The EFM predicted a flexural mechanism with light shear damage witnessed by the shear damage parameter $\alpha > 0$ and lateral strength of 39 kN. Unlike the discrete model, the EFM couldn't predict the initial peak of lateral strength caused by the attainment of the tensile strength in the bed joints.

The comparison between numerical and experimental damage is presented in Figure 6.6, where the deformed shape is shown at zero and maximum positive and negative displacements attained in the last cycle. The energy dissipated by the specimen at each cycle was compared with the numerical counterparts. The AEM model reproduced with a good agreement the energy dissipated by the specimen, with noticeably differences only in the last runs when the units cracking increased the dissipated energy. This phenomenon wasn't reproduced by the AEM model, where units were represented as fully rigid. The EFM predicted the greater differences in terms of dissipated energy which was almost null, as the wall specimen exhibited a hybrid mechanism whereas the macroelement predicted a pure flexural behaviour.

6.6.2 MB2

The specimen MB2 showed the first damage at a level of drift of 0.15% with bi-diagonal step-wise cracks in the joints, then developed up to a drift of 0.25-0.30%, when units were affected by the first cracks. After 0.40% of drift ratio, the clay units' cracks increased at the centre of the panel and at the corners. The horizontal width of the gaps in the head joints also increased. Several further cracks developed in the units at drift of 0.60-0.70%, widespread throughout the wall. Then, at 0.80% of drift, the test was stopped due to a drop of strength. At that drift level, the spalling of many blocks had occurred. The MB2 panel developed a hybrid behaviour. First, it was characterised by a gaping response with step-wise bi-diagonal cracks through head and bed joints. Then, after 0.40% of drift ratio, a shear failure mechanism with cracks through units occurred. The experimental versus numerical hysteretic curves are presented in Figure 6.7, whereas Figure 6.8 shows the specimen and models damage patterns at the end of the test.

The AEM model underestimated the maximum lateral strength with a peak value of 111 kN, almost constant up to the end of the test, where the experimental peak value was 126 kN with a residual strength of 115 kN. The energy dissipated, presented in Figure 6.8, was underestimated by the AEM in the last cycles. Nevertheless, the AEM model of MB2 exhibited a hybrid mechanism with a gaping behaviour at the initial cycles and the progressive shear damage increasing the target displacement, consistently with the experimental test. A premature tensile cracking was observed at 0.06% of drift ratio in the horizontal bed joints of the AEM model, where the specimen exhibited cracks at the same location for 0.15% of imposed drift. Increasing the target displacement, diagonal step-wise cracks developed in both the specimen and the AEM model, in both directions through the vertical dry joints and the horizontal glue mortar bed joints. Despite the model wasn't able

to capture the block cracking, due to the absence of the units discretisation, failure mechanisms, lateral stiffness and residual lateral strength were in agreement with the experimental outcomes.

Figure 6.6 Experimental versus AEM and EFM deformed shape of MB1 at zero and at maximum positive and negative drift attained in the last cycle

Figure 6.7 Experimental versus AEM and EFM force-displacement curves and dissipated energy for MB2

Figure 6.8 Experimental versus AEM and EFM deformed shape of MB2 at zero and at maximum positive and negative drift attained in the last cycle

The EFM predicted a flexural-gaping behaviour in the first cycles when a peak lateral strength of 113 kN was attained. Then, a shear failure mechanism occurred after 0.4% of drift ratio, in agreement with the experimental findings. The residual lateral strength predicted by the EFM was 97 kN, lower than the experimental counterpart, which was around 115 kN; the peak value was underestimated as well (113 kN and 126 kN for EFM and experimental test, respectively). Differently from the AEM, the EFM well captured the

energy dissipated in the last cycles, whereas it was overestimated for cycles from 0.4% to 0.6% of drift ratio.

6.6.3 MB3

The specimen MB3 showed the first visible cracks at a level of drift of 0.10-0.30%, with step-wise cracks in the joints and through the units. At a level of drift of 0.40%, a drop of strength occurred due to the development of a corner-to-corner crack along the two diagonals, passing through units. The test was stopped at a level of drift of 0.50% due to an extensive damage level and a significant drop of strength. The panel showed a shear failure mechanism with bi-diagonal cracks passing through units.

Similarly to what was already seen for MB2, the AEM model of MB3 predicted the diagonal shear cracking as well as the residual strength capacity attained by the specimen. The model underestimated the maximum lateral strength capacity, predicting a maximum base shear of 155 kN, where the specimen reached 170 kN. However, the absence of a failure surface in the brick units prevented the discrete model capability to reproduce diagonal cracks passing through the clay blocks. The AEM model underestimated the energy dissipated, especially in the last cycles.

The EFM predicted a shear mechanism with a peak lateral strength of 153 kN and a residual of 133 kN, slightly underestimating the experimental values. On the other hand, the energy dissipated was in good agreement with the experimental test. The comparison, for each cycle, between the energy dissipated by the specimen and the numerical models and the experimental versus numerical force-displacement curves are presented in Figure 6.9. The comparison in terms of damage patterns is presented in Figure 6.10.

6.6.4 MB4

The specimen MB4 developed step-wise bi-diagonal cracks passing through bed and head joints, starting from 0.05%-0.10% of drift ratio. The step-wise cracks spread throughout the panel with increasing the imposed drift, growing in number, length and width. The specimen MB4 showed a gaping behaviour with negligible damage in the units and without any strength degradation. The test was stopped at 2% of drift ratio, whereas the peak force of 277 kN occurred at 0.10-0.20% of drift ratio. As already shown by MB1, the reduction of strength after the attainment of the peak can be related to the loss of the tensile strength contribution of the mortar bed joints.

The AEM model predicted a gaping behaviour with peak and residual strength consistent with the experimental ones. The experimental versus numerical force-displacement curve is presented by Figure 6.11. The numerical model presented a peak of lateral strength due to the attainment of the tensile strength in the glue mortar, around 0.05% of drift ratio, in advance of the experimental test, which reached the peak around the 0.1-0.2% of drift ratio. The maximum base shear attained by the AEM model was equal to the experimental value (i.e. 277 kN), where the residual lateral strength was 238 kN (240 kN experimentally).
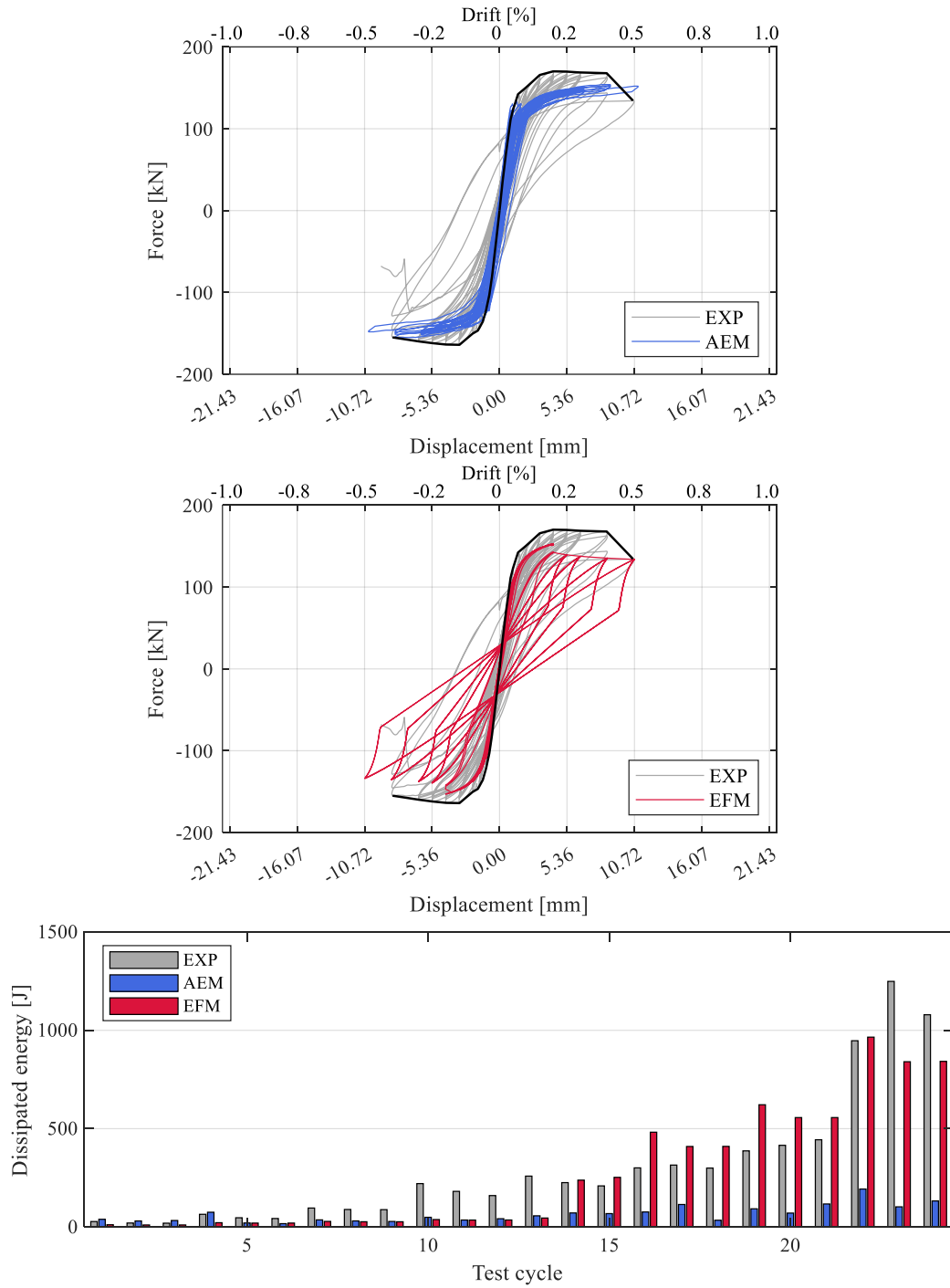
Figure 6.9 Experimental versus AEM and EFM force-displacement curves and dissipated energy for MB3

MB3
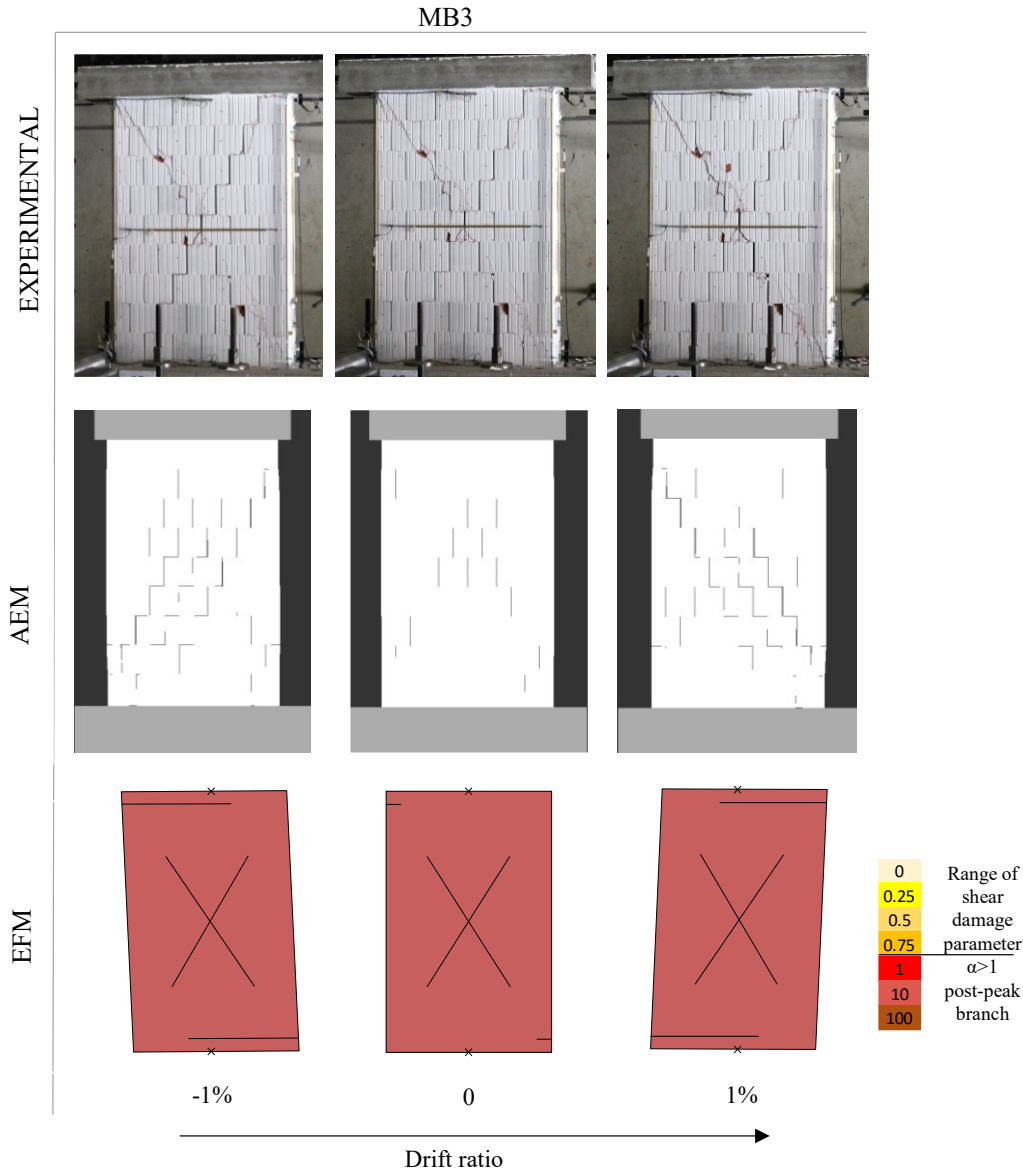
Figure 6.10 Experimental versus AEM and EFM deformed shape of MB3 at zero and at maximum positive and negative drift attained in the last cycle

In the AEM, the first damage in bed joints occurred around 0.05-0.1% of drift ratio, followed by damage on head joints with the first springs separation in the dry vertical joints around 0.37% of drift ratio. Increasing the applied displacement, diagonal step-wise cracks developed in the wall, increasing their width as also shown by the specimen. The AEM model reproduced satisfactorily the gaping behaviour presented by the specimen, showing the classical step-wise diagonal cracks with the development of triangular masonry wedges. The experimental versus numerical deformed shape is presented in Figure 6.12. Comparing

the energy dissipated by the specimen and by the AEM model, a good agreement was found in every cycle (Figure 6.11).

The EFM experienced a pure "gaping" behaviour with a maximum lateral strength of 235 kN and a residual of 225 kN, both slightly lower than the experimental values. As the EFM strength criterion associated to the gaping behaviour was derived from the flexural one, the energy dissipated was underestimated.

6.6.5 MB5

The specimen MB5 showed the first cracks in the bed- and head joints at a level of drift of 0.05-0.1%. These cracks grew up after 0.1% of drift ratio, developing step-wise diagonal cracks. Then, up to a level of drift of 0.50%, the cracks developed in the units at the upper corners grew up, spalling some shells. From 0.60% of drift ratio, new diagonal cracks developed in the units, spreading in the panel up to the attainment of the ultimate conditions at a level of drift of 1%. The test was stopped when the spalling of several units along the diagonal was evident, and a sudden strength degradation occurred. The specimen MB5 presented a hybrid behaviour with a gaping response and step-wise diagonal cracking through the bed and head joints at the beginning of the test. Then, the wall developed a shear response with failures of the units.

In the AEM simulation, the model exhibited a small peak of strength, similar to the ones presented by MB1 and MB4, when loaded in the positive direction. That peak did not occur in the experimental test, where the force-displacement curve showed a more significant stiffness deterioration with respect to the numerical curve (Figure 6.13). The AEM model exhibited a residual strength capacity lower with respect to the experimental one, which showed a greater energy dissipation and stiffness deterioration at the end of the test. The maximum lateral strength predicted by the model was 312 kN, where the specimen reached a maximum base shear of 354 kN, whereas the residual values were closer (320 kN and 310 kN for the specimen and the AEM model respectively). Despite the differences found in the force-displacement curve, the AEM model showed the same behaviour presented by the specimen with an initial pure gaping behaviour with the development of diagonal cracks and masonry wedges in the initial cycles. The shear damage and the unit failures experienced by the specimen at the end of the test were underestimated. In this model, clay units were divided to allow the failure of the unit, but only a few cracks passing through the blocks located at the wall top left corner were detected, whereas the specimen showed several units cracked in compression located at the wall corners. This phenomenon explains the differences in the comparison between energy dissipated by the model and the specimen presented for each cycle in Figure 6.14.
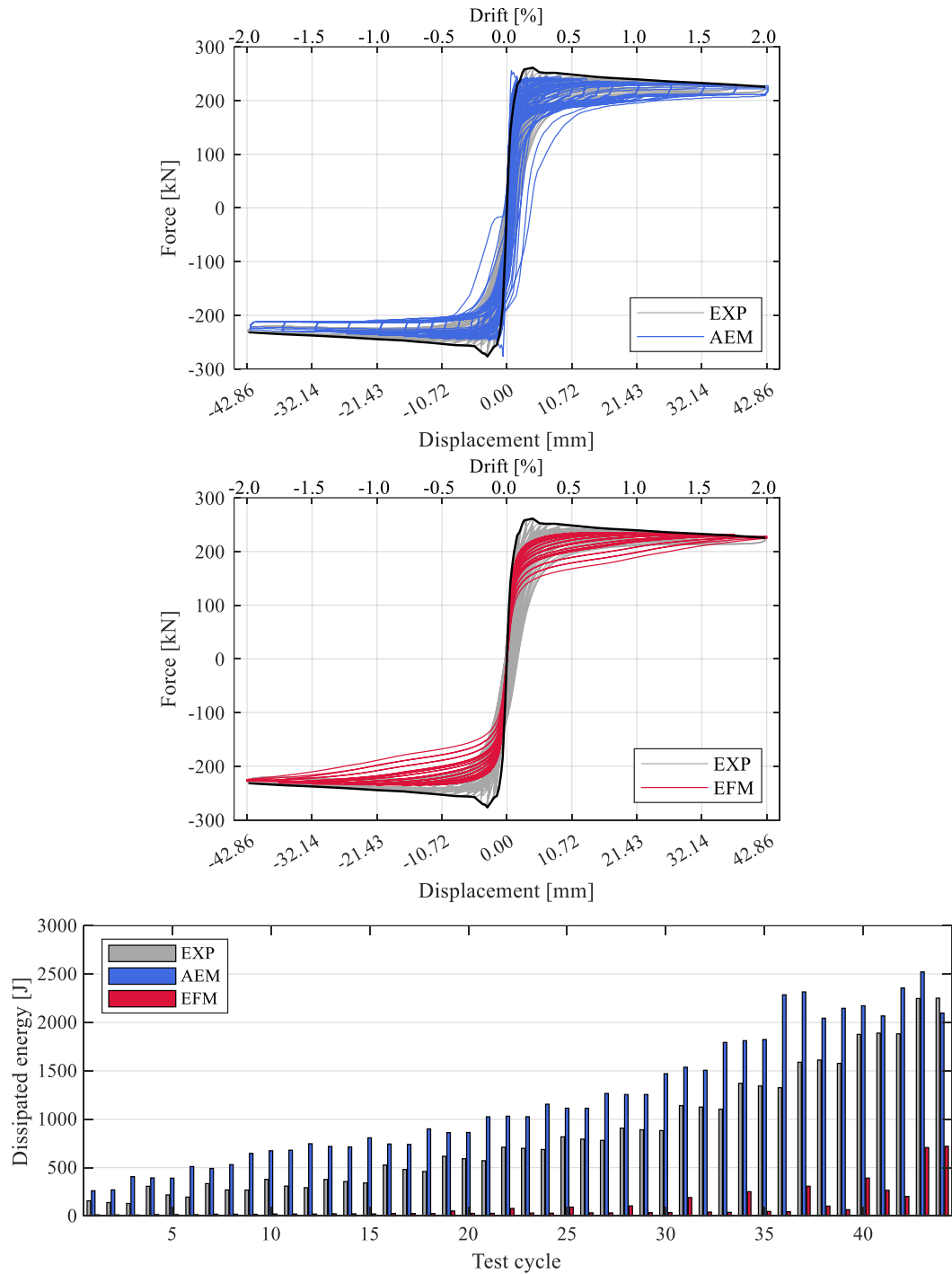
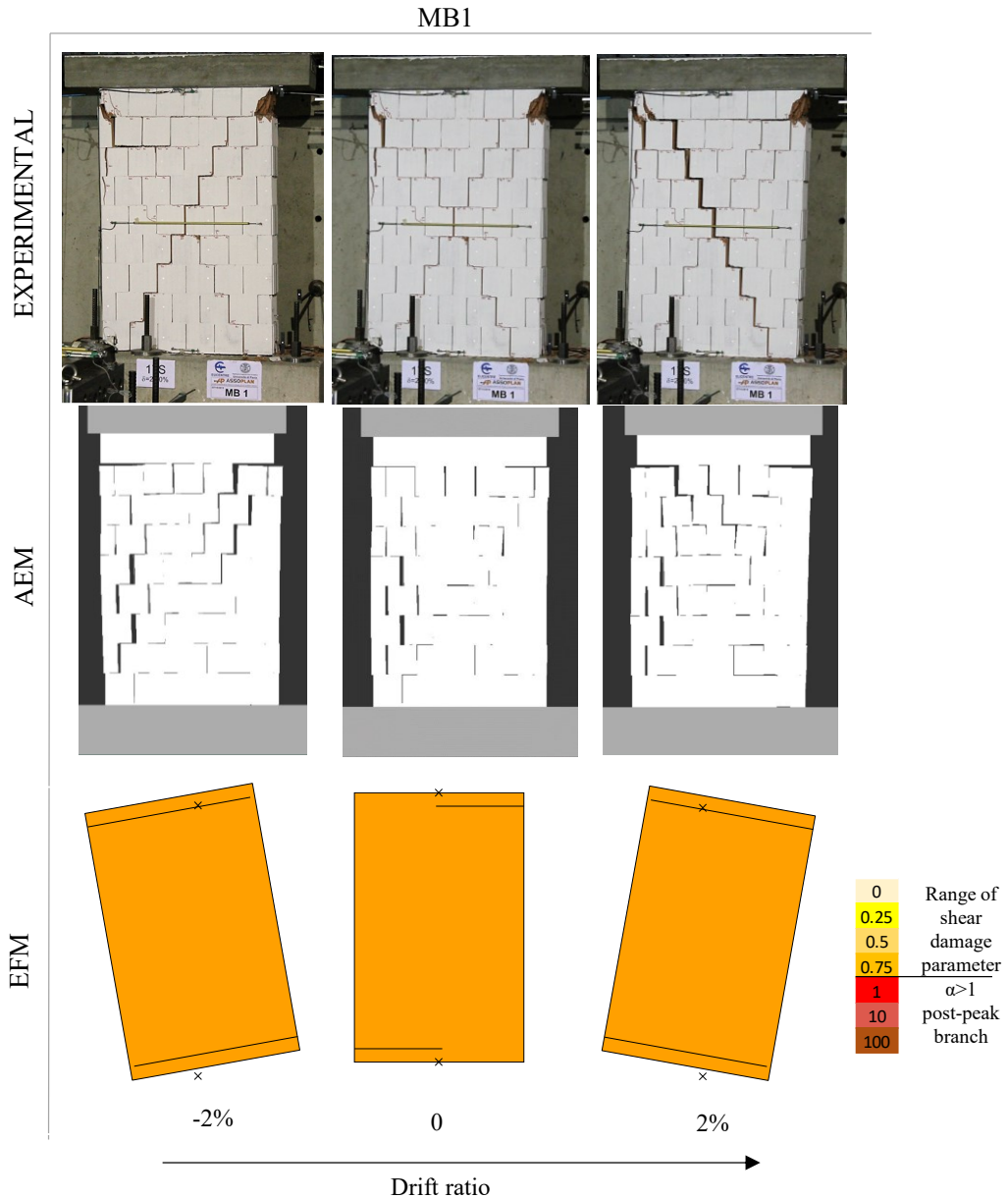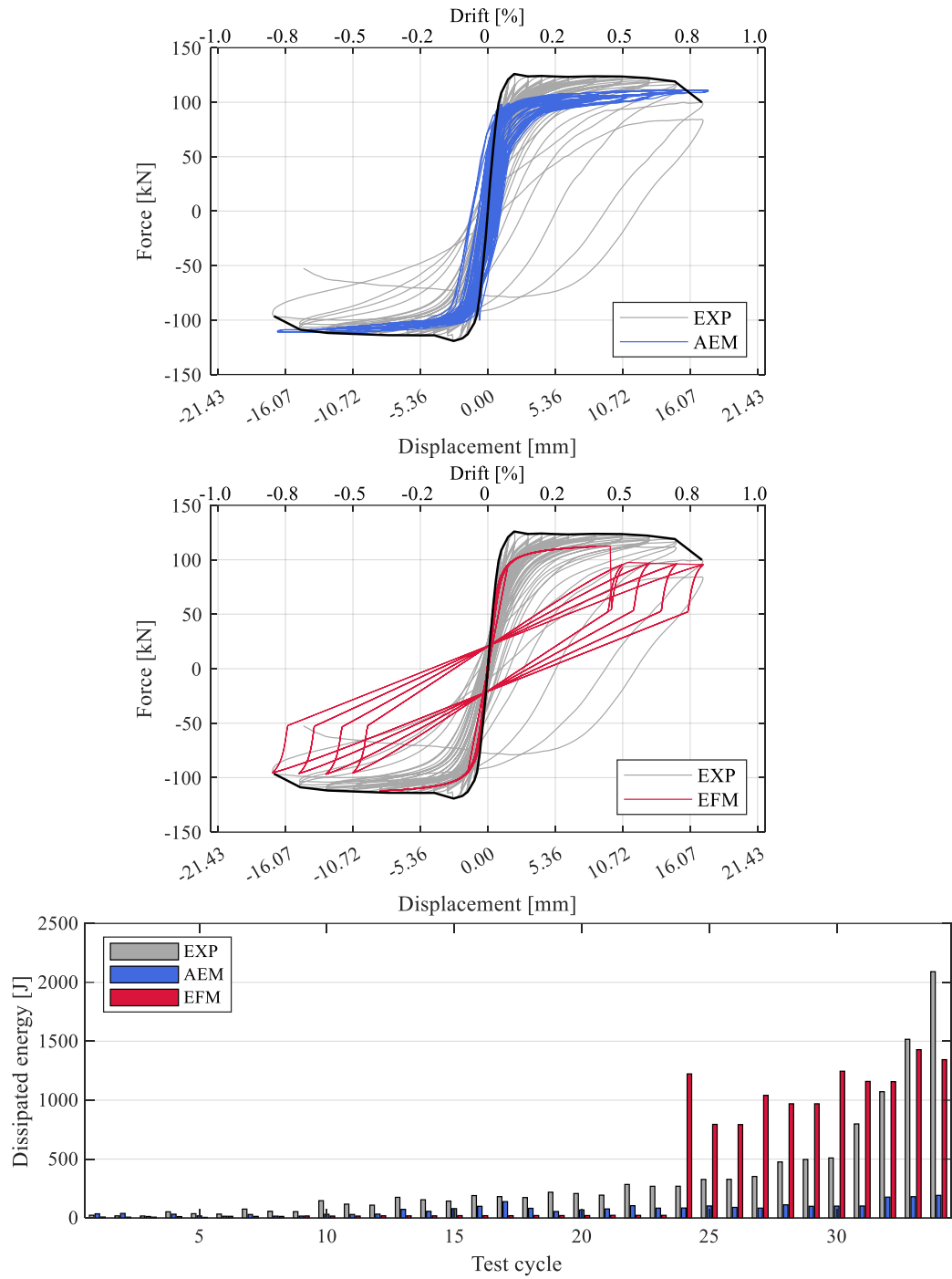Figure 6.11 Experimental versus AEM and EFM force-displacement curves and dissipated energy for MB4
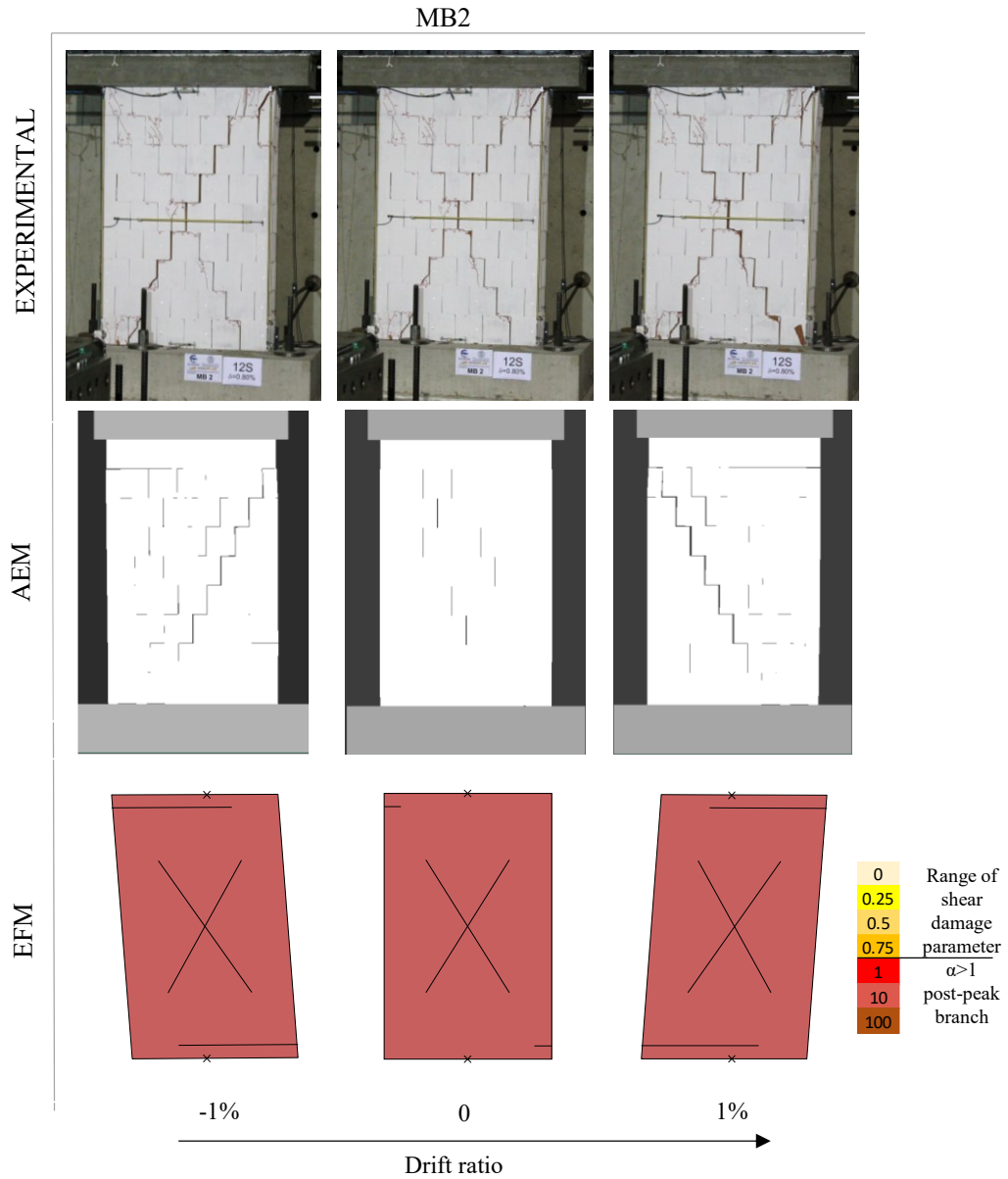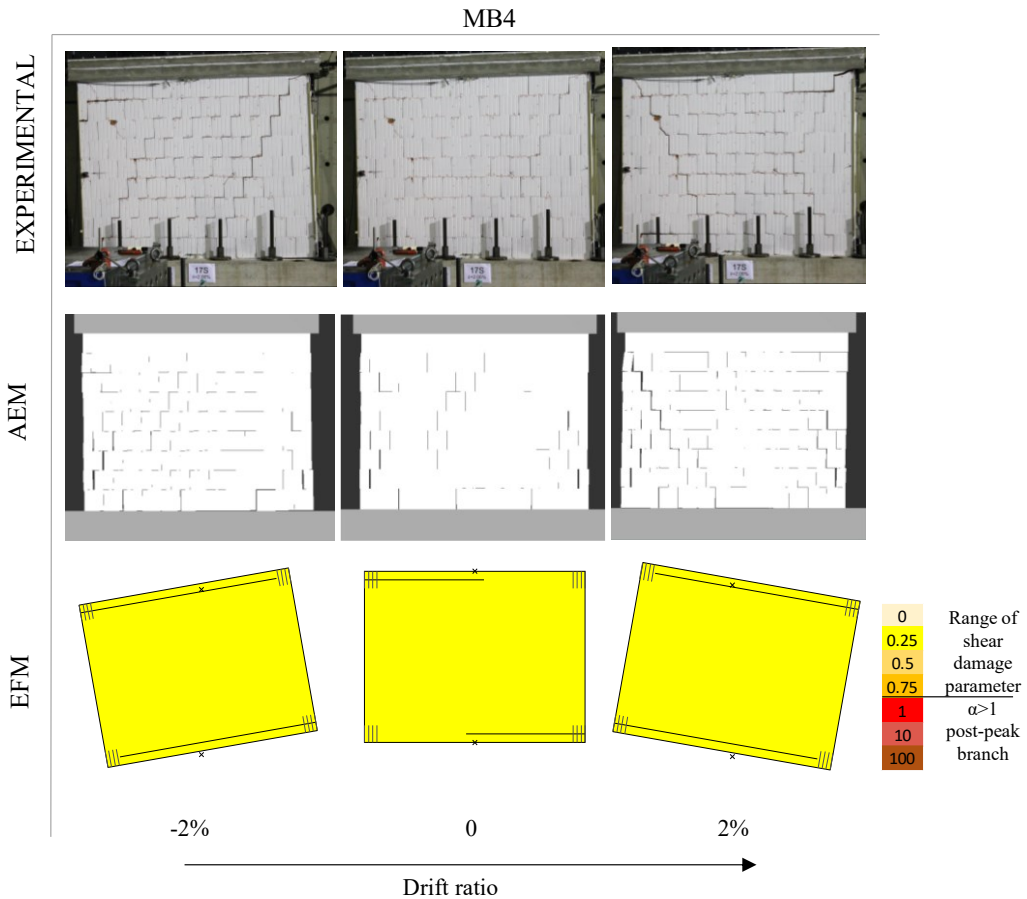
Figure 6.12 Experimental versus AEM and EFM deformed shape of MB4 at zero and at maximum positive and negative drift attained in the last cycle

The EFM predicted a gaping mechanism with a peak lateral strength capacity of 332 kN kept constant up to the last cycle. The energy dissipation was significantly underestimated, although light shear damage occurred. Both numerical models predicted a gaping mechanism contrary to what was exhibited by the specimen. This was also caused by the slightly different loading protocol employed in this last experiment. Indeed, this test was interrupted and re-started due to a problem with the vertical actuator and the specimen was maybe already damaged in the first considered cycles, causing a more extensive damage propagation and early stiffness deterioration. This also explains the need to reduce the glue mortar elastic and shear modulus (of factor 2) to reproduce the experimental stiffness with the AEM model.
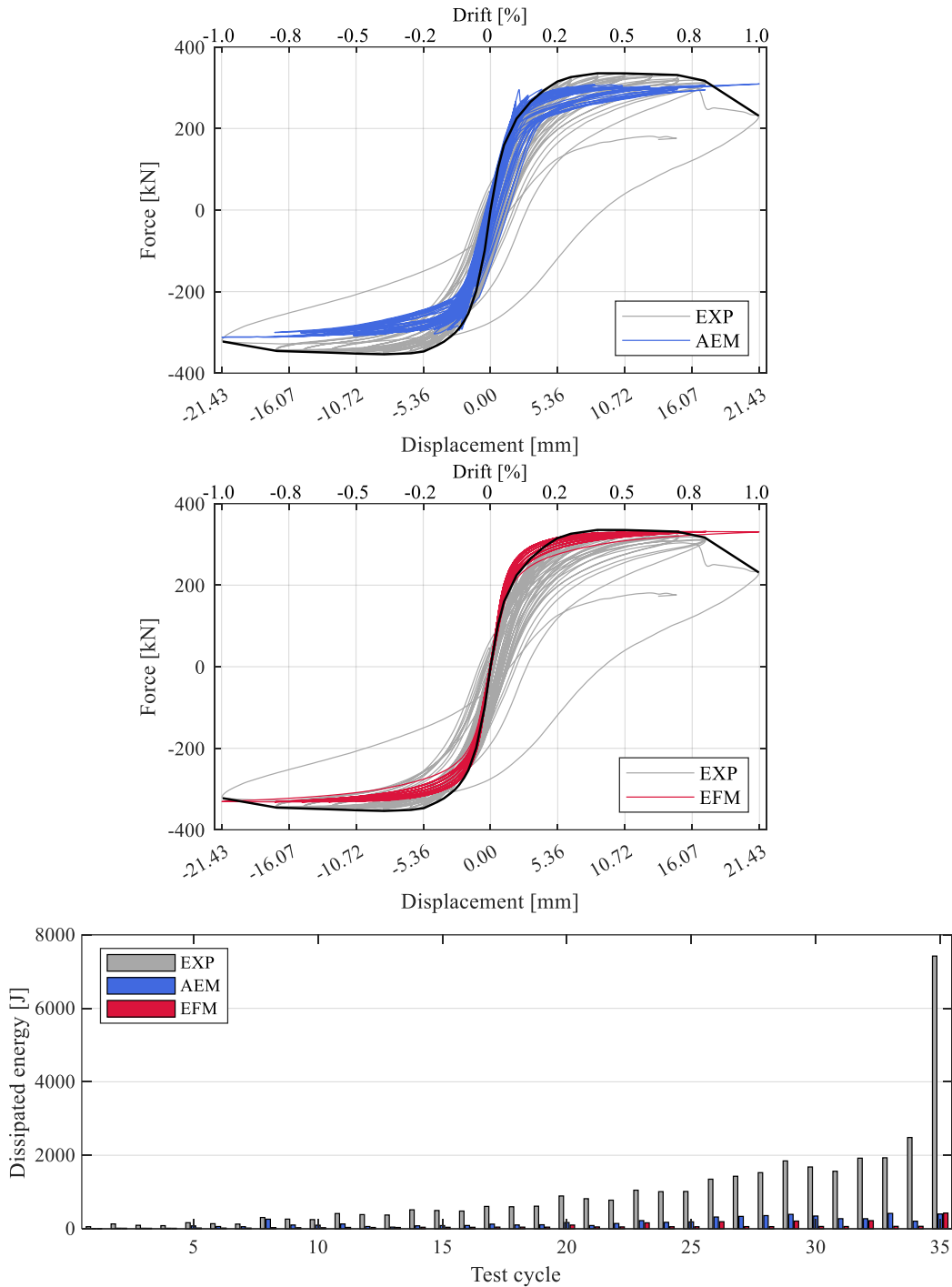
Figure 6.13 Experimental versus AEM and EFM force-displacement curves and dissipated energy for MB5
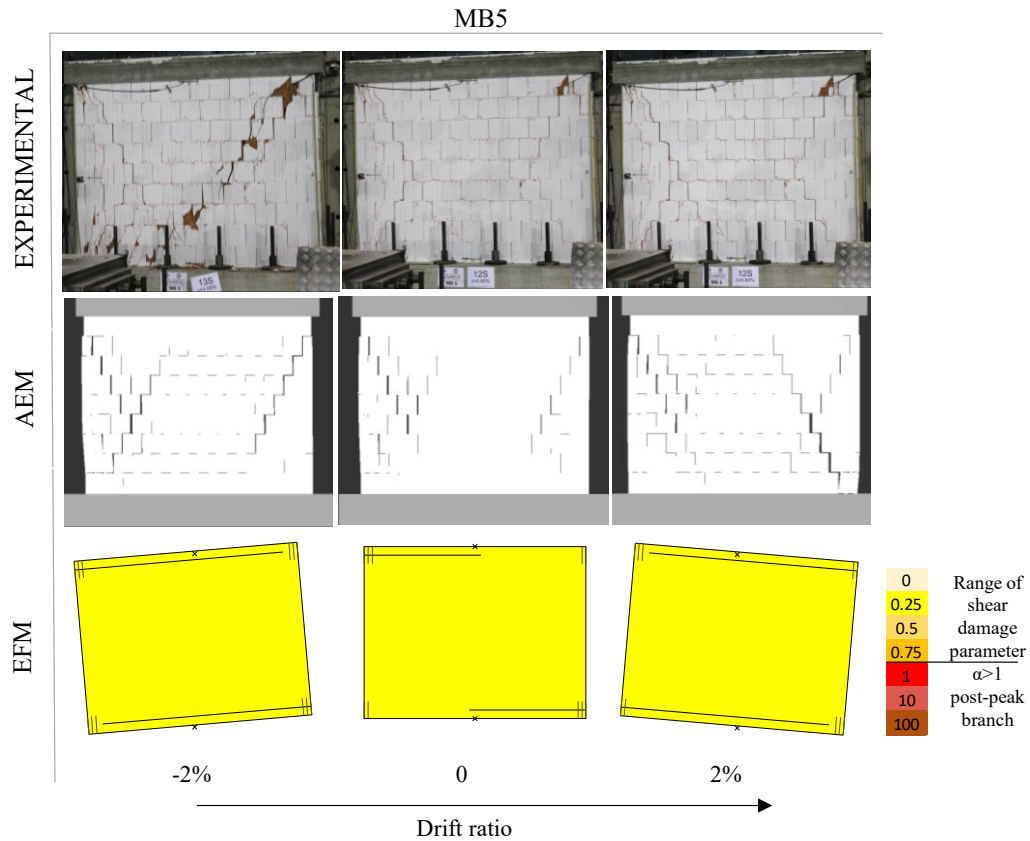
Figure 6.14 Experimental versus AEM and EFM deformed shape of MB5 at zero and at maximum positive and negative drift attained in the last cycle

6.7 Conclusions and future developments

A recent experimental campaign performed by Morandi et al. (2021) investigated the seismic performance of masonry with unfilled head joints in order to evaluate the applicability of this solution in moderate seismic areas. In this work, a discrete numerical model was validated with the aim of extending the experimental results and developing a reliable benchmark for the validation of simplified models.

The AEM has already proved to be capable of reproducing masonry mechanical behaviour, and several authors used it for component tests and full-scale tests simulations. However, based on the author's knowledge, it was never applied to masonry with unfilled head joints and thin-layer glue mortar bed joints. In this study, the capability of AEM to reproduce this masonry typology was investigated. First, the mechanical properties employed in the AEM model were obtained from the available characterisation tests, then shear-compression tests on five walls with different compression levels and aspect ratios were performed, and the results were compared with the experimental outcomes (summarised in Table 6.6). Moreover, a simplified modelling approach, the EFM by macroelement was employed for the simulation of the same tests performed using the AEM. A new strength criterion,

implemented to describe the "gaping" behaviour experienced by the specimens, was tested, simulating the five shear-compression tests.

The AEM well predicted the hysteretic response, failure mode and damage pattern of the five tests. The gaping behaviour experienced by the specimens MB1 and MB4 was well captured in terms of force-displacement hysteretic curve, damage and energy dissipation. On the other hand, when the failure mode involved the failure of units, the model couldn't reproduce the cracks passing through blocks with good accuracy, leading to different hysteretic curves and energy dissipation. Future development of this work may try to overcome this problem, mainly related to the units' discretisation.

The EFM predicted the same failure mechanisms experienced by the specimens and the lateral strength with good agreement. The EFM was also capable of predicting the energy dissipated in the shear failure modes, whereas it underestimated the dissipation of the gaping mechanism. Table 6.6 summarises the lateral strength capacities and failure modes obtained with the AEM and EFM models compared to the experimental tests. Despite the differences found between AEM and experimental results when the specimen exhibited shear or hybrid failures, the AEM model successfully captured the gaping behaviour of MB1 and MB4, including the first peak caused by the tensile strength of the glue mortar bed joints.

Table 6.6 Material property of horizontal joint material in AEM

	Experimental			EFM			AEM		
	V_{peak} [kN]	V_{res} [kN]	failure mechanism	V_{peak} [kN]	V_{res} [kN]	failure mechanism	V_{peak} [kN]	V_{res} [kN]	failure mechanism
MB1	75	44	"Gaping"-Flexural	39	39	"Gaping"-Flexural	71	38	"Gaping"
MB2	126	115	"Gaping"-Shear	113	97	"Gaping"-Shear	111	110	"Gaping"-Shear
MB3	170	157	Shear	153	133	"Gaping"-Shear	155	150	"Gaping"-Shear
MB4	277	240	"Gaping"	235	225	"Gaping"	277	238	"Gaping"
MB4	354	320	"Gaping"-Shear	332	330	"Gaping"	312	310	"Gaping"

These encouraging results suggest the AEM model can be used to extend the experimental findings investigating the dynamic response of this masonry typology, testing the behaviour of single piers individually or in more complex structural systems. Future development of this study may also involve the use of the AEM to perform nonlinear dynamic analyses of URM piers subjected simultaneously to 3D displacement time histories at top and bottom. This would allow substructuring of a detailed component model from a complete building model analysed with the EFM.

References

Akkar S, Sandikkaya MA, Senyurt M, Azari Sisi A, Ay BO, Traversa P, Douglas J, Cotton F, Luzi L, Hernandez B, Godey S (2014) Reference database for seismic ground-motion in Europe (RESORCE), Bull Earthq Eng 12:311-339.

Bracchi S, Galasco A, Penna A (2021) A novel macroelement model for the nonlinear analysis of masonry buildings . Part 1 : Axial and flexural behavior. Earthq Eng Sructural Dyn 50:2233–2252. https://doi.org/10.1002/eqe.3445.

Bracchi S, Penna A (2021) A novel macroelement model for the non-linear analysis of masonry buildings. Part 2: Shear behavior. Earthq Eng Struct Dyn 50:2212–2232. https://doi.org/10.1002/eqe.3444.

European Committee for Standardization (CEN); (2005) Eurocode 8: Design of structures for earthquake resistance – Part 3: General rules, seismic actions and rules for buildings, Design Code EN 1998-3. Eur Comm Stand Brussels.

European Committee for Standardization (CEN); Eurocode 6: Design of masonry structures, Part 1--1: General rules for reinforced and unreinforced masonry structures. Eur Comm Stand Belgium.

D.M. 17/01/2018 (2018) Norme Tecniche per le Costruzioni (NTC2018), Gazzetta Ufficiale, n. 42 del 20/ 02/2018- Supplemento ordinario n.8 (in Italian).

D.M. 20/11/1987. (1987) Norme tecniche per la progettazione, esecuzione e collaudo degli edifici in muratura e per il loro consolidamento, Gazzetta Ufficiale, n. 285 del 05/12/1987 (in Italian).

Jäger W, Schöps P eter (2008) Proposals for an advanced design model of masonry under lateral loads for the implementation in Eurocode 6-1-1. ESECMaSE Project.

Karbassi A, Nollet M-J (2013) Performance-based seismic vulnerability evaluation of masonry buildings using applied element method in a non-linear dynamic-based analytical procedure. Earthq Spectra 29:399–426. https://doi.org/https://doi.org/10.1193/1.4000148.

Kaushik HB, Rai DC, Jain SK (2007) Stress-strain characteristics of clay brick masonry under uniaxial compression. J Mater Civ Eng 19:728–739.

Kawai T (1978) New discrete models and their application to seismic response analysis of structures. Nucl Eng Des 48:207–229.

Keys RA, Clubley SK (2017) Establishing a predictive method for blast induced masonry debris distribution using experimental and numerical methods. Eng Fail Anal 82:82–91. https://doi.org/10.1016/j.engfailanal.2017.07.017.

Lagomarsino S, Penna A, Galasco A, Cattari S (2013) TREMURI program: An equivalent frame model for the non-linear seismic analysis of masonry buildings. Eng Struct 56:1787–1799. https://doi.org/10.1016/j.engstruct.2013.08.002.

Magenes G, Calvi GM (1997) In-plane seismic response of brick masonry walls. Earthq Eng Struct Dyn 26:1091–1112.

Malomo D, Morandini C, Crowley H, et al (2021) Impact of ground floor openings percentage on the dynamic response of typical Dutch URM cavity wall structures. Bull Earthq Eng 19:403–428. https://doi.org/10.1007/s10518-020-00976-z.

Malomo D, Pinho R, Penna A (2019) Applied Element Modelling of the Dynamic Response of a Full-Scale Clay Brick Masonry Building Specimen with Flexible Diaphragms. Int J Archit Herit. https://doi.org/10.1080/15583058.2019.1616004.

Mann W, Müller H (1982) Failure of shear-stressed masonry: an enlarged theory, tests and application to shear walls. In: Proceedings of the British Ceramic Society 223–235.

Mayorca P, Meguro K (2003) Modeling Masonry Structures using the Applied Element Method. Seisan Kenkyu,j 55:581–584.

Meguro K, Tagel-Din H (2000) Applied element method for structural analysis: Theory and application for linear materials. Struct Eng Eng 17:21–35.

Morandi P, Albanesi L, Magenes G (2021) In-Plane Cyclic Response of New Urm Systems with Thin Web and Shell Clay Units. J Earthq Eng 25:1533–1564. https://doi.org/10.1080/13632469.2019.1586801.

Penna A, Lagomarsino S, Galasco A (2014) A nonlinear macroelement model for the seismic analysis of masonry buildings. Earthq Eng Struct Dyn 43:159–179. https://doi.org/10.1002/eqe.2335

Pulatsu B, Bretas EM, Lourenço PB (2016) Discrete element modeling of masonry structures: Validation and application. Earthquakes Struct 11:563–582. https://doi.org/10.12989/eas.2016.11.4.563.

Tomaževič M, Lutman M, Bosiljkov V (2006) Robustness of hollow clay masonry units and seismic behaviour of masonry walls. Constr Build Mater 20:1028–1039. https://doi.org/10.1016/j.conbuildmat.2005.05.001.

7. Using the Applied Element Method for the numerical prediction of debris distribution

Morandini, C., Senaldi, I., Casarotti, C. and Penna, A. Numerical prediction of masonry debris distribution after an earthquake *(to be submitted).*

Abstract

The vulnerability of historical centres and the problem encountered in the post-earthquake rescue operations due to the presence of debris pointed out the need to account for the space occupied by rubble in the emergency plans to avoid the slow-down of the emergency vehicles. Predicting the amount and extent of debris after an event is crucial to avoid infrastructure interruption and prioritise strengthening interventions. However, the available approaches for evaluating debris distribution are mostly based on relationships derived from experimental observations and thus limited data. Numerical simulations may significantly contribute considering multiple building configurations, materials and seismic input. If, on the one hand, advanced modelling strategies are capable of simulating the structural response up the collapse and consequently can be employed for predicting debris distribution, on the other hand, the time required for the analyses restrains their application. On the contrary, simplified modelling strategies allow performing a large number of analyses, but they cannot reproduce the building collapse. In this work, discrete numerical models, based on the Applied Element Methods (AEM), were employed to predict the distribution of debris, combining their use with the more simplified Equivalent Frame Models (EFM). Moreover, a first attempt is presented for simulating the behaviour of double-leaf stone masonry structures with AEM models. Both AEM and EFM modelling strategies were validated through the simulation of experimental tests on individual walls and a full-scale building. The proposed methodology for the evaluation of the extent of debris demonstrates the possibility of integrating the use of simplified and advanced models to predict the collapse and the space occupied after an earthquake, offering a valid alternative to the available simplified empirical formulae.

Keywords: collapse, debris, earthquake, emergency plan, historical city centres

7.1 Introduction

Masonry structures represent a large portion of the Italian building stock, including churches, residential and monumental buildings. Recent and past earthquakes confirmed their vulnerability due to several factors (e.g. weak material properties, loads distribution, irregular bond arrangement, weak connections with orthogonal walls and floors, flexible diaphragms and interaction with adjacent structures), which influence the global and local

response to lateral actions. The lack of proper construction details, frequent in the historical centres built before the introduction of earthquake-proof standards, contributes to the activation of out-of-plane (OOP) mechanisms. The seismic response of existing masonry buildings is often governed by local mechanisms that prevent exploiting the structural capacity provided by developing a global response governed by in-plane mechanisms. These brittle responses more easily cause partial or global collapses with debris falling and possible obstructing the adjacent roads.

Identifying the possible collapse mechanisms and predicting the space occupied by debris become crucial for emergency management after a seismic event. Indeed, emergency vehicles have to reach at least the relevant buildings (e.g. hospitals, schools, police stations) immediately after an earthquake, and, more generally, they have to access the urban centres for rescue operations. Then, the need to move people due to unusable buildings may increase the roads demand, where their capacity may be reduced by the presence of debris (Goretti and Sarli 2006). In this context, the development of reliable models for predicting the collapse mechanisms and the consequent space occupied by debris become crucial to plan strengthening interventions on the more vulnerable structures to avoid the obstruction of the town's access.

Figure 7.1 Examples of local out-of-plane seismic damage to buildings, observed after the Central Italy sequence of 2016-2017 (Photos: A. Penna – adapted from (Penna et al. 2022))

Several researchers analysed the problem of the seismic risk and loss assessment of historical city centres (e.g. Bernabei et al. 2021), evaluating the probability that falling debris occlude, partially or totally, the urban streets. A comprehensive review of the presently available methodologies to assess the amount of debris generated after a seismic event is presented by Bernardini et al. (2020). In their research, they compared the amount of debris predicted with different approaches with the one produced by a real earthquake. According to Bernardini et al. (2020), the available methods can be divided into three groups. The first group includes methods based on geometrical aspects, building height and street width and does not consider buildings' vulnerability or earthquake intensities (Ferlito and Pizza 2011; Italian technical commission for seismic micro-zoning 2014). The second group includes methods considering geometrical characteristics, earthquake intensities and

building vulnerability, assessing the amount of debris through empirical relationships (Quagliarini et al. 2016; Santarelli et al. 2018). The third group also accounts for buildings' damage grade, determining the maximum probable distance that debris can reach (Artese and Achilli 2019). The abovementioned approaches evaluate the probable amount of debris with experiments-based relationships, which are unavoidably limited to the specific conditions that occurred in the considered event and the amount of debris measured in the in-situ surveys.

This work was carried out with the aim of proposing a procedure to analyse a large number of possible building types and seismic inputs, predicting the possible collapse and the volume and space occupied by produced debris, based on the structural characteristics and on the seismic action. To this aim, an efficient numerical tool is needed to process a large number of dynamic analyses using different ground motions and building typologies, able to represent the structural response up to the complete collapse. The use of advanced numerical models based on discrete methods (e.g. DEM, AEM) allows explicitly representing each masonry component and their interaction, including elements separation and detachment. The Applied Element Method, belonging to Rigid Body and Spring Model (RBSM) family and originally proposed by Meguro and Tagel-Din (2000) was selected in this endeavour. Thanks to his efficient solver, the AEM allows the numerical investigation of masonry structures up the collapse in a reasonable time, but still does not allow performing a significant number of analyses. The combined use of advanced modelling approaches and simplified strategies permits investigating a larger number of configurations considering a more extensive suite of ground motions.

In this work, a new procedure was proposed combining the use of simplified Equivalent Frame Models (EFM) to predict the global response of unreinforced masonry buildings and a discrete modelling approach to evaluate the possible collapse mechanisms and the amount of debris produced.

According to the proposed methodology, two models were developed for each case study: an EFM, representing the entire building, and a partial AEM model, considering only the portion of the structure potentially involved in the local mechanism. The EFM was used to analyse the global response of the structure performing incremental dynamic analyses with the input ground motions presented in 7.3.1. Among these, the input motions that may cause the collapse were selected, monitoring the exceedance of established displacement thresholds. A set of displacement histories obtained from the global EFM models was then applied to the partial AEM models to investigate the collapse mechanism and to evaluate the volume of debris produced. Those displacements described the boundary condition of the portion involved in the local mechanism. This further investigation performed with discrete models was conducted considering the displacements obtained in a selection of the analyses executed with the global EFM models.

Both EFM and AEM models were validated through the simulation of quasi-static tests on individual walls and a full-scale building shake-table test. Those experiments were conducted as a part of a campaign that involved characterisation tests on materials, shear-

compression tests on structural components and three full-scale shake-table tests. The related research project was realised at the Eucentre laboratory of Pavia, Italy, in collaboration with the Italian Department of civil protection, and it was focused on the vulnerability assessment and mitigation of existing masonry buildings (Magenes et al.,2010a). The three specimens tested were realised to represent three levels of strengthening interventions. The prototype considered in this work was the first specimen, a double-leaf stone masonry building with flexible timber diaphragms named Building 1.

Both numerical models (EFM and AEM) were calibrated simulating the shear-compression tests on walls and then validated replicating the shake-table test performed on the unreinforced prototype (Building 1). In the following, the employed modelling strategy is presented for both EFM (7.1.1) and AEM models (7.1.2), then the shear-compression tests (7.1.3) and their numerical simulation (7.1.4) are presented.

7.1.1 Equivalent Frame Model (EFM)

Experimental and post-earthquake observations indicated that in a masonry structure deformations are located in recurrent areas while others work as rigid parts. The EFM modelling strategy is based on this assumption and it idealises masonry structures with a frame of rigid nodes and deformable elements (i.e. spandrels and piers), as depicted in Figure 7.2a. Each deformable portion is modelled as a macroelement. In this work, the research version of TREMURI software (Lagomarsino et al. 2013) was used, considering the macroelement model proposed by Penna et al. (2014) for spandrel elements and the one improved by Bracchi et al. (2021) for pier elements.

A macroelement is a two-node element with eight degrees of freedom (DOFs), and it consists of three main parts: a central body where only shear deformations are allowed and where two internal DOFs are placed, and two zero-thickness spring interfaces governing the axial-flexural behaviour, where six DOFs are located, Figure 7.2b. The shear damage model is based on the one proposed by Gambarotta and Lagomarsino (1997), Figure 7.2d, whereas the behaviour of the top and bottom interfaces is described by the no-tension model with the bilinear law in compression proposed by Bracchi et al. (2021), Figure 7.2c, or Penna et al. (2014), for piers and spandrels, respectively. The macroelement response is described by eight parameters: the density, ρ, the elastic and shear moduli of masonry, E_m and G_m, f_m and f_t, which are the compressive and tensile strength, and Gc_t e β that are phenomenological parameters governing the nonlinear shear response. Gc_t, controls the macroelement inelastic shear deformability, and β influences the slope of the post-peak softening branch. The shear damage variable α_s represents the damage level, and it is equal to 1 when the panel attains to the maximum peak shear strength, increasing in the post-peak softening branch. Damage levels and the influence of the parameter α_s are reported in Figure 7.2d. The shear failure is predicted by multiple shear strength criteria implemented in the macroelement by Bracchi and Penna (2021). In this work, the strength criterion was selected to be representative of the expected failure mode (i.e. diagonal shear failure due to the attainment of the tensile strength of masonry). The selected strength criterion is the one proposed by Turnšek and Sheppard (1980), accounting for the masonry tensile strength at the centre of the panel, f_{tu}, and with the correction proposed by Magenes and Calvi (1997) to consider the influence of the shear span ratio in the global criterion (7.1).

$$V = \frac{f_{tu}lt}{b(1 + \alpha_v)}\sqrt{\frac{N}{f_{tu}lt} + 1} \qquad (7.1)$$

Where α_v is the shear span ratio, and it is equal to h_0/l. h_0 is the distance between the section with zero moment and the section with the maximum moment, and l is the wall length. b accounts for the shear stress distribution at the centre of the panel and it depends on the ratio between the height and the length of the panel:

$$\begin{cases} 1.5 \; for \frac{h}{l} \geq 1.5 \; (i.e.\, for\, sleder\, panels) \\ \qquad 1 < h/k < 1.5 \\ 1 \; for \frac{h}{l} \leq 1 \; (i.e.\, for\, squat\, panels) \end{cases}$$

The damage level of the macroelement is associated with the damage parameter α_s
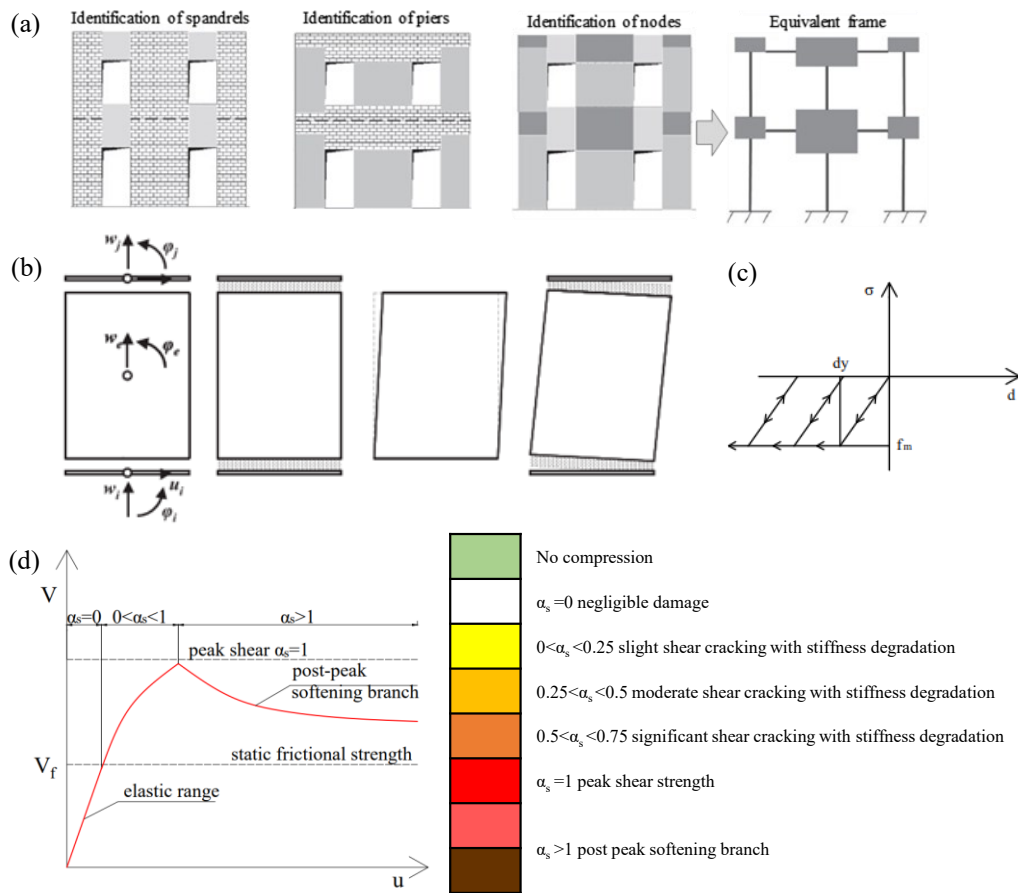
Figure 7.2 a) EF discretisation (Lagomarsino et al. 2013), b) macroelement (Penna et al. 2014), c) contitutive model in compression (Bracchi et al. 2021) and d) shear damage model (Gambarotta and Lagomarsino 1997) and damage color legend

Piers' mechanical properties of the global EFM were calibrated through the simulation of shear-compression tests, discussed in 7.1.3 and 7.1.4. and then validated through the simulation of the dynamic shake-table test carried out on the specimen named Building 1 (Magenes et al. 2010a).

7.1.2 Applied Element Method (AEM)

The AEM can be classified as a Rigid Body and Spring Model (RBSM). According to the AEM , masonry structures are represented as an assemble of rigid elements connected by zero-thickness springs interfaces, where material properties are lumped, and it can explicitly represents the actual brick arrangement. The material model in compression is the one developed originally by El-Kashif and Maekawa (2004) with a tension cut-off without any softening branch. The Coulomb friction model represents the sliding along mortar joints. Each spring interface is characterised by a normal and a shear stiffness evaluated through equations (2)-(5), where the nomenclature can be found in Figure 7.3. Springs placed between units and representing mortar-unit interaction are here named unit-mortar springs ($_{b\text{-}mo}$). Their normal ($k_{n,b\text{-}mo}$) and shear ($k_{s,b\text{-}mo}$) stiffnesses are evaluated considering mortar and unit springs in series by equations (7.2) and (7.3). In order to capture the possible cracking through brick, units may be further divided into two elements connected by unit-unit springs interfaces, evaluating their stiffnesses ($k_{n,b\text{-}b}$ and $k_{s,b\text{-}b}$) by equations (7.4) and (7.5). Where E_b, G_b, E_{mo} and G_{mo} are the unit and mortar Young's and shear moduli, respectively.

$$\frac{1}{k_{n,b-mo}} = \frac{a - l_{mo}}{E_b \, d \, t} + \frac{l_{mo}}{E_{mo} \, d \, t} \qquad (7.2) \qquad \frac{1}{k_{s,b-mo}} = \frac{a - l_{mo}}{G_b \, d \, t} + \frac{l_{mo}}{G_{mo} \, d \, t} \qquad (7.3)$$

$$\frac{1}{k_{n,b-b}} = \frac{a_b}{E_b \, d \, t} \qquad (7.4) \qquad \frac{1}{k_{s,b-b}} = \frac{a_b}{G_b \, d \, t} \qquad (7.5)$$
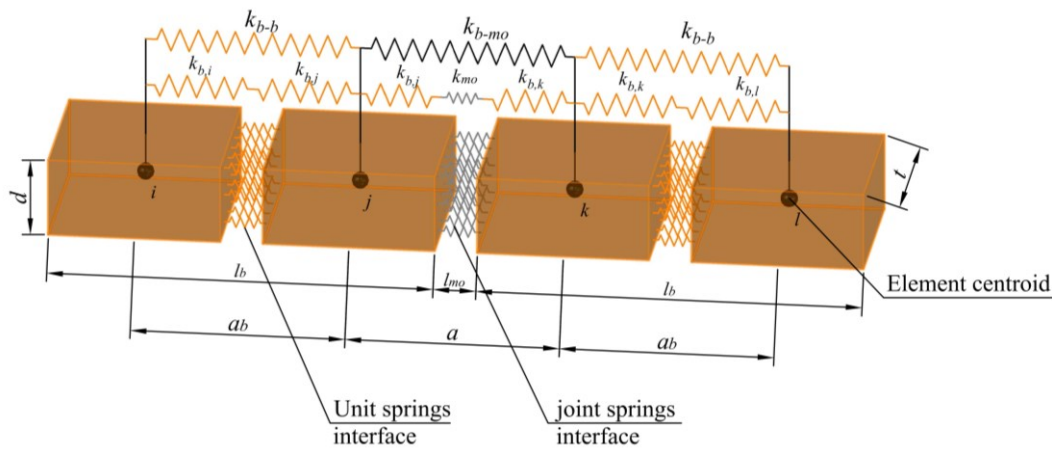
Figure 7.3 Masonry discretisation

7.1.3 Shear-compression tests

Five walls with different heights and compression levels were tested in a double-bending condition, applying a constant vertical load and a horizontal displacement history to the top beam. The tests were performed at the Eucentre laboratory of Pavia (Italy) by Magenes et al. (2010b). Geometry and compression level were chosen to be representative of the actual condition in the full-scale shake-table test.

Specimens were constructed on a reinforced concrete beam fixed to the rigid floor of the laboratory. The test set-up consisted of two actuators, rigidly connected to the steel beam fixed to the top spreader beam, which applied a constant vertical load, and a third one to apply a horizontal displacement history to the top beam. The vertical actuators also avoid any rotation, maintaining horizontal the top beam during the test. The first three cycles were performed in force control and the others in displacement control. At each cycle, the target displacement was reached three times with an increasing loading velocity with the target displacement, keeping a constant duration for each test. The tests were interrupted at the attainment of a significant drop of strength or at displacement corresponding to a drift level of 3%. The tests were performed on four specimens, two slender, named CS01 and CS02 (1.25 m x 2.5 m x 0.32 m) and two squat, named CT01 and CT02 (2.5 m x 2.5 m x 0.32 m).

The vertical compression of the specimen was chosen to be representative of the expected conditions of masonry panels in the full-scale shake-table tests of the experimental campaign. The maximum compression level expected in the dynamic tests was 0.2 MPa. As this value was considerably lower than the compressive strength of the masonry, in order to obtain a more general study on the material tested, the applied vertical compression levels (σ_0) were 0.2 MPa in CS02 and CT02 and 0.5 MPa in CS01 and CT01 specimens. The results of the tests on the five specimens are summarised in Table 7.1. Where E_m is the Young modulus and f_{tu} is the tensile strength of masonry inferred from the shear-compression tests.

Table 7.1 Summary of the results of the shear-compression tests (Magenes et al, 2010b)

	CS01	CS02	CT01	CT02
σ_0 [MPa]	0.5	0.2	0.5	0.2
Base Shear [kN]	94	48	234	154
Drift	0.5%	0.8%	0.5%	0.6%
Failure mechanism	shear	flexural-shear	shear	shear
f_{tu} [MPa]	0.16	0.10	0.13	0.10
E_m [MPa]	1650	3600	2400	1600

All four specimens exhibited a shear failure mechanism with diagonal cracking at the end of the tests. CS02, due to its low vertical stress, exhibited initial flexural cracks before failing in shear. The two squat piers exhibited a clear shear failure with diagonal cracks.

7.1.4 Simulation of the shear-compression tests

The mechanical properties of AEM and EFM models were calibrated through the simulation of shear-compression tests on panels CS01, CS02, CT01 and CT02. In this section, the comparison between experimental and numerical results is presented.

The shear-compression tests with the EFM were simulated, idealising each panel as a macroelement subjected to double-fixed boundary conditions and a cyclic test in displacement control. The shear failure is predicted by multiple shear strength criteria implemented by Bracchi and Penna (2021). Consistently to what was experimentally observed, the strength criterion assumed for the macroelement is the one proposed by Turnšek and Sheppard (1980) corresponded to the diagonal tensile failure of the masonry panel. The macroelement mechanical parameters, derived from characterisation tests (Table 7.4 and Table 7.1) and further refined through the simulation of shear-compression tests on panels, are summarised in Table 7.2. Where E_m and G_m are the elastic moduli and the shear modulus of masonry, f_m e f_t are the compressive strength and the tensile strength, and G_{ct} e β are phenomenological parameters governing the nonlinear shear response. G_{ct}, controlling macroelement inelastic shear deformability, and β, which influences the slope of the post-peak softening branch (Penna et al. 2014).

Table 7.2 Mechanical properties of the EFM macroelement

	E [MPa]	G [MPa]	f_m [MPa]	f_t [MPa]	Gc_t	β
CS01	1800	500	3.28	0.15	2.5	0.5
CS02	2500	400	3.28	0.075	1	0
CT01	1800	400	3.28	0.13	2.6	0.8
CT02	1800	300	3.28	0.085	2	0.6

In the AEM model, each block was modelled separately to replicate the specimen units dimensions and arrangement. Each stone unit was idealised into an equivalent regular block. This strategy was adopted to simplify the model and to use regular elements in a faster procedure. The height and thickness of the stone units were identified at each course and assumed for the regular AEM blocks as shown in Figure 7.4.

The mechanical properties assigned to the mortar-units interface of the AEM model were initially derived from characterisation tests and the available empirical and theoretical formulae (Jäger et al. 2004; Malomo et al. 2018). Then the interface parameters were refined through the simulation of shear-compression tests on panels and summarised in Table 7.3. E_i and G_i are the elastic and the shear moduli, and f_m and f_t are the compressive and tensile strength, respectively. The G/E ratio was assumed 0.35. The modelling strategy adopted for the AEM idealises the stone units as single elements without introducing any other failure surface inside each block. This allowed to reduce the computational cost. This simplification allowed cracks to propagate into interfaces between stone units and those properties governed the specimen failure.
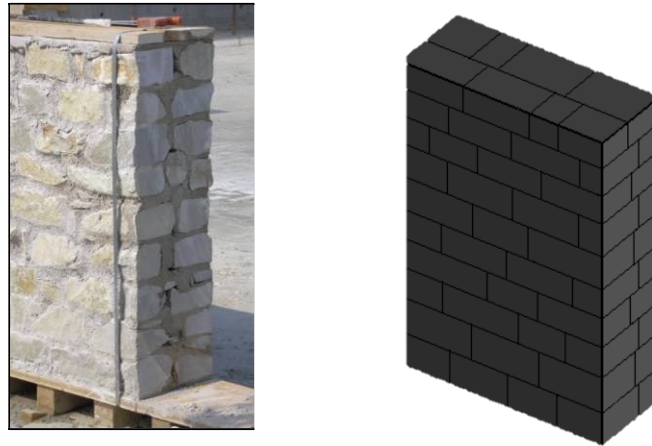
Figure 7.4 Experimental specimen tested in the vertical compression test (left, Magenes et al. 2010c) and its AEM counterpart (right).

Table 7.3 Mechanical properties of the mortar-units interface of the AEM model

	E_i [MPa]	G_i [MPa]	f_m [MPa]	f_t [MPa]
CS01	1130	395	3.28	0.17
CS02	1960	590	3.28	0.17
CT01	883	310	3.28	0.05
CT02	883	310	3.28	0.05

Figure 7.5 and Figure 7.6 report the comparison between experimental and numerical results of the shear-compression test on specimen CS01. The panel exhibited a diagonal shear failure with a maximum shear strength of 94 kN. The test was interrupted at 0.5% of maximum drift when the specimen exhibited a significant drop of lateral strength. Both models were able to represent the failure mode, the initial lateral stiffness and the lateral strength in terms of maximum base shear. The discrete model showed cracks at one edge and at the centre of the panel as exhibited by the experimental specimen. The macroelement of the EFM model presented a shear mechanism (attaining its peak shear strength when the shear damage parameter α was equal to 1).

Figure 7.7 and Figure 7.8 report the comparison between experimental and numerical shear-compression tests of CS02. The specimen CS02 showed a hybrid failure mechanism with a rocking behaviour in the first cycles of the experimental test, characterised by low energy dissipation in the hysteresis loops, cracks concentrated at the panel's edges, and diagonal cracks through the two leaves located at the centre of the panel in the last cycles with significant energy dissipation. The maximum base shear reached in the experimental test was 48 kN. Both the EFM and the AEM models presented the same failure mechanism, initial stiffness and maximum lateral strength shown by the specimen. The EFM model presented the flexural partialisation of the external sections and a shear failure mode with diagonal cracks at the centre of the panel. The parameter α represented the damage in the

EFM model, and the maximum shear strength was attained when α>1. The AEM model successfully predicted the hysteretic loop and the development of cracks at the base and propagated at the centre of the panel in the last cycles.

Figure 7.5 Comparison between the experimental and the numerical EFM and AEM response of CS01 in the shear-compression test

Figure 7.6 Comparison between numerical a) EFM and b) AEM) and c) experimental damage of CS01

In Figure 7.9 and Figure 7.9 the experimental vs numerical results of the shear-compression test on CT01 are reported. The specimen was subjected to a vertical compression of 0.5 MPa, and it initially showed horizontal cracks at the base. In the last cycles of the experimental test, the specimen developed diagonal cracks located at the centre of the panel. The experimental test was interrupted at a drift level of 0.5% due to a significant drop of the lateral strength. The maximum base shear was 234 kN.

The EFM model showed the same failure mode observed in the experimental tests with the initial partialisation of the external sections of the panel and the diagonal shear failure with

cracks located at the centre of the wall. The same behaviour was also observed in the AEM model, with cracks starting from the top corner and developing through the centre of the pier. Both numerical models successfully predicted the hysteretic curve observed experimentally, with minor differences in the last cycles when the experimental test showed a greater energy dissipation due to the significant shear damage. These differences were caused by the shear damage model used in the EFM whereas the AEM model slightly underestimated the energy dissipated due to the simplification introduced in the idealisation of stone blocks and their arrangement, which did not allow local deformation and failure into the units and may limit sliding along cracks.
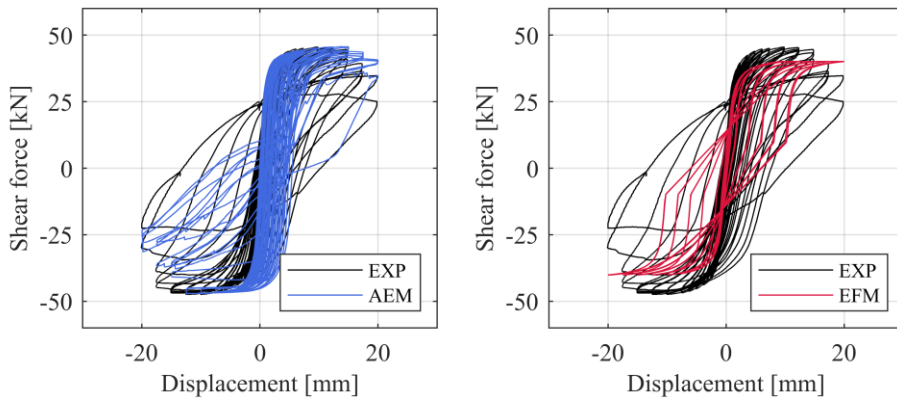
Figure 7.7 Comparison between the experimental and the numerical EFM and AEM response of CS02 in the shear-compression test
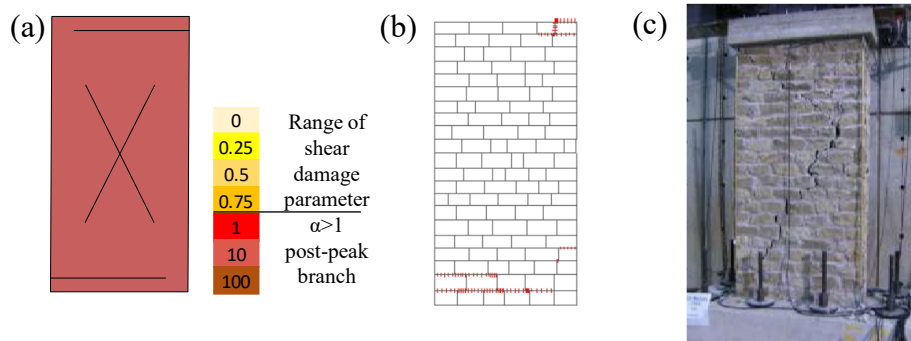
Figure 7.8 Comparison between numerical a) EFM and b) AEM) and c) experimental damage of CS02
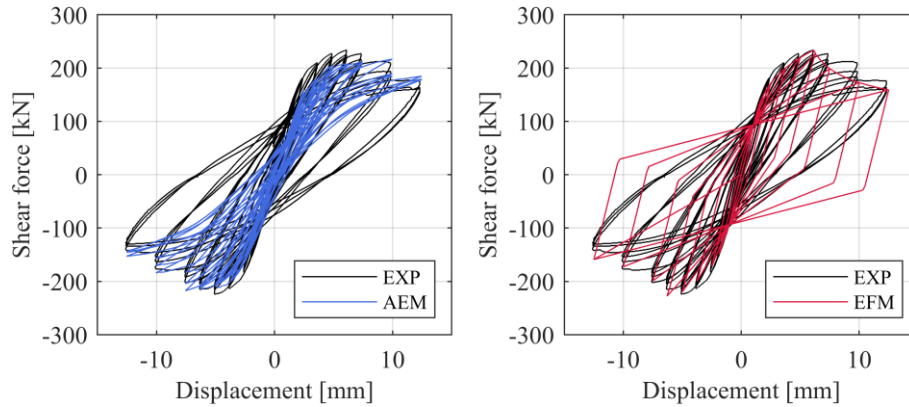
Figure 7.9 Comparison between the experimental and the numerical EFM and AEM response of CT01 in the shear-compression test
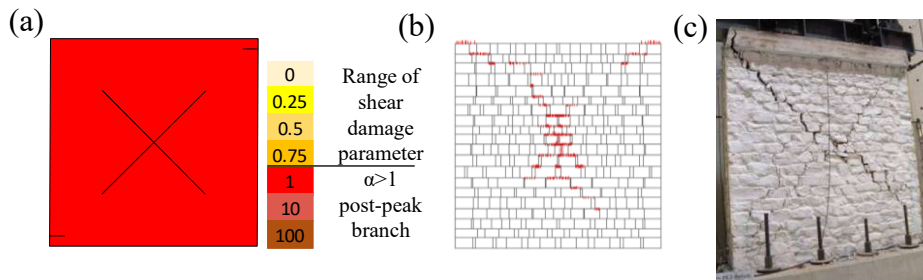
Figure 7.10 Comparison between numerical a) EFM and b) AEM) and c) experimental damage of CT01

The specimen CT02 was tested under a vertical compression level of 0.5 MPa in the first cycles. Then the test was interrupted due to a problem in the vertical actuators, and it was started again with a lower compression level (0.2 MPa). This might have modified the perfect fixed condition in the first cycles. The first cracks developed at a drift level of 0.15% when the specimen exhibited a flexural mechanism and lateral stiffness deterioration.

Diagonal cracks developed at a drift level of 0.2%, corresponding to the attainment of the maximum base shear of 154 kN. The test was interrupted at 0.6% of drift ratio when the specimen exhibited significant diagonal cracks passing through the stone units. The comparison between experimental and numerical results of the shear-compression test on specimen CT02 is reported in Figure 7.11 and Figure 7.12. The interruption of the test, the execution with two different compression levels, and the uncertain boundary condition may cause an underestimation of the lateral strength capacity obtained in the numerical simulation with the AEM model, performed with constant vertical stress of 0.2 MPa, due to the differences in the setup. Both EFM and AEM models exhibited the same damage mode obtained in the experimental test, satisfactorily reproducing the hysteretic curve with minor differences in the last cycles.
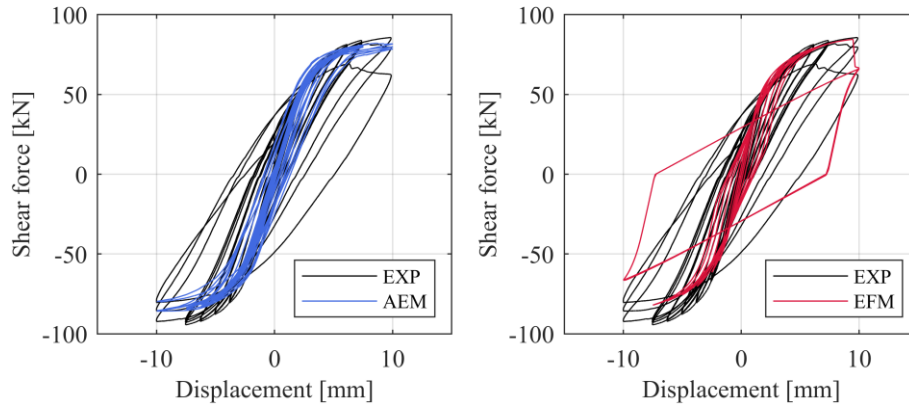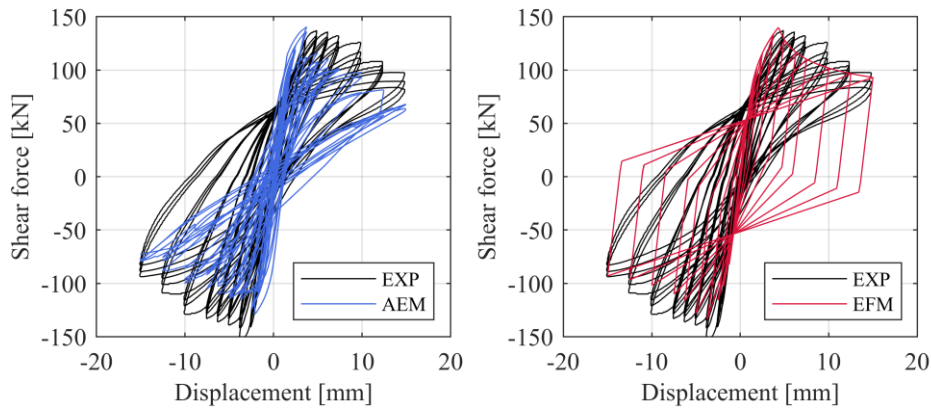
Figure 7.11 Comparison between the experimental and the numerical EFM and AEM response of CT02 in the shear-compression test
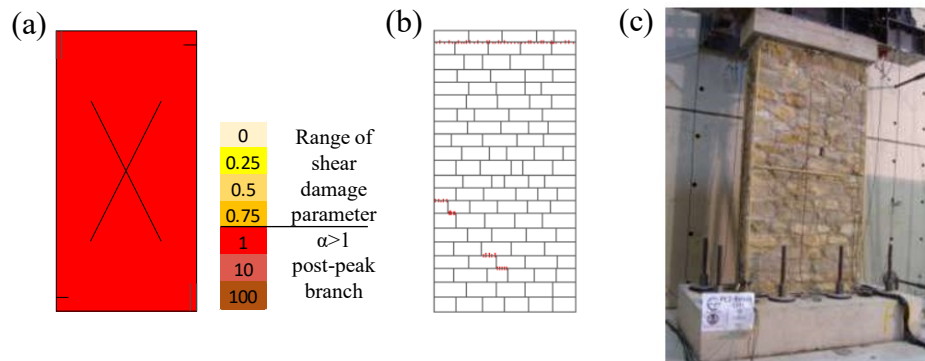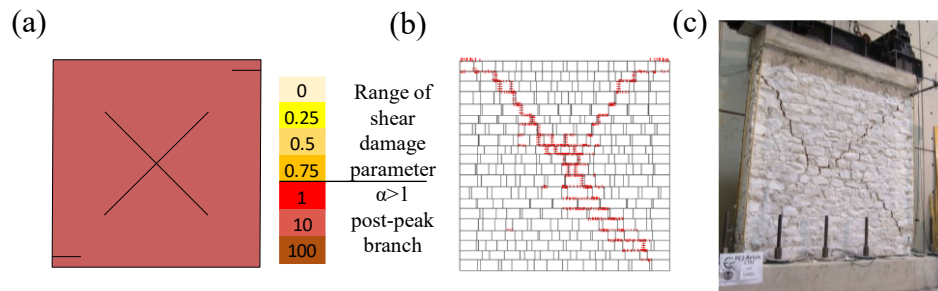

Figure 7.12 Comparison between numerical a) EFM and b) AEM) and c) experimental damage of CT02

7.2   Validation of the numerical models

The numerical models adopted in this work have been validated through the simulation of a shake-table test performed at the Eucentre laboratory of Pavia, on a full-scale prototype named Building 1 and presented in section 7.2.1.

7.2.1 Building prototype

Within the framework of the research project No.2 of the Executive Eucentre Project 2005-2008 ("Numerical and experimental evaluation of the indications of the OPCM 3274 concerning existing masonry buildings") and the Reluis Project 2005-2008, Line 1 ("Assessment and reduction of the vulnerability for existing masonry buildings") an extended experimental campaign aiming at the evaluation of the seismic vulnerability of stone masonry buildings was carried out. This project included three shake-table tests on full-scale stone masonry buildings, with the same geometry and material properties, which differ for the adopted strengthening interventions employed in Building 2 and Building 3, whereas Building 1 was un-reinforced. In this work, the first test carried out on the unreinforced specimen, Building 1, was taken as a reference to validate the numerical procedure introduced above. Interesting readers may refer to Magenes et al. (2010a, 2014)

and Senaldi et al. (2014) for further information on experimental tests. The first prototype, Building 1 consisted of a double-leaf stone masonry building with flexible timber diaphragms and its geometry is presented in Figure 7.13.
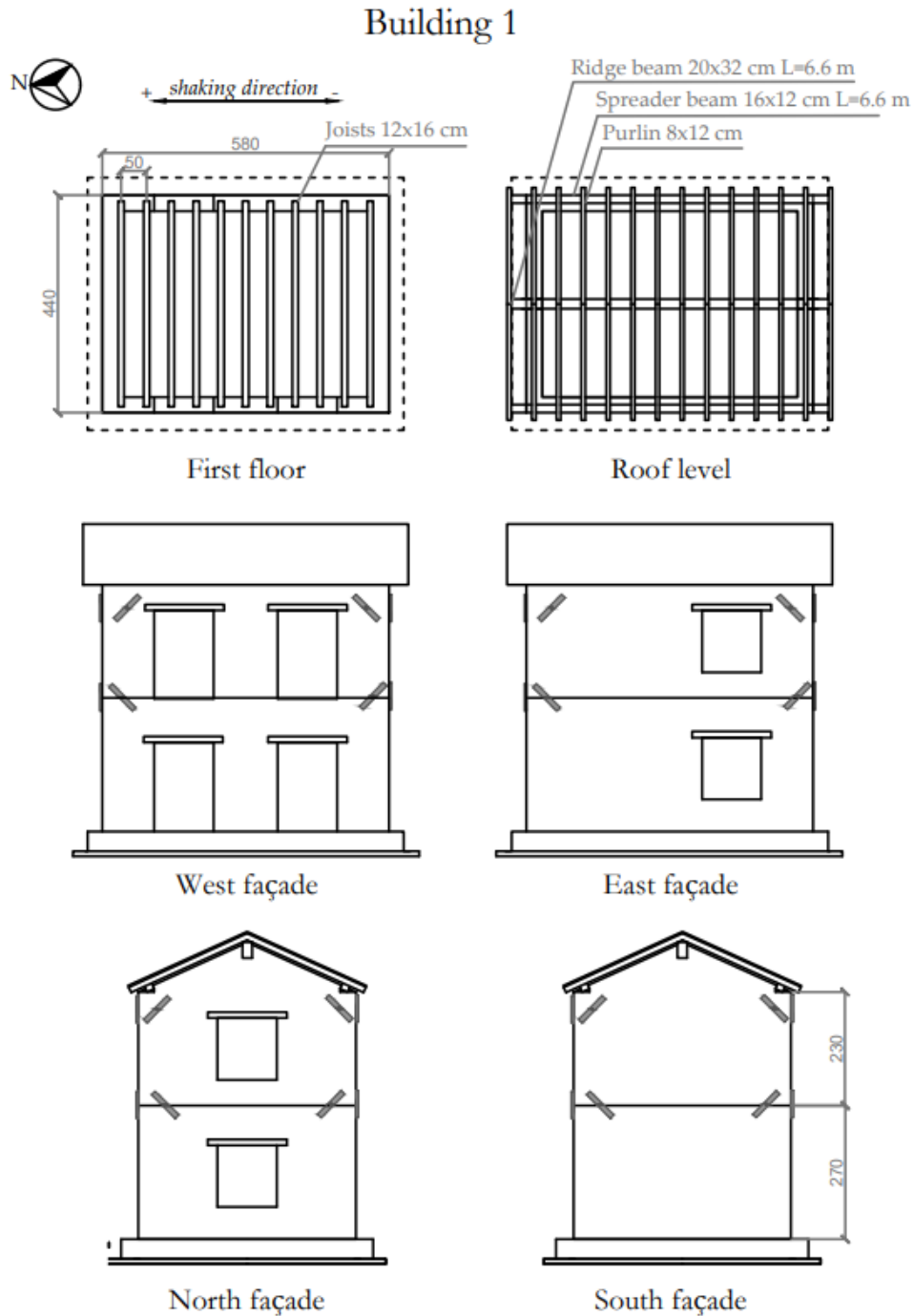
Building 1

Figure 7.13 Plan and elevation views of Building 1

The two-storey building had a footprint of 5.8 m x 4.4 m and was 5 m high at the roof base, whereas the ridge beam was at 6 m (Figure 7.14). The East and West walls were parallel to the shaking direction. The double-leaf stone masonry was 32 cm thick, and the timber floor was supported by the longitudinal walls (i.e. East and West) internal leaf. The interlocking between stone elements guaranteed the connection between longitudinal and transversal walls. The timber floor was a typical Italian floor, and it consisted of a 3 cm thick plank layer nailed to the timber beams. The roof was made by timber joists nailed to the ridge beam and to the spreader beams. A plank layer was nailed to the joists, where plain roofing tiles were placed. In Table 7.4 the mechanical properties of stone masonry, obtained by simple compression and diagonal compression tests, are reported (Magenes et al. 2010c). Where f_m is the compressive strength, E is the Young modulus, f_t is the tensile strength and G is the shear modulus.

In the last test, external tie rods, positioned in the construction phase, were tensioned to prevent the collapse of the upper portion of the North façade and the gable due to the overturning mechanism and allowing the structure to develop a global response.

Figure 7.14 Building 1 construction phases: floor and roof connections (left) and diaphragms construction (right) (Magenes et al. 2010a)

Table 7.4 Masonry mechanical properties from characterisation tests (Magenes et al. 2010c)

	f_m [MPa]	E [MPa]	f_t [MPa]	G [MPa]
Mean	3.28	2550	0.137	840
St.Dev.	0.26	345	0.031	125
c. o. v.	8%	13.5%	21.8%	14.8%

An incremental dynamic analysis was performed simulating the loading protocol applied in the experimental shake-table test. The applied acceleration time-histories were obtained by the accelerogram recorded during the 15th of April Montenegro (1979) earthquake at the Ulcinj-Hotel Albatros station (Magenes et al. 2010b). The signal was scaled at different intensities and the nominal PGA (Peak Ground Acceleration) and actual PTA (Peak Table Acceleration) values recorded on the shake-table are reported in Table 7.5.

Table 7.5 Summary of the nominal PGA and actual PTA of the dynamic test performed on Building 1

Test	1	2	3	4	5	6
Nominal PGA [g]	0.05	0.1	0.2	0.3	0.4	0.4 (*TR)
Recorded PTA [g]	0.07	0.15	0.32	0.52	0.64	0.75

The building prototype presented in-plane damage with cracks widespread in the longitudinal façades (i.e. East and West) until test 4, when the local mechanism involving the overturning of the upper part of the North façade started (as shown in Figure 7.15).
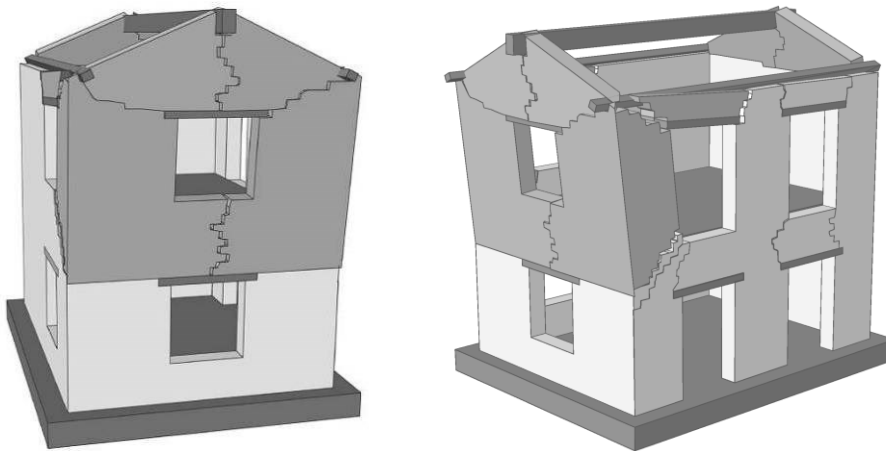
Figure 7.15 Collapse mode exhibited by the specimen during the test 5-0.4g- (Magenes et al. 2010a)

Test 6 – 0.4g-TR- was performed after the activation of the longitudinal tie rods placed at the floor levels and the addition of cable bracing at the roof level. Thanks to this retrofitting intervention, the building specimen exhibited in-plane widespread damage avoiding the overturning of the upper North façade.

Both the Equivalent-Frame (EFM) and the discrete (AEM) models were validated through the simulation of the shake-table test on Building 1. First, the dynamic test was simulated with the global EFM, up to the activation of the local overturning mechanism. Then, the portion of the building involved in the local mechanism was represented with an AEM model, and the 0.4g test was simulated to verify the activation of the OOP mechanism. The

comparison between the experimental and the numerical results is presented in the following sections.

7.2.2 Global EFM

In the global model of Building 1, the macroelements proposed by (Penna et al. 2014) and by (Bracchi et al. 2021) were adopted for spandrel and pier elements, respectively. The mechanical parameters of piers were calibrated simulating the in-plane shear-compression tests presented in the previous section 7.1.4, whereas the spandrels parameters adopted were the ones proposed by (Guerrini et al. 2021), Table 7.6 and Table 7.7, respectively.

Table 7.6 spandrels mechanical parameters

E [MPa]	G [MPa]	f_m [MPa]	c [MPa]	μ	Gc_t	β
2030	560	3.3	0.137	0.261	10	0

Table 7.7 piers mechanical parameters

	E [MPa]	G [MPa]	f_m [MPa]	f_t [MPa]	Gc_t	β
Squat piers	2500	400	3.28	0.075	1	0
Slender piers	1800	300	3.28	0.085	2	0.6

The geometry of the equivalent frame model deformable portions (i.e. spandrels and piers) had been identified with the discretisation criterion proposed by Lagomarsino et al. (2013). According to such criterion, piers height is determined by the average height between the adjacent openings, considering the floor height in the case of corner elements. The geometry of spandrel elements, when the opening distribution is regular, is defined considering the average between the vertical alignments of the surrounding openings, where the spandrel length is equal to the opening one. The geometry of the EFM deformable elements, presented in Figure 7.16, is consistent with the crack pattern experienced by the specimen in the shake-table test.
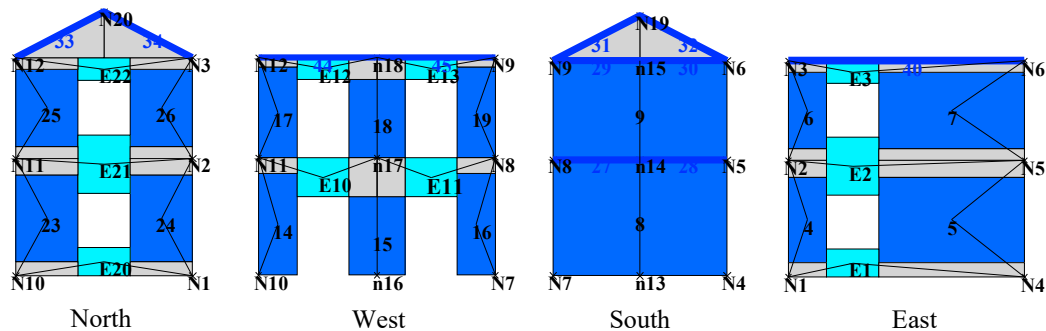
Figure 7.16 Equivalent Frame Model of Building 1

The first-floor diaphragm was modelled as a four-node orthotropic membrane, and those properties are reported in Table 7.8, where E_1 and E_2 represent the normal stiffness in the two directions and G_{12} is the shear stiffness, evaluated according to Brignola et al. (2009).

$$\begin{cases} E_{1,eq} = \dfrac{E_j A_j}{t_m s_j} \\[3mm] E_{2,eq} = \dfrac{E_p t_p}{t_m} \\[3mm] G_{12,eq} = \dfrac{\chi}{A}\left(\dfrac{s_j}{k_{ser}s_n} + \dfrac{\chi}{G_p A_p} + \dfrac{s_j{}^2}{12 E_p I_p}\right)^{-1}\dfrac{t_p}{t_m} \end{cases} \qquad (7.6)$$

Where:

E_j, A_j, s_j are the elastic modulus, the cross-section area and the spacing of the timber joists

$E_p, G_p, A_p, I_p, t_p,$ are the elastic modulus, the shear modulus, the cross-section area, the moment of inertia and the thicknessof the timber planks

s_n is the nail spacing

k_{ser} is the stiffness of the nailed connection evaluated according to Eurocode 5 (CEN; 2004) as $\rho^{1.5}d^{0.8}/30$ where ρ and d are the planks density and the nail diameter

χ is the shear factor for rectangular sections, equal to 1.2

t_m is the thickness of the equivalent membrane.

To account for the weak connections between joists and walls, the value of $E_{1,eq}$ and $E_{2,eq}$ obtained with (7.6), were further adjusted, comparing numerical and experimental displacement of walls parallel to the shaking direction.

Table 7.8 floor equivalent membrane properties

	E_1 [MPa]	E_2 [MPa]	G_{12} [MPa]
1st floor	9000	500	4

The roof diaphragm was modelled with elastic equivalent trusses, which are also used to represent the link provided by the spreader beams and the ridge beam at second and roof levels. The ridge beam was modelled as a rigid beam in order to transfer the seismic actions to the North and South gables, whereas the stiffness of the equivalent trusses representing the roof diaphragm was preliminarily evaluated according to Brignola et al. (2009). In addition, the contribution of the portion involved in the OOP mechanism to the stiffness was considered. Then, the equivalent trusses axial stiffness was iteratively calibrated through the shake-table test simulation, ending to 3.3 kN/mm. It has to be noted that the value obtained with this procedure is a secant stiffness representative of the average experimental behaviour. Indeed, the roof-gables system was subject to a progress stiffness deterioration with increasing seismic intensity, as the experimental incremental dynamic

analyses (IDA) were performed on the same building specimen, with the consequent damage accumulation. The stiffness of the equivalent trusses representing the timber spreader beams was assumed to be equal to the timber one (i.e. E=11000 MPa). The actual masses are considered by assigning the masonry density to the macroelements and to the rigid nodes and introducing any other contribution (e.g. floor, roof) as additional nodal mass (i.e. lumped into the node).

7.2.2.1   Nonlinear static analyses

Nonlinear static analyses were carried out considering uniform and modal horizontal loading patterns. Uniform load distribution considers increasing horizontal forces proportional to the nodal masses, whereas, in modal distribution, the forces are proportional to the product of nodal masses for the nodal height. The pushover curves obtained with the two loading patterns were compared with the experimental backbone curve. The comparison, Figure 7.17, shows a good agreement in terms of lateral stiffness and strength between the experimental backbone and numerical uniform pushover curve, whereas the modal distribution led to a lower lateral strength capacity.
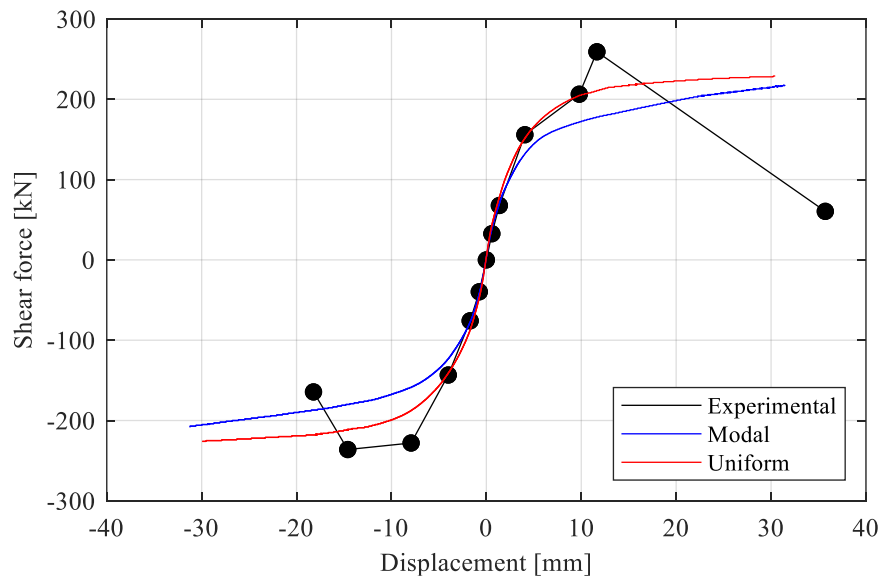
Figure 7.17 Experimental versus numerical pushover curves obtained in the pushover analyses with modal and uniform load pattern

The specimen experienced a local overturning mechanism started at run 4 (0.3g). The comparison of the capacity curve and damage should be considered up to the activation of the local mechanism, as the EFM neglects the OOP contribution. For this reason, the comparison presented in Figure 7.18 is related to the experimental crack pattern after test 4 (0.3g), and the corresponded numerical damage is considered at the maximum displacement attained by the specimen during that test. It has to be noted that figures related

to the numerical model have been mirrored to be consistent with the experimental crack pattern presented in the elevation views.

Numerical pushover analyses also gave a good approximation of the damage mechanism activated and in-plane deformations presented by the structure during the dynamic test. Both West and East wall piers showed flexural damage when loading in positive and negative directions, with major deformations located on the first storey. However, the model could not capture the occurrence of the out-of-plane mechanism, which was studied with the AEM, presented in the following sections.
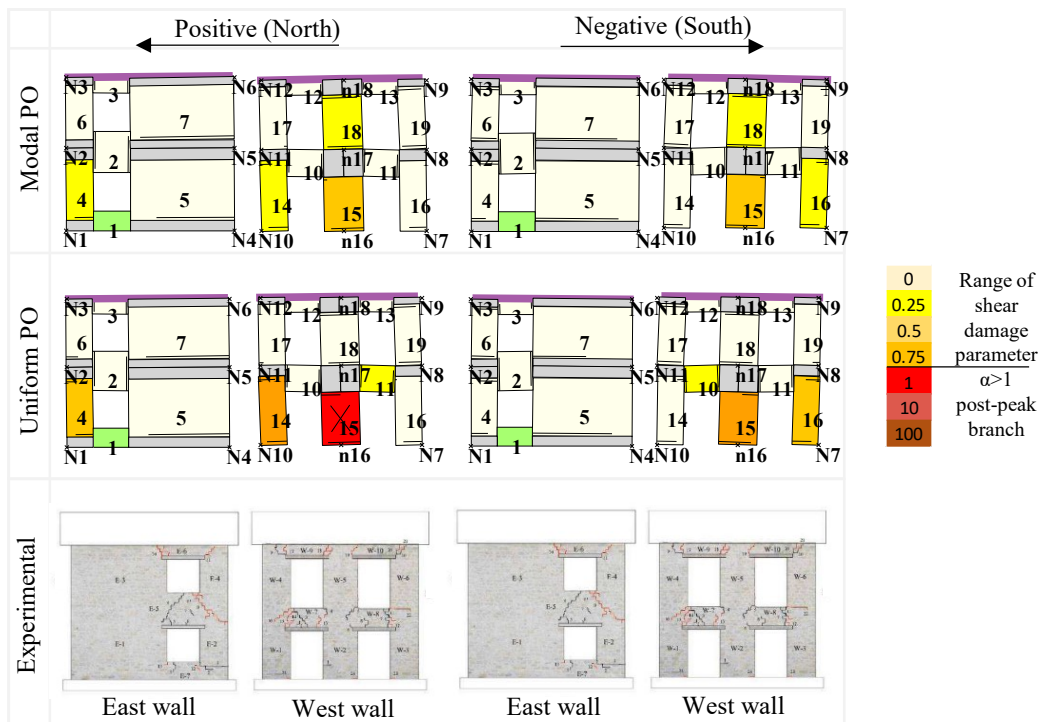
Figure 7.18 Experimental versus numerical crack pattern obtained with modal and uniform load patterns in the pushover analyses (magnified lateral displacement, damage at 10 cm of 2nd floor average displacement)

7.2.2.2   *Simulation of the shake-table test*

In order to validate the EF model, nonlinear dynamic analyses have been performed to simulate the experimental tests applying the acceleration time-histories recorded in the shake-table, which were truncated in order to reduce the duration of the numerical analyses. The experimental loading protocol was considered up to the activation of the local overturning mechanism, which occurred at test 4 - 0.3g of PGA -. The experimental loading protocol was applied, considering the four dynamic tests subsequently to account for the accumulated damage.

The Rayleigh damping model implemented in TREMURI computer program required the selection of two coefficients for the mass and stiffness proportional contributions. The damping coefficient was calibrated by performing a sensitivity analysis by comparing the hysteretic response of the numerical model with the one of the experimental test. The selected damping coefficient was kept constant, for each test, in an interval that includes the last significant mode period (T_n) and the first mode period (T_1) amplified to account for the inelastic response of the structure and the consequent elongation of the first period due to the stiffness deterioration. The elongated period was evaluated considering the secant stiffness of the specimen in test 4 (0.3g of PGA), corresponding to the activation of the out-of-plane mechanism. The last significant mode was taken as the one allowing to consider at least the 85% of the effective mass in the direction of the analysis. Modes with a period out of that interval were overdamped. A damping ratio of 5% was selected for the first run (0.05g of PGA), than reduced to 4.5% for the second run (0.1g of PGA), 3% for the third (0.2g of PGA) and to 2% for the others (0.3g, 0.4g, 0.4g-R of PGA), accounting for the progressive damage which produces a more dissipative behaviour in the last stages of testing (as also noted by Penna et al. (2016) and Kallioras et al. (2019)).

According to the experimental results, the numerical model showed in-plane damage in the longitudinal façades up to test 4, when the out-of-plane (OOP) mechanism had been activated. Figure 7.19 presented the numerical versus experimental hysteretic curves comparison up to the activation of the overturning mechanism (run 4 - 0.3g of PGA).

The comparison showed a fair agreement in terms of force-displacement hysteretic curves, with slight differences in the East façade, where the experimental specimen exhibited larger displacement from the first run -0.05g of PGA-. These differences can be related to the light damage suffered by the prototype during the transportation onto the shake-table from the construction site. Indeed, as discussed by Senaldi (2012), several cracks were detected in the spandrels of the longitudinal walls, with an average residual width of about 0.4 mm, which is consistent with the differences encountered between experimental and numerical displacements in the first runs.

Nevertheless, the model was not able to capture the OOP displacement due to the activation of the local mechanism corresponding to the maximum displacement attained during run 4 (0.3g of PGA). In Figure 7.20 the displacement histories of the top East and West walls during test 3 (0.2g of PGA) and test 4 (0.3g of PGA) are reported. As expected, the model slightly underestimated the lateral stiffness in the first runs (0.05g, 0.1g of PGA), whereas it was well captured in the central runs (0.2g, 0.3g of PGA). This was due to the assumption of a secant stiffness constant value for both 1st floor and roof diaphragms.

Figure 7.21 shows the deformed shape of East and West walls at 14 s and 21s of tests 3 and 4, when the façade reached the maximum positive and negative displacement. That points are marked with blue circles in Figure 7.20. As already noted, despite the model cannot replicate the upper North façade overturning, the longitudinal walls satisfactorily reproduced the in-plane damage exhibited by the specimen. Piers and spandrels presented

light shear damage and initial flexural cracking during test 3, which increased in test 4, consistently with what was observed experimentally.
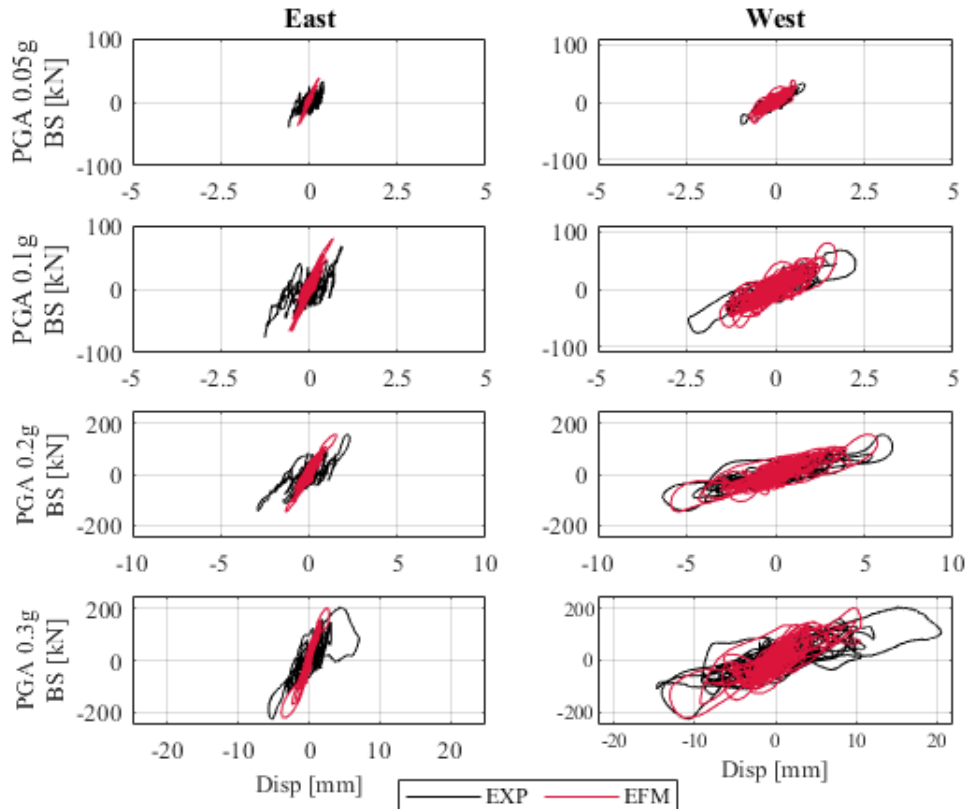
Figure 7.19 Base shear vs top East and West walls displacement in the first four tests before the activation of the overturning mechanism (from 0.05g to 0.3g of PGA).

7.2.3 Local AEM model

The AEM model represented only the part of the structures involved in the overturning mechanism, interesting the roof, the upper part of the South façade, the gable and the portions of the longitudinal façades delimited by cracks (Figure 7.22). The material properties of the interface connecting two adjacent stone units were calibrated through the simulation of shear-compression tests discussed 7.1.4 and reported in Table 7.9.

Table 7.9 Material properties of the interface connecting stone units in the AEM model

E_i [MPa]	G_i [MPa]	f_m [MPa]	f_t [MPa]
1130	395	3.28	0.17

The timber roof was explicitly represented by modelling spreader and ridge beams, planks and nailed and screwed connections. An elastic material represented timber elements with an elastic modulus E of 11000 MPa and a shear modulus G of 700 MPa. Nails and screws

were explicitly modelled, introducing single normal and shear springs where the material properties were evaluated according to Eurocode 5 (CEN; 2004) and they are summarised in Table 7.10.
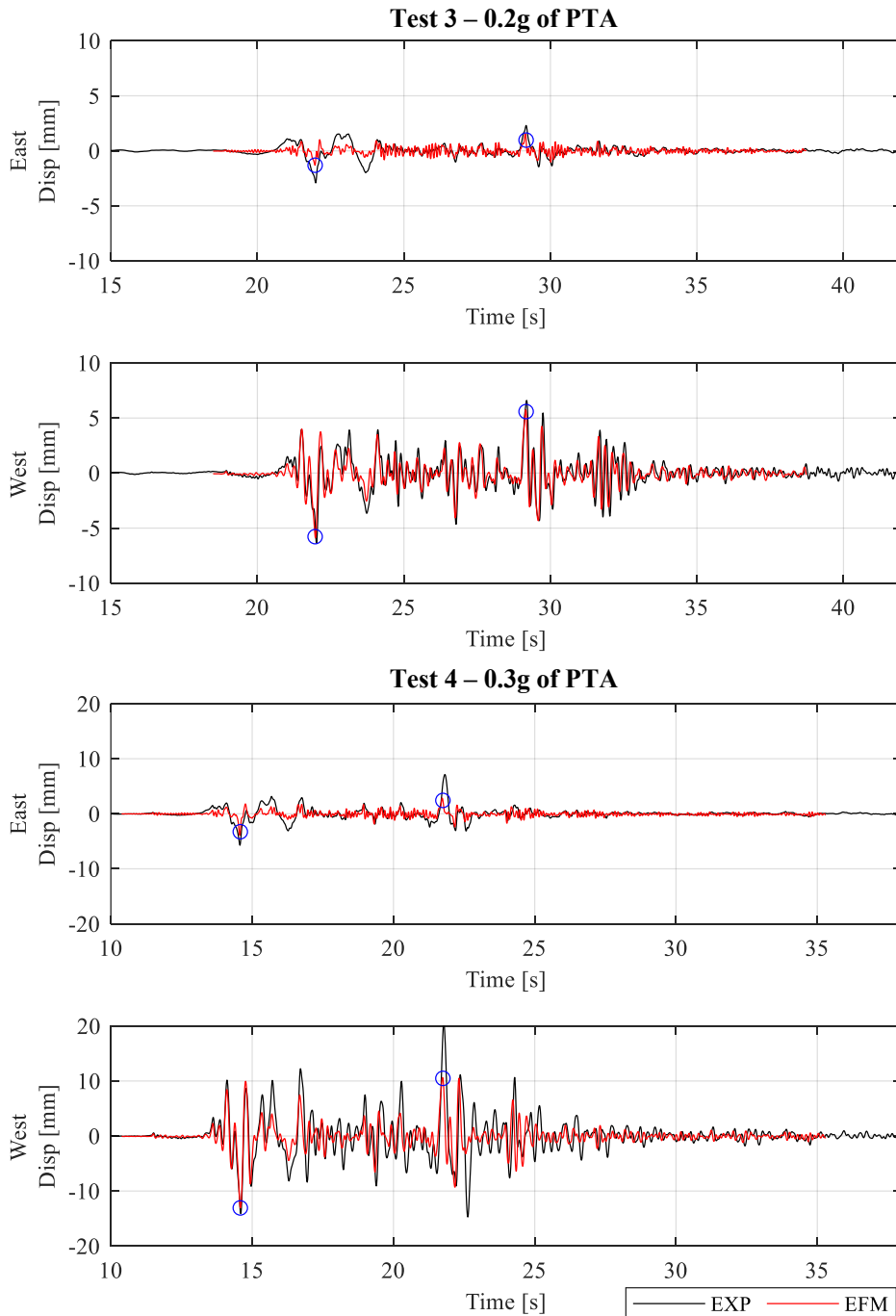
Figure 7.20 Displacement history of the west wall (2nd floor level) during test 3 -0.2g of PGA- and 4 -0.3g of PGA-, where blu circles mark the maximum displacement attained by the EFM
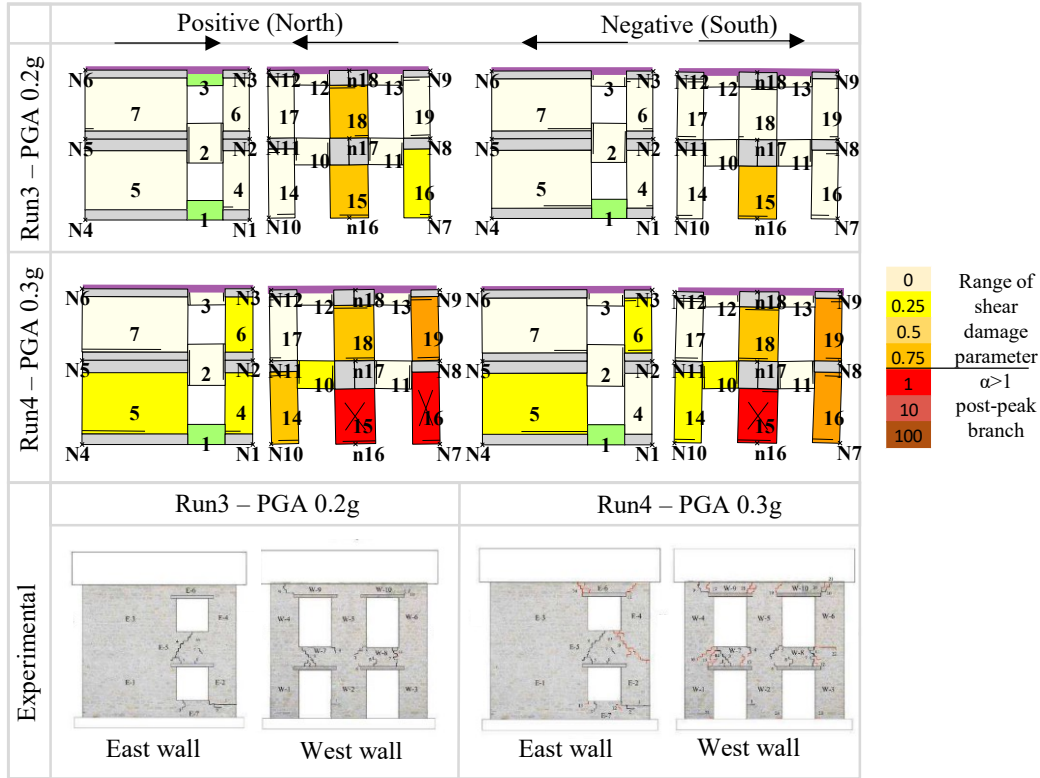
Figure 7.21 Deformed shape of East and West walls during test 3 (0.2g of PGA) and 4 (0.3g of PGA) at maximum positive and negative displacement

Table 7.10 Characteristics of roof connections

	Elements connected	Φ [mm]	S_n [mm]	K_{ser} [N/mm]	$K_{\varphi 0}$ [kNmm/rad]	F_t [kN]
Nails	Planks - purlins	3	90	1180	4778	1.16
Screw	Purlins- spreader beam	14	-	4046	-	13.75
Nails	Purlins- ridge beam	3	-	1180	-	2.1

7.2.3.1   *Simulation of the shake-table test*

The AEM model was then validated by simulating the shake-table test corresponding to a PGA of 0.4 g, applying to the local model the same boundary conditions experienced by the considered sub-structure in the experimental test on the full-scale specimen. The displacement histories recorded at the points that corresponded to the edges of the sub-structure involved in the overturning mechanism were applied to the corresponding points of the AEM model (Figure 7.22). To account for the damage obtained in the previous tests (nominal PGA from 0.05g to 0.3g), the cohesion and tensile strength of the material interface between stone units were reduced where existing cracks are located. The local

AEM model satisfactorily reproduced both the damage pattern exhibited by the specimen at the end of the test and the displacement history of the ridge beam recorded during the experimental test (PGA 0.4g -Figure 7.23).
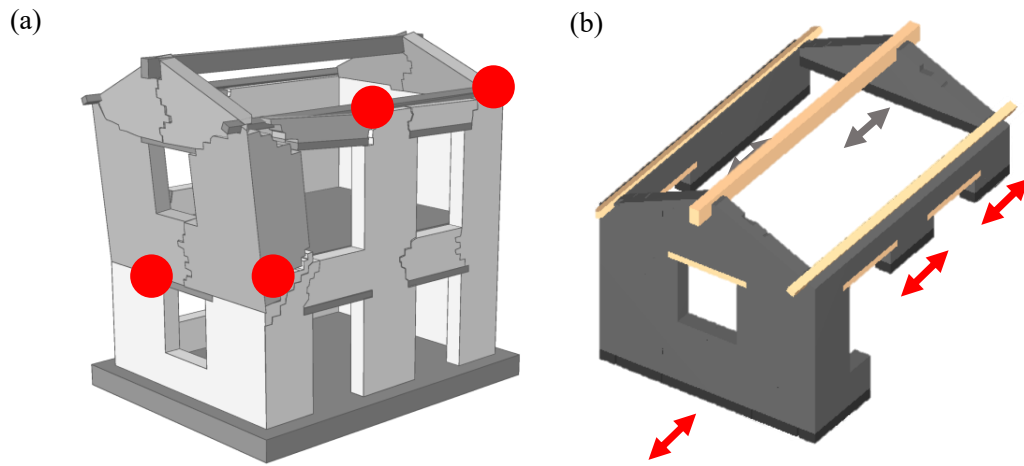
Figure 7.22 a) location of sensors where accelerations were recorded in the experimental tests, b) corresponding points where displacement histories were applied in the numerical simulation
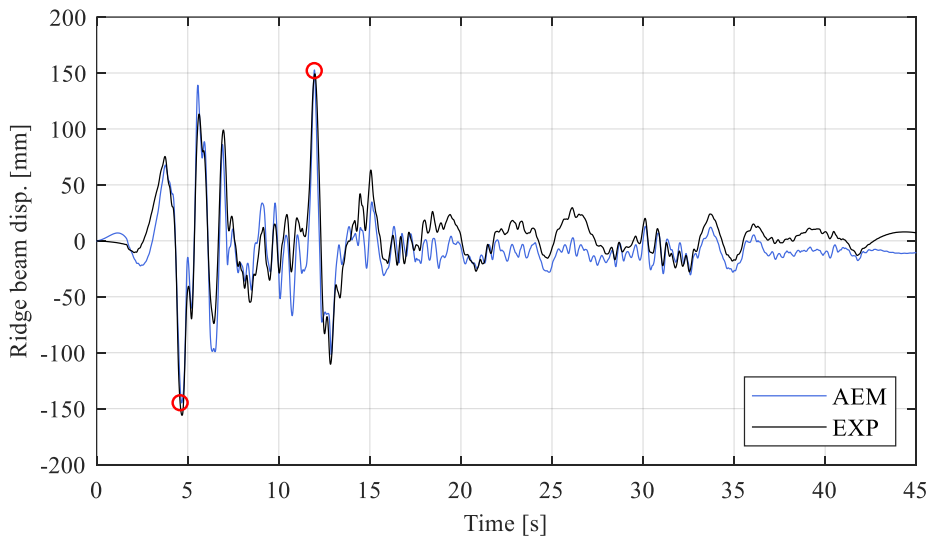
Figure 7.23 Experimental versus numerical ridge beam horizontal displacement, where red circles mark the maximum displacement attained by the ridge beam

Figure 7.24 presents the deformed shape obtained with the AEM model at maximum displacement recorded in both directions, whereas Figure 7.25 shows the damage exhibited by the sub-structure in the AEM model at the end of the test. The damage pattern obtained in the model was consistent with what was observed experimentally. The gable of the South

wall rotated with the support beam without any visible cracks. However, that rotation is evident in the deformed shape. The cracks developed in the previous runs deteriorated, propagating to the opening corners of the longitudinal walls, consistently with the experimental crack pattern.

(a)   (b)
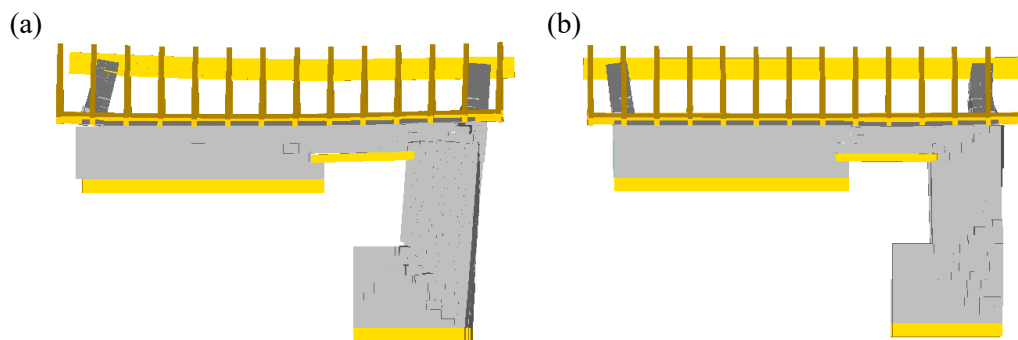
Figure 7.24 a) deformed shape of the sub-structure at 5 s, and b) 12 s (the related points are marked in red in Figure 7.23).

(a)   (b)
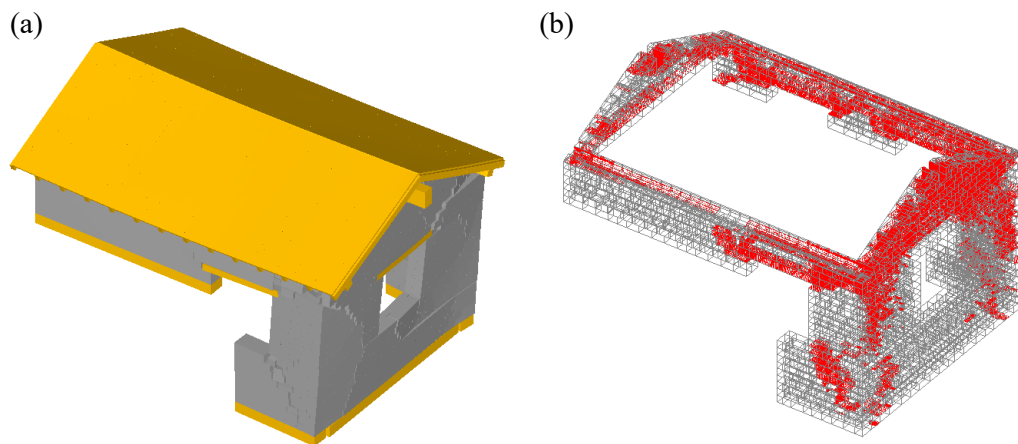
Figure 7.25 a)3D deformed shape at 5s of the AEM model (the related point is marked in red in Figure 7.23) and b) damage pattern at the end of the test 5 - 0.4g of PGA - -.

7.3   Global analyses

In this section, the proposed procedure was applied to selected case studies. The building prototypes were double-leaf stone masonry buildings of two storeys, named BUILD A, B, and C. BUILD A and B had flexible timber diaphragms. Floors were made by timber joists, 15x20 cm, and a 3 cm plank layer, whereas the double-pitch timber roof consisted of purlins, 10x15 cm, resting on 25x40 cm ridge beam, with 3 cm plank layer and tiles. BUILD B had the same characteristics as BUILD A with the addition of tie rods placed at the floor levels to improve the wall-to-wall connections, whereas BUILD C was reinforced with strengthening and stiffening interventions at both floor and roof diaphragms. The plan geometry of the three buildings had been derived from Building 1, as well as longitudinal and transversal walls, which had the same geometry of West and East façades, respectively.

In section 7.3.1, the selection of ground motions employed for the dynamic analyses with the global EFM model is presented.

7.3.1 Seismic ground motions

In order to obtain a meaningful prediction of debris produced by possible collapses, two sets of accelerograms from real earthquake records were considered as seismic input. The two reference records were selected from two different earthquake scenarios, respectively, due to anthropogenic and natural tectonic activity. These two scenarios were selected due to their employment in the experimental shake-table tests performed at the Eucentre laboratory of Pavia by Kallioras et al. (2021), as the debris assessment protocol proposed in this work requires consistent use of acceleration and displacement input time-histories, which were available from data recorded in those experiments. The experimental campaign performed by Kallioras et al. (2021) involved three twins building specimens tested under the same loading protocol and applying one, X, two, X and Z, or three, X, Y and Z, components of the considered seismic motions to investigate the effect of the vertical component on the dynamic response of URM buildings. Each set of accelerograms employed in this work was obtained by scaling in amplitude the reference acceleration time-history, recorded in the experimental test, to attain different levels of PGA.

The first ground motion considered was recorded for the 2018 Zeerijp earthquake (MW 3.4) in Groningen, the Netherlands, and it was caused by gas extraction activities. These phenomena usually produce surface earthquakes characterised by low magnitude and short duration. The vertical and the horizontal components had comparable intensities, and peaks were not synchronised. This is due to the short source-to-site distance, which resulted in a sensible time lag between the arrival of vertical and horizontal motions at the site. The second ground motion was recorded in the Central Italy earthquake sequence in 2016 near Visso (MW 5.9). This ground motion is characterised by vertical and horizontal components high amplitude and synchronised peaks. Interested readers may refer to Kallioras et al. (2021) for further details on the tests and the relative employed acceleration inputs.

In this work, the acceleration and displacement histories recorded in the second of the three tests performed by Kallioras et al. (2021) were considered (i.e. the one involving both X and Z acceleration components), as future developments of this work may investigate the influence of the vertical component. However, in the study discussed in the present chapter, only the X component was applied. For the sake of consistency, both acceleration and displacement time-histories employed in this work were the ones recorded at the specimen foundation. Those records were scaled at different levels of PGA, from 0.2g to 1.2g and used to perform individual Incremental Dynamic Analyses (IDA) with the numerical models. Figure 7.26 and Figure 7.27 present acceleration and displacement, X and Z, time-histories recorded at the specimen foundation in the second experimental shake-table test performed by Kallioras et al. (i.e. the one where only X and Z motion components were applied).

Figure 7.28 presents acceleration response spectra, acceleration versus displacement response spectra and normalised response spectra (with respect to the PGA) of horizontal (X) and vertical (Z) components of Zeerijp and Visso records. The fundamental mode periods in X and Z direction of the considered building are also reported. Both X and Z Visso response spectra present a significant amplification at the building fundamental period (2.5 in X and 4 in Z), whereas Zeerijp spectra have lower increments (1.5-2).

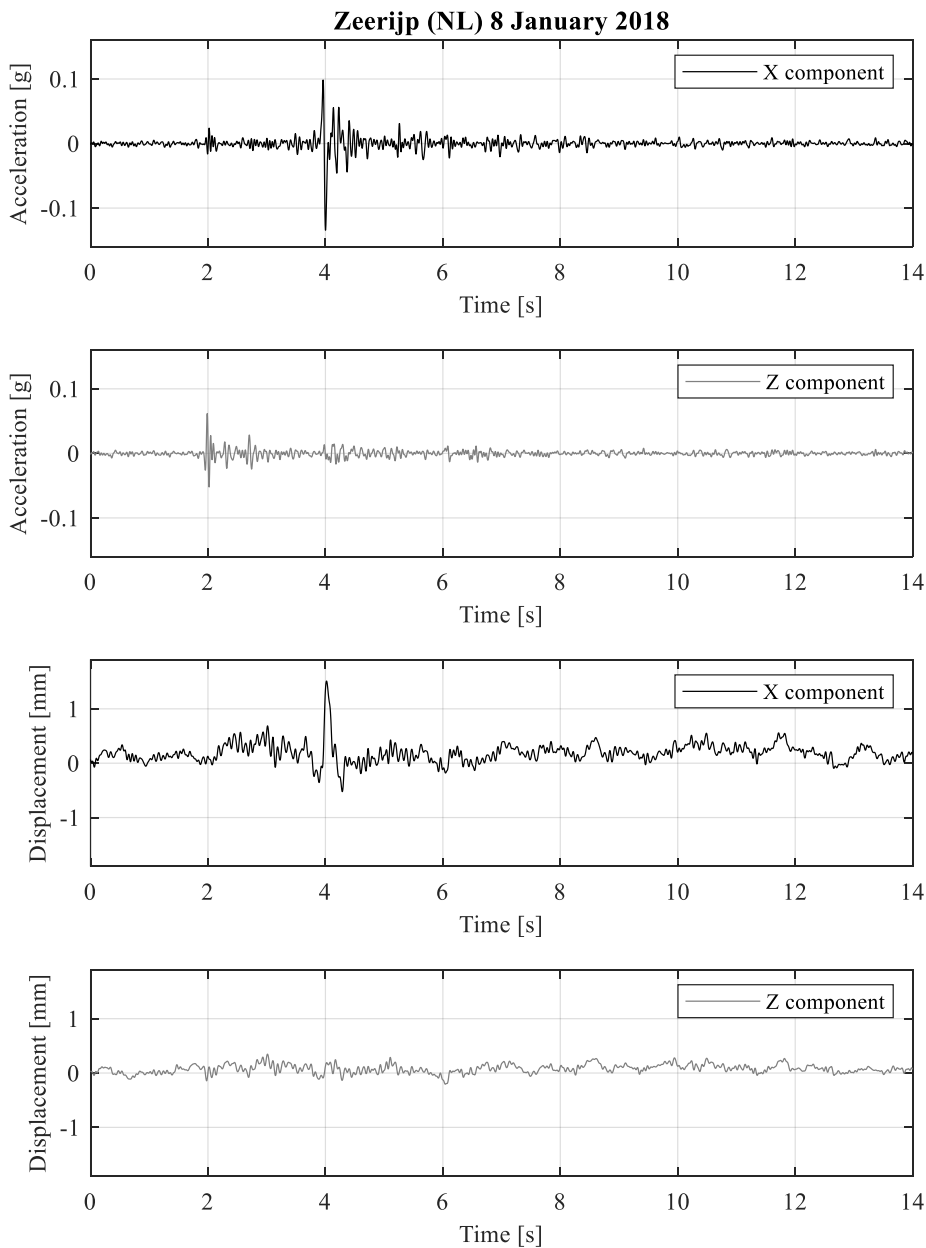Figure 7.26 Acceleration and displacement X and Z components time-histories of Zeerijp ground motion
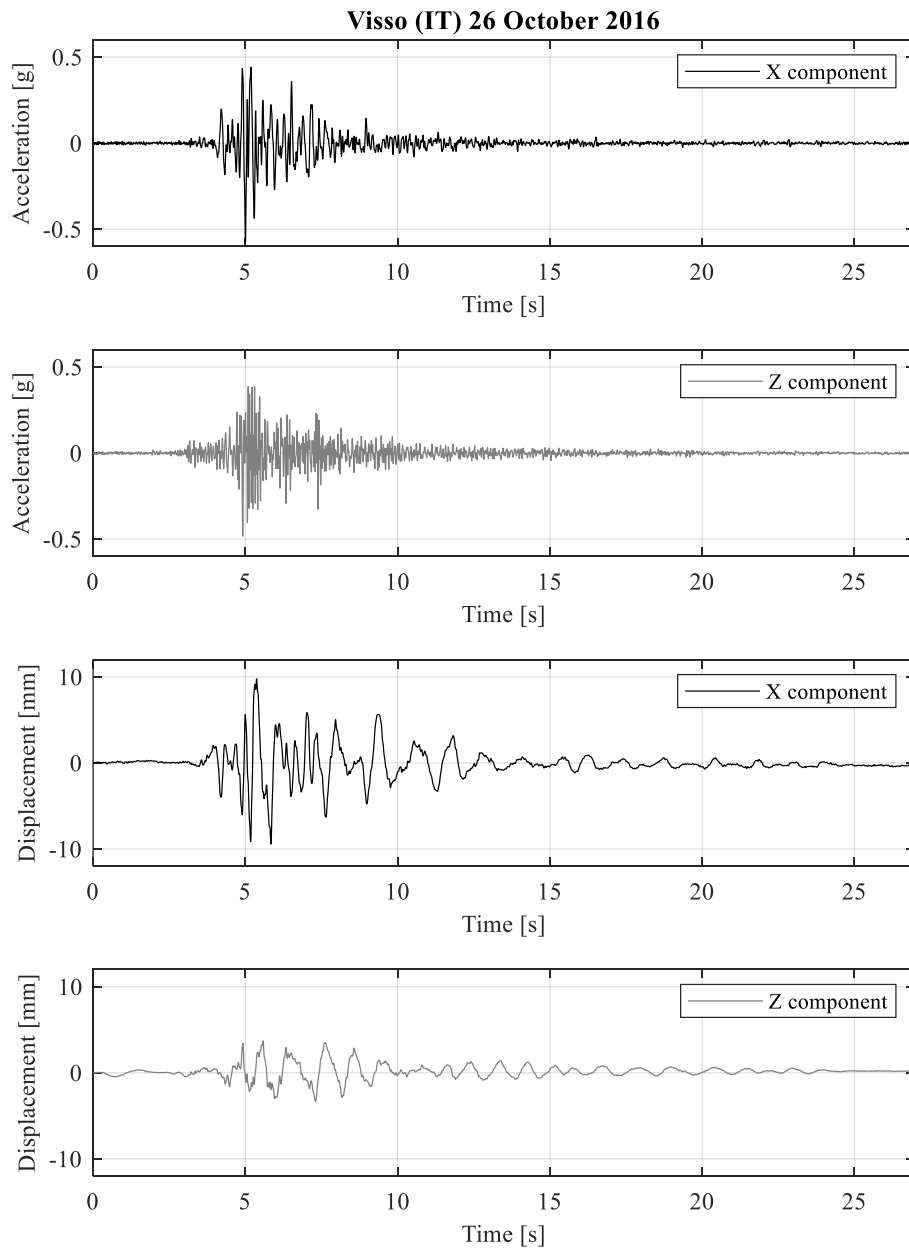
Figure 7.27 Acceleration and displacement X and Z components time-histories of Visso ground motion
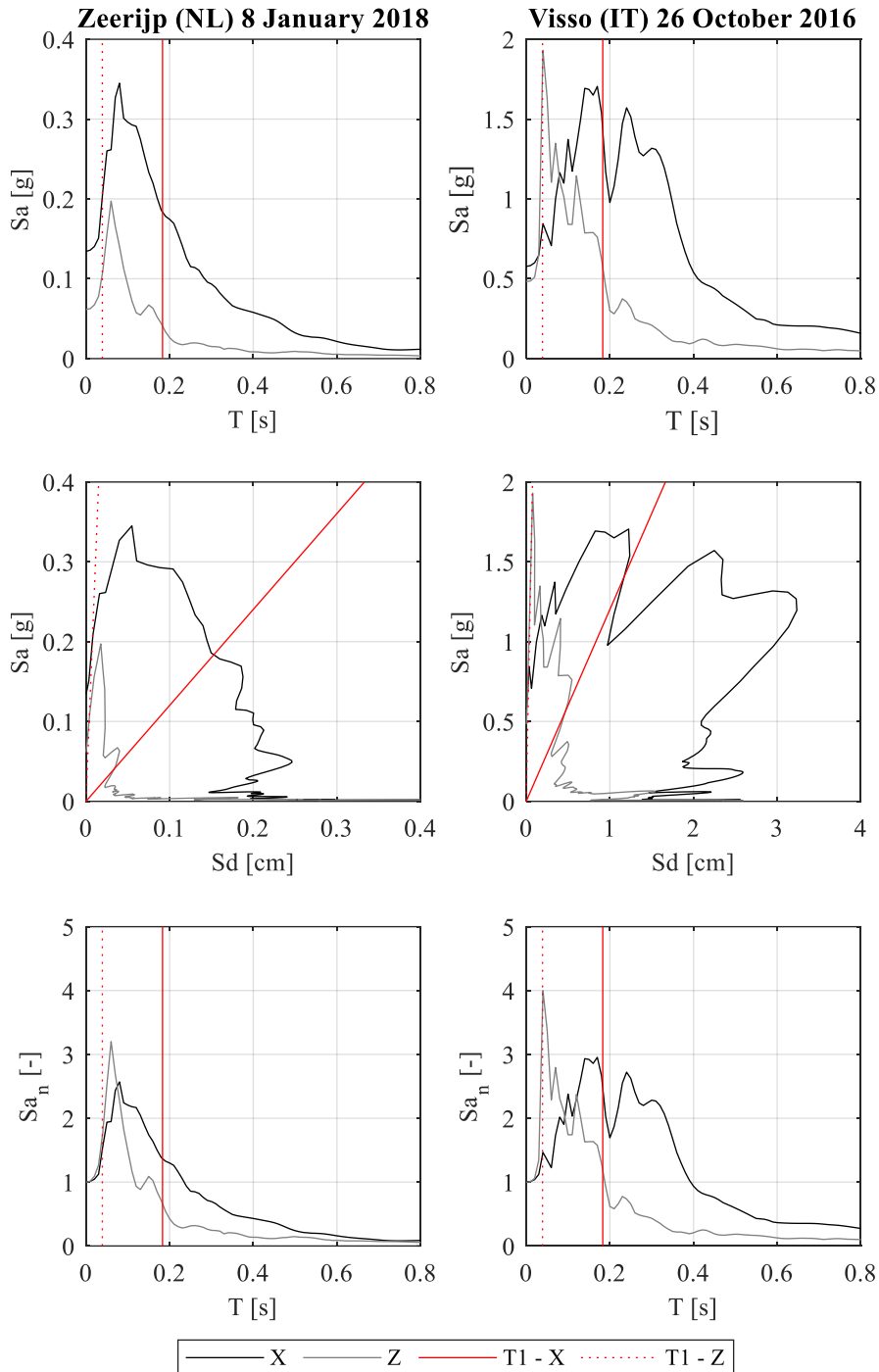
Figure 7.28 Horizontal and vertical acceleration response spectra (top), spectral acceleration-displacement diagrams (centre) and normalised acceleration response spectra (bottom) of Zeerijp and Visso records

7.3.2 Case study BUILD A

The first case study considered was the two-story building whose plan and elevation views are reported in Figure 7.29. The floor and the roof were flexible timber diaphragms, whereas the thickness of the walls were equal to 45 cm at ground level and 30 cm at first level. The proposed procedure involves the use of simplified models based on the EFM to perform a set of Incremental Dynamic Analyses (IDA) using different seismic records. Among these, a subset of analyses where established displacement thresholds are attained is selected. Then, the corresponding signals and intensity levels are considered for the local analyses, performed using AEM models.

7.3.2.1   EF model

The EFM of BUILD A was built with the same assumption on floors, discretisation criteria and material properties adopted in the simulation of the experimental test, presented in section 7.3.. The model is shown in Figure 7.30.

As discussed in 7.2.2.2 the Rayleigh damping model implemented in TREMURI computer program required the selection of two coefficients for the mass and stiffness proportional contributions. The damping coefficient calibrated in the simulation of the experimental test (section 7.2) varied from 5% in the first run, when the building was undamaged, to 2% of the last runs, when the specimen exhibited a more dissipative behaviour. The EFM of BUILD A was used to perform individual IDA, without accounting for the damage accumulation, tending to point to 5% of damping ratio. On the other hand, the energy dissipated also depends on the intensity level of the seismic action, and a lower value of the damping coefficient should be considered for high intensities. To account for this phenomenon, a damping coefficient of 4%, lower than the value assigned to the undamaged model presented in 7.2.2.2, was considered for the IDA. The assumption of a constant 4% of damping ratio for the IDA also allowed avoiding damping-dependent results.

The selected damping coefficient was kept constant in an interval that includes the last significant mode period (T_n) and the first mode period (T_1) amplified to account for the inelastic response of the structure and the consequent elongation of the period due to the stiffness deterioration. The elongated period was evaluated performing pushover analyses (Figure 7.33) with mass and first mode proportional load patterns and considering the secant stiffness of the building when the base shear capacity experienced a drop of 20%. This assumption is equal to the hypothesis of ductility of 7. The last significant mode was taken to consider at least 85% of the effective mass in the direction of the analysis. Modes with a period out of that interval were overdamped. The EFM of BUILD A is presented in Figure 7.30.

7.3.2.2   Displacement limits

The proposed methodology requires a criterion to select the dynamic analyses to be investigated with the AEM. To this aim, a set of displacement limits were defined to select the intensity level that may cause collapses. Nonlinear pushover analyses with mass and first mode proportional distributions were performed for the two loading directions with

the aim of defining displacement limits related to the attainment of the post-peak 50% strength deterioration. As the considered building types have flexible diaphragms, different displacement limits were defined for each longitudinal façade. The lateral strength drop was due to the attainment of elements drift limits, set based on the experimental shear-compression tests on piers presented in 7.1.3 and on the experiments performed on spandrel elements by Graziotti et al. (2011). A drift limit of 0.4% was set for shear failure mode in both spandrels and piers, whereas the flexural failure was assumed equal to 0.7% and 1.5% of drift for piers and spandrels, respectively.

Pushover analyses on the two longitudinal walls were performed assuming first mode (modal) and mass (uniform) proportional load patterns. The longitudinal walls (i.e East and West) were considered individually. A displacement limit for the 2nd floor displacement had been obtained for each analysis, on each wall, and for each direction, corresponding to the reduction of the 50% of the lateral strength capacity. The obtained displacement limits are summarised in Table 7.11, whereas the individual walls' pushover curves are presented in Figure 7.31. These thresholds consider only the attainment of the In-Plane (IP) individual walls capacity. Figure 7.32 presents the damage pattern of East and West walls at the end of the pushover analyses.

Table 7.11 Walls IP limits for the 2nd floor displacement

	2nd floor			
	d_{lim}^{-} [mm]		d_{lim}^{+} [mm]	
	Modal	Uniform	Modal	Uniform
East wall	-22	-32	20	28
West wall	-20	-30	20	30

The downwind first-floor pier of the West wall attained the flexural drift limit suggesting the possible activation of an OOP mechanism involving the transversal North or South façade (depending on the loading direction). Similarly, the damage at the end of the modal pushover analyses was concentrated on the first floor of the East wall. On the contrary, in the uniform pushover analyses, the East wall experienced the failure of the ground-floor piers with the attainment of the shear and flexural drift limits in the central and the external piers, respectively. The absence of rigid diaphragms coupling the longitudinal walls did not allow the development of a global response. The response of longitudinal walls is expected to be almost uncoupled. Thus, different displacement thresholds were defined for the two façades. However, the global response of BUILD A was analysed by performing pushover analyses with uniform and modal load patterns in both directions.
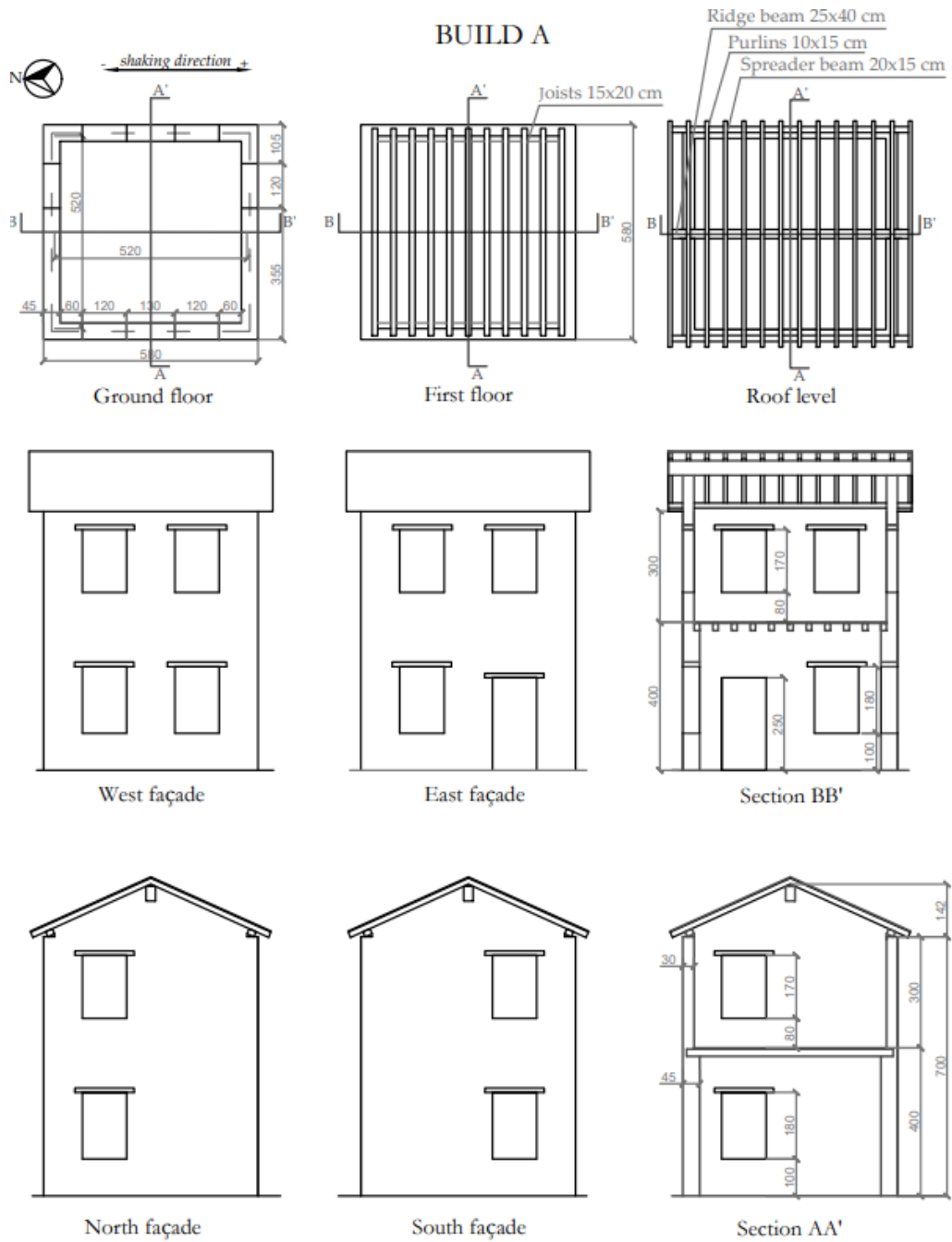
Figure 7.29 Plans, elevation views and sections of BUILD A
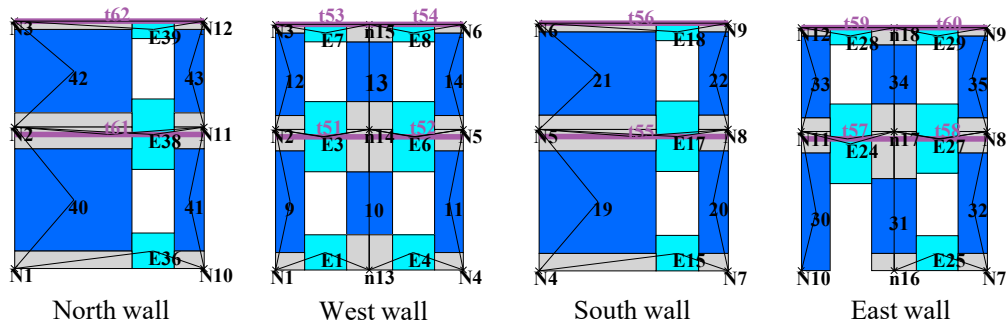
Figure 7.30 EFM model
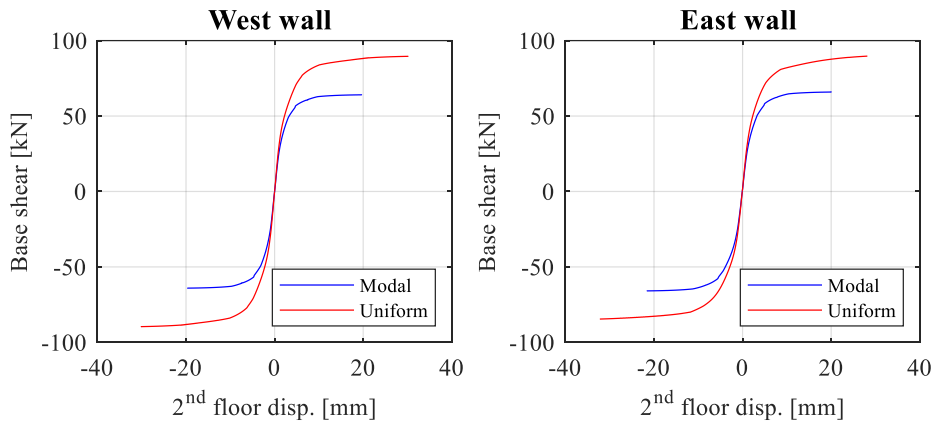
Figure 7.31 Base shear versus 2nd floor displacement pushover curves of longitudinal walls (i.e. East and West)

Figure 7.33 and Figure 7.34 present the displacement versus base shear curves and the deformed shapes obtained with the global model. As deformations and damage were concentrated in the West façade, node 15, located at 2nd floor level, was assumed as a control node, and its displacement history is plotted in the global pushover curves. The last point of the PO was determined at the attainment of a drop of 50% of lateral strength, reached at -31 mm and -39 mm of West wall top displacement in the negative direction and 31 mm and 39 mm in the positive direction with uniform and modal pushover, respectively. In both global pushover curves, the two longitudinal walls were almost uncoupled due to the presence of flexible floors. The damage was mainly located at the ground level of the West wall, where external piers showed flexural damage and the central squat pier failed in shear.
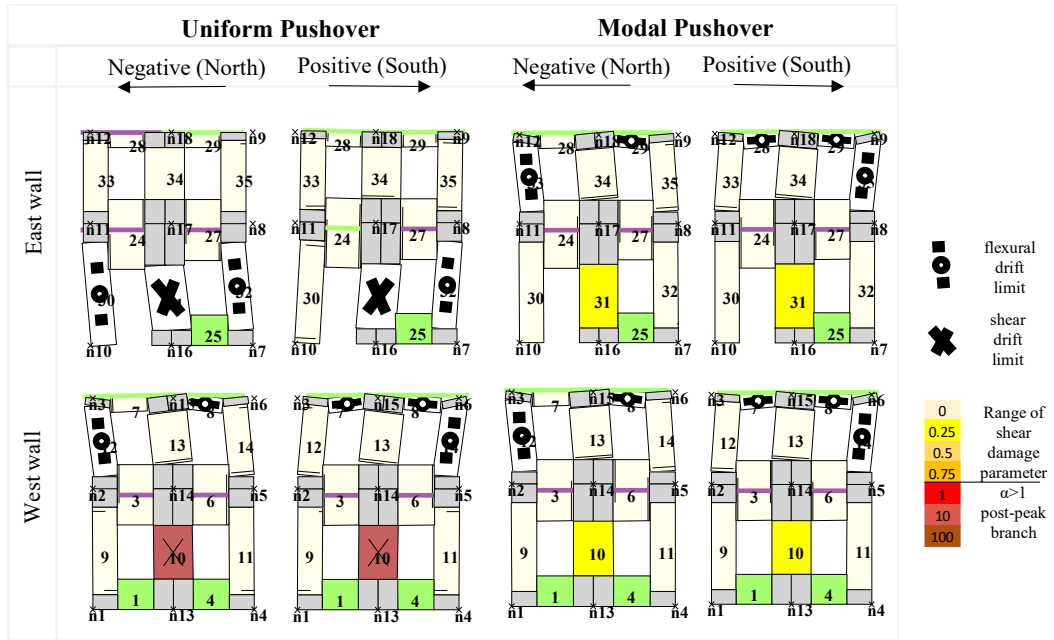
Figure 7.32 Damage pattern at the end of the pushover analyses on East and West individual walls
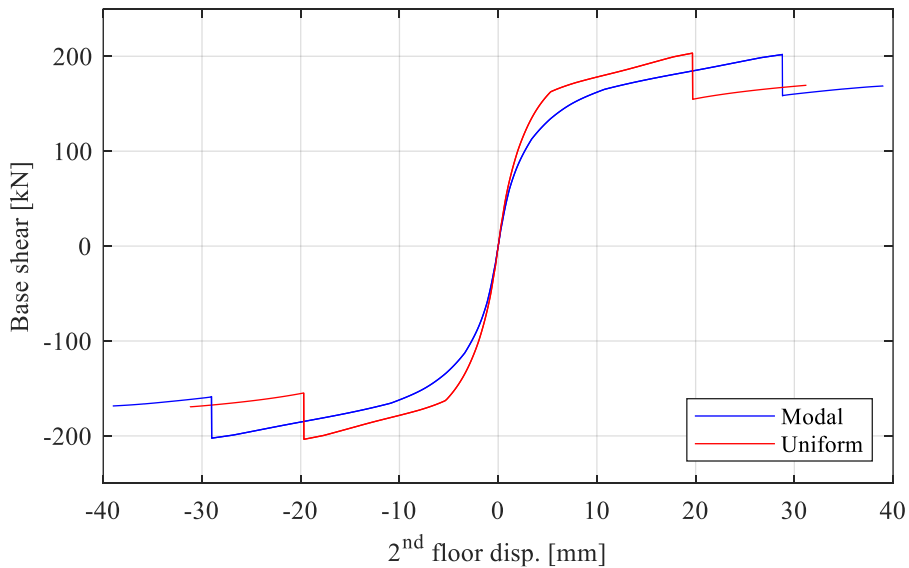
Figure 7.33 Global pushover curves with first mode (modal) and mass (uniform) proportional load pattern
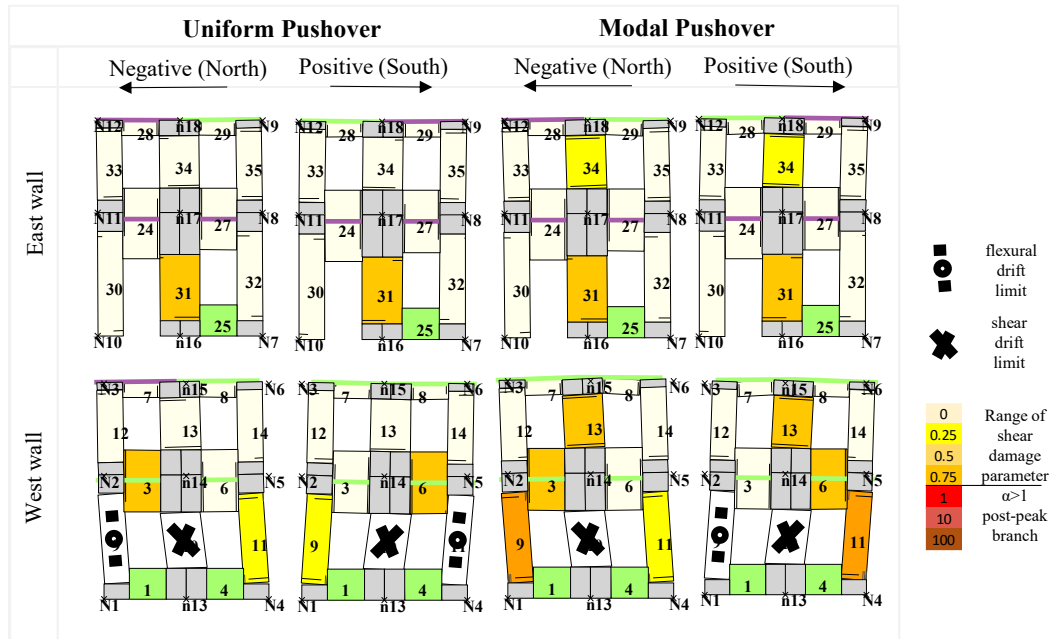
Figure 7.34 Damage pattern of East and West walls at the end of the pushover analyses performed with the global model

7.3.2.3   IDA

Incremental dynamic analyses were performed considering the two records presented in 7.3.1, scaled at six different intensity levels, corresponding to a PGA from 0.2 g to 1.2 g. The scaled records were applied in the North-South direction.

The results of the 12 IDA are presented in terms of average displacement time-histories of 1st and 2nd floor (Figure 7.35) and base shear versus average 1st and 2nd floor displacements (Figure 7.36).

In the IDA with the scaled Visso records, the model attained a base shear much higher in the negative direction than the capacity obtained in the pushover curves. This result is due to the higher modes and the dynamic effects, which produced different dynamic responses and load distribution with respect to the pushover analyses. In Figure 7.37 the maximum negative and positive displacements attained by the East and West walls at the second floor were compared with the selected displacement thresholds. The displacement limits obtained by the global pushover analyses were identified as 'GT', whereas the thresholds obtained performing pushover analysis on individual façades are identified as 'FT'.
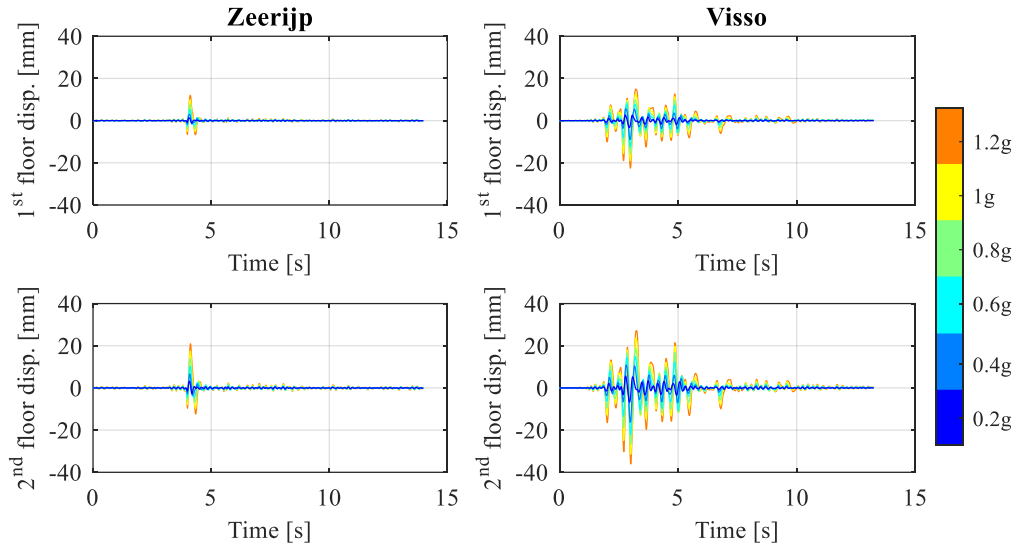
Figure 7.35 Average 2nd floor displacement time-histories obtained in the IDA performed on BUILD A
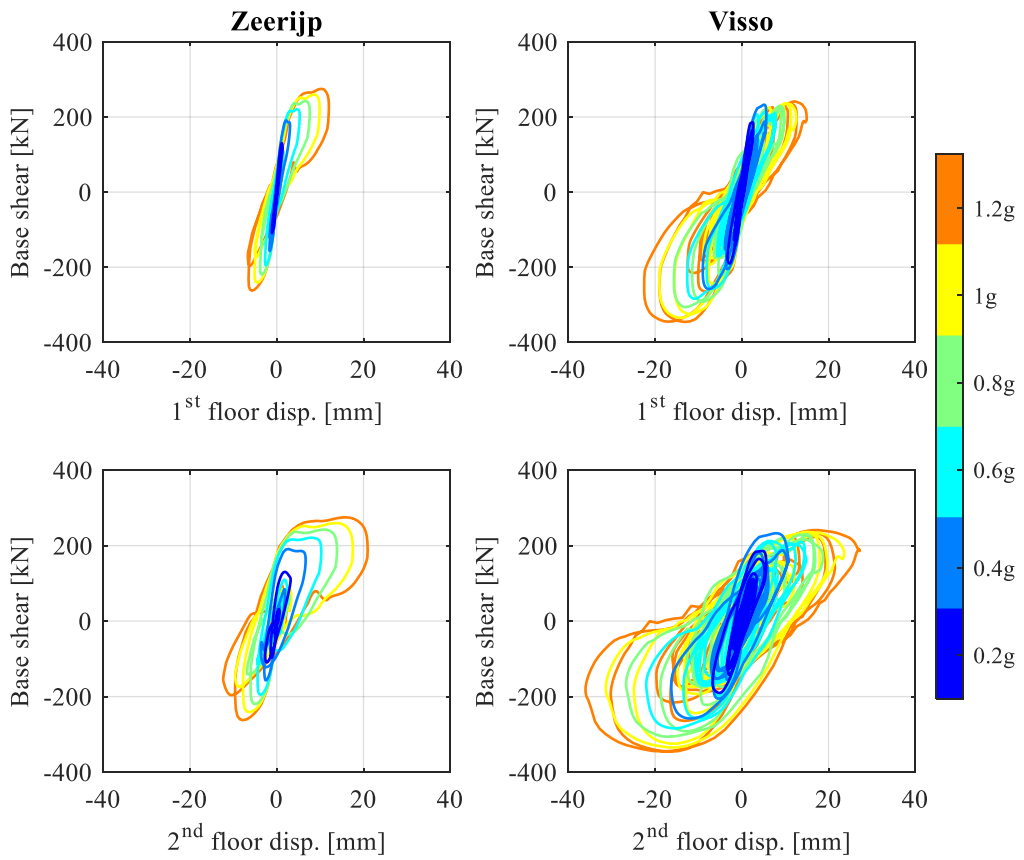
Figure 7.36 Base shear versus average 1st and 2nd floor displacement hysteretic curves obtained in the IDA performed on BUILD A
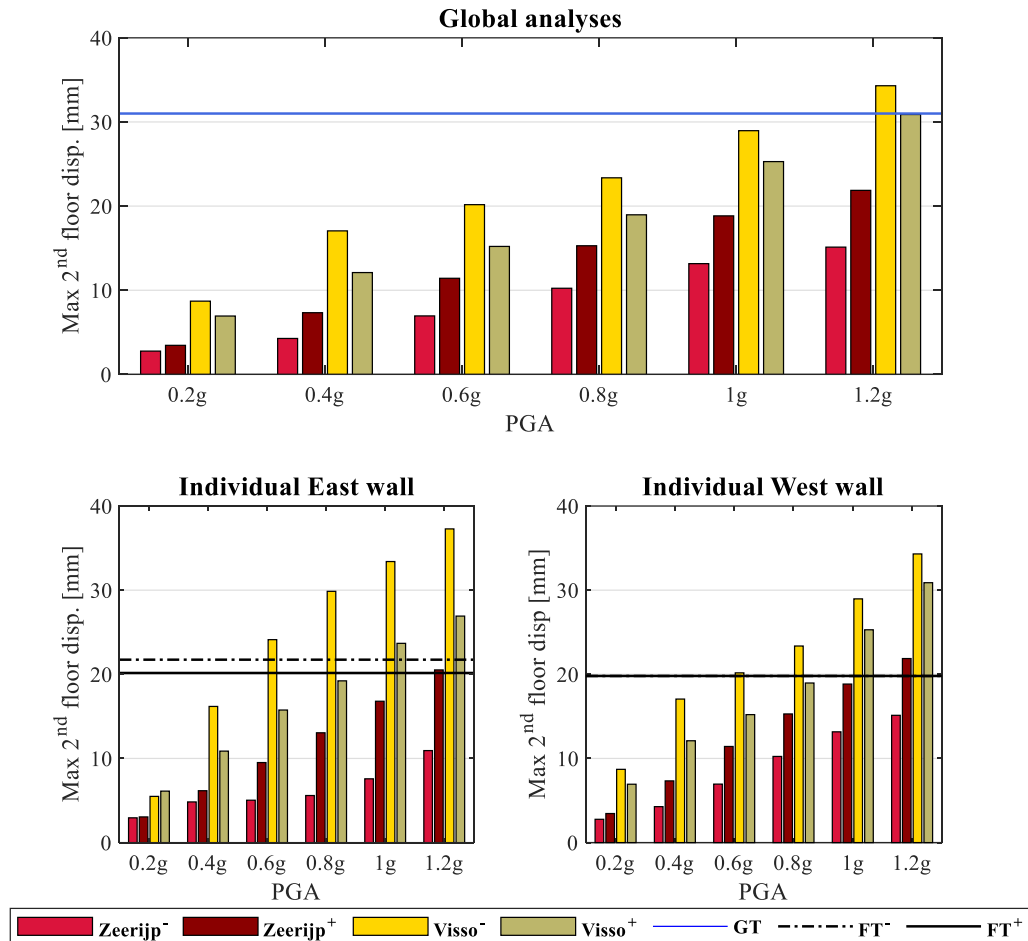
Figure 7.37 2nd floor maximum displacement attained by the control node of the global model and 2nd floor maximum displacement attained by East and West walls of the individual façade models in the IDA performed on BUILD A

The first attainment of GT displacement limit occurred in the sixth run corresponded to 1.2 g of PGA for Visso series, where Zeerijp set did not attain the GT threshold. The first attainment of the FT displacement thresholds for both East and West walls occurred at runs 3 and 6, corresponding to 0.6 g and 1.2 g for Visso and Zeerijp, respectively (runs 3 and 6). These intensity levels were considered for the analyses performed with the local AEM model in section 7.4.

7.3.3 Case study BUILD B

The second case study considered was the two-story building with the same geometrical characteristics of the first case, BUILD A, presented in Figure 7.29. Both floor and roof were flexible timber diaphragms, whereas the thickness of the walls was equal to 45 cm at ground level and 30 cm at first level. In addition, tie rods Φ8 were introduced at the first

floor and at the roof levels and tensioned to prevent the development of OOP mechanisms. The EFM of BUILD B was developed by adding the tie rods to the EFM model of BUILD A.

7.3.3.1 *Displacement limits*

As discussed in 7.3.2.2, a set of displacement limits were identified, performing pushover analyses on the individual longitudinal façades and on the global 3D EFM model. Pushover analyses on the two longitudinal walls were performed assuming first mode (modal) and mass (uniform) proportional load patterns. The longitudinal walls (i.e East and West) were considered individually. A displacement limit for the 2nd floor displacement had been obtained for each analysis, on each wall, and for each direction, corresponding to the reduction of the 50% of the lateral strength capacity. The obtained displacement limits are summarised in Table 7.12, whereas the individual wall' pushover curves are presented in Figure 7.36.

Table 7.12 Walls IP limits for the 2nd floor displacement

	2nd floor			
	d_{lim}^{-} [mm]		d_{lim}^{+} [mm]	
	Modal	Uniform	Modal	Uniform
East wall	-20	-24	21	20
West wall	-25	-23	25	23
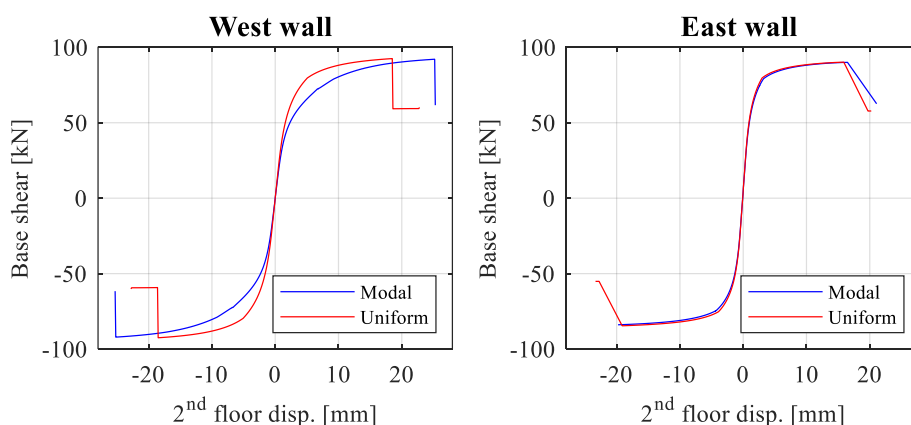
Figure 7.38 Base shear versus 2nd floor displacement pushover curves of longitudinal walls (i.e. East and West)

Figure 7.39 presents the damage pattern of East and West walls at the end of the pushover analyses. In contrast to what was observed in BUILD A, where the individual walls suggested the activation of an overturning mechanism involving the upper part of the façade, in BUILD B, they showed in-plane damage located on the ground floor. This difference is due to the introduction of tensioned tie rods. Both walls experienced the failure of the ground-floor piers with the attainment of the shear and flexural drift limits in the

central and the external piers, respectively. Due to the absence of rigid diaphragms coupling the response of the longitudinal walls, different displacement thresholds were defined for the two façades. As discussed in 7.3.2.2, also the global response of BUILD B was analysed by performing pushover analyses.
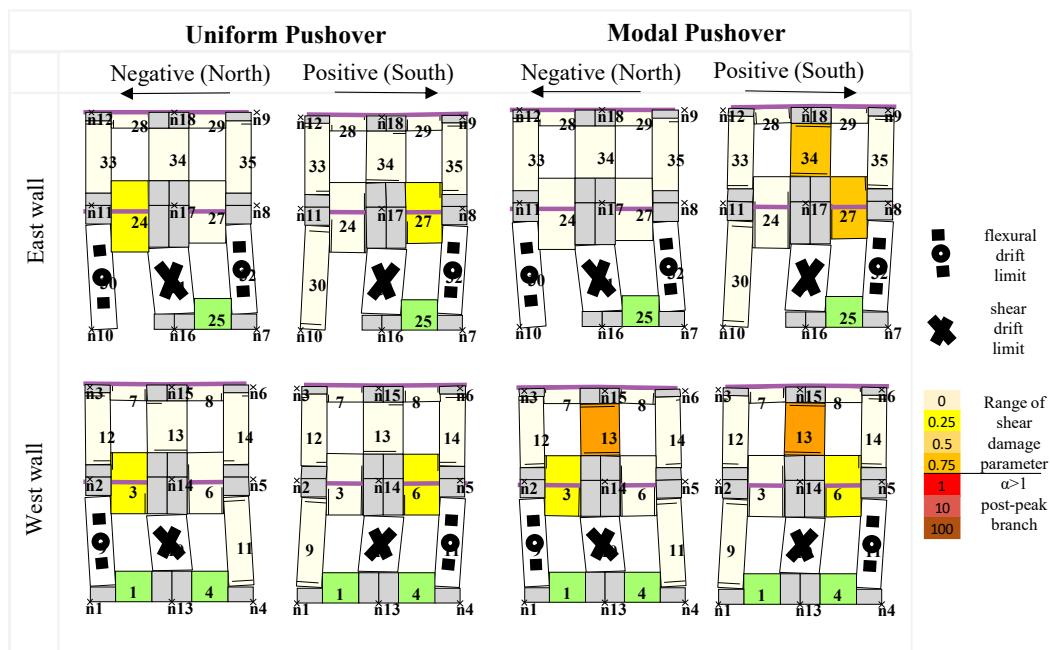
Figure 7.39 Damage pattern of East and West walls at the end of the pushover analyses performed on individual façades

Figure 7.40 and Figure 7.41 present the displacement versus base shear curves and the deformed shapes obtained. As deformations and damage were concentrated in the West façade, node 15, located at 2nd floor level, was considered as a control node and its displacement histories are plotted in the global pushover curves. The last point of the PO was determined at the attainment of a drop of 50% of lateral strength, reached at -29 mm and -32 mm of the West wall top displacement in the negative direction and 29 mm and 32 mm in the positive direction with uniform and modal pushover, respectively. In both uniform and modal pushover, the two longitudinal walls were almost uncoupled due to the presence of flexible floors. The damage was mainly located at the ground level, where external piers showed flexural damage, and the central squat pier of the West façade failed in shear.
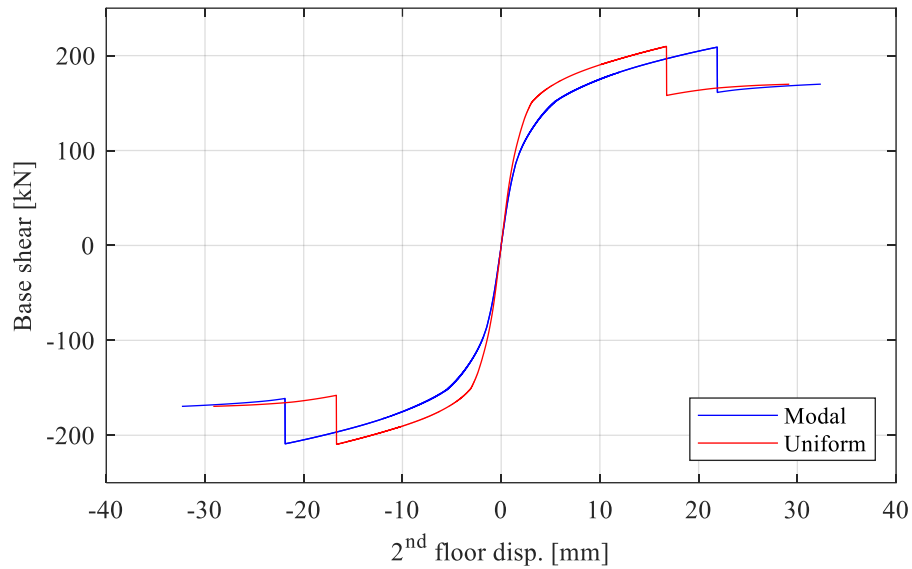
Figure 7.40 Pushover curves with first mode (modal) and mass (uniform) proportional load pattern
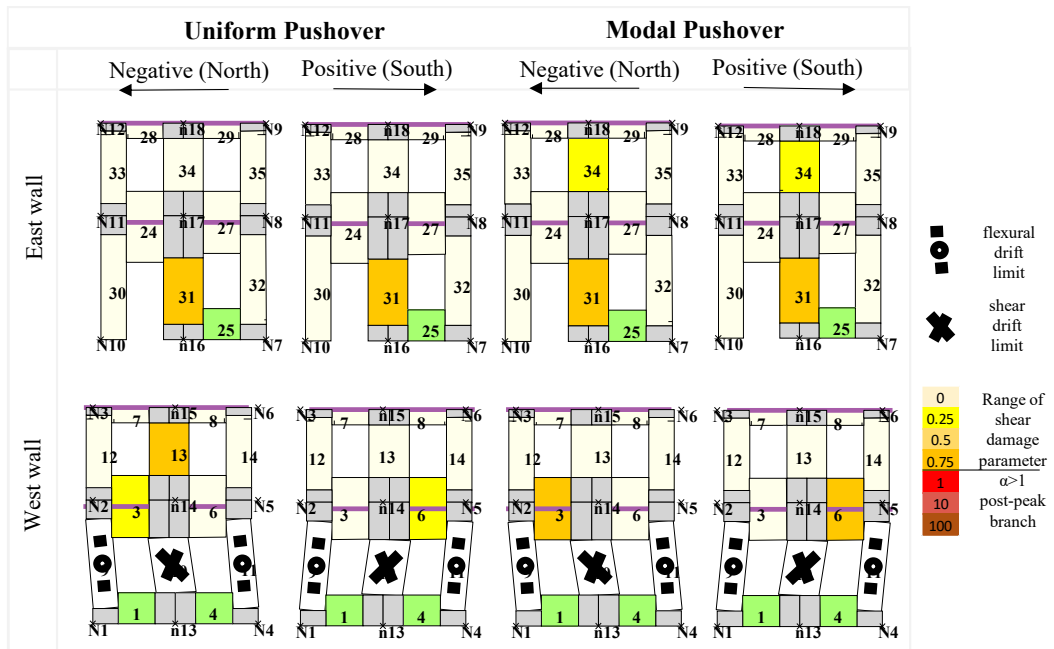
Figure 7.41 Damage pattern of East and West walls at the end of the pushover analyses performed on the global model

7.3.3.2   IDA

Incremental dynamic analyses were performed considering the two records presented in 7.3.1, scaled at six different intensity levels, corresponding to a PGA from 0.2 g to 1.2 g. The results of the 12 IDA are presented in terms of average displacement time-histories of 1st and 2nd floor (Figure 7.42) and base shear versus average 1st and 2nd floor displacements (Figure 7.43). As discussed in the previous section for BUILD A, with Visso scaled records, also BUILD B attained a base shear, in the negative direction, much higher than the capacity obtained in the pushover curves, due to the dynamic effects which produced different dynamic responses and load distribution with respect to the pushover analyses.
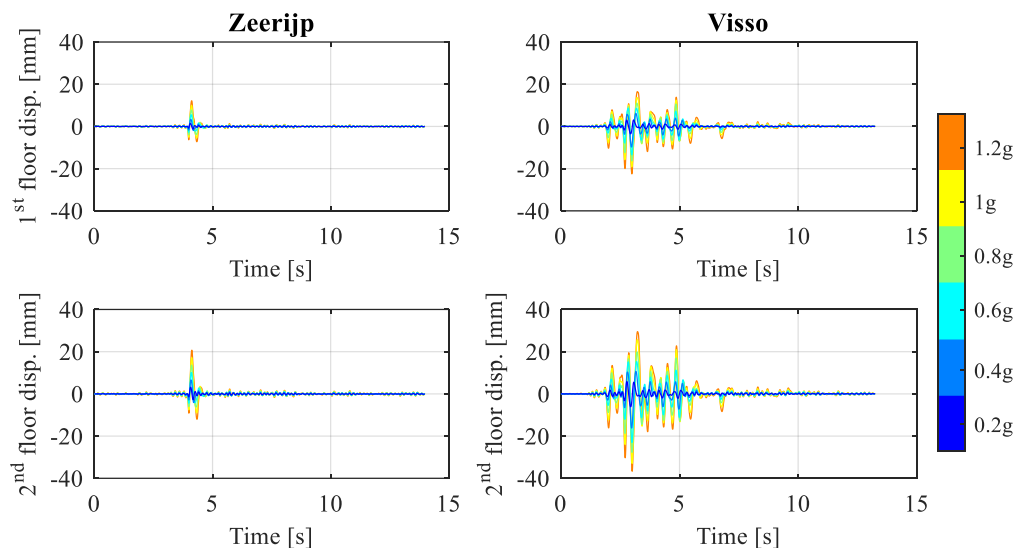
Figure 7.42 Average 2nd floor displacement time-histories obtained in the IDA performed on BUILD B

In Figure 7.44 the maximum negative and positive displacements of the control node at 2nd floor of the West wall of the global model and at the 2nd floor of individual wall models were compared with the selected displacement thresholds. The displacement limits obtained by the global pushover analyses were identified as 'GT', whereas the thresholds obtained performing pushover analysis on individual façades are identified as 'FT'.

The first attainment of GT displacement limit occurred in the third run, corresponding to 1 g of PGA for Visso series, whereas the global displacement threshold was not attained with Zeerijp records. The first attainment of the FT displacement thresholds for both East and West walls occurred at runs 3, corresponding to 0.6 g for Visso, whereas the FT limits weren't attained in the Zeerijp series. However, as the displacement attained by the West wall individual model was close to the threshold, both Visso and Zeerijp records scaled at 0.6 g and 1.2 g of PGA were considered for the analyses performed with local AEM models.
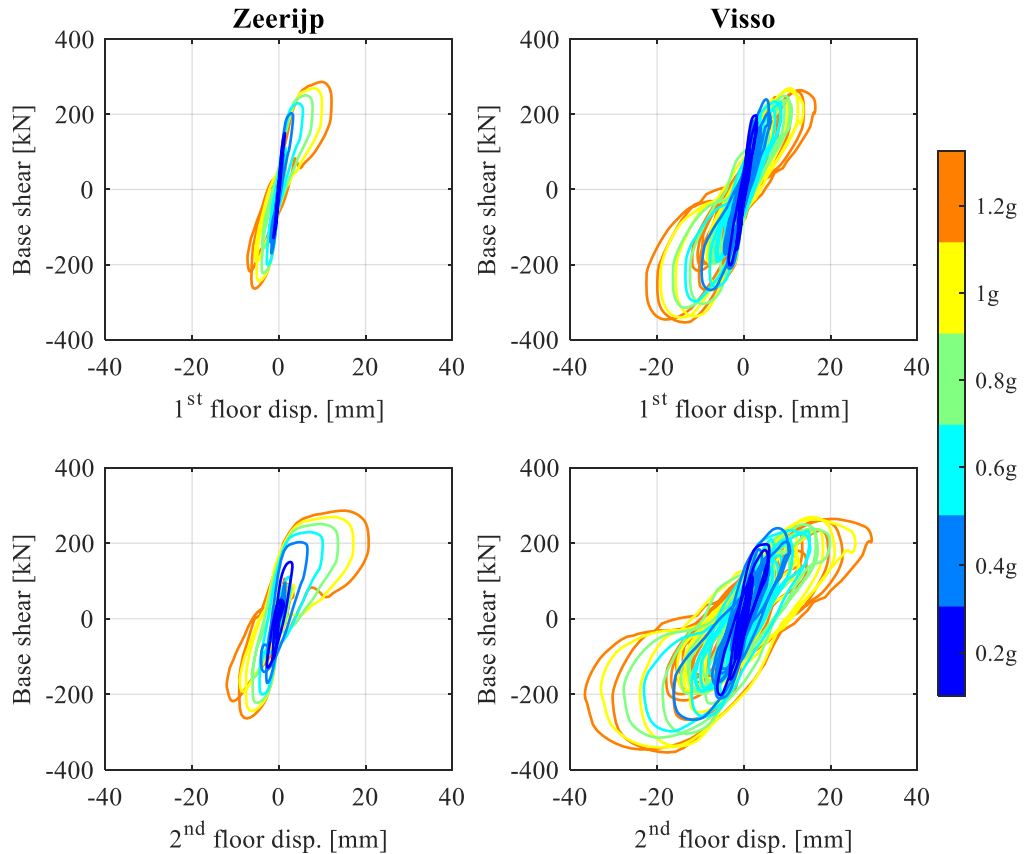
Figure 7.43 Base shear versus average 1st and 2nd floor displacement hysteretic curves obtained in the IDA performed on BUILD B

7.3.4 Case study BUILD C

The third case study was a two-story building with the same geometrical characteristics of BUILD A, presented in Figure 7.29, reinforced with strengthening and stiffening intervention at both first floor and roof. The purpose of this work was to assess the extent of debris produced by the local collapses, which can eventually occur in existing buildings, not designed to withstand earthquakes or retrofitted before the introduction of the more recent codes with specific seismic details requirements (Modena et al. 2011; Sisti et al. 2019; Sorrentino et al. 2019). After the Friuli (1976) and Irpinia (1980) earthquakes, codes endorsed replacing flexible diaphragms with reinforced concrete slabs to avoid local mechanisms encouraging the global building response. The Umbria-Marche, 1997-1998, and the more recent Central Italy earthquakes proved the ineffectiveness of such strengthening interventions, which may cause local out-of-plane mechanisms or complete collapses of masonry under a still intact roof when the quality of mortar is poor. Indeed, the additional weight and stiffness introduced may further weaken the existing masonry, causing the retrofitted structures to collapse (Decanini et al. 2004).

For this reason, the strengthening intervention considered for BUILD C was a typical retrofitting intervention in Italy in the 1980s. Both first floor and roof were reinforced with concrete slabs connected with steel bars to the existing timber structure (joists or purlins). The first-floor concrete slab was assumed to be connected to walls through elements called 'dovetail', typically employed to anchor the reinforced diaphragm to the existing masonry without the need to remove the existing floor to build the reinforced concrete (RC) ring beam. Instead, a RC ring beam was employed at the roof level and connected through steel bars to the walls below. Indeed those interventions usually followed the renovation of the roof, allowing the employment of RC ring beams on the building perimeter connected to the concrete slab which covered the timber structure. No other intervention to improve the quality of the stone masonry was considered.
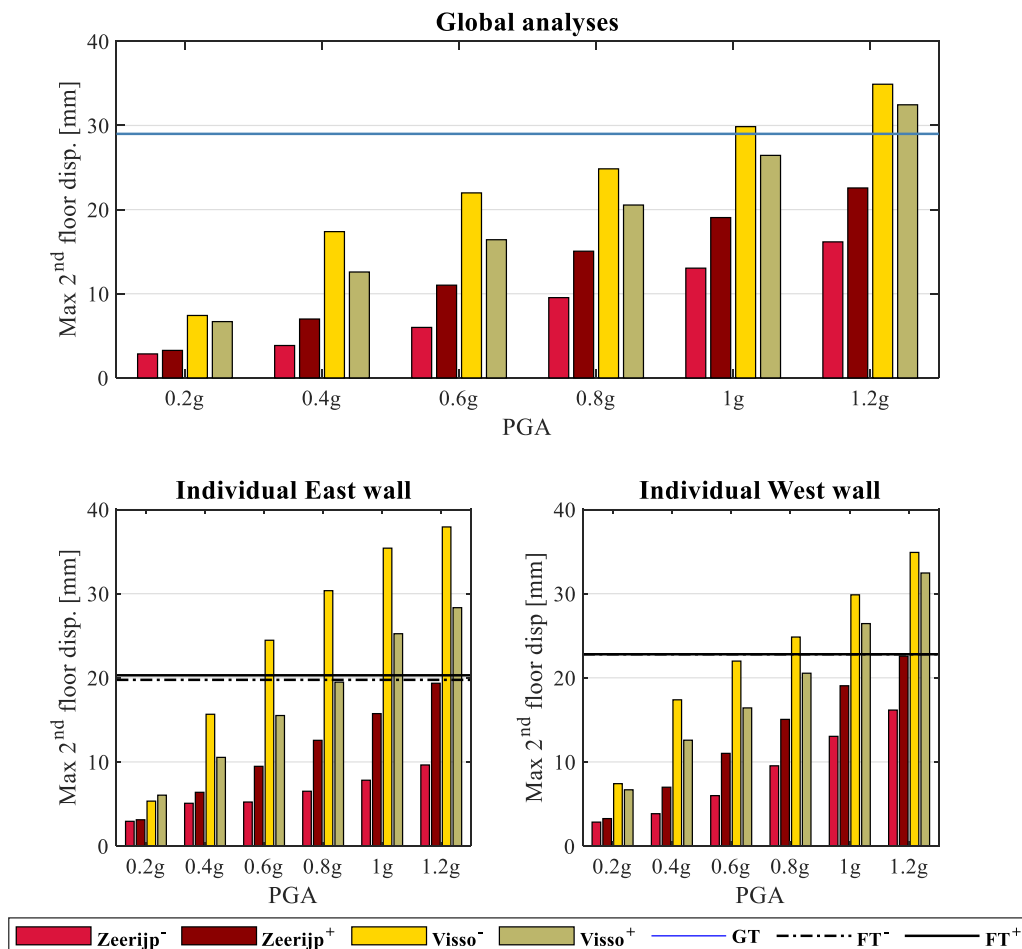
Figure 7.44 2nd floor maximum displacement attained by the control node of the global model and 2nd floor maximum displacement attained by East and West walls of individual façade models in the IDA performed on BUILD B

7.3.4.1 Displacement limits

BUILD C differed from the BUILD A and BUILD B for the presence of diaphragms, connected to the existing masonry through 'dovetail' anchors (at the first floor) and RC ring beam fixed to the wall through proper steel bars (at roof level), employed to ensure the benefic box behaviour avoiding the developing of local mechanisms. For this reason, contrary to the previous cases, individual wall pushover analyses would not contribute with significant information as the strengthening intervention was conceived to couple the response of the longitudinal walls. Global pushover analyses were then performed, and the related ultimate displacements attained by the 2nd floor are reported in Table 7.13.

Figure 7.45 presents the force-displacement curves obtained by the global pushover analyses with uniform and modal load patterns. Figure 7.46 shows the damage pattern presented by East and West walls at the end of the analyses. The last point of the PO was determined at the attainment of a drop of 50% of lateral strength. The minimum displacement attained by the control node at the 2nd floor of the West wall corresponding to that drop was considered as a displacement limit for the IDA. The damage was mainly located at the ground level, where external piers showed flexural damage and the central squat pier failed in shear. A soft-storey mechanism was also experienced by BUILD C, as already seen in the previous cases, but the presence of rigid diaphragms allowed the building to exploit its strength and displacement capacity attaining the global failure at larger displacements compared to BUILD B and BUILD A (26 mm, 19 mm and 23 mm respectively) and base shear (245 kN, 209 kN and 203 kN, respectively).
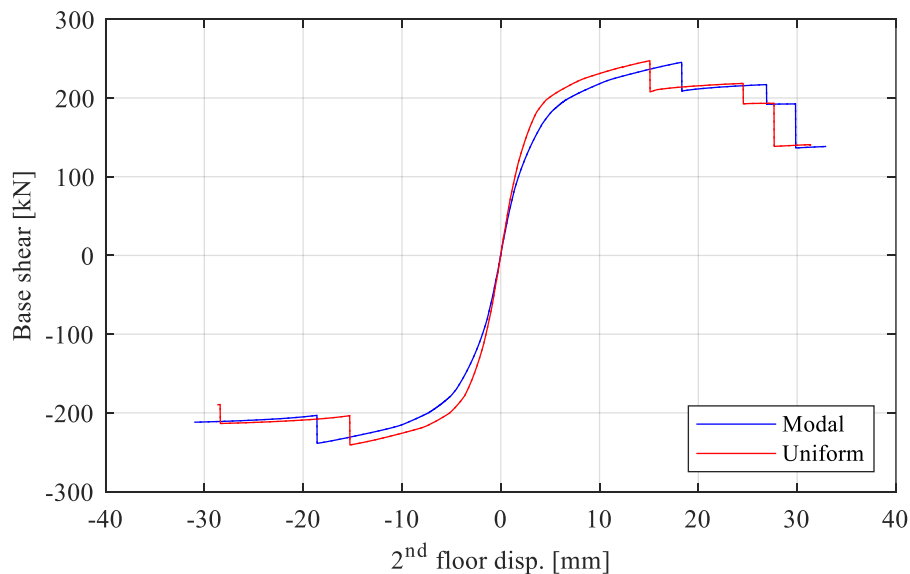
Figure 7.45 Pushover curves with first mode (modal) and mass (uniform) proportional load pattern

Table 7.13 Ultimate 2nd floor displacement attained in the PO

Average 2nd floor			
d$_{lim}$$^{-}$ [mm]		d$_{lim}$$^{+}$ [mm]	
Modal	Uniform	Modal	Uniform
-26	-26	30	32
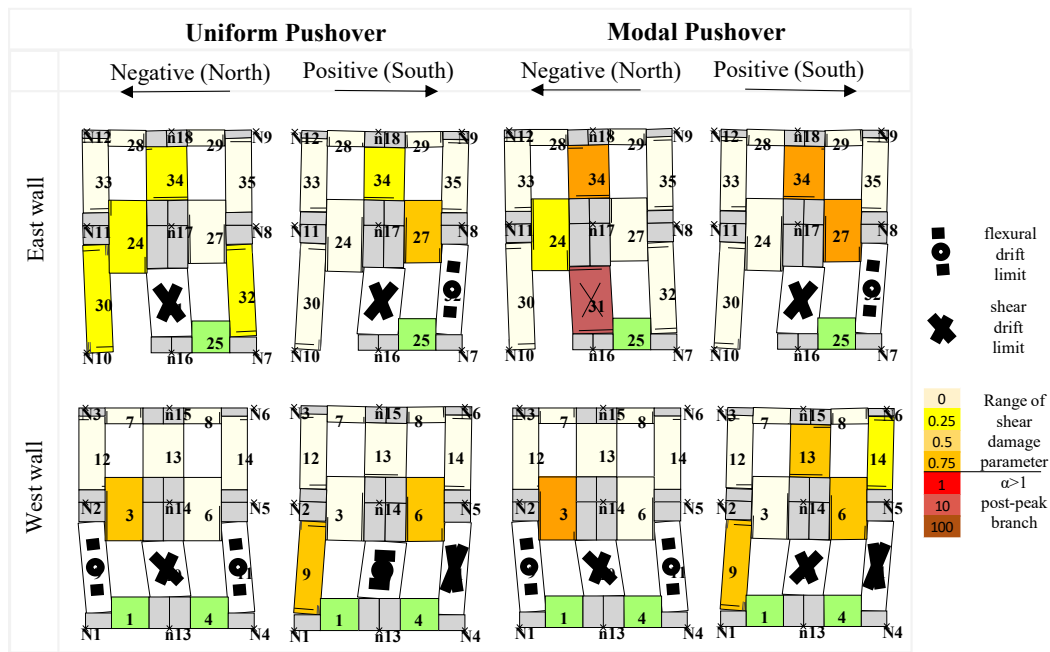
Figure 7.46 Damage pattern of East and West walls at the end of the pushover analyses

7.3.4.2   IDA

Incremental dynamic analyses were performed considering the two records presented in 7.3.1, scaled at six different intensity levels, corresponding to a PGA from 0.2 g to 1.2 g. The results of the 6 IDA are presented in terms of average displacement time-histories of 1st and 2nd floor (Figure 7.47) and base shear versus average 1st and 2nd floor displacements (Figure 7.48). As discussed in the previous section for BULDA and BUILD B, with Visso scaled records, BUILD C attained a base shear, in the negative direction, much higher than the capacity obtained in the pushover curves, due to the dynamic effects which produced different dynamic responses and load distribution with respect to the pushover analyses. In Figure 7.49 the maximum negative and positive 2nd floor at second-floor displacements were compared with the selected displacement thresholds obtained by the global pushover analyses and identified as 'GT'.
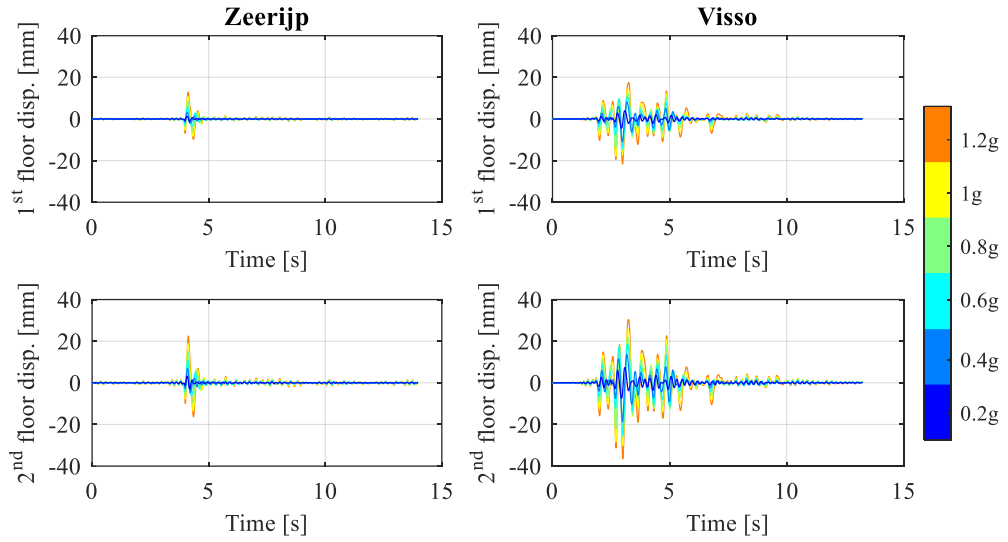
Figure 7.47 Average 2nd floor displacement time-histories obtained in the IDA performed on BUILD C
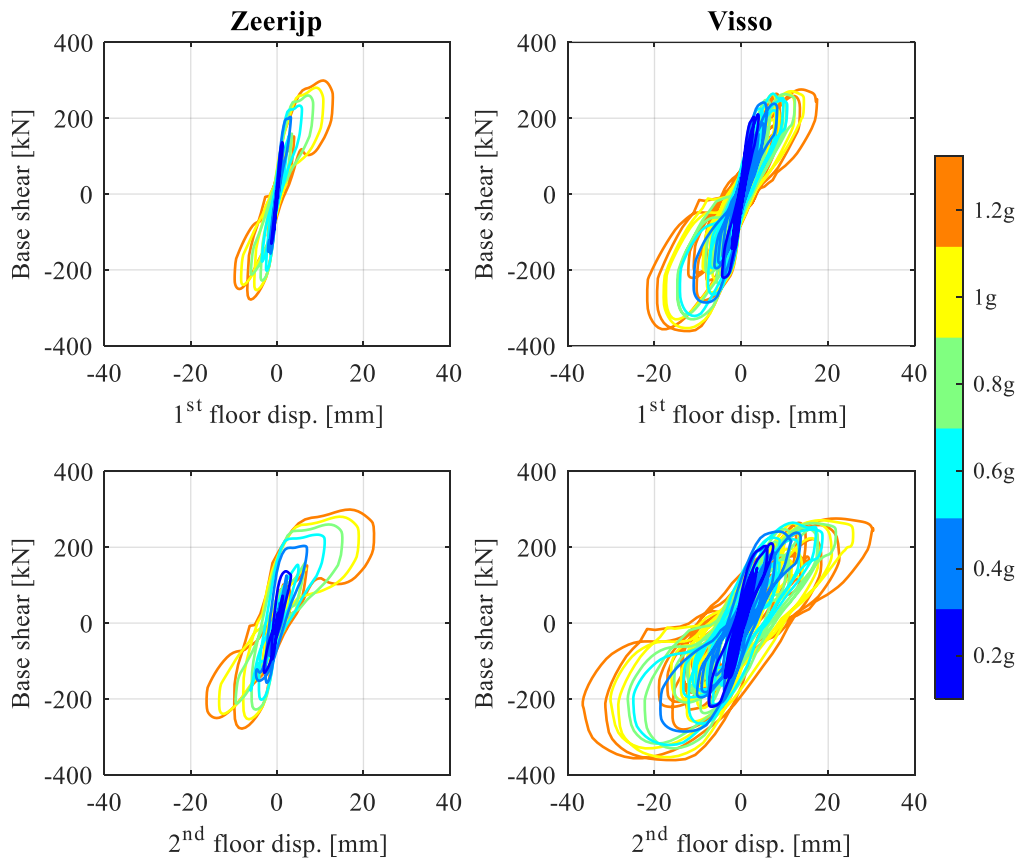
Figure 7.48 Base shear versus average 1st and 2nd floor displacement hysteretic curves obtained in the IDA performed on BUILD C

The first attainment of GT displacement limit occurred in the fourth run, which corresponded to 0.8 g for Visso records, whereas Zeerijp series never attained those thresholds. As global pushover analyses could not provide information on the eventual development of local failure, the same intensity levels considered for BUILD A and BUILD B (i.e. 0.6g and 1.2g for Visso and Zeerijp, respectively) were analysed using the AEM local models.
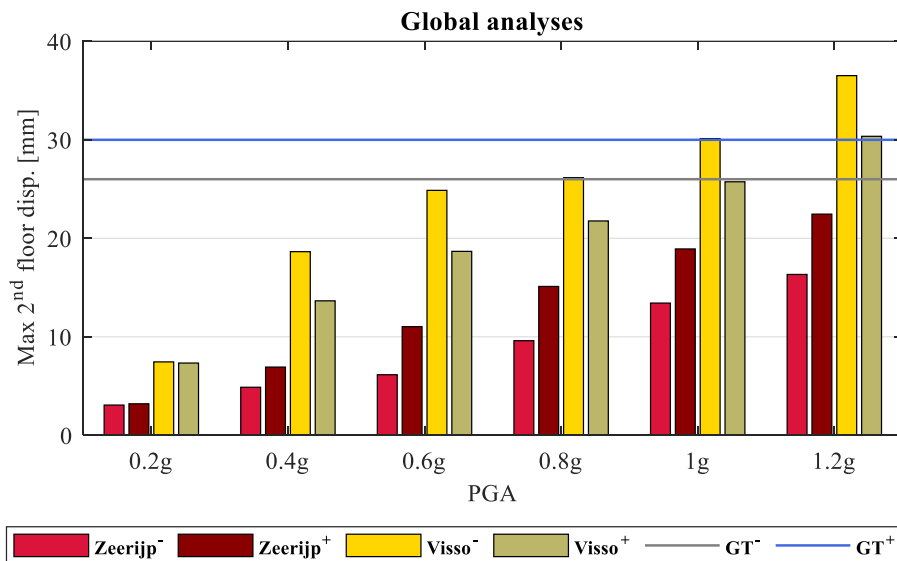
Figure 7.49 2nd floor average maximum displacement in the IDA performed on BUILD C

7.4   Local analyses

7.4.1 Local AEM models

The AEM model represented the portion of the structures involved in the overturning mechanism causing the collapse of the façade adjacent to the street. That portion involves the façade, the roof, the upper part of the opposite façade (i.e. the gable), and the portions of the longitudinal façades delimited by the openings. The material properties of masonry are reported in Table 7.9.

The timber roof was explicitly represented by modelling spreader and ridge beams, planks and connections. An elastic material represented timber elements with Young modulus E equal to 11000 MPa and shear modulus G equal to 700 MPa. Nails and screws were explicitly modelled, introducing single normal and shear springs where the material properties were evaluated according to Eurocode 5 (CEN; 2004) and they are summarised in Table 7.10. A weak connection was assumed in BUILD A between purlins and the ridge beam consisting of two nails of 3 mm of diameter, whereas a screw with 14 mm of diameter was assumed to connect purlins and spreader beams. Planks were assumed nailed to the purlins through a couple of 3 mm nails with 90 mm of spacing. An equivalent linear

material was assigned to the springs representing the roof connections, assigning the equivalent properties reported in Table 7.10.

The connection between purlins was improved in the partial model of BUILD B, whereas the tie rods introduced in the EFM were not modelled in the AEM model, as the nodal displacements already account for the effect of that connections.

The strengthening intervention employed in BUILD C was explicitly modelled in the AEM model, introducing the reinforced concrete (RC) slab at both first floor and roof and the RC ring beam at the roof level. The dovetail anchors were also explicitly modelled by connecting the RC slab to the existing masonry through steel links. Similarly, the RC ring beam at the roof level was connected to the RC slab, the ridge beam, and the existing masonry. Both first floor and roof RC slabs were connected through steel anchors to the timber joists and purlins. Finally, BUILD D represented a variation of BUILD C where the concrete slabs were assumed infinitely rigid and the connections between the ring beam, concrete slabs and masonry were assumed perfectly fixed.

Absolute displacement histories were applied to the boundary of the partial model, where displacements were obtained by adding the ground displacement and the relative displacement obtained by the EFM analyses. The ground displacement histories were the ones recorded in the experimental shake-table tests performed by (Kallioras et al. 2021), scaled consistently with the PGA, whereas the relative displacements were obtained by the EFM analyses at nodes corresponding to the boundary of the partial model. The local AEM model of the South façade, as well as its boundary conditions and displacement histories application points, are presented in Figure 7.50.

Model   Boundary conditions   Displacement histories
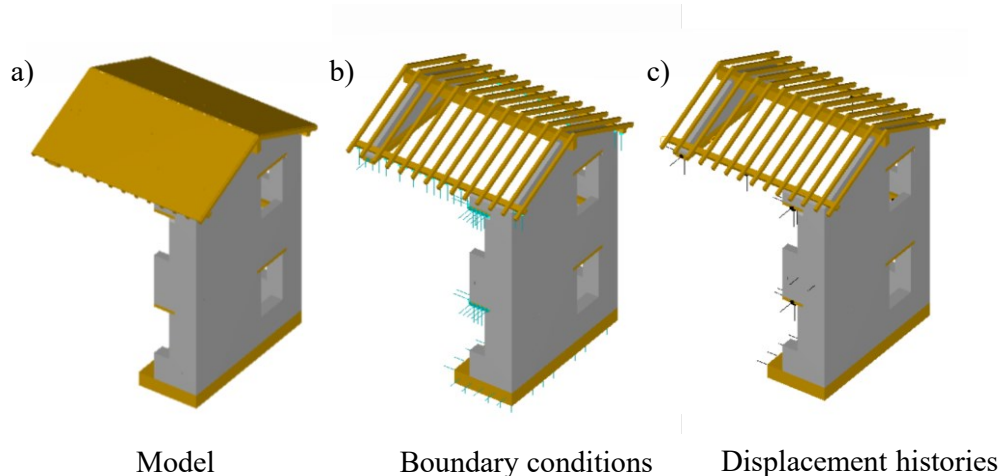
Figure 7.50 a) Model, b) boundary conditions and c) displacement histories application points

7.4.2 AEM analyses results

IDA were performed on the local model applying the absolute displacement histories obtained from the global EFM and the experimental records. The intensity levels causing the exceedance of the displacement thresholds in the EFM were considered (i.e. 0.6 g and 1.2 g for Visso and Zeerijp records, respectively).

Figure 7.51 presents the results obtained with the three local AEM models when displacement histories obtained with Visso record scaled at 0.6g of PGA were applied. The upper part of BUILD A North façade experienced an OOP mechanism, two-way bending with all sides supported at the beginning and without the top side's restraint after the roof's detachment from the wall below. This response was due to the weak connection between the North façade and the timber roof and the poor interlocking between orthogonal walls, which couldn't provide a proper restraint to avoid the development of the overturning mechanism. However, due to the weak connection between masonry leaves and the poor mechanical properties, cracks propagated throughout the upper North façade and its orthogonal walls, avoiding the detachment of wall portions that may rotate around the horizontal hinges, overturning. At the end of the analysis, the partial model of BUILD A presented heavy and widespread damage, with cracks 1-3 cm wide.

Similarly, BUILD B showed a typical two-way bending mechanism at the beginning. In this case, the presence of the vertical restraints provided by the orthogonal walls, due to the presence of the tie rods, allowed the development of a two-way bending OOP mechanism. After the detachment of the gable from the timber roof, diagonal cracks developed and the upper part of the North façade collapsed, causing the ridge beam to fall. Thanks to the improved connection between purlins and an arch effect pushing on the sidewalls, the timber roof remained standing.

BUILD C and BUILD D presented a two-way bending mechanism at the beginning. Indeed, thanks to the good connection between the ring beam and the existing walls, the upper part of the façade was supported at all sides and developed horizontal hinges at first-floor level and mid-span. Then, the cracks developed along the perimeter of the ring beam had widened, causing the separation of the upper side of the wall and the partial collapse of the façade.

Analogous results were obtained when the Zeerijp record, scaled at 1.2g, was considered. The acceleration record presents a peak around 4s. Due to the high intensity of this signal, the South façade already presented widespread damage when the peak arrived, causing the separation of the external masonry leaf and the detachment of the gable from the roof with the consequent overturning of the upper part of the South wall. The collapse sequences obtained with the Zeerijp record scaled at 1.2g of PGA are presented in Figure 7.52. The retrofitting interventions employed in BUILD B and BUILDC-D proved to be capable of providing restraint against the overturning mechanism of the façade. However, their employment may be insufficient when the quality of masonry is poor, causing the local expulsion of the outer leaf and the pounding of the ring beam and the RC slab, as occurred to BUILD C and D in Zeerijp series. Table 7.14 summarises the results of debris extent

evaluation, where V_t, A_t, V_f and A_f are volume and area of debris fallen outside the perimeter of the building and on the front side of the façade involved in the overturning mechanism. The maximum distance, D_{max}, attained by debris was measured from the closest building façade, as presented in Figure 7.53.

Visso 0.6g - collapse sequence

BUILD A	3 s **	6 s **	15s	Near collapse*
BUILD B	4 s **	11 s	13.5 s	Collapse
BUILD C	3 s **	6 s	7 s	Collapse
BUILD D	3 s **	7 s	9 s	Collapse

* Crack pattern   ** Magnified
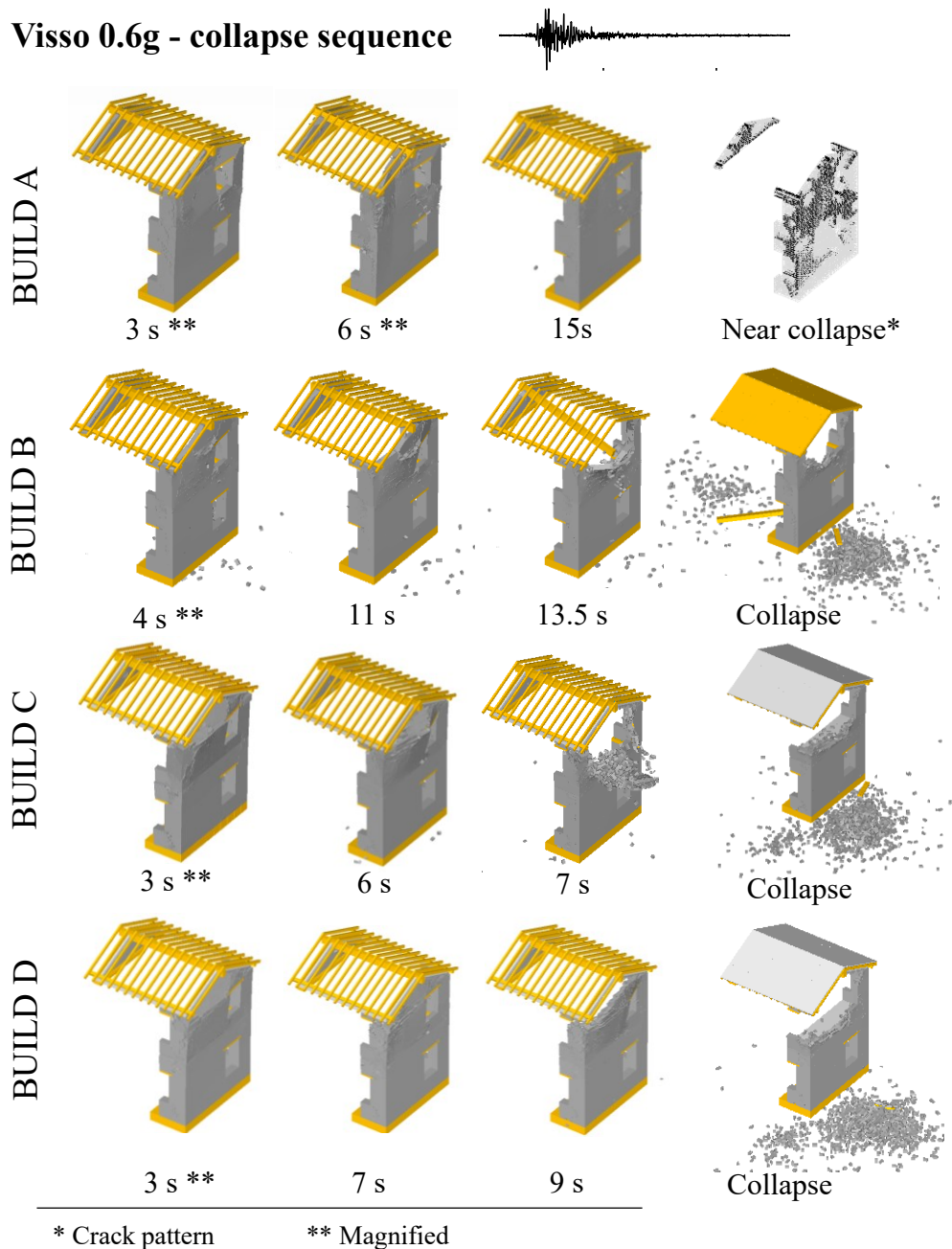
Figure 7.51 Collapse sequence of the North façade with Visso scaled record (the unscaled acceleration time-history is shown in Figure 7.27)
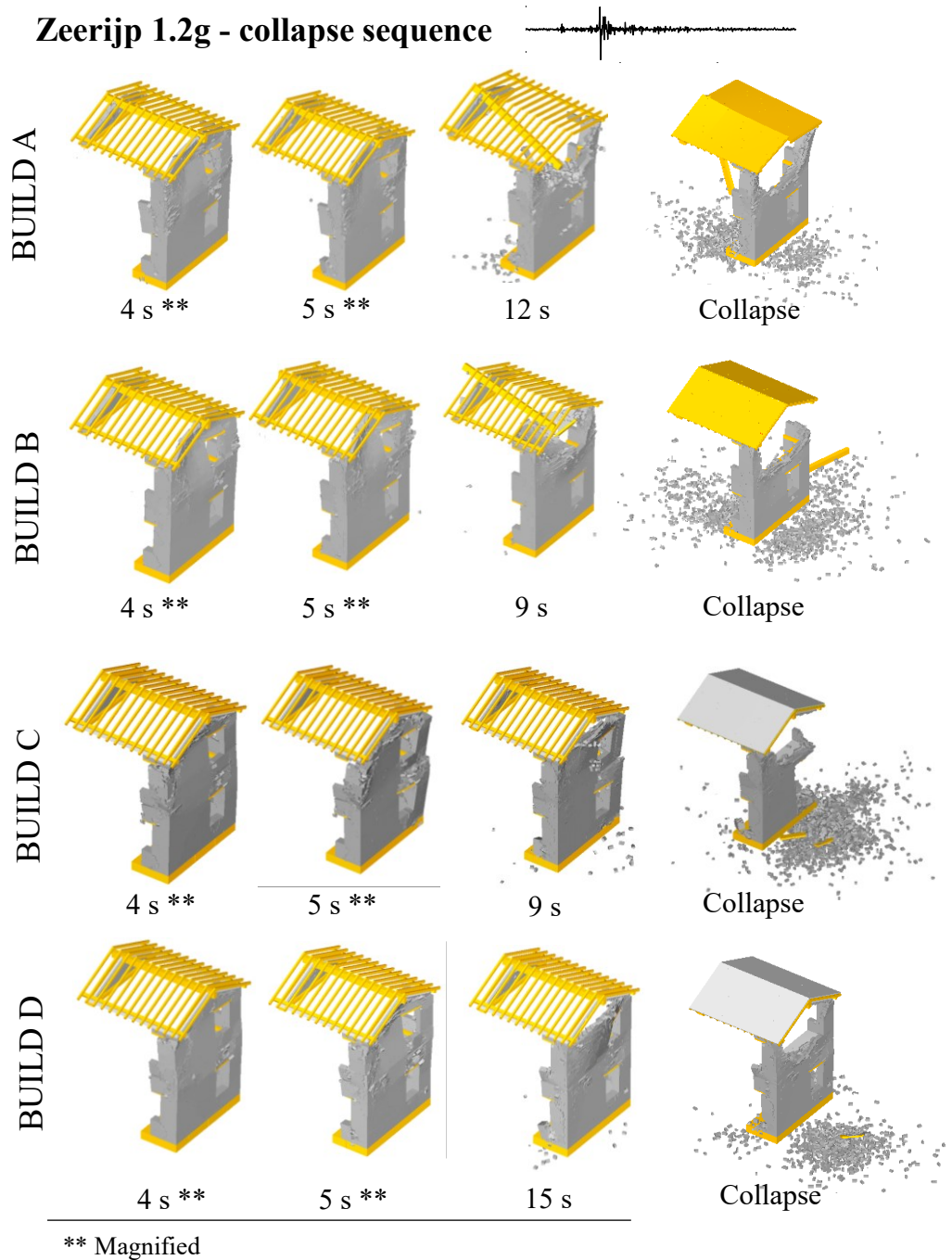
Figure 7.52 Collapse sequence of the South façade with Zeerijp scaled record (the unscaled acceleration time-history is shown in Figure 7.27)

The amount of debris was evaluated at several distance intervals to the building perimeter, reporting the debris distribution obtained with each local analysis. The results are reported for the Zeerijp and Visso series in Figure 7.55 and Figure 7.54, where each bar, *i*, of the

histograms represents the volume of debris measured between a distance D_{i-1} and D_i from the building perimeter. The average cumulative volume is also presented.

Most of the produced debris (more than 70%) fell within a distance equal to the H/2, where H is the building height. At a distance equal to H (i.e. 7 m in this case), more than 95% of debris volume has been measured. These results are consistent with empirical formulae proposed by other researchers to measure the probability of occupancy of adjacent streets (Bernardini et al. 2020), confirming that geometrical consideration may be adopted for the fast assessment of the extent of debris.

Table 7.14 Characteristics

Record	PGA [g]	BUILD	Damage	V_t [m³]	V_f [m³]	D_{max} [m]	A_t [m²]	A_f [m²]
Visso	0.6	A	Near collapse	-	-	-	-	-
		B	Collapse	3.29	2.73	12.80	373	177
		C	Collapse	2.84	2.62	12.25	254	120
		D	Collapse	3.68	3.46	20.80	386	277
Zeerijp	1.2 g	A	Collapse	1.48	1.00	12.05	409	135
		B	Collapse	3.74	2.04	11.20	317	124
		C	Collapse	6.32	5.92	14.06	338	203
		D	Collapse	2.67	2.63	12.70	212	142
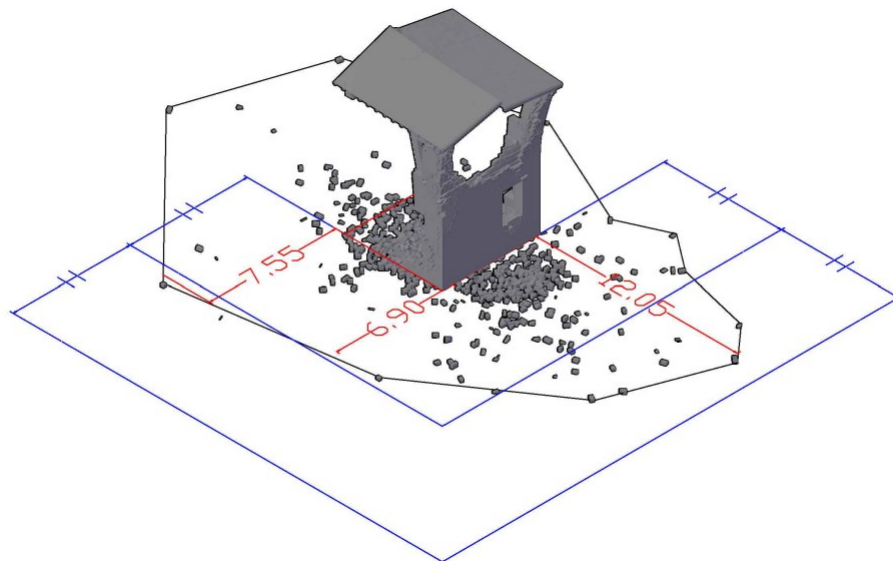
Figure 7.53 Debris extent evaluation (BUILD A Zeerijp 1.2 g)
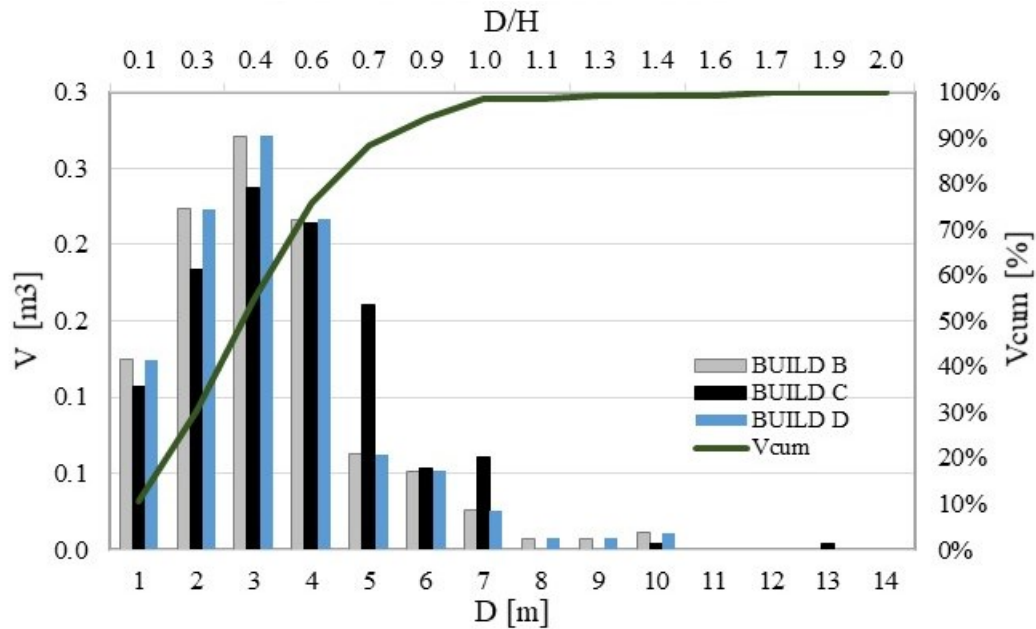
Figure 7.54 Debris distribution obtained in Visso series
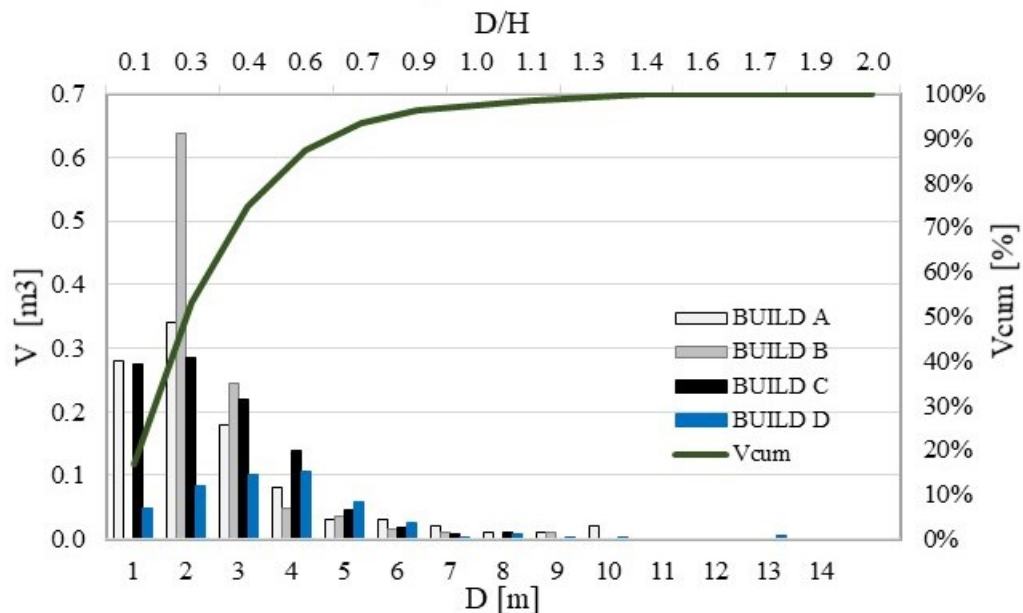
Figure 7.55 Debris distribution obtained in Zeerijp series

Finally, it is worth noting that the application of the proposed procedure to integrate EFM and AEM models allowed to save time with respect to the adoption of the AEM only. Indeed performing a single dynamic analysis may require more than a day using a global AEM model, whereas with the EFM only few minutes.

For the case studies presented in sections 7.3 and 7.4, each EFM dynamic analysis required approximately 10 minutes, 3 hours considering the whole set of signals, whereas each analysis performed with the AEM sub-structure needed around 12 hours (approximately 4 days for the 8 analyses). Considering a global AEM model for each tested case study and the 2 records scaled at 6 intensity levels, would take around 48 days. The creation of EFM and AEM models for all the considered case studies required approximately 15-20 days, saving a total of about a month.

The benefit of the procedure increases with the number of signals considered and with the dimensions of the building with respect to the reduced portion investigated with the local model, compensating for the time required by the creation of double models, which was almost doubled. The advantage of the procedure can be significant when performing risk studies, which require a wide set of analyses.

7.5   Final remarks

Recent earthquakes drew attention to the vulnerability of existing buildings towards seismic actions and the problem of access to historical centres, as the capacity of streets may be reduced by the presence of debris, limiting rescue operations. In this context, assessing the vulnerability of masonry structures, which represent a large part of existing constructions, evaluating the possible failure mechanisms, and the related amount of debris became crucial to prioritise strengthening interventions. In the last decades, several researchers focused their efforts on the problem of the seismic assessment of historical centre constructions and the evaluation of the probability that falling debris occlude, partially or totally, the urban streets. The available approaches for the prediction of debris amount are mainly built on empirical relationships based on post-earthquake observations and consequently related to a limited number of seismic events and structural typologies. In this context, the development of reliable models for predicting the collapse mechanisms and the amount and the extent of debris represents a valid alternative, allowing to consider a large number of input motions, simulating the structural response at different intensity levels of the seismic action.

The most advanced numerical tools accurately simulate the building response up to the complete collapse, but this feature is usually paid with a large computational time required for the analyses, which limits the employment of such modelling approaches to seismic risk studies where a large suite of input is required. On the other hand, simplified numerical modelling strategies allow performing a larger number of analyses in a reasonable time but cannot simulate the building collapse. An integrated modelling strategy is proposed in this work to overcome this limit by combining the use of simplified tools and more advanced models.

The proposed procedure involves the development of global models using a simplified modelling approach to assess the structural response under a selection of ground motions and local models with a more advanced modelling approach that allows the simulation of the collapse under a selected set of inputs. The Equivalent Frame Model (EFM) was employed in this work to analyse the global response of three case studies, whereas a

numerical tool based on the Applied Element Method (AEM) was considered for the local analyses. Both EFM and AEM models were preliminarily validated through the simulation of shear-compression tests on individual walls and a shake-table test on a full-scale stone masonry building. The simulation of these tests was also performed to validate the AEM modelling strategy adopted for modelling a double-leaf stone masonry structure, which - as far as the author is aware of - has never been replicated with this tool before.

Incremental dynamic analyses were performed with two records scaled at different intensity levels for demonstration purposes, but the procedure allows the employment of a larger selection of ground motions. Among the employed scaled records, the input motions causing collapse were selected, monitoring the exceedance of established thresholds, and considered in the local analyses with the AEM models. A set of nodal displacement histories was obtained from the global EFM models for each analysis exceeding the displacement thresholds. Those displacement histories were added to the ground displacement to get absolute displacements and applied to the partial AEM model. The absolute nodal displacements described the boundary condition of the portion involved in the local mechanism, allowing to analyse smaller models and saving time. After each local analysis, the amount and extent of debris produced by the collapse were measured. The results confirmed the validity of some of the available empirical relationship that relates the maximum distance attained by debris to the building height. Although two records with different characteristics and intensity levels were employed for the dynamic analyses, no significant differences were found in terms of failure mode and distribution of debris, which amount seems to be only related to the distance from the building perimeter.

Moreover, using AEM models allowed investigating the effectiveness of different strengthening interventions to prevent OOP mechanisms. In the past, strengthening interventions on structures characterised by the poor quality of the masonry frequently caused the separation of walls' outer leaves, the pounding of the ring beam or the crumbling of masonry. These effects should be reproduced and evaluated only by using a numerical model able to represent the interaction among masonry components and structural elements, such as the AEM model employed in this work. The capability to simulate the effect of strengthening interventions on existing masonry buildings' response is a crucial feature to predict the post-earthquake scenario in historical city centres.

The proposed methodology demonstrates the possibility of efficiently integrating the use of simplified and advanced models to predict the extent of debris after an earthquake, offering a valid alternative to simplified empirical formulae. Future developments of this work may include the investigation of different building typologies with different geometry and materials, including aggregates and the study of the effect of the vertical component of the seismic action. Moreover, the ability of EFM to consider a large suite of input motions should be exploited using the proposed procedure for seismic risk studies, including information on the extent and amount of produced debris.

References

Artese S, Achilli V (2019) A gis tool for the management of seismic emergencies in

historical centers: How to choose the optimal routes for civil protection interventions. ISPRS Ann Photogramm Remote Sens Spat Inf Sci 42:99–106. https://doi.org/10.5194/isprs-Archives-XLII-2-W11-99-2019.

Bernabei L, Mochi G, Bernardini G, Quagliarini E (2021) Seismic risk of Open Spaces in Historic Built Environments: A matrix-based approach for emergency management and disaster response. Int J Disaster Risk Reduct 65:102552. https://doi.org/10.1016/j.ijdrr.2021.102552.

Bernardini G, Lucesoli M, Quagliarini E (2020) Sustainable planning of seismic emergency in historic centres through semeiotic tools: Comparison of different existing methods through real case studies. Sustain Cities Soc 52:101834. https://doi.org/10.1016/j.scs.2019.101834.

Bracchi S, Galasco A, Penna A (2021) A novel macroelement model for the nonlinear analysis of masonry buildings . Part 1 : Axial and flexural behavior. Earthq Eng Sructural Dyn 50:2233–2252. https://doi.org/10.1002/eqe.3445.

Bracchi S, Penna A (2021) A novel macroelement model for the nonlinear analysis of masonry buildings. Part 2: Shear behavior. Earthq Eng Struct Dyn 50:2212–2232. https://doi.org/10.1002/eqe.3444.

Brignola A, Pampanin S, Podestà S (2009) Evaluation and control of the in-plane stiffness of timber floors for the performance-based retrofit of URM buildings. Bull New Zeal Soc Earthq Eng 42:204–221. https://doi.org/10.5459/bnzsee.42.3.204-221.

Decanini L, De Sortis A, Goretti A, et al (2004) Performance of masonry buildings during the 2002 Molise, Italy, earthquake. Earthq Spectra 20:191–220. https://doi.org/10.1193/1.1765106.

European Committee for Standardization (CEN); (2004) EN 1995-1-1:2004, Eurocode 5. Design of timber structures. Part 1–1: General rules and rules for buildings.

Ferlito R, Pizza AG (2011) Modello di vulnerabilità di un centro urbano. Metodologia per la valutazione speditiva della vulnerabilità della viabilità d'emergenza. Ing sismica 28:31–43.

Gambarotta L, Lagomarsino S (1997) Damage models for the seismic response of brick masonry shear walls. Part II: the continuum model and Its applications. Earthq Eng Struct Dyn 26(4):441–462. https://doi.org/10.1002/(SICI)1096-9845(199704)26:4<441::AID-EQE651>3.0.CO;2-0.

Goretti A, Sarli V (2006) Road network and damaged buildings in urban areas: Short and long-term interaction. Bull Earthq Eng 4:159–175. https://doi.org/10.1007/s10518-006-9004-3.

Graziotti F, Magenes G, Penna A, Fontana D (2011) Experimental cyclic behaviour of stone masonry spandrels. In. Proceedings of the 15th World Conference on Earthquake Engineering 1–10.

Guerrini G, Salvatori C, Senaldi I, Penna A (2021) Experimental and numerical assessment of seismic retrofit solutions for stone masonry buildings. Geosci 11:. https://doi.org/10.3390/geosciences11060230.

Italian technical commission for seismic micro-zoning (2014) Handbook of analysis of emergency conditions in urban scenarios (Manuale per l'analisi della condizione limite dell'emergenza dell'insediamento urbano) (CLE). (in italian), 1st edn. Rome, Italy.

Jäger W, Irmschler HJ, Schubert P (2004) Mauerwerk-Kalender 2004. Ernst & Sohn Verlag für Architektur und technische Wissenschaften.

Kallioras S, Graziotti F, Penna A (2019) Numerical assessment of the dynamic response of a URM terraced house exposed to induced seismicity. Bull Earthq Eng 17:1521–1552. https://doi.org/10.1007/s10518-018-0495-5.

Kallioras S, Graziotti F, Penna A, Magenes G (2021) Effects of vertical ground motions on the dynamic response of URM structures: Comparative shake‐table tests. Earthq Eng Struct Dyn. https://doi.org/10.1002/eqe.3569.

Lagomarsino S, Penna A, Galasco A, Cattari S (2013) TREMURI program: An equivalent frame model for the nonlinear seismic analysis of masonry buildings. Eng Struct 56:1787–1799. https://doi.org/10.1016/j.engstruct.2013.08.002.

Magenes G, Penna A, Galasco A (2010a) A full-scale shaking table test on a two-storey stone masonry building. In: Proceedings of the 14th European Conference on Earthquake Engineering.

Magenes G, Penna A, Galasco A, Da Paré M (2010b) In-plane cyclic shear tests of undressed double-leaf stone masonry panels. In: Proceedings of the 8th International Masonry Conference. Dresden, Germany.

Magenes G, Penna A, Galasco A, Rota M (2010c) Experimental characterisation of stone masonry mechanical properties. In: Proceedings of the 8th International Masonry Conference.

Magenes G, Penna A, Senaldi IE, et al (2014) Shaking table test of a strengthened full-scale stone masonry building with flexible diaphragms. Int J Archit Herit 8:349–375. https://doi.org/10.1080/15583058.2013.826299.

Malomo D, Pinho R, Penna A (2018) Using the applied element method for modelling calcium silicate brick masonry subjected to in-plane cyclic loading. Earthq Eng Struct Dyn 47:1610–1630. https://doi.org/10.1002/eqe.3032.

Meguro K, Tagel-Din H (2000) Applied element method for structural analysis: Theory and application for linear materials. Struct Eng Eng 17:21–35.

Modena C, Valluzzi MR, Da Porto F, Casarin F (2011) Structural aspects of the conservation of historic masonry constructions in seismic areas: Remedial measures and emergency actions. Int J Archit Herit 5:539–558. https://doi.org/10.1080/15583058.2011.569632.

Penna A, Lagomarsino S, Galasco A (2014) A nonlinear macroelement model for the seismic analysis of masonry buildings. Earthq Eng Struct Dyn 43:159–179. https://doi.org/10.1002/eqe.2335.

Penna A, Rosti A, Rota M (2022) Seismic Response of Masonry Building Aggregates in

Historic Centres: Observations, Analyses and Tests. In: Bento R, De Stefano M, Köber D, Zembaty Z (eds) Seismic Behaviour and Design of Irregular and Complex Civil Structures IV. Geotechnical, Geological and Earthquake Engineering, vol. 50. Springer, pp 19–36.

Penna A, Senaldi IE, Galasco A, Magenes G (2016) Numerical Simulation of Shaking Table Tests on Full-Scale Stone Masonry Buildings. Int J Archit Herit 10:146–163. https://doi.org/10.1080/15583058.2015.1113338.

Quagliarini E, Bernardini G, Wazinski C, et al (2016) Urban scenarios modifications due to the earthquake: ruins formation criteria and interactions with pedestrians' evacuation. Bull Earthq Eng 14:1071–1101. https://doi.org/10.1007/s10518-016-9872-0.

Santarelli S, Bernardini G, Quagliarini E (2018) Earthquake building debris estimation in historic city centres: From real world data to experimental-based criteria. Int J Disaster Risk Reduct 31:281–291. https://doi.org/10.1016/j.ijdrr.2018.05.017.

Senaldi IE (2012) The influence of floor and roof diaphragms on the seismic response of existing masonry buildings. PhD Dissertation, ROSE School, Pavia.

Senaldi IE, Magenes G, Penna A, et al (2014) The effect of stiffened floor and roof diaphragms on the experimental seismic response of a full-scale unreinforced stone masonry building. J Earthq Eng 18:407–443. https://doi.org/10.1080/13632469.2013.876946.

Sisti R, Di Ludovico M, Borri A, Prota A (2019) Damage assessment and the effectiveness of prevention: the response of ordinary unreinforced masonry buildings in Norcia during the Central Italy 2016–2017 seismic sequence. Bull Earthq Eng 17:5609–5629. https://doi.org/10.1007/s10518-018-0448-z.

Sorrentino L, Cattari S, da Porto F, et al (2019) Seismic behaviour of ordinary masonry buildings during the 2016 central Italy earthquakes. Bull Earthq Eng 17:5583–5607. https://doi.org/10.1007/s10518-018-0370-4.

Turnšek V, Sheppard P (1980) Shear and Flexural Resistance of Masonry Walls. In: Proceedings of the International Research Conference on Earthquake Engineering. Skopje, Macedonia, pp 517–573.

8. Conclusions and future developments

8.1 Summary and conclusions

In this thesis, the integrated use of different modelling approaches was proposed to overcome traditional modelling issues in balancing approximation level and computational effort. A discrete model based on the Applied Element Method (AEM) was chosen and used in combination with more simplified modelling methods or individually. In this context, the AEM model was employed as a benchmark to validate more simplified modelling approaches starting from a limited number of experimental tests and extending their results to different configurations. The capability of AEM model to represent the structural response up to the complete collapse was employed to predict the extent of debris produced after a seismic event, combining the use of different modelling approaches. In the following, the main goals and findings of this work are summarised.

- In Chapter 3 the problem of the reliability of the Equivalent Frame Model (EFM) in the presence of irregular opening distribution was investigated. The effectiveness of three commonly employed discretisation criteria for EFM was studied, comparing the in-plane response of walls with multiple opening configurations. First, an AEM and an EFM model were validated, simulating the experimental cyclic quasi-static tests on individual walls and a full-scale regular URM building façade. Then irregular façades obtained from the regular baseline combining different opening sizes and horizontal/vertical misalignments were studied, performing pushover analyses with the EFM and AEM models. In general, the average (AVG) and limited (LIM) effective height criteria resulted in a good prediction, suggesting that they are equally valid and should be preferred to MIN. The comparison between the obtained lateral responses showed minor differences in some cases and more significant in others, especially when the irregularity consisted of an opening with a reduced size. The comparison between the AEM models crack pattern and the EFM discretisation highlighted that, in case of very little openings, multiple small-size non-deformable regions are created, even in portions affected by damage propagation in the AEM analyses. This led to a stiffer response and a higher base shear resistance prediction, especially when the minimum effective height criterion (MIN) was adopted. Moreover, the results suggested that small openings can be neglected in the EF discretisation unless their presence significantly alters the stress distribution. Indeed, their presence did not influence the lateral response predicted by the AEM models. Finally, significant differences in initial stiffness and base shear capacity were found between AEM models and EFM when the irregular opening layout leads to a pier with a small aspect ratio. In that situation, the development of a diagonal compressed strut produced a reduction of the effective length of the pier. A solution for this problem

was proposed and tested by comparing EFM results with the AEM benchmark, solving the inconsistent lateral response prediction of the EFM. The work presented in this chapter proved the ability of the AEM model to extend the experimental results to different configurations not considered experimentally, providing a reliable benchmark for the evaluation of EFM predictions.

- Chapter 4 presents the use of the AEM model to investigate the effect of the ground floor openings percentage on the dynamic response of a URM cavity wall building. The model was calibrated against the experimental shake-table test performed on a full-scale building. Then, the dynamic response of a set of buildings with different geometrical configurations, including variations of the ground floor openings percentage, was investigated under several acceleration time histories. The same incremental uniaxial loading protocol employed in the experimental shake-table test was applied consecutively to the numerical AEM models in the first set of analyses, accounting for the effect of damage accumulation. Then, triaxial acceleration time histories were employed independently from each other. The results of the two sets of numerical simulations confirmed that the overall strength decreases with increasing opening percentage and deformations and failure mechanisms concentrate at the ground floor. When considering the triaxial seismic excitation, the extent of damage was again proportional to the percentage of openings at the ground floor and in the case of large percentages (i.e. >80%) torsional mechanisms governed the collapse, further increasing the vulnerability to horizontal actions. Moreover, the fragility functions derived with single-degree-of-freedom (SDOF) systems calibrated against AEM model results were presented as an example of the possible employment of an integrated modelling strategy to perform seismic risk studies.

- Chapter 5 presents the AEM simulation of the dynamic response of a cavity wall building retrofitted with a light timber system. The modelling strategy was validated against quasi-static cyclic shear-compression tests on a retrofitted and bare calcium silicate wall. Then, a full-scale shake-table test was simulated to validate the AEM model of the retrofitted building specimen against experimental results. A set of models of the same building with different geometrical configurations of the retrofitting system was then tested under the experimental uniaxial loading protocol to investigate the sensitivity of the seismic performance to different retrofit layouts. The study showed a significant influence of the horizontal and vertical frame spacing variations and element size. Reducing retrofit frame spacing and increasing timber element size improved the seismic performance, limiting global deformation and damage. On the other hand, the reduction of timber frame size produced more significant displacement and damage, emphasising the soft storey mechanism experienced by the baseline specimen. The AEM modelling strategy proved to be capable of reproducing the retrofit behaviour and the dynamic response of the strengthened specimen, allowing the investigation of its sensitivity to variations of the frame configuration and element size.

- Chapter 6 presents the AEM modelling strategy employed for the simulation of the in-plane response of masonry walls with unfilled head joints. This masonry typology was tested experimentally to evaluate its response under seismic actions and its applicability in moderately seismic areas. In this context, the AEM model may be employed for extending experimental results, providing additional information on the static and dynamic response of this masonry typology under different loading conditions. To this aim, the AEM model was validated against experimental outcomes of cyclic in-plane static tests performed on five walls with different geometry and under various compression levels. This is the first application of the AEM to the analysis of masonry with vertically perforated clay units assembled with thin layer mortar bed joints and unfilled head joints. The AEM model proved to be capable of predicting the hysteretic response, failure mode and damage pattern of the five walls tested. The gaping behaviour experienced by two of the specimens was well captured in terms of force-displacement hysteretic curve, damage and energy dissipation. On the other hand, when the failure mode involved the masonry units, the model could not accurately reproduce the cracks passing through blocks. The EFM was also employed for the simulation of the five walls to investigate the reliability of a new strength criterion implemented to describe the gaping behaviour. The EFM predicted the hysteretic response, damage and energy dissipated in walls failing in shear with a good agreement, but it underestimates the dissipation of the gaping mechanism. However, the encouraging results obtained with both models suggest they can be jointly employed for future studies.

- In Chapter 7 an integrated modelling strategy was employed for the prediction of the extent of debris produced by the collapse of URM buildings. The proposed procedure involved dynamic analyses performed using global EFM to assess the building performance under a selection of acceleration time histories scaled at different intensity levels. Local AEM models were then employed to simulate the collapse under a limited number of input motions. Both EFM and AEM were preliminarily calibrated against experimental shear-compression test outcomes on individual walls and validated against the shake-table test performance of a full-scale stone masonry building. This study also represents the first attempt to simulate double-leaf stone masonry structures using AEM. After validation, incremental dynamic analyses were performed on three EFM of the same building with different strengthening interventions, applying two records scaled at several intensity levels up to 1.2 g of PGA. Among all global EFM analyses, only those exceeding an established displacement threshold were selected and considered for the local AEM analyses. A set of nodal displacement histories was obtained from each EFM simulation and combined with the ground displacement to apply absolute displacement histories to the AEM model. In fact, the obtained nodal displacement histories constituted the boundary conditions of the portion involved in the local mechanism, allowing to consider smaller models and saving computational time and memory. After each analysis, the volume of debris and the

area occupied were measured, also evaluating the maximum distance attained from the building perimeter. The results confirmed the validity of empirical formulae that relate the maximum distance attained by debris to the building height. Moreover, AEM models allowed for studying the effect of different strengthening interventions on the building response. Three case studies of buildings with equal geometry and material properties were considered. The first one was an unreinforced building representative of Italian historical construction, while the second one was retrofitted only with tie rods and the third one included strengthened and stiffened reinforced concrete diaphragms and ring beams. These retrofit interventions were detailed according to the Italian practice preceding the enforcement of modern seismic codes (i.e. after L'Aquila (2009) earthquake), and were explicitly modelled to evaluate their influence on the global building response and their capacity to prevent out-of-plane mechanisms and collapses. The AEM proved its ability to simulate the effect of the introduction of concrete slab and ring beams on the dynamic response of the building, reproducing phenomena frequently observed in structures characterised by a poor quality of masonry, such as separation of the outer leaf and pounding of the concrete elements with a consequent collapse.

8.2 Future research

The following topics also require future research attention:

- The further enhancement of the EFM reliability employing AEM simulations as a benchmark for analysing different irregularities, including different opening layouts and materials with respect to the ones considered in this thesis. The investigations should also include the presence of discontinuities, lintels, and existing damage that should be accounted for in the definition of the EF geometry.

- The AEM model presented in Chapter 5 should be employed for assessing the effect of the considered retrofitting system on the dynamic response of different building typologies, evaluating the possible employment of this retrofit in different contexts than the Dutch building stock. This further investigation may also involve the use of the AEM model to provide a benchmark for the calibration of more simplified models to be employed in a more comprehensive risk assessment.

- The response of masonry with unfilled head joints should be further investigated numerically using the AEM and EFM models developed in this work. These may include dynamic excitations, out-of-plane tests on single components and dynamic analyses on entire buildings to evaluate the seismic response of structures built with this masonry typology. Following the proposal of this thesis, an integrated strategy can be employed to investigate the global response of full-scale buildings with the EFM, and the local behaviour, including an accurate evaluation of the OOP response of individual walls extracted from the global model, with the AEM.

-   The integrated strategy employed in Chapter 7 for demonstration purposes should be applied to employ a wider selection of ground motions to use the EFM responses to derive fragility functions and associate a more comprehensive risk assessment with the amount/extent of debris produced by the collapse. Different building configurations should also be investigated, including various structural typologies and buildings in aggregate, which often characterised Italian historical centres. Moreover, the effect of the vertical components of the seismic excitation should also be investigated.

-   The development of a code to integrate different modelling strategies in a readily-use tool to combine the use of EFM and AEM models, automatically providing the input absolute displacement histories obtained from the global analyses to be applied to the local models evaluating the amount of produced debris.

APPENDIX A: The Applied Element Method

The Applied Element Method (AEM) is a simplified micro-modelling approach (Lourenço et al. 1996), and it can be classified as a Rigid Body and Spring Model (RBSM) (D'Altri et al. 2020). According to the original formulation (Meguro and Tagel-Din 2000), in AEM, a structure is virtually divided into rigid elements connected by springs where material properties, deformations and failures are lumped. Each element has 6 degrees of freedom, and it is connected to the others through sets of one normal and two shear springs, distributed at elements faces. Each set of springs represents stresses and strains of a given area, allowing for a deformable assembly of elements that do not change their shape during the analysis. AEM automatically predicts cracks location, elements separation and collisions, being a reliable approach to represent structure behaviour from the elastic field to complete collapse.

In 2D, the structure is divided into rigid elements with three degrees of freedom, connected by pairs of normal and shear springs, located at elements edges (Figure A.1). Springs normal and shear stiffnesses are given by equations (1) and (2):

$$k_n = \frac{E\,d\,t}{a} \qquad (1) \qquad\qquad k_s = \frac{G\,d\,t}{a} \qquad (2)$$

Where E and G are the elastic and shear moduli, respectively, d is the distance between adjacent springs, t is the element thickness, and a is the elements centroid distance.
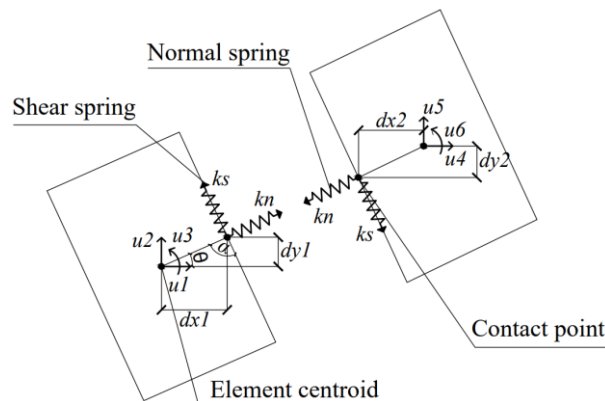

Figure A.1 Springs location and contact points (adapted from Meguro and Tagel-Din 2000)

The numerical simulations performed by Meguro and Tagel-Din (Meguro and Tagel-Din 1994,1999,2001a,2001b,2002; Tagel-Din and Meguro 1998,2000) proved that the AEM could accurately evaluate displacement and internal stress even in case of a high-stress gradient or in shear-dominant cases reducing elements size. Poisson's effect can also be considered.

In dynamic analyses, the damping matrix takes into account the sources of damping that are not implicitly considered. The sources of damping accounted by the analysis are: cracking, energy dissipation due to different loading/unloading stiffnesses of compression springs, energy dissipation due to the opening and closure of cracks, friction between elements during the contact and collision and rebounding (Meguro and Tagel-Din 2002). The other sources of damping can be accounted for in a damping matrix that is proportional to the mass matrix and is calculated based on the first mode deformation.

Collisions and recontact are considered in the AEM through the definition of collision springs added where contact between elements occur.

When springs between two elements in touch reach the separation strain, they are removed, and these elements behave as two separate rigid body. When a collision occurs, normal and shear springs are added at the contact point. The normal spring direction is the one of the line connecting the two elements centroid, while the shear spring direction is tangent to the circular elements. Collision springs exist when elements are in contact and are removed after separation. The collision is checked only between near elements to reduce the computational time. Elements shape is assumed circular to simplify the collision check procedure.

The normal spring stiffness of contact or collision springs is evaluated as:

$$k_n = \frac{E\,d\,t}{D} \qquad\qquad (3)$$

Where E is the Young modulus, t is the element thickness, D is the distance between element centroids, and d is the contact distance, assumed equal to 1/10 of the element size.

The shear spring stiffness is assumed 1/100 of the normal one. Compression failure is not allowed, and k_n is assumed constant.

The energy dissipated in the collision is taken into account assuming different loading and unloading stiffnesses. The kinetic energy lost in the collision is considered through the rebound factor r, which is the ratio between element velocity before and after the collision. It varies between 0 and 1. It is 0 when the collision dissipates all the kinetic energy, and it is 1 when the velocity is the same after the collision.

The rebound factor r is set by the user choosing the unloading stiffness factor n, which is equal to 1 when there is no energy dissipated during the contact and the unloading stiffness

is equal to the loading one. In contrast, n is infinity when all the kinetic energy is lost. The relation between r and n is reported in (4).

$$r = \frac{1}{\sqrt{n}}$$

(4)

AEM for masonry

According to the AEM, a structure can be divided into an assembly of rigid elements connected by nonlinear spring interfaces where material properties are lumped and where deformations and failures occur. The AEM is naturally suitable to represent the natural anisotropy of masonry, which can be discretised in unit elements connected by springs. Thus, according to the simplified modelling strategy (Lourenço 1996), units are expanded in both directions, including mortar joints thickness, which is reduced to zero-thickness interfaces,Figure A.2. The springs, which account for brick-mortar interaction, are placed at the actual joints location, and they are here named joint springs (Figure A.3). Units can be further divided into sub-elements connected by unit springs, accounting for brick material proprieties.
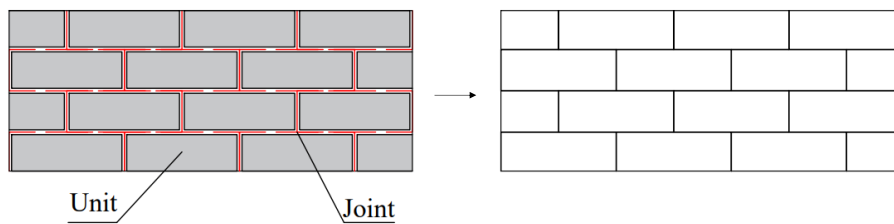

Figure A.2 In simplified micro-modelling units are expanded in both directions, and mortar joints are modelled with zero-thickness interfaces
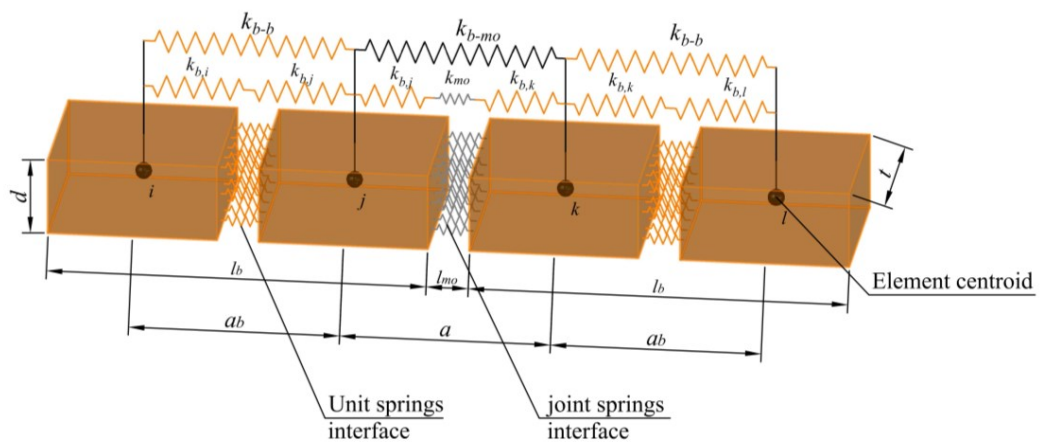

Figure A.3 Masonry discretisation

Each spring interface is characterised by a normal and a shear stiffness evaluated through equation (1)-(4). The reference nomenclature can be found in (Figure A.3). Springs placed between bricks units and representing mortar-brick interaction are here named joint springs. Their normal ($k_{n,b\text{-}mo}$) and shear ($k_{s,b\text{-}mo}$) stiffnesses are evaluated considering mortar and brick springs in series through equation (9) and (10). To capture the possible cracking through bricks, units are further divided into sub-elements connected by unit springs interfaces. Their normal and shear stiffnesses ($k_{n,b\text{-}b}$ and $k_{s,b\text{-}b}$) are evaluated by equation (11) and (12). Where E_b, G_b, E_{mo} and G_{mo} are the unit and mortar Young's and shear moduli, respectively.

$$\frac{1}{k_{n,b-mo}} = \frac{a - l_{mo}}{E_b\ d\ t} + \frac{l_{mo}}{E_{mo}\ d\ t} \quad (5) \qquad \frac{1}{k_{s,b-mo}} = \frac{a - l_{mo}}{G_b\ d\ t} + \frac{l_{mo}}{G_{mo}\ d\ t} \quad (6)$$

$$\frac{1}{k_{n,b-b}} = \frac{a_b}{E_b\ d\ t} \quad (7) \qquad\qquad \frac{1}{k_{s,b-b}} = \frac{a_b}{G_b\ d\ t} \quad (8)$$

To properly represent masonry behaviour, five failure type have to be considered: (1) joint debonding, (2) sliding along bed joints or head joints, (3) cracking of bricks under direct tension, (4) diagonal tensile cracking of bricks under shear-compression and (5) crushing, shown in Figure A.4.

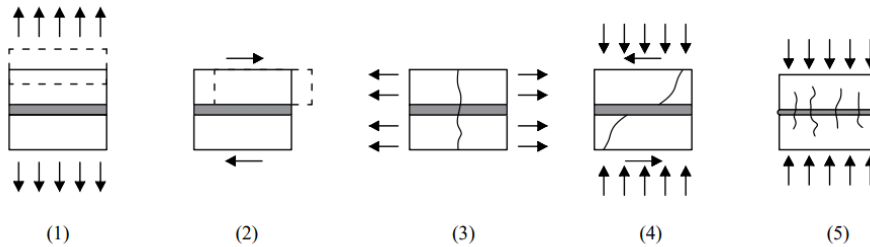$$(1) \qquad\qquad (2) \qquad\qquad (3) \qquad\qquad (4) \qquad\qquad (5)$$

Figure A.4 Masonry failure mechanisms: (1) joint debonding, (2) sliding along joints, (3) unit direct tension cracking, (4) shear-compression cracking of unit and (5) crushing

Failure modes (1) and (2) are joint mechanisms, and they can be represented by Coulomb's friction model with a tension cut off. Failure modes (3) and (4) are related to unit properties, accounted by unit spings. While considering crushing phenomena (5), a compression cap can be introduced. The multi-surface model proposed by Lourenço and Rots (1997) (Figure A.5a) combines the compression cap with Coulomb's friction law and a tension cut-off to account for joints failure modes (1)-(2) and (5), which involves both mortar and units.

Each failure mode is associated with a yielding surface of the plasticity model. Cohesion, Figure A.5b and bond tensile strength, Figure A.5c, are constant until the stress reaches the yielding surface. After that, in the original formulation, such parameters are defined by an exponential equation. The compressive strength follows the material model originally developed by Maekawa and El-Kashif (2004) for concrete, with hardening and softening

branches before and after the peak strength, respectively, Figure A.5d. The brick material failure envelope is given by (9)
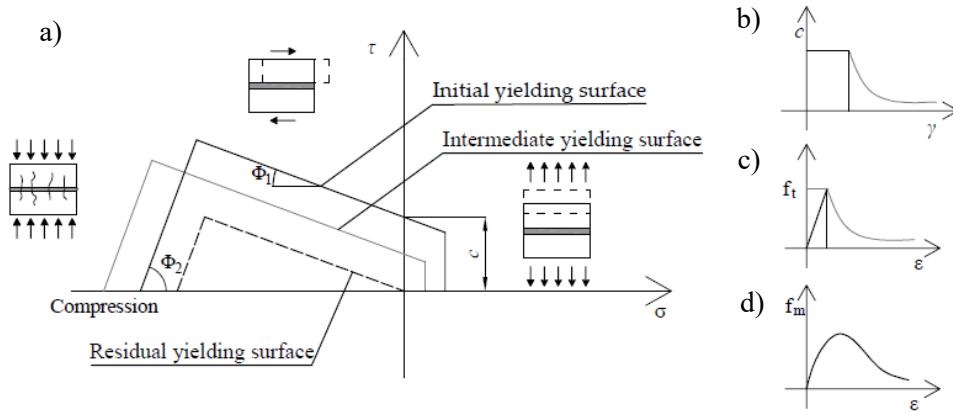

Figure A.5 Failure criteria for joint springs: a) linearised composite interface cap model, b) cohesion degradation, c) bond degradation, and d) hardening/softening compressive model (adapted from Pandey and Meguro, 2004)

Each failure mode is associated with a yielding surface of the plasticity model. Cohesion, Figure A.5b and bond tensile strength, Figure A.5c), are constant until the stress reaches the yielding surface. After that, in the original formulation, such parameters are defined by an exponential equation. The compressive strength follows the material model originally developed by Maekawa and El-Kashif (2004) for concrete, with hardening and softening branches before and after the peak strength, respectively, Figure A.5d). The brick material failure envelope is given by (9)

$$\frac{f_b}{f_b{}'} + \frac{f_t}{f_t{}'} = 1 \tag{9}$$

Where f_t and f_b are the principal tensile and compressive stresses and $f_t{}'$ and $f_b{}'$ are the uniaxial tensile and compressive strength, respectively.

The linearised failure multi-surface model here presented is derived from Lourenço and Rots (1997), and introduced by Mayorca and Meguro (2003) in the AEM. The failure surfaces f_i are presented in the follow.

The tension cut-off function f_1 is given by:

$$f_1(\sigma, \kappa_1) = \sigma - \bar{\sigma}_1 \tag{10}$$

$$\overline{\sigma_1} = \begin{cases} f_t\left(1 - \dfrac{f_t}{G_t^{I}}\kappa_1\right) & , \kappa_1 \leq \dfrac{2G_t^{I}}{f_t} \\[4mm] 0 & , \kappa_1 > \dfrac{2G_t^{I}}{f_t} \end{cases} \tag{11}$$

Where $\overline{\sigma_1}$ is the yield stress, f_t is the bond strength, and κ_1 is the hardening parameter. G_t^{I} is the mode I fracture energy (pure tension).

The yielding function of the Coulomb criterion, f_2, is:

$$f_2(\sigma, \kappa_2) = |\tau| - \sigma tan(\phi_1) - \overline{\sigma_2} \tag{12}$$

$$\overline{\sigma_2} = \begin{cases} c\left(1 - \dfrac{c}{G_t^{II}}\kappa_2\right) & , \kappa_2 \leq \dfrac{2G_t^{II}}{c} \\[4mm] 0 & , \kappa_2 > \dfrac{2G_t^{II}}{c} \end{cases} \tag{13}$$

Where $\overline{\sigma_2}$ is the yield stress, c is the joint cohesion, κ_2 the hardening parameter, and G_t^{II} is the mode II fracture energy (pure shear). ϕ_1 is the friction angle.

The compression cap is given by:

$$f_3(\sigma, \kappa_3) = |\tau| + \sigma tan(\phi_2)(\overline{\sigma_3} - \sigma) \tag{14}$$

$$\overline{\sigma_3}(\kappa_3) = \begin{cases} \sigma_i + (\sigma_p - \sigma_i)\sqrt{\dfrac{2\kappa_3}{\kappa_p} - \dfrac{\kappa_3^2}{\kappa_p^2}}, & \kappa_3 \leq \kappa_p \\[4mm] \sigma_p + (\sigma_m - \sigma_p)\left(\dfrac{\kappa_3 - \kappa_p}{\kappa_m - \kappa_p}\right)^2, & \kappa_p < \kappa_3 \leq \kappa_m \\[4mm] \sigma_r + (\sigma_m - \sigma_r)\left(\dfrac{\kappa_3 - \kappa_m}{\sigma_m - \sigma_r}\right)^2, m = 2\left(\dfrac{\sigma_m - \sigma_p}{\kappa_m - \kappa_p}\right), & \kappa_m < \kappa_3 \end{cases} \tag{15}$$

Where σ_i, σ_m, σ_p, σ_r, κ_m and κ_p are parameters obtained from uniaxial tests on masonry prisms.

Associated flow rules are adopted for f_1 and f_3, while non-associated flow rule is adopted for f_2 with the corresponding plastic potential given by $g_2 = |\tau| - c$.

The AEM code employed in this work simplified the previous model:

- Cohesion and tensile strength are set to zero after the attainment of the yield point without any softening branch (Figure A.5b,c, black line).
- A linearised version of the Lourenco&Rots multi-surface model is assumed (Figure A.6)
- The simplified multi-surface model is adopted for both mortar-brick and brick-brick nonlinear springs
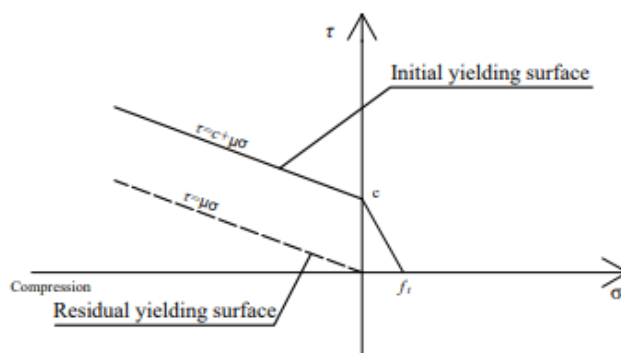
Figure A.6 Simplified multi-surface model adopted in the employed AEM code

The use of a micro-modelling approach required the definition of several mechanical proprieties to describe the behaviour of each masonry component. Experimental characterisation tests usually do not provide all the material properties needed for mortar and bricks separately. For this reason, a pre-processing procedure to define each material model parameter has to be employed (Malomo et al. 2018a).

Regarding the equivalent elastic properties of mortar-brick interface, as suggested by several authors (Mayorca and Meguro 2003; Malomo et al. 2018b), they can be firstly deduced through homogenisation formulae and then further adjusted through the comparison with experimental or theoretical initial lateral stiffness. Several theoretical (Jäger et al. 2004; Kaushik et al. 2007) and empirical (U.B.C. 1991; Matysek and Janowski 1996; Brooks and Baker 1998; Ciesielski 1999) formulae can be employed for a first estimate, then equivalent Young and shear moduli of mortar-brick interface can be further refined through the simulation of in-plane shear compression tests, comparing the numerical lateral stiffness with the theoretical or the experimental one.

Experimental characterisation tests typically provide mechanical parameters to describe material models as Young modulus and compressive strength of masonry, compressive strength of mortar and bricks, cohesion, friction coefficient, and tensile strength of mortar joints.

References

Brooks JJ, Baker A (1998) Modulus of Elasticity of Masonry. Mason Int 12:58–63.

Ciesielski R (1999) The dynamic module of elasticity of brick walls. In: Proceedings of the Conference of the Committee of Civil Engineering PZITB: Lublin, Poland.

D'Altri AM, Sarhosis V, Milani G, et al (2020) Modeling Strategies for the Computational Analysis of Unreinforced Masonry Structures: Review and Classification. Arch Comput Methods Eng 27:1153–1185. https://doi.org/10.1007/s11831-019-09351-x.

Jäger W, Irmschler HJ, Schubert P (2004) Mauerwerk-Kalender 2004. Ernst & Sohn Verlag für Architektur und technische Wissenschaften, Berlin.

Kaushik HB, Rai DC, Jain SK (2007) Stress-strain characteristics of clay brick masonry under uniaxial compression. J Mater Civ Eng 19:728–739.

Lourenço PB (1996) Computational strategies for masonry structures. PhD Thesis. Delft University of Technology, Delft, The Netherlands.

Lourenço PB, Rots JG (1997) Multisurface Interface Model for Analysis of Masonry Structures. J Eng Mech 123:660–668. https://doi.org/10.1061/(ASCE)0733-9399(1997)123:7(660).

Maekawa K, El-Kashif KF (2004) Cyclic cumulative damaging of reinforced concrete in post-peak regions. J Adv Concr Technol 2:257–271.

Malomo D, DeJong MJ, Penna A (2018a) Distinct Element modelling of the in-plane cyclic response of URM piers subjected to shear-compression. Earthq Eng Sructural Dyn 48:1322–1344.

Malomo D, Pinho R, Penna A (2018b) Using the applied element method for modelling calcium silicate brick masonry subjected to in-plane cyclic loading. Earthq Eng Struct Dyn 47:1610–1630. https://doi.org/10.1002/eqe.3032.

Mayorca P, Meguro K (2003) Modeling Masonry Structures using the Applied Element Method. Seisan Kenkyu,j 55:581–584.

Matysek P, Janowski Z (1996) Analysis of factors affecting the modulus of elasticity of the walls. In: Proceedings of the Conference of the Committee of Civil Engineering PZITB: Lublin, Poland.

Meguro K, Hakuno M (1994) Application of the extended distinct element method for collapse simulation of a double-deck bridge. Struct Eng Earthq Eng 10:17–27. https://doi.org/10.2208/jscej.1994.483_17.

Meguro K, Tagel-Din H (1999) Simulation of buckling and post-buckling behavior of structures using applied element method. Bull. Earthq. Resist. Struct. IIS, Univ. Tokyo 32 125–135.

Meguro K, Tagel-Din H (2000) Applied element method for structural analysis: Theory and application for linear materials. Struct Eng Eng 17:21–35.

Meguro K, Tagel-Din H (2001a) Applied element method: a new efficient tool for design of structure considering its failure behaviour. Inst Ind Sci (IIS), Univ Tokyo, Japan, Sept 1–20.

Meguro K, Tagel-Din H (2001b) Applied Element Simulation of RC Structures under Cyclic Loading. J Struct Eng 127:1295–1305. https://doi.org/10.1061/(ASCE)0733-9445(2001)127:11(1295).

Meguro K, Tagel-Din H, Meguro K (2002) Applied Element Method Used for Large Displacement Structural Analysis. J Nat disaster Sci 24:25–34.

Pandey BH, Meguro K (2004) Simulation of brick masonry wall behavior under in-plane

lateral loading using applied element method. 13th World Conf Earthq Eng Vancouver, BC, Canada, August 1–6.

Tagel-Din H, Meguro K (1998) Consideration of Poisson's ratio effect in structural analysis using elements with three degrees of freedom. Bull Earthq Resist Struct Res Ctr 31:41–50.

Tagel-Din H, Meguro K (2000) Analysis of a small scale RCbuilding subjected to shaking table tests using applied element method. 12WCEE New Zealand 1–8.

U.B.C. (1991) International Conference of Building Officials. Uniform Building Code. In: International conference of building officials, USA. Whittier, USA.

APPENDIX B: The Equivalent Frame Model

The Equivalent Frame Model (EFM) is nowadays one of the most popular modelling approaches for the seismic analysis of masonry structures, representing an acceptable compromise between accuracy and computational efficiency. In this work, the EFM-based program TREMURI, developed by Lagomarsino et al. (2013) was employed, and it is referred to in this appendix.

The EFM strategy idealises masonry structures into a frame of deformable regions and rigid nodes. This simple layout is derived from experimental and post-earthquake observations indicating that damage is located in recurrent areas (spandrels and piers) where others work as rigid parts. In the EFM, spandrels are identified as the elements between two aligned vertical openings, and piers, the main elements carrying vertical loads and providing resistance towards horizontal actions, are defined according to a discretisation criterion. Rigid nodes are the portions delimited by those deformable elements. Spandrels allow to couple the lateral response of pier elements, also influencing their boundary conditions restraining their end rotation and, thus, affecting the lateral capacity of masonry panels. An example of the idealisation of a masonry wall into an equivalent frame is presented in Figure B.1.
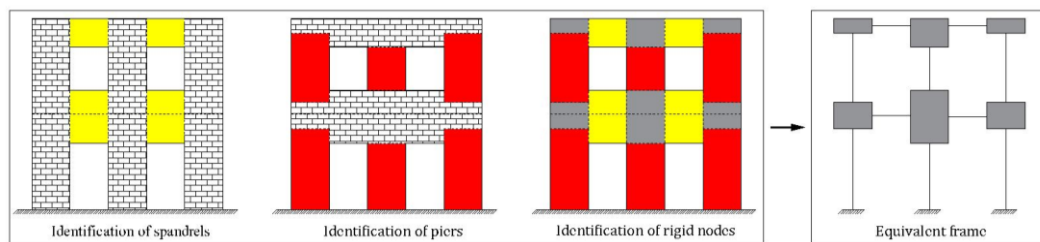

Figure B.1 Wall idealisation according to the EFM (adapted from Lagomarsino et al. 2013)

The EFM is suitable to idealise three-dimensional masonry structures when the behaviour under lateral actions is dominated only by the in-plane response, as out-of-plane contributions are usually neglected (Galasco et al. 2004). In a three-dimensional model (Figure B.2), walls are the bearing elements and floors are modelled as 3 or 4-node orthotropic membranes having only planar stiffness. Walls are modelled as planar frames where internal nodes are bi-dimensional with 3 degrees of freedom (DOFs). 3D nodes connect walls at their intersections and have 5 DOFs, as the rotation around Z-axis is neglected due to the membrane behaviour adopted for floors and walls (Galasco et al. 2004). The nodal mass related to the out-of-plane DOFs is shared with the corresponding DOFs of the nearest two 3D nodes. A Rayleigh viscous damping is considered in dynamic analyses.
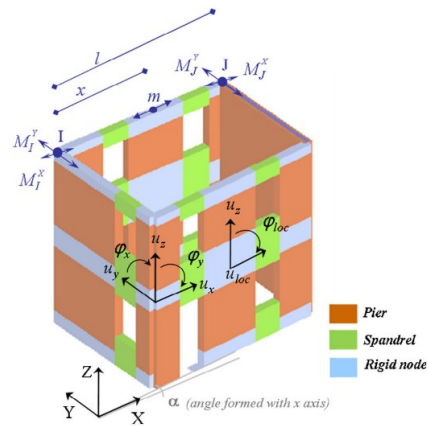
Figure B.2 3D model with 3D and 2D nodes identification and out-of-plane mass sharing
(Lagomarsino et al. 2013)

Nonlinear macroelement models

A nonlinear macroelement represents each spandrel and pier element. In order to have a nonlinear model for seismic analysis, the macroelement has to satisfy some specific requirements. It has to represent the masonry panel elastic properties, evaluate lateral strength associated with shear and flexure-rocking, and produce a physically consistent cyclic response under lateral loading (Penna et al. 2014).

The macroelement proposed by Gambarotta and Lagomarsino (1996) satisfies the aforementioned requirements when used to simulate experimental tests (e.g. Galasco et al. 2004). The macroelement is a two-node element able to replicate the cyclic behaviour of masonry panels because of its kinematical structure with two additional degrees of freedom at the centre of the body, which allows the description of both shear and coupled axial-flexural behaviour.

The macroelement models implemented in TREMURI program and, thus employed in this thesis, are the macroelement proposed by Penna et al. (2014) and Bracchi et al. (2021a; 2021b), and they represent an evolution of the original model proposed by Gambarotta and Lagomarsino (1996). In this section, the macroelement approach is briefly discussed.

The macroelement is a two-node element composed of three parts: a central body with two internal degrees of freedom, where only shear deformations are allowed, and two external zero-length spring interfaces responsible for the axial-flexural behaviour Figure B.3a. The macroelement kinematics can be described by eight degrees of freedom, six nodal displacement components ($u_i, w_i, \varphi_i, u_j, w_j, \varphi_j$) and two internal components (w_e, φ_e). The internal shear force is constant along the element axis ($V_i=V_j=V$). Indeed, no distributed transversal actions are considered. The external interfaces can be considered infinitely rigid in shear and characterised by a no-tension elasto-plastic model in compression, accounting for the material limited compressive strength associated with toe-crushing phenomena. With these assumptions, the macroelement kinematic and compatibility relations result to

be significantly simplified, with a consequent reduction of the actual degrees of freedom of the model (Bracchi et al. 2021a). In the macroelement proposed by Penna et al. (2014), a bilinear constitutive model with stiffness degradation (Figure B.3b) has been assigned to the external interfaces. Bracchi et al. (2021) modified the compressive model accounting for residual displacements and increased energy dissipation (Figure B.3c), which also implemented an iterative correcting algorithm to overcome the inability to capture both the axial and flexural stiffness of the element simultaneously. A noteworthy point of this macroelement is the fully mechanically-based shear behaviour and the analytically-integrated formulation of the coupled axial-flexural response, which further reduces the computation time.
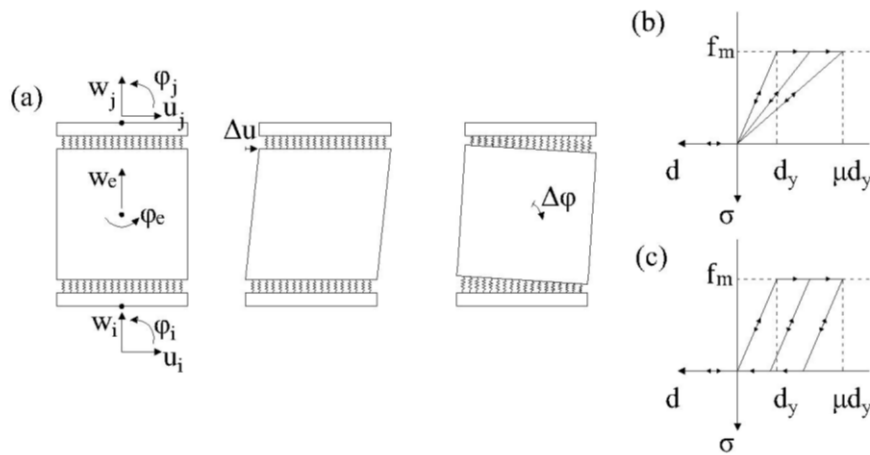

Figure B.3 The macroelement (a) and the compressive law of Penna (b) and Bracchi (c)

The macroelement model of masonry piers considers horizontal mortar joints as possible sliding surfaces and provides shear strength to the central body of the element. The shear strength of piers is based on the contributions of cohesion and friction. The central body kinematics is described by relative transversal displacement u, which includes the elastic component u_{el} and plastic sliding s (Figure B.4a). The element damage and shear deformability are concentrated in the central part of the pier.

β and c_t are phenomenological parameters governing the nonlinear shear response. Gc_t, controls the macroelement inelastic shear deformability, and β influences the slope of the post-peak softening branch. The shear damage variable α_s represents the damage level, and it is equal to 1 when the panel attains the maximum peak shear strength, increasing in the post-peak softening branch. The shear model and the influence of the parameter α_s are presented in Figure B.4b.
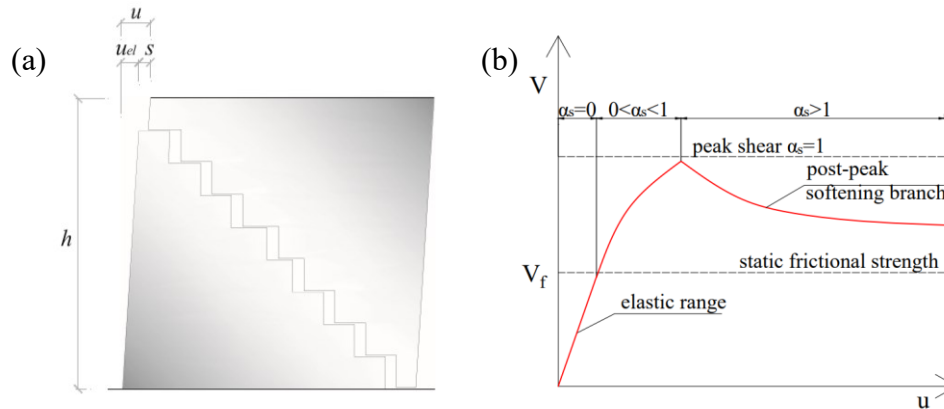
Figure B.4 Panel shear deformation and plastic sliding (a), shear force versus displacement:
identification of shear and displacement components (b) (adapted from Penna et al. 2014)

In the macroelement proposed by Penna et al. (2014), the shear behaviour was described by a Coulomb criterion where a preliminary evaluation of equivalent cohesion and friction coefficient was needed to reproduce the shear strength according to the adopted strength criterion. This is equivalent to linearising the strength criterion in the neighbourhood of a point corresponding to the axial load obtained from the self-weight analysis (N_0). This procedure involves several approximations. First of all, the strength criterion has to be selected a priori, and then the equivalent shear strength parameters are calculated before the analysis and kept constant, neglecting any variation of axial load and boundary conditions. Moreover, the evaluation of the equivalent shear strength parameters can be performed for a limited number of elements. Similarly, the parameters governing the nonlinear shear deformability (i.e. β and Gc_t) are selected before the analyses, typically calibrated on experimental results obtained from a shear-compression test performed on a panel representing the same masonry of the modelled structure and kept constant for all elements. The new formulation of the macroelement proposed by Bracchi et al. (2021b) addresses these issues by automatically evaluating the equivalent cohesion and friction coefficient according to the shear strength criteria implemented in the new macroelement and reported in the following.

1) The strength criterion proposed by Mann and Müller (1982), accounts for the brick tensile failure, f_{bt}, and is converted into a global strength criterion introducing the correction proposed by Magenes and Calvi (1997), considering the influence of the shear span ratio, α_v. Where α_v is equal to h_0/l. h_0 is the distance between the section with zero moment and the section with the maximum moment, and l and t are the wall length and thickness, respectively.

2) The shear strength criterion proposed by Turnšek and Sheppard (1980), is associated with the attainment of the tensile strength of masonry, f_{tu}. Where b is a coefficient accounting for the shear stress distribution in the centre of the wall and it is a function of the aspect ratio.

3) The shear strength is evaluated by referring to the compressed part of the section after a crack has developed, where f_{vlt} is the shear strength associated with cracks in the units (CEN 2005).

4) The shear strength is associated with stepped cracks through the mortar joints in the whole cross-section or 5) with sliding along bed joints of a cracked cross-section (Magenes and Calvi 1997). Where the corrections reported in 6) are proposed by Mann and Müller (1982) to account the presence of weak head joints. The pure sliding along bed joints can be considered with 4) without the factor $(1 + \alpha_v)$ proposed by Magenes and Calvi and without the correction proposed by Mann and Muller.

$$(1) \quad V_{res} = \frac{f_{bt}lt}{2.3(1 + \alpha_V)}\sqrt{1 + \frac{N_0}{f_{bt}lt}} \qquad (2) \quad V_{res} = \frac{f_{tu}lt}{b(1 + \alpha_V)}\sqrt{1 + \frac{N_0}{f_{tu}lt}}$$

$$(3) \quad V_{res} = lt\,\frac{1.5f_{vlt}ltN_0}{N_0 + 3f_{vlt}\alpha_V lt} \qquad (4) \quad V_{res} = \frac{lt}{1 + \alpha_V}\left(\bar{c} + \bar{\mu}\frac{N_0}{lt}\right)$$

$$(5) \quad V_{res} = lt\,\frac{\left(1.5\bar{c} + \bar{\mu}\frac{N_0}{lt}\right)}{1 + 3\bar{c}\alpha_V / \left(\frac{N_0}{lt}\right)} \qquad (6) \quad \begin{cases} \bar{\mu} = \kappa\mu \\ \bar{c} = \kappa c \end{cases}, \qquad where\ \kappa = \frac{1}{1 + \mu tan\theta_c}$$

The shear strength is usually calculated as the minimum between the one corresponding to sliding along the joints and the one corresponding to the development of cracks in the units.

The shear strength formulation of the macroelement proposed by Bracchi and Penna (2021b) involves equivalent cohesion and friction to be used in a macroscopic Coulomb-like criterion. The automatic evaluation of the equivalent shear parameters is obtained by linearising the adopted strength criterion, which is the one that results in the minimum shear strength.

References

Bracchi S, Galasco A, Penna A (2021a) A novel macroelement model for the nonlinear analysis of masonry buildings . Part 1 : Axial and flexural behavior. Earthq Eng Sructural Dyn 50:2233–2252. https://doi.org/10.1002/eqe.3445.

Bracchi S, Penna A (2021b) A novel macroelement model for the nonlinear analysis of masonry buildings. Part 2: Shear behavior. Earthq Eng Struct Dyn 50:2212–2232. https://doi.org/10.1002/eqe.3444.

CEN (2005) Eurocode 6: Design of masonry structures, Part 1-1: General rules for reinforced and unreinforced masonry structures. Eur Comm Stand Belgium.

Galasco A, Lagomarsino S, Penna A, Resemini S (2004) Non-linear Seismic Analysis of Masonry Structures. Proceedings of the 13th World Conf Earthq Eng Paper No. 843, Vancouver, Canada.

Gambarotta L, Lagomarsino S (1996) On the dynamic response of masonry panels. In: national conference "masonry mechanics between theory and practice." Messina, Italy.

Lagomarsino S, Penna A, Galasco A, Cattari S (2013) TREMURI program: An equivalent frame model for the nonlinear seismic analysis of masonry buildings. Eng Struct 56:1787–1799. https://doi.org/10.1016/j.engstruct.2013.08.002.

Magenes G, Calvi GM (1997) In-plane seismic response of brick masonry walls. Earthq Eng Struct Dyn 26:1091–1112.

Mann W, Mülller H (1982) Failure of shear-stressed masonry: an enlarged theory, tests and application to shear walls. In:Proc Br Ceram Soc 223–235.

Penna A, Lagomarsino S, Galasco A (2014) A nonlinear macroelement model for the seismic analysis of masonry buildings. Earthq Eng Struct Dyn 43:159–179. https://doi.org/10.1002/eqe.2335.

Turnšek V, Sheppard P (1980) Shear and Flexural Resistance of Masonry Walls. Proceedings of the International Research Conference on Earthquake Engineering. Skopje, Macedonia, pp 517–573.